# Constraining the Evolution of Spiral Galaxies over Cosmic Time with Observations and Simulations

**Qian-Hui Chen**

A thesis submitted for the degree of

*Doctor of Philosophy*

The Australian National University

Research School of Astronomy & Astrophysics


Australian National University

September 2025

*To my beloved parents, my partner,*
*the wonderful Universe that connects us all,*
*and the beautiful Earth we call home.*

# Disclaimer

I hereby declare that the work undertaken in this thesis has been conducted by me alone, except where indicated in the text. I conducted this work between October 2021 and March 2025, during which period I was a PhD student at the Australian National University. This thesis, in whole or any part of it, has not been submitted to this or any other university for a degree.

This thesis has been compiled as a Thesis by Compilation in accordance with relevant ANU policies. The first two main chapters in this thesis have been published in peer-reviewed journals and the third main chapter has been submitted to Monthly Notices of the Royal Astronomical Society. I have made significant contribution to each of these journal articles and have written the text of the papers myself, except where indicated otherwise.

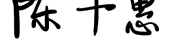

Qian-Hui Chen

14 September 2025

# Acknowledgements

My PhD has been full of complex emotions – ranging from the joy of solving intricate programming problems and publishing papers, to the disappointment of inconsistencies between theories and observations or simulations, the loneliness of being far from my family, the frustration of facing discrimination as a person of colour, and unwelcome blue and stress from time to time. Revealing the underlying physics from data has never been easy, sometimes even challenging the knowledge I thought I know about the Universe. Yet, I am deeply grateful to have survived this PhD journey and grown into a better person, not only academically but also personally, thanks to the endless love and support of several incredible people. They reminded me of my talent and passion for astrophysics, helping me overcome obstacles and persevere through the toughest moments.

I would like to begin by expressing my heartfelt gratitude to my parents. Although our family is never even close to middle class, they never discouraged me from pursuing a career in astronomy, even though it might not lead to financial stability quickly. I am especially grateful for my mother's wisdom in encouraging me to choose a path I am most passionate about, so I would never live with regret. Despite not having had the opportunity to attend college themselves, my parents have always shown a keen interest in my studies, often sharing their suggestions notably on choosing a colour bar for my plots. However, I still carry a sense of guilt for being unable to care for my mother when she was diagnosed with a brain tumour during COVID-19 pandemic. They never blamed me and even tried to conceal it from me, shielding me from worry. Their selflessness and numerous support mean the world to me. I know they are proud of me, and I want them to know that I am equally proud to have been born into such a loving family.

I express my deepest gratitude to everyone who has recognised and valued my talent and ability, with special thanks to my supervisors, Katie Grasha and Emily Wisnioski. I cannot count the times I shared my fears and tears in their offices, only to leave feeling encouraged and understood. I am profoundly grateful to Katie for designing my exceptional PhD projects and meanwhile leaving me the space to grow as an independent thinker and researcher. More importantly, she reminded me that the true goal of a PhD is not just scientific achievement but also personal growth and becoming a better *person*. Without Katie's belief in me, I might still be that timid undergraduate doubting myself and crying in a quiet bathroom. It took her over an year to establish my self-confidence which I believe will benefit me for a lifetime. I extend my sincere thanks to Emily for her wise scientific guidance, invaluable career advice, and her kindness, which always felt like the preach of an angel – listening with empathy and offering care. Her office has been a sanctuary for me where my research outcomes were all welcomed, and critical feedback was echoed with practical solutions. I am especially grateful for Emily's willingness to

share her experiences and thoughts as an introvert in academia, which made me feel less alone in my journey. I also thank my co-supervisors Andrew Battisti and Paul Torrey for their support and constructive criticism which have greatly enhanced my research.

I owe a huge thank you to my friends who supported me throughout my PhD journey. If my PhD journey makes me eligible for a "Dr." in astronomy, my friends certainly deserve a "Dr." in cheering me up. I am deeply grateful to my partner, Eb Chomkul, for taking care of me during my sick and frustrated moments, and for his endless love that helps me see myself more clearly and live a happier life. Special thanks to Eb for his constant companionship, giving meaning to every small and peaceful moment we shared. He is an expert in "brainwashing", repeatedly whispering "you are perfect" in my ear. I also want to thank Hye-Jin Park (Hayden) for her kindness and non-stop 24/7 support, like a peer-version of "Ka-mily". It has always been safe and comforting to share my true thoughts with Hayden, and I greatly appreciate her sincere feedback. I also owe a huge thank you to my senior peers, Zefeng Li and Yifei Jin, whose invaluable advice and guidance have stimulated my career development. I truly cherish the valuable friendships I built during my PhD, including my housemate Peixin Zhu and my officemates Zenghua Zhou, Arunima, and Purvi Udhwani. Thank you all for listening to my random rants and enduring my think-out-loud moments in the office – you have made my office life colourful. To all my other friends who have encouraged me or lent a helping hand during this journey – Dingyuan Cao, Maja Jabłońska, Radhika Achikanath Chirakkara, Paula Boubel and many others – thank you. Each of you has played a role in making this challenging journey a little brighter, and I am endlessly grateful for your support.

Finally, I want to extend my gratitude to Canberra, the bush capital. This village has witnessed my growth into a better person – one who conducts better research, sees herself more clearly, and holds a deeper appreciation for nature. The natural beauty of Canberra have provided me with precious opportunities for introspection. Canberra has also brought me friendships beyond the realm of astronomy. I am especially grateful to my climbing friends, Hay Chan and Joyce Yung, for their unshakable belief in me, even when I struggled to believe in myself. Their kindness, paired with their comforting cooking, has been a consolation for my homesickness. Canberra is also where I met my two beloved pet rabbits, Auriga and Sesame, who bring me daily joy and emotional support with their endless fluffy cuddles. I am thankful to everything happened to me in Canberra, both the good and the bad, as they have all shaped me into the person I am today – a unique character in this world and in history.

# Abstract

Spiral structures are observed in approximately two-thirds of massive galaxies in the local Universe, yet their formation mechanisms and impact on gas and stellar distributions remain debated. Theories such as density wave theory, dynamic spiral theory, and tidal-induced spiral theory offer different explanations, each predicting distinct material flows across spiral arms, but observational constraints on the dominant mechanisms remain inconclusive. This thesis aims to bridge this gap by investigating how spiral arms regulate the distribution of gas and stars across different cosmic epochs and environments.

Using adaptive optics with the Multi-Unit Spectroscopic Explorer (MUSE) from the Middle Age Galaxy Properties with Integral Field Spectroscopy (MAGPI) survey, I resolve spiral structures in galaxies at $z \sim 0.3$, achieving $0.6 - 0.8''$ spatial resolution. At $z \sim 0$, I study nearby spiral galaxies from the TYPHOON survey, which provides a large field-of-view covering the entire optical disc. At both redshifts, I compare the star formation rate (SFR) and gas-phase metallicity across the leading edge, spiral arms, and trailing edge. While I find evidence supporting density wave theory in both epochs, this thesis also reveals signatures of dynamic spiral theory, with galaxies lacking clear azimuthal offsets in SFR or metallicity at $z \sim 0$ and $z \sim 0.3$. Interestingly, an interacting galaxy at $z \sim 0$ exhibits an azimuthal offset opposite to the prediction of density wave theory, potentially driven by the ongoing merger event. At $z \sim 0.3$, I further analyse the stellar age distribution using $D_{4000}$ as a proxy, emphasizing the need for appropriate timescale tracers in studying spiral galaxies.

To interpret these observational results in a broader context of long-term evolution, I use Auriga level 3 cosmological zoom-in simulations to investigate the temporal stellar age distributions. Tracking the stellar age pattern across the past 5 Gyr, I find that the simulated spiral galaxies typically exhibit younger stellar populations on their leading edges, consistent with density wave theory. However, my analysis also shows that mergers and fly-bys can erase the age pattern built by spiral potential, with azimuthal variations recovering within two snapshot (~600 Myr). These results highlight the interplay between external environmental perturbations and internal spiral dynamics in shaping stellar age distributions and propagating star formation over time.

By integrating IFU observations with simulations, this thesis offers new insights into both the short-term dynamics and long-term evolution of spiral arms. While no single theory fully explains the origin of all spiral structures in the low-$z$ Universe, my findings suggest that external perturbations can temporarily erase azimuthal variations imprinted by spiral potentials, helping to reconcile discrepancies between theoretical predictions and observed galaxies. Future work will expand this framework to higher-redshift ($z = 1 - 3$)

observations and higher temporal-resolution simulations, enabling a statistical test of density wave theory by tracking the evolution of azimuthal variations in gas and stellar populations.

# Contents

# List of Figures

# List of Tables

Chapter 1

# Introduction

## 1.1 Spiral structures in disc galaxies

Galaxies are systems of stars, gas, dust and dark matter bounded by gravity. The most well-known galaxy is our home galaxy – the Milky Way, appearing as a shimmering band in the night sky, often imagined as a silver river in Chinese culture. The dust lane of the Milky Way is imagined as an emu in Indigenous Australian traditions. Throughout history, humans have gazed at the night sky, marvelling at the diverse shapes and morphologies of celestial objects, long before understanding their true nature or vast numbers.

Galaxies with spiral structures are beautiful treasures in the Universe, first observed by Lord Rosse in the "Whirlpool" galaxy – Messier 51 back in 1845 (Steinicke 2012). Spiral galaxies typically consist of a rotational disc, a bulge, potentially a black hole in the centre, a stellar halo and a dark matter halo. Spiral arms are regions in a shape similar to the cross-section of a nautilus shell, exhibiting higher surface brightness compared to the surrounding disc. There are concentrations of gas clouds and young bright stars, usually along with intense star formation activities in the spiral arms.

In 1926, Edwin Hubble developed a classification scheme (Hubble 1926) based on the galaxy morphology, although he named the observed galaxies as "extragalactic nebulae". This Hubble scheme includes two sections: elliptical galaxies and spiral galaxies (Figure 1.1). Historically, elliptical galaxies were termed 'early-type galaxies', while spiral galaxies were called 'late-type galaxies'. This terminology was based on analogy with classification of stars in use at the time, as noted by Hubble himself in a footnote, no temporal connotation was intended by the naming convention. Later, subsequent discoveries revealed that this naming convention does not align with the actual evolutionary pathways of galaxies (Conselice 2014).

Spiral galaxies are among the most commonly observed galaxy types in the local Universe. The citizen science project Galaxy Zoo (Lintott et al. 2008; Willett et al. 2017), which engaged over 120,000 volunteers to classify galaxy morphologies based on images from the Sloan Digital Sky Survey (Adelman-McCarthy et al. 2008), found that more than two-

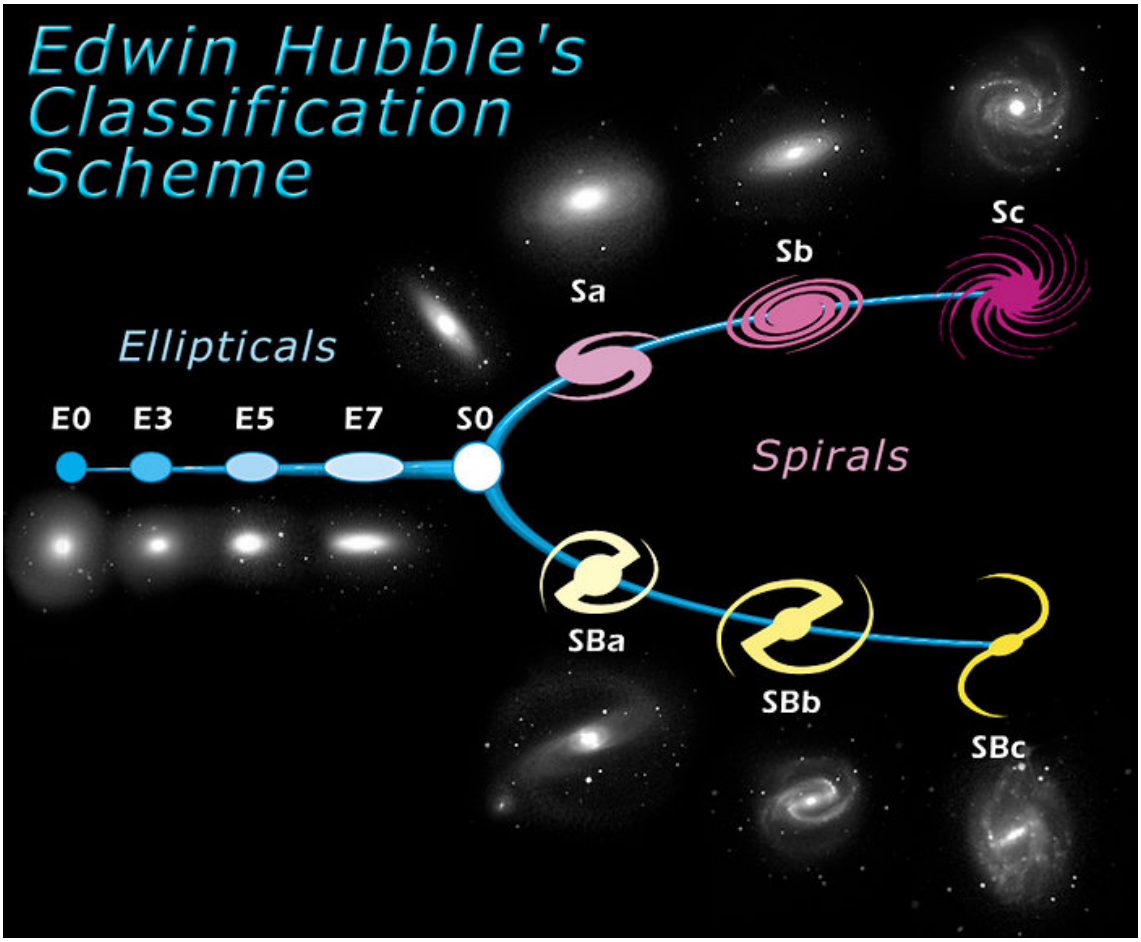


**Figure 1.1:** Edwin Hubble's classification scheme, commonly known as the 'Hubble Fork' (Hubble 1926). The left branch represents elliptical galaxies, with a number designating their ellipticity: 'E0' denotes nearly spherical galaxies, while 'E7' represents the most elliptical. The right branch depicts spiral galaxies, divided into two groups based on the presence of a central stellar bar. Spiral galaxies are further classified from 'Sa' to 'Sc,' reflecting the tightness of their spiral arms: 'Sa' galaxies have tightly-wounded arms and prominent central bulges, whereas 'Sc' galaxies exhibit more open arms and smaller bulges. Image credit: NASA & ESA.

**Figure 1.2:** A broad range of morphologies in spiral galaxies has been observed in the local Universe, including a spiral galaxy undergoing an merger event, a flocculent spiral galaxy, a barred-spiral galaxy and a multi-armed spiral galaxy. Upper left: M51 observed with Hubble Space Telescope (HST). Upper right: combined observation of NGC 628 from HST and JWST. Lower left: NGC 1300 observed with HST. Lower right: NGC 1376 observed with HST.

thirds of massive galaxies in the local Universe ($0.001 < z < 0.25$) exhibit spiral features. The morphologies of these spiral galaxies display remarkable diversity, ranging from grand-design spirals with prominent two-armed structures to multi-armed and flocculent spirals, and from tightly wound to open-armed features (see Fig 1.2). Astronomers have detected spiral structures in [CII] gas at a redshift of 4.41 (BRI 1335–0417; Tsukui & Iguchi 2021), dating back more than 12 billion years. With the latest generation of telescopes such as James Webb Space Telescope (JWST), we can now resolve galaxies at high redshifts and investigate their morphologies in greater detail. The diversity in spiral structures persists across cosmic time (Kuhn et al. 2024). The mechanisms driving spiral features and their role in organising material in the disc remains a debated topic.

Spiral galaxies constitute a significant fraction of all galaxies but also host the majority of star formation. Spiral galaxies exhibit higher star formation rate surface density ($\Sigma_{\rm SFR}$) than elliptical galaxies with similar gas density (Martig et al. 2013; Medling et al. 2018; Cano-Díaz et al. 2019). Despite numerous observations and studies, the precise role of

spiral arms in regulating star formation and structuring the interstellar medium (ISM) in galaxy disc remains debated. In the sections below, I introduce several well-known theories explaining the origin of spiral structure and their theoretical prediction of stellar dynamics, ISM distributions and regulation of star formation.

## 1.2 Origin of spiral structures

### 1.2.1 Mathematical description of spiral arms

The morphology of spiral arms can be parametrised using i) the number of spiral arms, ii) pitch angle $\theta$, iii) starting azimuth, iv) amplitude or contrast of arm versus disc, and v) lifetime of the arms. The pitch angle (Fig 1.3) is defined as the angle $\theta$ between the tangent of spiral arms and a circle at any radius $R$:

$$\tan\theta = \frac{1}{R}\frac{dR}{d\phi}, \tag{1.1}$$

where $\phi$ is the azimuth angle measured counter-clockwise from the positive $x$-axis to the point. The looser the spiral arm is, the larger the pitch angle is. This morphological complexity highlights the challenges in uncovering the physical mechanisms behind the formation of spiral arms, suggesting that multiple theories may be required to fully explain their origins. The following sections introduce several theories successfully explain the origin of some spiral galaxies in the Universe.

### 1.2.2 (Quasi-stationary) density wave theory

A long-standing challenge in understanding the origin of spiral arms is the *winding problem*, concerning the origin of spiral arms. The simplest idea of spiral arms assumes that material within the spiral arms remains concentrated and fixed, without flowing in or out of the spiral arms. However, since spiral structures at different radii rotates at the same orbital speed, the angular velocity decreases with increasing radius. This would cause the spiral arms to wind progressively tighter with each orbit until they disappear, leading to the "winding problem". Lin & Shu (1964) proposed the quasi-stationary density wave theory, which addressed the winding problem, inspired by the initial idea of a kinematic density wave in Lindblad (1960).

In density wave theory, spiral arms are not rigid material structures but instead form from gravitational perturbations. Instead, they are regions of enhanced gravitational potential, with stars and gas continuously flowing in and out. This process is often likened to cars moving through a traffic jam — slowing down as they enter and accelerating once they pass

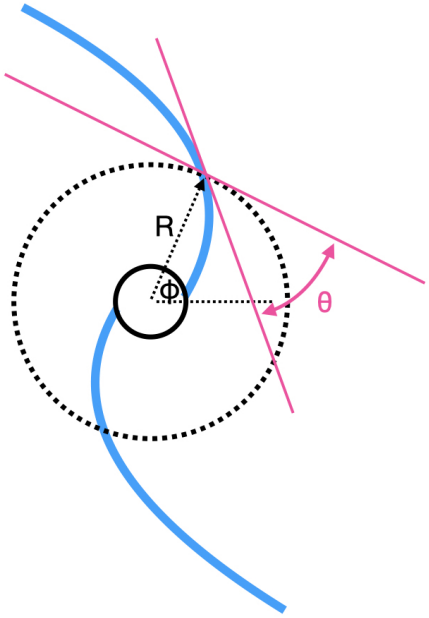


**Figure 1.3:** The pitch angle at any radius $R$ is calculated following Eq. 1.1. The pink lines indicate the tangent of spiral arm and the circle.

through. In this hypothesis, spiral arms are rigid-body orbiting the galaxy with constant shapes, solving the winding problem. Density wave spiral arms are long-lived features in galaxies and they rotate slowly at a fixed angular velocity, known as the pattern speed, across the entire galaxy disc. Meanwhile, the material in the disc rotates at decreasing angular velocities with increasing radii. This differential rotation leads to the dynamics – material rotates together with the spiral arms only at the co-rotation radius ($R_{CR}$). Within the $R_{CR}$, stars and ISM overtake the spiral arms, mixing with the material on the leading edge of the arms (see Fig 1.4). Observations (Choi et al. 2015; Peterken et al. 2019) have found direct evidence supporting the quasi-stationary density wave theory by measuring the pattern speed and the angular velocity of material.

### 1.2.3 Dynamic spiral theory

Unlike density wave theory, dynamic spiral theory predicts that spiral arms are transient and recurrent (Sellwood & Carlberg 1984, 2014), instead of long-lived. The decreasing angular velocity at larger radii causes local gravitational instabilities to be sheared and amplified into a spiral shape. This mechanism is called swing amplification (Julian & Toomre 1966; Toomre 1981). Toomre (1964) define a dimensionless parameter to quantify the disc stability at different radii:

$$Q(R) = \frac{\sigma_R}{\sigma_{R,\mathrm{crit}}}, \text{ where } \sigma_{R,\mathrm{crit}} = \frac{3.36 G f \Sigma(R)}{\kappa(R)}. \tag{1.2}$$

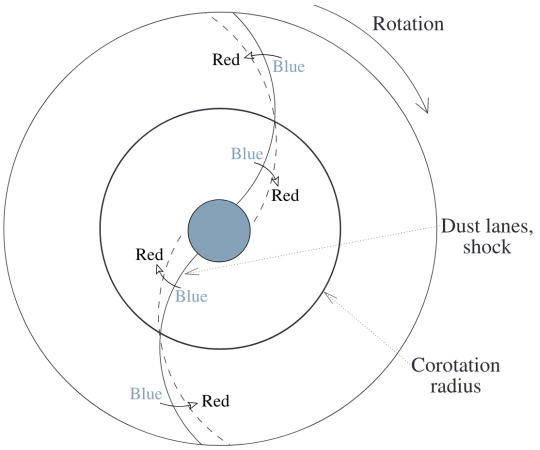


**Figure 1.4:** Theoretical prediction of density wave theory on the spatial distribution of young (blue) and old (red) stars (Martínez-García et al. 2009a).

Here, $\sigma_R$ is the radial velocity dispersion at the radius of $R$, and $\kappa$ is the Lindblad epicycle frequency, calculated as:

$$\kappa(R) = \sqrt{R\frac{\partial\Omega^2}{\partial R} + 4\Omega^2}, \tag{1.3}$$

where $\Omega$ is the angular frequency. $\Sigma(R)$ represents the radial surface density, $G$ is the gravitational constant and $f$ is a constant that accounts for a fraction of the surface density, ranging between 0 and 1. In Sellwood & Carlberg (2014), $f$ is set to 0.3 to suppress vigorous bar-forming instabilities in the disk. Swing amplification occurs when Toomre's $Q$ lies between 1 and 2, leading to the formation of spiral arms as superpositions of unstable waves. $N$-body simulations based on dynamic spiral theory successfully reproduce multi-arm spiral galaxies (Sellwood & Carlberg 1984; Baba et al. 2009; Fujii et al. 2011). These simulations reveal that spiral structures continuously form and dissolve due to gravitational instabilities.

A key consequence of these transient spiral arms is their role in regulating star formation. The accumulation of gas fell into the arms promotes the formation of new stars, which in turn increases the disc's velocity dispersion over time. As stellar feedback injects energy into the disc, Toomre's $Q$ gradually rises to $\gtrsim$ 2 after a few rotations, leading to the dissipation of spiral structures. However, the interplay between self-gravity and shear ensures that spiral arms are continuously regenerated: shear stretches the spiral arms into smaller segments, typically a few kpc in size, while self-gravity reconnects these fragments to reform large-scale structures. Simulations typically incorporate effective gas cooling to maintain Toomre's $Q$ within the range of $1 - 2$ in order to successful generate dynamic spiral arms that persist for ~10 Gyr (e.g., Fujii et al. 2011).

In summary, dynamic spiral theory predicts that spiral arms rotate together with the rest of the disc, exhibiting decreasing angular velocities with increasing radii. Material

subsequently falls into the regions of minimum potential from both sides of the spiral arms. As a result, there is no differential rotation between the disc material and the spiral arms, in contrast to density wave-driven spiral arms.

### 1.2.4 Tidal-induced spiral arms

Galaxy interactions are commonly observed in the Universe and often display distinctive tidal features, such as tails, bridges, and even spiral structures penetrating into the galaxy centre (e.g., M 51; Rosse 1850). The first successful model is presented in Holmberg (1941) to show that tidal forces from a passing companion could induce the formation of spiral arms. Tidal-induced spiral theory typically predicts the formation of grand-design spiral galaxies (Semczuk et al. 2017, 2018; Antoja et al. 2022).

An intriguing question remains: how do spiral arms from tidal interaction rotate compared to the rest of the disc, and how long can these spiral structures persist? Many studies, mostly based on simulations (Semczuk et al. 2017; Oh et al. 2008; Pettitt & Wadsley 2018) and a few observations (e.g., Rots & Shane 1975), suggest that tidal-induced spiral arms are kinematic density waves, instead of material spirals or quasi-stationary density waves. Only at large radii, the spiral arms may be material arms with little gas passing through the spiral arms (Meidt et al. 2013). This implies that at most radii, the angular velocity of the spiral arms differs from the rest of the disc ($\Omega_p \neq \Omega$). Kinematic density waves share similarities with quasi-stationary density waves (Sec 1.2.2), as both predict gas and stars moving into and out of the spiral arms. However, the key difference lies in the spiral pattern speed: for kinematic density waves, the pattern speed is no longer fixed across the galaxy disc. Instead, Oh et al. (2008) calculated the pattern speed of a tidal-induced spiral arms and found that they decrease with radius, following $\Omega_p(\mathrm{R}) = \Omega(\mathrm{R}) - \kappa(\mathrm{R})/2$. Therefore, material rotates faster ($\Omega > \Omega_P$) and enters the spiral arms from the concave side. Some of the stars follow elliptical orbits that are generally not closed, under the tidal influence of the passing companion. Simulations further show that tidal-induced spiral arms wind up slowly as time passes. For example, in a simulation of M 51 (Dobbs et al. 2010), M 51b will induce spiral arms with a pitch angle of 5-6° after 1 Gyr, which is $\sim 4$ times slower than material within the spiral arms.

### 1.2.5 Other theories

There are many other theories that successfully explain the origin of some spiral features, including bar-driven spiral arms, stochastic star formation, and asymmetries in dark matter distribution. In this section, I will include a brief overview of several other theories.

### Bar-driven spiral arm

Bars are often observed in spiral galaxies (Figure 1.1). Elmegreen & Elmegreen (1982) found that 70% grand-design spiral galaxies have their arms starting at the end of a bar while 30% do not. It is under debate whether bar and spiral arms share the same pattern speed or are coupled via non-linear interactions (Mo et al. 2010). Some observations (Elmegreen et al. 2007; Salo et al. 2010; Bittner et al. 2017) found that strong bars correlate with strong spiral arms, with one possible explanation being that the arms are driven by the bar at the same pattern speed (Tagger et al. 1987). Block et al. (2004) raised a parameter of $Q$ – the maximum of tangential force amplitude normalized by mean radial force – and found a impressively clear correlation between the maximum of $Q_b$ (in the bar) and $Q_s$ (in the spiral arms) based on observation of 12 nearby barred-spiral galaxies. This correlation has been seen in some later studies (e.g., Buta et al. 2009; Salo et al. 2010), but not in others (e.g., Buta et al. 2005; Durbala et al. 2009). The process by which a bar drives spiral arms remains an open question, and a larger observational sample is needed to resolve the debate.

### Stochastic star formation

Mueller & Arnett (1976) and Gerola & Seiden (1978) proposed that stochastic self-propagating star formation – when stars in the spiral arm regions die, the ejection of gas and radiation by supernova winds compresses the nearby material, which subsequently triggers the next cycle of star formation – can lead to the formation of spiral arms in flocculent spiral galaxies. Due to the decreasing angular velocity at larger radii, the newly borne stars are sheared into material spiral arms. In this hypothesis, spiral arms are short-lived, with a lifetime of approximately one generation of stars, and recur in the neighbourhood. However, it is challenging to identify flocculent spiral arms due to their lower contrast against the surrounding disc compared to grand-design and multi-arm spirals.

### Asymmetries in dark matter distribution drive formation of spiral arms

Some simulations (Tutukov & Fedorova 2006; Chang & Chakrabarti 2011; Khoperskov et al. 2013) have reported that asymmetries in the dark matter halo or interactions between the dark matter sub-halos and the main halo galaxy can form spiral structures. However, it is difficult to distinguish from other mechanisms such as tidal-induced spiral arms, since both baryon particles and dark matter are involved in galaxy interactions, or from spiral arms driven by bar instability.

## 1.3 Observational constraints

Different theories predict distinct behaviours for stars and the ISM. Observing the 2D distribution of stars and the ISM can help identify the dominant mechanism driving spiral arms in galaxies. In this section, I review theoretical expectations for the distribution of stars and the ISM, observational tracers, and previous studies, with a focus on the three leading theories in Sec 1.2 – density wave theory, dynamic spiral theory, and tidal-induced spiral arms.

### 1.3.1 Star formation rate

Giant molecular clouds (GMCs) are molecular gas clumps that typically have a mass of $10^5 - 10^6 M_\odot$, a size of a few tens of parsec, a temperature of $\sim 10-20$ K and a density on the order of $n_{\rm H_2} \simeq 100 - 300$ cm$^{-3}$. Star formation takes place when the most massive GMCs and cores collapse due to gravity. Assuming that GMCs are self-regulating, homogeneous and isothermal spheres, ignoring any turbulence, GMCs start to collapse when their mass exceeds the Jeans Mass ($M_{\rm J}$; Draine 2011):

$$M_{\rm J} = \frac{\pi^{5/2}}{6} \frac{c_s^3}{\sqrt{G^3 \rho}} \simeq 40 M_\odot \left(\frac{c_s}{0.2{\rm km\ s^{-1}}}\right)^3 \left(\frac{n_{\rm H_2}}{100{\rm cm^{-3}}}\right)^{-1/2}, \tag{1.4}$$

where we adopt the molecular hydrogen mass as $3.4\times10^{-24}$g. Here,

$$c_s = \sqrt{\frac{5 k_{\rm B} T}{3 m_{\rm p}}}, \tag{1.5}$$

where $m_{\rm p}$ is the proton mass, $k_{\rm B}$ is the Boltzmann constant and $T$ is the temperature. Without any other pressure force, molecular hydrogen collapse at a free-fall timescale ($\tau_{\rm ff}$) when GMCs is more massive than $M_{\rm J}$:

$$\tau_{\rm ff} = \sqrt{\frac{3\pi}{32 G \rho}} \simeq 3.6 \times 10^6 {\rm yr} \times (\frac{n_{\rm H_2}}{100{\rm cm^{-3}}})^{-1/2} \tag{1.6}$$

The $\tau_{\rm ff}$ is shorter than the observed lifetime of GMCs (Chevance et al. 2020, 2023), which implies the needs of non-thermal pressure against the gravity, such as turbulence and magnetic fields.

Spiral arms provide a denser environment for GMCs, increasing the likelihood of cloud collisions (Dobbs & Pettitt 2015; Baba et al. 2017; Hunter et al. 2023; Horie et al. 2024). The resulting increase in $n_{\rm H_2}$ leads to a lower $M_{\rm J}$ and a shorter $\tau_{\rm ff}$. Additionally, collisions between smaller GMCs can give rise to more massive GMCs (Hsu et al. 2023). Conse-

quently, the over-density in spiral arms promotes the formation of new stars (Querejeta et al. 2024).

All spiral arm theories agree that star formation rates (SFRs) are enhanced within spiral regions, which is supported by observations. However, different theories propose distinct two-dimensional distributions of SFR, particularly regarding offsets on either side of the spiral arms. In quasi-stationary density wave theory (Roberts et al. 1975), gas entering a spiral arm potential experiences a shock at the potential minimum (traced by CO), followed by delayed star formation downstream (traced by H$\alpha$). The offset arises from the finite timescale for shocked gas to cool and collapse. Fujimoto (1968) further showed that this offset scales with the gas sound speed, as hotter gas resists compression, delaying collapse until further downstream. If star formation occurs after gas clouds pass through the minimum potential of the density waves (left spiral arm in Fig.1.5), the peak of the SFR surface density is predicted to appear on the leading edge inside the $R_{CR}$ and on the trailing edge outside $R_{CR}$. Conversely, if star formation occurs as gas clouds approach the density waves (right spiral arm in Fig.1.5), $\Sigma_{SFR}$ should peak on the trailing edge inside $R_{CR}$. Both hypotheses in density wave theory predict an offset in $\Sigma_{SFR}$ across the spiral arms. In contrast, dynamic spiral theory predicts a symmetric distribution of $\Sigma_{SFR}$ on either side of the spiral arms, with the highest $\Sigma_{SFR}$ occurring along the arms themselves. For tidally induced spiral arms, kinematic density waves are expected to drive azimuthal offsets in $\Sigma_{SFR}$, similar to the behaviour predicted by quasi-stationary density wave theory. Differently, a tidally-driven spiral system is likely to feature a fly-by or merging satellite, accompanied by ram-pressure gas stripping in the outskirts (Pettitt et al. 2017; Semczuk et al. 2018).

SFR can be measured using various indicators (Calzetti 2013), each sensitive to different timescales. O- and B-type stars, with short lifespans of 10–300Myr, are ideal tracers of recent star formation activity. These young massive stars emit ionising photons that excite and ionise the surrounding gas, enabling SFR calibrations across wavelengths from ultraviolet (UV) to optical and infrared (IR). To examine the spatial distribution of star formation in spiral galaxies, a resolved SFR calibration is required. Integral-field spectroscopy (IFS) gives the ability to resolve galaxies spatially and obtain a spectrum for each pixel in the form of three-dimensional data cubes. This allows us to measure not only SFR, metallicity (Sec 1.3.2), also the mean stellar age (Sec 1.3.3) in each pixel.

**SFR traced by UV**

According to black-body radiation and Wien's displacement law, the spectral energy distribution peaks at

$$\lambda_{\text{peak}} = \frac{b}{T}, \tag{1.7}$$

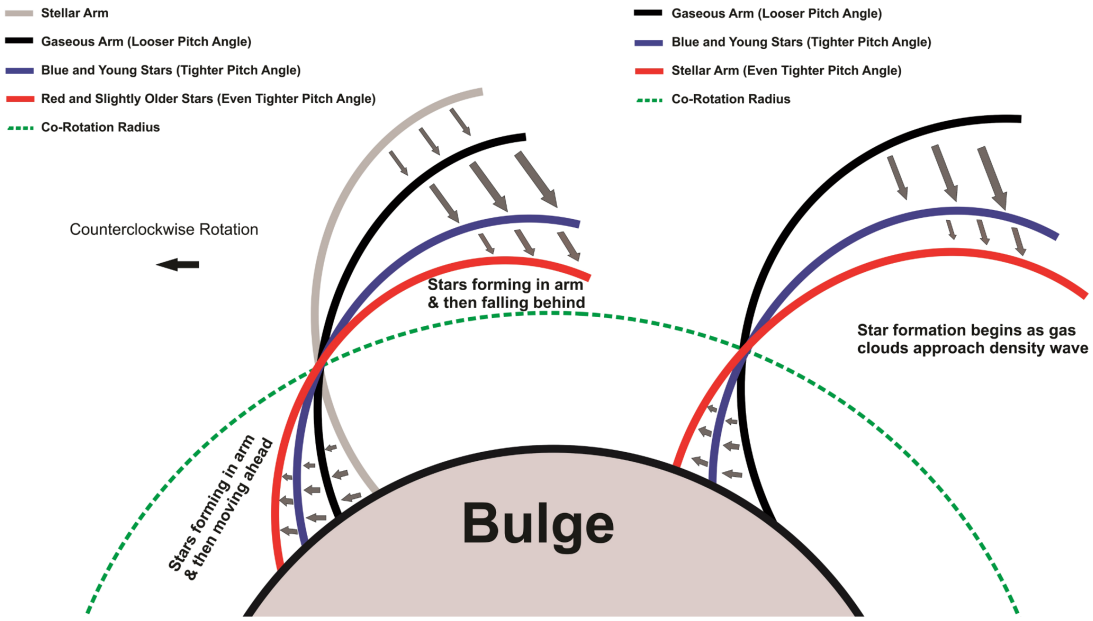


**Figure 1.5: Left arm:** predicted locations of gas, young and old stars, assuming star formation occurs after gas clouds *pass through* the density waves. **Right arm:** predicted location of gas, young and old stars, assuming star formation occurs as gas clouds *approach* the density waves. These two configurations of gaseous and stellar spiral arms are not fixed but evolve dynamically within a spiral galaxy. Their exact arrangement is determined by multiple complex factors, including gas density, the equation of state, and the relative velocities of the gas, stars, and spiral potential. This figure is adopted from Figure 1 in Pour-Imani et al. (2016).

where $b$ is the Wien's displacement constant ($2.89 \times 10^{-3}$ m·K). Massive O and B stars, with their higher effective temperatures, have shorter $\lambda_{\rm peak}$. As a result, their UV flux is significantly brighter than that emitted at longer wavelengths, and also outshines the UV emission from older, less massive stars, since massive stars are intrinsically more luminous across all wavelengths. Therefore, UV emission flux is a powerful tool to trace SFR.

For a Kroupa stellar initial mass function (IMF; Kroupa 2001), assuming solar metallicity and constant star formation over 100 Myr, the UV luminosity can be converted to SFR as:

$$\mathrm{SFR(UV)} = 3 \times 10^{-47} \lambda\, L(\lambda), \tag{1.8}$$

where $\lambda$ is the wavelength in unit of angstrom (Å; $10^{-10}$m), $L(\lambda)$ is luminosity of UV flux in unit of erg $\mathrm{s}^{-1}$, and SFR(UV) is in unit of $\mathrm{M}_\odot\ \mathrm{yr}^{-1}$. This UV calibration is influenced by dust attenuation, as dust absorbs photons in the UV range and re-emit in the IR wavelength.

**SFR traced by optical emission lines**

When hydrogen atoms are ionised and subsequently recombine with electrons, the electrons cascade down through energy levels, emitting light at specific wavelengths. Transitions from higher levels ($n \geq 3$) to $n = 2$ produce emission lines in the Balmer series, including bright lines such as H$\alpha$ (6563Å) and H$\beta$ (4861Å). These Balmer emission lines are among the most important SFR calibrations at optical wavelengths (Kennicutt 1998), due to these emission lines being among the brightest optical emission lines. Assuming a Kroupa IMF, solar metallicity and constant star formation activity in the past ≥6 Myr, SFR can be calculated based on H$\alpha$ as:

$$\mathrm{SFR}(\mathrm{H}\alpha) = 5.5 \times 10^{-42} L(\mathrm{H}\alpha), \tag{1.9}$$

where $L(\mathrm{H}\alpha)$ is the H$\alpha$ luminosity in units of erg $\mathrm{s}^{-1}$. This calibration is most accurate for galaxies with stellar mass $\sim 10^{9.5}\mathrm{M}_\odot$ (Brinchmann et al. 2004) while underestimate SFR in more massive galaxies. The H$\alpha$-based SFR is primarily sensitive to stars with $M \gtrsim 20 M_\odot$ and ages < 10 Myr. However, this calibration is influenced by dust attenuation, as dust can scatter light and absorb ionising photons. This absorption reduces the number of photons available to ionise hydrogen, thereby decreasing $L(\mathrm{H}\alpha)$.

For the observational data used in this thesis, rest-frame optical spectra are generally covered, making H$\alpha$ an ideal SFR indicator. All of the spiral galaxies in this thesis are face-on thin disc galaxies, which minimises the impact of dust on $L(\mathrm{H}\alpha)$. Therefore, Chapter 2 and Chapter 3 adopt H$\alpha$-based SFR calibration.

**SFR traced by IR**

Radiation from young stars heats up the nearby dust, which is reflected in brighter fluxes in thermal IR wavelength than cool dust around the old stellar populations. According to Stefan–Boltzmann law, the luminosity of a star is proportional to $T^4$. The hotter dust is dominantly heated by young and hot stars, making them an ideal SFR tracer in IR (e.g., 24 $\mu$m and 70 $\mu$m) than the cooler dust heated by old stellar populations. SFR is often measured from the total IR flux ($L_{\rm TIR}$) as:

$$\mathrm{SFR(TIR)} = 2.8 \times 10^{-44} L_{\rm TIR}, \tag{1.10}$$

assuming solar metallicity, constant star formation over the past 100 Myr and a Kroupa IMF (Calzetti 2013). A more recent work (Cluver et al. 2017) calibrated the SFR from IR emission flux with SINGS/KINGFISH observation sample as:

$$\log\mathrm{SFR}\ (\mathrm{M_\odot yr^{-1}}) = 0.889 \pm 0.018\ \log L_{12\mu m}(L_\odot) - 7.76 \pm 0.15. \tag{1.11}$$

### 1.3.2 Gas-phase metallicity

Astronomy classifies all elements heavier than hydrogen and helium under the term "metal". This is because in the *Big Bang* theory, nucleosynthesis produced the nuclei of hydrogen, helium, and a very limited amount of lithium (Grohs & Fuller 2022) in the first ~20 minutes following Big Bang. All elements heavier than hydrogen and helium are synthesised later through stellar nucleosynthesis, hence, are called as "metals".

Stars generate metals through stellar nucleosynthesis and eject enriched metals into the ISM during their final evolutionary stages. As such, metallicity serves as a key parameter for tracing the star formation history of galaxies. Moreover, metals act as coolants in nebular gas clouds (Smith et al. 2008), enabling the gas to subsequently collapse, and form new stars. By witnessing the birth and death of successive generations of stars, metallicity becomes an essential tool for studying galaxy evolution. In resolved studies of extragalactic astronomy, gas-phase metallicity is traced using emission lines from star forming regions, while stellar metallicity is traced with absorption lines. Therefore, gas-phase metallicity is generally easier to measure than stellar metallicity and this thesis will focus on gas-phase metallicity.

The most abundant metal by mass in the gas-phase ISM is oxygen. It is primarily synthesised and released into the ISM through core-collapse supernovae (Type II supernovae, or SNe II), which occur when a massive star ($\mathrm{M} > 8\mathrm{M_\odot}$) reaches the end of its short lifespan ($10^6$ – $10^7$ years). This process produces a large amount of $\alpha$-elements – including C, O, Ne, Mg, Si, S, Ca, Ar, and Ti – with relatively less iron (Goodwin & Pagel 2005). In

contrast, Type Ia supernovae (SNe Ia) are triggered when a dying white dwarf accretes material from a close binary companion and reaches the Chandrasekhar limit of 1.44 $M_\odot$ (Chandrasekhar 1931). SNe Ia produce mostly iron-group elements (Matteucci et al. 2006).

Oxygen is commonly used as a tracer for gas-phase abundances due to its high prevalence in the ISM and its relatively low depletion onto dust grains, unlike iron. The oxygen abundance in the ISM is usually calculated as:

$$12 + \log_{10}(\mathrm{O/H}) \equiv 12 + \log_{10}(N_\mathrm{O}/N_\mathrm{H}), \tag{1.12}$$

where $N$ represents the atomic number of each element. Because $N_\mathrm{O}$ is several orders of magnitude smaller than $N_\mathrm{H}$, taking the logarithm transforms this small ratio into a more readable single-digit number. The addition of 12 is a historical convention that shifts the values into a positive range, which typically falls between 8 and 9. For example, Pilyugin et al. (2003) report an oxygen abundance of 8.90 for the centre of the Milky Way, based on the electron temperature method.

There are various methods to estimate gas-phase metallicity from observational data, among which the most common methods are the electron temperature ($T_e$) method (direct method) and strong-line diagnostics (indirect method). Photons from massive young stars ionise the surrounding gas, forming H II regions. Metals within these H II regions, including but not limited to oxygen, act as coolants, significantly reducing the $T_e$. A lower $T_e$ decreases the rate of collisional excitation of ions, thereby reducing the flux of collisionally excited emission lines. Temperature-sensitive collision-excited lines thus constrain the metallicity in the gas-phase ISM. A commonly used observation for the direct method involves auroral lines, such as [O III]$\lambda$4363 and [N II]$\lambda$5755.

Auroral lines are typically weak and challenging to detect in galaxies with higher metallicities where auroral lines are faint (Kewley & Ellison 2008). To address this limitation, various indirect methods using strong emission lines have been developed to estimate gas-phase metallicity. These indirect methods are either (i) calibrated empirically against the direct method to establish correlations or (ii) based on theoretical photoionisation models of H II regions, such as `MAGPPINGS` (Sutherland & Dopita 1993) and `CLOUDY` (Ferland et al. 2013). A variety of indirect methods has been proposed and calibrated. This scenario arises from the fact that systematic offsets are found between different metallicity indicators (Kewley & Ellison 2008) and that spectroscopic surveys often cover only a limited set of emission lines within a narrow wavelength range. Here I briefly introduce several commonly-adopted strong-line diagnostics using optical lines (Fig 1.6).

- Diagnostics involving [NII]$\lambda$6584/H$\alpha$, also known as N2, have been calibrated in

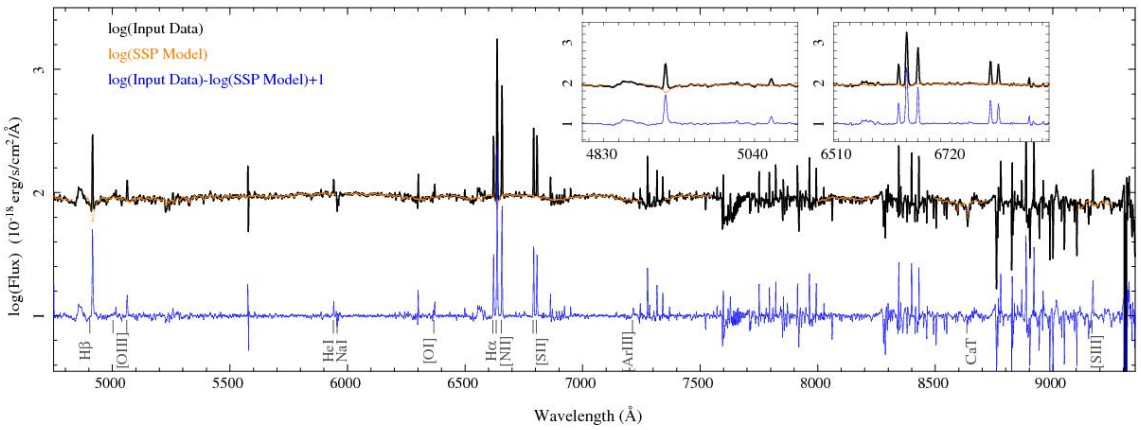


**Figure 1.6:** Spectrum of a typical H II region from NGC 6754, highlighting some optical emission lines commonly used for metallicity calibration. This figure is adopted from Sánchez et al. (2015).

numerous studies (e.g., Denicoló et al. 2002; Pettini & Pagel 2004; Yin et al. 2007; Pérez-Montero & Contini 2009; Marino et al. 2016; Brown et al. 2016). Due to their reliance on emission lines in the red wavelength range, N2 diagnostics exhibit less dependence on the ionisation parameter [1], with fluctuations of $\lesssim 1$ dex across varying ionisation conditions. The N2S2-N2H$\alpha$ diagnostic proposed by Dopita et al. (2016) combines the N2 ratio with the [NII]$\lambda$6574/[SII]$\lambda\lambda$6717, 31 ratio. This combination is insensitive not only ionisation parameter, but also ISM pressure within $4 \leq \log(P/k) \leq 7$, and dust extinction.

- There are several diagnostics involving $R_{23} \equiv \frac{[\mathrm{OII}]\lambda\lambda 3727{,}9+[\mathrm{OIII}]\lambda\lambda 4959{,}5007}{\mathrm{H}\beta(4861\text{Å})}$ (e.g., Pagel et al. 1979; Kewley & Dopita 2002; Kobulnicky & Kewley 2004). Extinction correction is required before $R_{23}$ measurement due to the dust absorption in the blue wavelength. However, $R_{23}$ ratio is sensitive to ionisation parameter – defined as the ratio of ionised-hydrogen photon flux to hydrogen density – when 12 + log(O/H) $\leq$ 8.5 and sensitive to ISM pressure when 12 + log(O/H) > 8.5.
- Several diagnostics use O3N2 $\equiv \frac{[\mathrm{OIII}]\lambda 5007/\mathrm{H}\beta}{[\mathrm{NII}]\lambda 6584/\mathrm{H}\alpha}$, first introduced by Pettini & Pagel (2004). O3N2 relies on emission lines in both the blue and red wavelength ranges, making it sensitive to the specific dust correction that is applied. O3N2 is also strongly dependent on ionisation parameter, varying by 2 – 3 dex (Figure 1.7).
- The [NII]$\lambda$6584/[OII]$\lambda\lambda$3727, 9 ratio is among the most reliable metallicity diagnostic in optical spectrum (Jensen et al. 1976; Dopita & Evans 1986; Kewley & Dopita 2002; Kewley et al. 2006). Due to the wide span of wavelength, this diagnostic requires extinction correction before metallicity measure-

[1] The ionisation parameter is defined as the ratio of the mean hydrogen-ionising photon flux to the hydrogen atom density. It increases with both the luminosity of the stellar population and the hardness of the ionising radiation field.

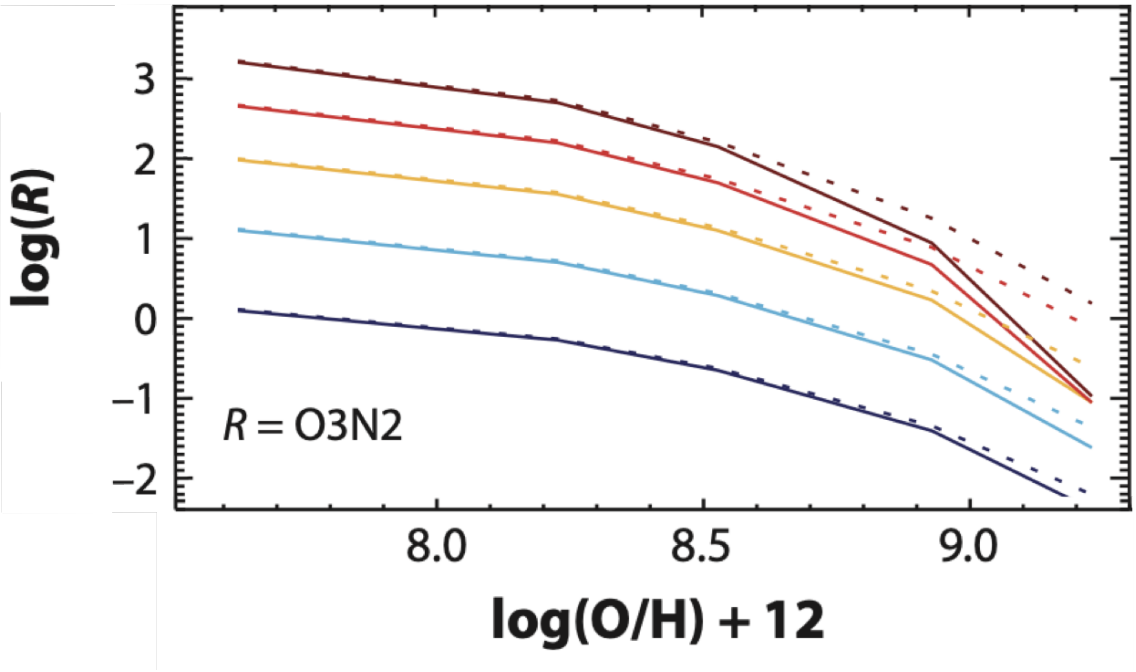


**Figure 1.7:** Metallicity diagnostics from Kewley et al. (2019), showing O3N2 emission line ratio versus gas-phase metallicity 12 + log(O/H). Lines with different colours (from blue to red) correspond different ionisation parameters log($U$) = (-3.98, -3.73, -3.48, -3.23, -2.98, -2.73, -2.48, -2.23, and -1.98). Solid (or dotted) lines are under the assumption of ISM pressure log($P/k$) = 5 (or 7).

ment. [NII]$\lambda$6584/[OII]$\lambda\lambda$3727, 9 ratio is *virtually* independent of ionisation parameter (Dopita et al. 2000) and has very little dependence on the ISM pressure between values of $4 \leq \log(P/k) \leq 8$. It is relatively insensitive to ionisation parameter and the hardness of ionising spectrum, making it insensitive to the presence active galactic nuclei (AGN) and diffuse ionised gas (DIG; Zhang et al. 2017a; Poetrodjojo et al. 2019).

Beyond measuring metallicity, it is crucial to understand how metallicity varies across different regions of galaxies and what drives these variations. Metals in the ISM are expected to reach localised equilibrium on sub-kpc scales within a short timescale (Krumholz et al. 2018; Sharda et al. 2021). On larger galactic scales, processes such as spiral arms, radial gas flows, gas accretion from the circumgalactic medium (CGM), and outflows also influence the metallicity in the gas-phase ISM. The combination of these processes can result in a complex (non-monotonic) evolution of the ISM metallicity over short timescales and small scales along both radial and azimuthal directions, but tending toward an increase in global metallicity with increasing cosmic time. Here, I will outline the theoretical expectations for azimuthal metallicity distributions under various spiral theories.

In density wave theory (Fujimoto 1968; Roberts et al. 1975), gas enters along the trailing

edge of the spiral arms, bringing the metal-enriched gas into the arms where shock waves are formed. Building on the work of Edmunds (1990), Ho et al. (2017) developed an analytical chemical evolution model for a grand-design spiral galaxy, following the quasi-stationary density wave theory (Figure 1.8). The model assumes that the spiral arms are trailing (left panel of Figure 1.9). In a closed-box system, with no gas accretion or outflows, the total metal content in the ISM increases over time as a result of stellar nucleosynthesis. However, as gas orbits within the disk, the local gas-phase metallicity fluctuates. The dynamic timescale for gas to travel between two spiral arms is sufficient for the formation of a few tens of generations of stars, depending on the galaxy's rotation curve and pattern speed. This self-enrichment process increases the gas-phase metallicity near massive stars located on the trailing edge of the spiral arms (upstream in Figure 1.8).

As the enriched gas continues orbiting and reaches the spiral arms, metal reaches a peak abundance, facilitates the cooling of GMCs and stimulates the formation of new stars. The intense cloud-cloud collisions and higher rates of supernovae within the spiral arms lead to a shorter mixing timescale. These processes efficiently dilute and mix the enriched gas with less metal-rich gas on the leading edge of the spiral arms (downstream in Figure 1.8). As a result, the model predicts a metallicity decrease as gas passes through the density waves and enters the leading edge.

The dynamic spiral theory offers a different perspective on the 2D metallicity distribution in galaxies. In this framework, spiral arms are material arms rather than density waves, and gas settles into the minimum potential of the spiral arms without crossing through them. As a result, gas-phase metallicity is locally enhanced within the spiral arms, with no systematic offset expected on either side of the arms.

In spiral galaxies undergoing tidal interactions, the metallicity distribution can vary significantly between different spiral structures. For instance, the metallicity in the bridge connecting the interacting satellite and the main galaxy is often distinct from material in the tail that is further from the satellite (Pettitt et al. 2017). In the case of M 51 (top left in Figure 1.2), the spiral arm connecting to its satellite galaxy, M 51b, exhibits higher metallicity compared to the spiral arm farther from M 51b (Wei et al. 2021). The complex gravitational potential in such systems can disrupt the metallicity distribution, introducing significant uncertainty in the presence of azimuthal metallicity variations.

In summary, gas-phase metallicity is a powerful observation tool to constrain the physics driving spiral features, reflecting the star formation history, although it comes with challenges such as precise measurement and non-negligible intrinsic scatter (Garcia et al. 2024).

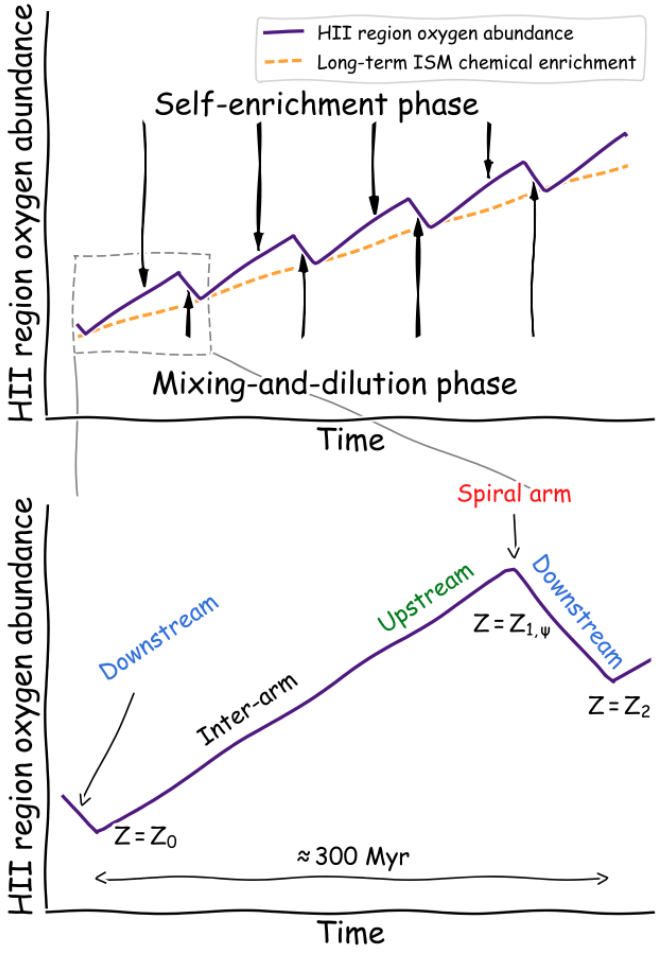


**Figure 1.8:** A schematic plot (Figure 9 in Ho et al. 2017) illustrates the predictions of the chemical evolution model in Ho et al. (2017). Metallicity is enhanced in the interarm regions due to self-enrichment, while it decreases downstream (leading edge) as a result of the mixing-and-dilution phase. Note that the figure is not drawn to scale.

### 1.3.3 Stellar age

Various methods are available to resolve stellar ages in IFS data cubes, including spectral fitting and the $D_{4000}$ index. To achieve a sufficient signal-to-noise ratio (SNR) for the spectral fitting process, some studies combine multiple pixels and their spectra into a single bin. Other studies focus on measuring the stellar ages of star clusters by first identifying and classifying individual cluster source (Shabani et al. 2018). I introduce several commonly used fitting methods for measuring stellar ages below.

#### Spectral fitting

Spectral represents the fluctuation of spectral energy across wavelengths. Spectral fitting is a versatile technique that involves multiple parameters, such as the IMF, stellar mass, star formation history, and dust, among others. By adjusting these parameters, the modelled

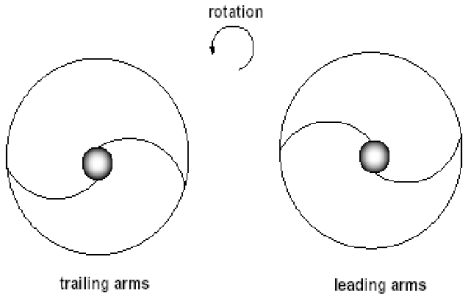


**Figure 1.9:** Trailing spiral arms (left) versus leading spiral arms (right). Gas rotates counter-clockwise. This figure is adapted from Capozziello & Lattanzi (2006).

spectrum is altered to minimise the residuals between the observed and modelled spectra, yielding the best-fit parameters. This process simultaneously provides several stellar properties, including the stellar age.

A range of public spectral fitting codes is available, such as `STARLIGHT` (Cid Fernandes et al. 2005), and `PPXF` (Cappellari & Emsellem 2004a; Cappellari 2017a). These codes support various stellar population models, including `SLUG` (da Silva et al. 2012), `MILES` (Vazdekis et al. 2015), and Binary Population and Spectral Synthesis (`BPASS`; Eldridge et al. 2017). While spectral fitting is a powerful tool, it requires spectra with a high SNR ($\gtrsim$ 20) to reliably determine the star formation history and mean stellar age, due to the degeneracy among age, metallicity and IMF, as well as uncertainty in dust attenuation.

### $D_{4000}$ index

When the SNR is insufficient to determine stellar ages by fitting SED, $D_{4000}$ serves as a loose indicator of stellar age based on the continuum. $D_{4000}$ is an spectral index defined around 4000Å as:

$$D_{4000} = \frac{\mathrm{Flux}_{\mathrm{restframe}}(4050\text{Å} - 4250\text{Å})}{\mathrm{Flux}_{\mathrm{restframe}}(3750\text{Å} - 3950\text{Å})}. \tag{1.13}$$

$D_{4000}$ increases with stellar age in the local Universe (Gallazzi et al. 2005), and is sensitive to timescale of $\sim$ 1 Gyr (Kauffmann et al. 2003a). This is because:

- Regions dominated by older stellar populations exhibit lower flux in the blue wavelength range (Eq. 1.7) due to the relative lack of young, bright stars.
- The atmospheres of older, metal-rich stars lead to more metal absorption lines such as calcium H (3934Å) and calcium K (3969Å), Magnesium (5175Å) and Sodium (5894 Å), further reducing the flux in the blue wavelength range.

Figure 1.10 shows the change of $D_{4000}$ along different stellar age. $D_{4000}$ increases in older

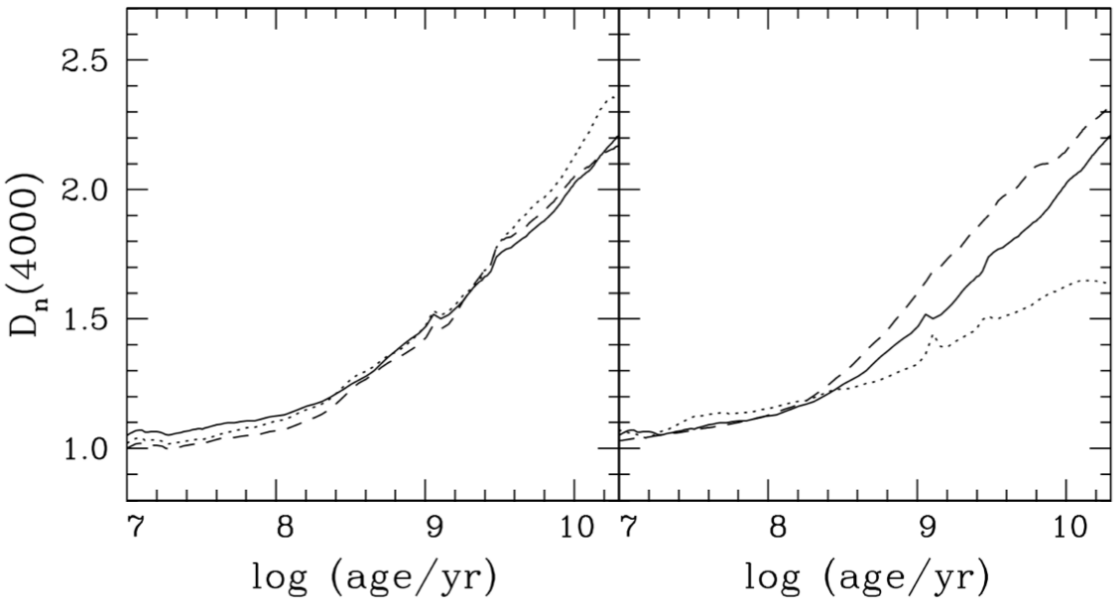


**Figure 1.10: Left:** Evolution of $D_{4000}$ following an instantaneous burst of star formation at solar metallicity, computed using different stellar libraries. Solid lines represent BC2003+STELIB, dotted lines correspond to Pickles (1998), and the dashed line represents Jacoby et al. (1984). **Right:** Sensitivity of $D_{4000}$ to bursts of different metallicity. The solid line represents a solar metallicity model, the dotted line corresponds to a 20% solar metallicity model, and the dashed line represents a 2.5 times solar metallicity model. This figure is adopted from Kauffmann et al. (2003a).

stellar populations and is sensitive to stellar metallicity.

The azimuthal distributions of stellar age relative to the spiral arms provide hints of the physical mechanism driving spiral features. According to the quasi-stationary density wave theory, spiral arms are regions of intense star formation activity. Inside the $R_{CR}$, newly formed stars overtake the density waves due to their faster angular velocity, transitioning to the leading edge of the spiral arms. As a result, the youngest stellar populations are expected within the density waves, with progressively older stellar populations found azimuthally further from the spiral arms. This presents as:

- a decreasing number of young stars while moving from the spiral arm's leading edge to the trailing edge of the next spiral arm, as massive young stars die;
- older mean stellar ages in pixels further from the spiral arms; and
- observable offsets between spiral arms identified using different tracers such as CO and H$\alpha$.

In contrast, the dynamic spiral theory suggests that newly formed stars remain within the spiral arms rather than passing through them. As a result, the youngest stellar populations

are concentrated in the spiral arms, with comparable mean stellar ages on either side, and no age gradient across the spiral arms is expected.

In spiral galaxies undergoing tidal interactions, satellite galaxies often host stellar populations distinct from those in the main galaxy (e.g., M 51b; Wei et al. 2021). Stars from the satellite orbit and fall into the main galaxy's gravitational potential. These ex-situ stars disrupting the age patterns established solely by the spiral arms. Meanwhile, the accreted gas stimulates new stars to form during the interactions. The timescale required for the stellar age distribution to stabilise after such interactions can be investigated through simulations (Dobbs et al. 2010; Pettitt et al. 2016).

## 1.4 Spiral galaxy simulations

Observations provide insights into the real Universe. However, observational data captures only a single snapshot of a galaxy at the moment of observation, making it challenging to study the long-term evolution. The impact of galaxy environments on spiral structures remains a topic of debate, and it is challenging to determine whether a galaxy has experienced tidal interactions, especially when the interacting satellite has already merged or passed by.

Simulations serve as a powerful tool to overcome some of the observational limitations. Built on our current physical understanding of the Universe, we can compare the outcome of simulations with observational data, allowing us to test and refine our physical models. Simulations allow us to trace the long-term evolution of individual spiral galaxies over cosmic time and track the merger history of the spiral galaxy. We need to keep in mind that simulations are built on assumptions and constrained by computational limitations, making the yielding galaxies imperfect representations of real ones but products of our physical understanding of the observed Universe.

The first simulated spiral galaxy was created by Holmberg (1941) using lightbulbs. Computer-based simulations of spiral galaxies date back to von Hoerner (1960) and Aarseth (1963) using $N$-body simulations, which explores the effects of interactions between individual particles on the structure of the systems such as galaxies and large-scale structure (Bagla 2005). In 1960s, the $N$-body simulations involved approximately $10-100$ particles, while by the 1980s, $N$-body simulations involved approximately $10^4$ particles (e.g., Sellwood & Carlberg 1984). In these pioneering simulations, spiral arms were found to be short-lived, transient features that dissolved into the galaxy disc within a few rotations due to kinematic heating and the increase in the Toomre's $Q$ parameter (see Section 1.2.3 and Dobbs & Baba 2014, and references therein). However, Fujii et al. (2011) revealed that multi-arm spiral structures could last for over 10 Gyr in their three-dimensional $N$-

body simulation involving $> 3 \times 10^6$ particles. This finding suggests that the transient nature of spiral features in earlier simulations is likely a consequence of the low particle numbers.

By the 2010s, numerical simulations incorporated over $10^6$ particles (Wada et al. 2011; Baba et al. 2013; Sellwood & Carlberg 2014), thanks to developments in computational power and numerical algorithms. Simulations have also become increasingly sophisticated to get more and more similar to the observed galaxies, by integrating essential physical processes such as hydrodynamics, star formation, stellar feedback, magnetic fields, chemical evolution and AGN.

Since the mid-2010s, many simulations have implemented cosmological models that start from smooth initial conditions based on the observed cosmic microwave background, yielding detailed predictions for galaxy formation and the large-scale structure of the universe (Vogelsberger et al. 2020). Notable examples include Illustris (Nelson et al. 2015), EAGLE (Crain et al. 2015), Simba (Davé et al. 2019), and VINTERGATAN (Agertz et al. 2021). These cosmological simulations have greatly advanced our understanding of large-scale structure formation and galaxy interactions.

Although the nature of dark matter and dark energy remains unclear, cosmological simulations can provide reliable predictions based on the ΛCDM model, where dark matter is collision-less and dark energy is represented by a cosmological constant, $\Lambda$. This is demonstrated by Aquarius (Springel et al. 2008), GHALO (Stadel et al. 2009), and ELVIS (Garrison-Kimmel et al. 2014). For the baryonic components (gas and stars), these simulations enable detailed studies of galaxy formation across multiple phases and multi scales, as shown in EAGLE (Schaye et al. 2015), Horizon-AGN (Dubois et al. 2014), and Magneticum (Bocquet et al. 2016).

To reduce computational cost and memory usage while improving baryon mass resolution, many of these simulations are designed as zoom-in simulations. Unlike large-volume cosmological simulations, zoom-in simulations focus on a smaller region of the universe – often observable universe – evolving it from the Big Bang to the present day with high resolution. Highlighted examples include Auriga (Grand et al. 2024), NIHAO (Wang et al. 2015), and FIRE (Wetzel et al. 2016). Cosmological zoom-in simulations provide detailed insights into the internal structures of galaxies and the physical processes that shape them. In recent years, they have become essential for studying the formation of galaxy morphology and substructures (e.g., bulges, bars, and spiral arms). They also offer a powerful option of investigating spiral structures that emerge from cosmological initial conditions, without relying on rigid spiral potentials.

There are many simulation-based studies tracing spiral structures and their evolution through various physical parameters, including SFR (Sec 1.3.1), gas-phase metallicity

(Sec 1.3.2), and stellar age (Sec 1.3.3). SFR is often found to be enhanced within spiral arms in simulations, both with and without an imposed fixed potential (e.g. Seo & Kim 2014; Kim et al. 2021; Robinson et al. 2025). 2D chemical evolution models implemented in simulations have enabled detailed tracking of azimuthal fluctuations in gas-phase metallicity (e.g. Spitoni et al. 2019; Khoperskov et al. 2023; Spitoni et al. 2023; Orr et al. 2023), revealing distributions broadly consistent with observational results. Stellar age is another powerful tracer for investigating the spiral features (e.g. Ardèvol et al. 2025) and dynamical evolution (e.g. Grand et al. 2012a; Dobbs et al. 2014, 2017) of spiral arms. Together, these simulations complement observational studies, providing deeper insights into the longevity and dynamics of spiral structure (e.g. Wada et al. 2011; Baba et al. 2013; Quinn et al. 2025; Palicio et al. 2025).

## 1.5 Thesis outline

The science goal of this thesis is to better constrain the impact of spiral arms on the 2D distributions of gas and stars, offering insights into the formation of spiral features and their long-term effects on galaxy evolution. My work involves observational data that spans from $z \sim 0.3$ to 0, and further incorporates simulations to understand the temporal azimuthal variation influenced by galaxy interactions. The first two chapters have been published in the Monthly Notices of the Royal Astronomical Society, while the third chapter submitted to the Monthly Notices of the Royal Astronomical Society.

The thesis is structured as follows: In Chapter 2, I investigate the role of spiral arms in shaping the 2D distribution of gas and stars at $z \sim 0.3$, using IFS data from the MAGPI survey, a MUSE large program. The adaptive optics enables the resolved observation of spiral structures at this redshift. By identifying the spiral regions, I analyse key ISM properties – $\Sigma_{\rm SFR}$ and gas-phase metallicity – as well as stellar age – traced by $D_{4000}$. These measurements across the leading edge, spiral arm regions, and trailing edge at different radii provide insights into how spiral arms regulate star formation and chemical enrichment. This study at $z \sim 0.3$ serves as a stepping stone for future resolved study of spiral galaxies at cosmic noon ($z \sim 2$) with JWST.

Chapter 3 focuses at the local Universe, examining the mechanisms that drive spiral structures in a sample of nine nearby spiral galaxies from the TYPHOON survey. This survey's step-and-stare method provides large field-of-view data with high spatial resolution (1.65"), allowing precise mapping of the spiral arm ridgeline. By tracing ISM properties along the azimuthal distance from the spiral arms, I quantify how star formation and metals respond to the spiral potential across multiple galaxies. This chapter offers a detailed statistical study to understand the physical processes governing star formation

and chemical mixing in spiral galaxies in the local Universe.

In Chapter 4, I extend this thesis from observations to simulations, using the Auriga cosmological zoom-in simulations to study the long-term evolution of spiral galaxies. Focusing on five simulated haloes that exhibit loose spiral features at $z = 0$, I track azimuthal variations in stellar age across all snapshots covering the past 5 Gyr. The merger trees of these simulated galaxies provide additional context on their interaction history, including satellite properties and their orbital dynamics. By comparing the simulations to observational results, this chapter explores how external perturbations and internal spiral potential shape the age distribution across galaxy disc over cosmic time.

Chapter 5 summarises the conclusion from the three studies included in this thesis and explores avenues for future possible research topics in this field.

Chapter 2

# The MAGPI Survey: Effects of Spiral Arms on Different Tracers of the Interstellar Medium and Stellar Populations at $z \sim 0.3$

## *Context and Contribution*

*This chapter has been previously published as* ***The MAGPI Survey: Effects of Spiral Arms on Different Tracers of the Interstellar Medium and Stellar Populations at z ~ 0.3****, by* ***Qian-Hui Chen, Kathryn Grasha, Andrew J. Battisti, Emily Wisnioski, Trevor Mendel, Piyush Sharda, Giulia Santucci, Zefeng Li, Caroline Foster, Marcie Mun, Hye-Jin Park, Takafumi Tsukui, Gauri Sharma, Claudia D.P. Lagos, Stefania Barsanti, Lucas M. Valenzuela, Anshu Gupta, Sabine Thater, Yifei Jin, and Lisa Kewley, 2024, MNRAS, 527, Issue 2, pp.2991-3005****. The work is slightly revised based on the thesis examiners' comments, compared to the published version. I have analysed the observation data. I have written the majority of the paper, with inputs and suggestions from co-authors.*

**Abstract**

Spiral structures are important drivers of the secular evolution of disc galaxies, however, the origin of spiral arms and their effects on the development of galaxies remain mysterious. In this work, we present two three-armed spiral galaxies at $z \sim 0.3$ in the Middle Age Galaxy Properties with Integral Field Spectroscopy (MAGPI) survey. Taking advantage of the high spatial resolution ($\sim$ 0.6 $''$) of the Multi-Unit Spectroscopic Unit (MUSE), we investigate the two-dimensional distributions of different spectral parameters: H$\alpha$, gas-phase metallicity, and $D_{4000}$. We notice significant offsets in H$\alpha$ ($\sim$ 0.2 dex) as well as gas-phase metallicities ($\sim$ 0.05 dex) among the spiral arms, downstream and upstream of MAGPI1202197197 (SG1202). This observational signature suggests the spiral structure

in SG1202 is consistent with arising from density wave theory. No azimuthal variation in H$\alpha$ or gas-phase metallicities is observed in MAGPI1204198199 (SG1204), which can be attributed to the tighter spiral arms in SG1204 than SG1202, coming with stronger mixing effects in the disc. The absence of azimuthal $D_{4000}$ variation in both galaxies suggests the stars at different ages are well-mixed between the spiral arms and distributed around the disc regions. The different azimuthal distributions in H$\alpha$ and $D_{4000}$ highlight the importance of time scales traced by various spectral parameters when studying 2D distributions in spiral galaxies. This work demonstrates the feasibility of constraining spiral structures by tracing interstellar medium (ISM) and stellar population at $z \sim 0.3$, with a plan to expand the study to the full MAGPI survey.

## 2.1 Introduction

In the local Universe, the majority of star formation takes place in spiral galaxies (Brinchmann et al. 2004) and up to two-thirds of all massive galaxies are spiral galaxies (Lintott et al. 2011; Willett et al. 2013). The interplay between star formation activity and the influence of spiral structures is closely related to 1) the physical conditions and distribution of the gas in the interstellar medium (ISM), and 2) the processes by which stars are created from the molecular gas. Spiral structures are complex and diverse, which is demonstrated by the variety in their number of arms, pitch angles, amplitudes and longevity (Dobbs & Baba 2014). Despite their ubiquitous nature, we know surprisingly little of the physical origin of spiral features and how they evolve over cosmic time (Sellwood & Masters 2022).

Previous studies investigating spiral-driven evolution have revealed the physical complexities of the origin of spiral features, including self-excited instabilities in equilibrium discs and gravitational instabilities due to interactions with companions, halos, and stellar bars. We summarise the two main physical mechanisms for the origin of spiral arms in disc galaxies:

- (Quasi-stationary) density wave theory (Lin & Shu 1966): spiral arms are density waves that evolve slowly and rotate at a fixed angular velocity (i.e., pattern speed) across the galaxy. The stars and gas in the disc orbit at different angular velocities, depending on their distances to the galaxy centre, which is called differential rotation. The co-rotation radius is the radius where the angular velocity of the material matches the pattern speed (e.g., Pour-Imani et al. 2016; Peterken et al. 2019). In this theory, the material is left behind the density wave outside the co-rotation radius but overtakes the density wave while inside the co-rotation radius. When entering the spiral potential, the gas will collapse (Toomre 1977) and undergo shocks (Roberts

1970; Bonnell et al. 2006), which are observable as periodic episodes of intense and instantaneous star formation (Aouad et al. 2020). The formation of a global spiral pattern from the density wave theory is caused by an instability of the disc as a direct result of self-gravity (Pettitt et al. 2017). According to the density wave theory, spiral galaxies with more than three spiral arms are less stable compared to grand-design spiral galaxies with two arms (Thomasson et al. 1990). Simulations report long-lived grand-design spiral galaxies which resemble the density wave theory, although the overall spiral pattern is transient and recurrent (Sellwood 2011; D'Onghia et al. 2013; Sellwood & Carlberg 2014). The maintenance (or the necessity of maintenance) of long-lived spiral waves is still an open question.

- Dynamic spirals (Sellwood & Carlberg 1984; Fuchs 2001; Dobbs & Baba 2014): in the dynamic material wave model, a leading density pattern transfers into a trailing one due to the shear caused by a differentially rotating disc. During the rotation, the leading mode is amplified into a spiral arm as a result of the self-gravity, through a mechanism called swing amplification (Goldreich & Lynden-Bell 1965). In this mechanism, spiral arms are simply a superposition of many unstable waves (Michikoshi & Kokubo 2016). There is no specific pattern speed for dynamic spirals or significant offset between the rotation of spirals and the disc. Thus, gas does not pass through the spiral arms but instead falls into the minimal potential from both sides of the arms (Dobbs & Bonnell 2008; Wada et al. 2011). The spirals generated by swing amplification are transient, recurrent, and short-lived (Sellwood & Carlberg 2014; Sellwood & Carlberg 2019). Swing amplification typically assembles flocculent or multi-armed galaxies but is capable of generating grand-design spiral arms (Baba 2015). Sellwood & Carlberg (1984) argue for short-lived (a few $\sim$ 100 Myr) dynamic spirals due to the heating from dissipation. On the other hand, Fujii et al. (2011) and D'Onghia et al. (2013) demonstrate the possibility of long-lasting (up to $\sim$ 10 Gyr) dynamic spirals using highly spatially-resolved N-body simulations.

The density wave theory and dynamic spiral theory are not exclusive to each other. Instead, the two mechanisms can explain the origin and assembly of different spiral arms. Many studies have been conducted to investigate the feasibility of these two theories through simulations. Since the 1970s, transitory spiral features have been seen in some simulations (Miller et al. 1970; Hohl 1971; Hockney & Brownrigg 1974), which gives us a glimpse of the fundamental physics of spirals. Assuming different models of spirals, simulations test and improve the theories by revealing the longevity of spiral arms (Oh et al. 2008; Fujii et al. 2011; Struck et al. 2011; D'Onghia et al. 2013; Sellwood & Carlberg 2014), distributions of ISM properties (Dobbs et al. 2010; Grand et al. 2012b,a; Pettitt et al. 2020),

motions of stars in spiral galaxies (Lindblad et al. 1996; Baba et al. 2013; Ramón-Fox & Bonnell 2022), etc. These studies find that both the density wave theory and dynamic spirals are viable mechanisms for the formation of spiral arms.

Although non-trivial and difficult, there have been many attempts to distinguish the physical mechanism driving the formation of spiral arms from observations in the local Universe. The density wave theory adopts a fixed pattern speed across the disc while the dynamic spirals induce the spiral arms to rotate with the disc at a radially decreasing angular velocity. The simplest detection of pattern speed is the co-rotation radius measured by the residual velocity maps of $^{12}C^{16}O$ and H I (Elmegreen et al. 1989; Canzian 1993; Sempere et al. 1995), although this method is highly subject to measurement uncertainties. Peterken et al. (2019) detect the pattern speed by mapping the ongoing star formation and previously formed young stars as a direct test of the density wave theory. Another indirect method to determine the pattern speed is to detect the location of spiral-shaped shock waves (hereafter spiral shocks). The density wave theory predicts spiral shocks to be found on one side of the stellar potential within the co-rotation radius and on the opposite side outside the co-rotation radius. This results in an offset whose width is determined by the difference between pattern speed and material speed. In the dynamic spiral theory, we do not expect an offset on both sides of the spiral arms, as the material in the disc does not cross the spiral arm potential. Therefore, the distributions of gas-phase ISM properties and stellar populations are different depending on the assumed theory, which enables us to interpret the observations and understand the origin of spiral arms in the observed galaxies. This method has been applied to several nearby galaxies (e.g., Egusa et al. 2004; Tamburro et al. 2008; Egusa et al. 2009; Pour-Imani et al. 2016; Abdeen et al. 2022), but not all observed galaxies are consistent with the prediction of the density wave theory (Foyle et al. 2011).

Integral Field Spectrographs (IFS) enable investigation into the radial and azimuthal distributions of stellar and gaseous ISM properties of galaxies. Large IFS surveys provide spatially-resolved distributions of oxygen abundances, kinematics, and stellar populations (Falcón-Barroso et al. 2006; Marino et al. 2012; Rodríguez-Baras et al. 2018; Kreckel et al. 2019; Grasha et al. 2022; Chen et al. 2023), to constrain the formation and evolution of spiral galaxies. These studies provide unprecedented insight into the dynamics and metal variations of spiral galaxies in the local Universe. However, most IFS studies of spiral galaxies are limited to spirals in the local Universe, leaving a gap in our understanding of spiral patterns in high-redshift galaxies, when the very first galaxies settled down to develop spiral features. Even though observations have found the existence of spiral galaxies up to $z \sim 2$ (Law et al. 2012; Margalef-Bentabol et al. 2022), the formation of these spiral galaxies remains mysterious. The formation of spiral arms is assumed to

happen in thin *rotating* discs (Toomre 1977; Sellwood & Carlberg 2014) while galaxy discs are thicker, more gas-rich and less stable at higher redshifts (Wisnioski et al. 2015; Crain et al. 2015). The effects of the ISM become increasingly important in the build-up of spiral arms at higher redshifts (Wada et al. 2011; Ghosh & Jog 2016). Spiral arms are also sensitive to environmental effects, including gas accretion and galaxy mergers (Wada et al. 2011; Martig et al. 2012; Dobbs & Baba 2014). To understand the physics of spiral formation and when it dominates the star formation activities in star-forming galaxies, we need to push detailed observations to higher redshifts. Using spatially-resolved IFS data targeting galaxies at a higher redshift, it is possible to discriminate density wave theory/dynamic spirals at an earlier stage of the formation of spiral galaxies.

Taking advantage of the adaptive optics of MUSE, the Middle Ages Galaxy Properties with Integral Field Spectroscopy (MAGPI; Foster et al. 2021) survey is carried out to target 60 massive galaxies and their satellites at $0.25 < z < 0.35$ ($3 - 4$ Gyr ago). Since the dynamical, morphological, and chemical properties of galaxies undergo significant transformation at $z \sim 0.3$, the MAGPI survey gives an important window in the cosmic timeline and fills up the gap in our understanding of the build-up of spiral features. The spatial resolution of MAGPI, which reaches 0.6 - 0.8 arcsec (full width at half maximum; FWHM), enables us to distinguish the spiral arms and the inter-arms without the use of gravitational lensing. In this work, we study the two-dimensional distributions of different ISM properties and stellar population in two spiral galaxies at $z \sim 0.3$ at a high spatial resolution, shedding light on the origin and growth of spiral arms. This paper demonstrates the feasibility of tracing ISM properties and their linkage to stellar spiral structures at $z \sim 0.3$, with a plan to expand the study to the full MAGPI spiral sample upon completion of the full dataset.

In this paper, we present our first work on exploring spiral galaxies with IFS observations at $z \sim 0.3$. We introduce our sample in Sec 2.2. We present our analysis of two gas ISM properties as well as stellar age in Sec 2.3 and the results are then discussed in Sec 2.4. Throughout this paper, we adopt the Chabrier (2003) initial mass function (IMF), and a flat cosmology with $\Omega_\Lambda = 0.7$, $\Omega_\mathrm{m} = 0.3$, $H_0 = 70$ km s$^{-1}$ kpc$^{-1}$.

## 2.2 Data and sample

### 2.2.1 Data

We use the observational data from the MAGPI[1] survey (35 fields at the time of starting this work, out of 56 MAGPI fields). MAGPI is a large program on the European

[1] https://magpisurvey.org

Southern Observatory Very Large Telescope (VLT) which is still in progress at the time of writing (Program ID: 1104.B-0536). The observations are achieved through $56 \times 4.4$h on-source exposures of independent fields with Ground Layer Adaptive Optics (GLAO) on VLT/MUSE. The MAGPI sample is also supplemented with two archival MUSE fields of massive clusters at $z \sim 0.3$: Abell 370 and Abell 2744.

The science goals, design, and observing technique are described in detail in Foster et al. (2021). In brief, the survey aims to reveal and understand the physical processes responsible for the rapid transformation of galaxies at intermediate redshift ($z \sim 0.3$), by mapping the detailed properties of stars and the ionised gas in galaxies. MAGPI will provide constraints on understanding the role of gas accretion and merging as well as tracing the metal mixing history of galaxies. It has a comparable *physical* spatial resolution to local surveys ($\sim$1$-$4 half-light radius/PSF FWHM; Foster et al. 2021) such as the Sydney-Australian-Astronomical-Observatory Multi-object Integral-Field Spectrograph (SAMI; Croom et al. 2021) and Mapping Nearby Galaxies at Apache Point Observatory (MaNGA; Bundy et al. 2015) surveys.

MAGPI uses the wide-field mode, yielding a $\sim 1 \times 1$ arcmin$^2$ field-of-view (FOV) sampled by $0.2 \times 0.2$ arcsec$^2$ spatial pixels (henceforth spaxels). The wavelength covers 4700 Å to 9350 Å and the spectral sampling is 1.25 Å/spaxel. The GLAO system ensures that all MAGPI targets are observed with an effective seeing of 0.65 arcsec FWHM in $V$-band, or better. For each primary target, the total on-source integration time per field is 4.4 hours, which ensures a signal-to-noise ratio of 5 Å$^{-1}$ per resolution element around 6000Å - 6500Å in the stellar continuum for individual spaxels at the half-light radius ($R_e$).

The data reduction process is briefly described in Foster et al. (2021) and will be provided in further detail in Mendel et al. (in prep). The raw data are processed using `PYMUSEPIPE` [2] (Weilbacher et al. 2020). The final processing of the individual MUSE science exposures is performed outside of the standard pipeline, using `CUBEFIX` (Cantalupo et al. 2019) and Zurich Atmosphere Purge sky-subtraction software (Soto et al. 2016). The synthetic white-light (i.e., collapsed MUSE spectrum), $r$- and $i$-band images for each field are created using the `MPDAF`[3] python package. The `PROFOUND` package (Robotham et al. 2018) is an image analysis package applied to the white-light images to detect objects and to produce a preliminary segmentation map. `PROFOUND` is also used on $r$- and $i$-band images created from the MUSE datacubes for photometric parameters.

[2] `https://github.com/emsellem/pymusepipe`
[3] `https://github.com/musevlt/mpdaf`

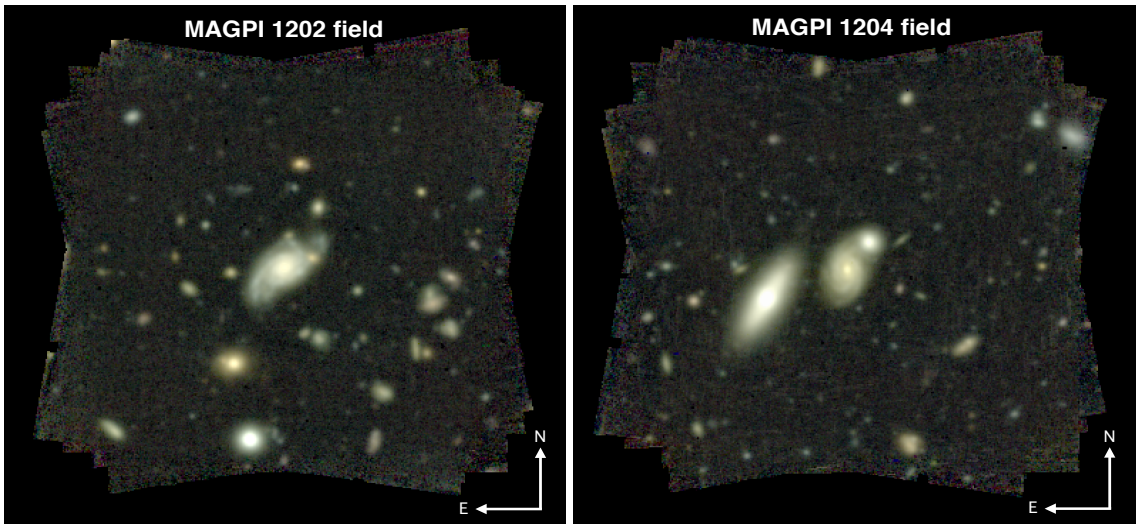


**Figure 2.1:** MUSE $g_{\rm mod}ri$ [4] composite images of the two well-defined spiral galaxies at the centre of each FOV of the MAGPI 1202 (left) and MAGPI 1204 (right) fields. Our pilot sample consists of MAGPI1202197197 (hereafter SG1202, at $z \simeq 0.2919$) and MAGPI1204198199 (hereafter SG1204, at $z \simeq 0.3163$), which are the large spiral galaxies located at the centre of each field. The companion galaxy to the northwest of SG1204 is a foreground galaxy at $z \simeq 0.254$.

### 2.2.2 Sample description

From the 35 observation-completed MAGPI fields (Oct 2022), we find 12 non-merging galaxies that prominently show grand-design or multi-armed spiral features from visual inspection. We exclude merging spiral galaxies to remove complexities that could be introduced to the stellar and gas properties from tidal interactions. Tidally-driven spiral arms are not discussed in this work. Fig 2.1 shows the coloured images of our pilot sample including two three-armed face-one spiral galaxies: MAGPI1202197197 (left of Fig 2.1, hereafter SG1202) and MAGPI1204198199 (right of Fig 2.1, hereafter SG1204). The pilot sample has the largest $R_e$ and the highest signal-to-noise ratio (SNR) among the 12 non-merging spiral galaxies, which allows for a detailed study and comparison between arm and interarm regions without the need for binning. This paper aims to demonstrate the feasibility of tracing spectral parameters and their linkage to spiral structures at $z \sim 0.3$. In our next paper, we will apply the methodology to the full MAGPI survey upon the completion of observation. The two spiral galaxies are part of a group according to the Galaxy and Mass Assembly Galaxy Group Catalog ($G^3Cv1$; Robotham et al. 2011) which indicates they are presumably under environmental effects from their companion galaxies. The physical parameters of galaxies in our pilot sample are listed in Table 2.1.

[4] $g_{\rm mod}$ covers part of the $g$ band redder than 4700Å.

| Galaxy | R.A. (degree) | Dec. (degree) | Inclination (degree) | P.A. (degree) | Redshift | $\log(M_*/M_\odot)$ | $R_e$ (kpc) | pitch angle (degree) |
|---|---|---|---|---|---|---|---|---|
| (1) | (2) | (3) | (4) | (5) | (6) | (7) | (8) | (9) |
| MAGPI1202197197 (SG1202) | 175.3388 | -1.5825 | 56.5 | 132.6 | 0.2920 | 10.88 ± 0.01 | 9.23 | 29.1°, 27.5°, 20.4° |
| MAGPI1204198199 (SG1204) | 175.6612 | -0.7943 | 46.9 | 175.0 | 0.3164 | 11.01 ± 0.01 | 10.09 | 16.7°, 19.4°, 21.0° |

**Table 2.1:** Physical parameters of our pilot sample galaxies from MAGPI in this study. **Column 1:** Galaxy name in the MAGPI survey and their short name in this work. **Column 2 & 3:** J2000 Coordinates of the galaxy in unit of degree. **Column 4 & 5:** Inclination and photometric position angle (P.A.) are measured with `PROFOUND` (Mendel in prep). **Column 6:** Redshift measured from `MARZ`. **Column 7:** Stellar mass of the spiral galaxies from Mun et al. (submitted), applying single population synthesis to stellar energy distribution fitting on HSC images following Taylor et al. (2011). The total stellar mass is obtained by summing the stellar mass in each pixel within the dilated mask from `PROFOUND`. **Column 8:** Half-light radius ($R_e$) determined with `PROFOUND` on $i$-band images. **Column 9:** Pitch angles of the spiral arms (see Sec 2.3.3) are listed clockwise from the north arm.

## 2.3 Data analysis and results

In this section, we present our analysis of the reduced MAGPI data including the spectral fitting processes, spaxel selection, the definition of spiral arms and inter-arm regions, and the measure of spectral parameters. Our goal is to constrain the origin of spiral features by studying the impacts of spiral arms on the gas ISM properties and stellar populations. We focus on the two-dimensional distributions of star formation rate (Sec 2.3.5), gas-phase metallicity (Sec 2.3.6) and stellar age (Sec 2.3.7) in the following analysis.

### 2.3.1 Emission line fits

Two dimensional spectral maps are obtained with `GIST` (Bittner et al. 2019), which is a pipeline with implemented `PPXF` (Cappellari & Emsellem 2004a; Cappellari 2017a) and `PYGANDALF` (Sarzi et al. 2006; Falcón-Barroso et al. 2006) routines. The `GIST` pipeline simultaneously extracts kinematics, emission lines and stellar population properties from full spectral fitting. There are several unique customisations made (Mendel et al. in prep and Battisti et al. in prep) for its use with MAGPI data when fitting emission lines:

- A binning scheme is used where if the signal-to-noise ratio of the continuum is too low for the adopted threshold for Voronoi bins, then a single integrated bin is adopted instead. Voronoi binning optimally preserves the maximum spatial resolution of two-dimensional data, given a constraint on the minimum signal-to-noise ratio (Cappellari & Copin 2012). The continuum fitting is based on binning scheme while the following emission line fits are on a spaxel level.
- A modified version of `PYGANDALF` is implemented that:
  - employs three different sets of input parameters including the flux, velocity and velocity dispersion, which is adjusted based on the best fit of the stellar component. The fitting that yields the lowest $\chi^2$ is considered as the final fitting results for the gas component. This modification is tailored to effectively handle low S/N emission lines.
  - estimates the errors on fluxes, velocities, and standard deviations for the emission lines, based on a Monte Carlo approach.

The emission line working group of the MAGPI survey adopts the light-weighted stellar templates from `SSP_Mist_C3K_Salpeter` (Charlie Conroy, private communication) and set the multiplicative Legendre polynomial to 12. The emission lines are fit as a Gaussian function which is independent of the chosen IMF. The targeted SNR of the stellar continuum for Voronoi binning is 10. The emission line fits are carried out with a single component tied to the brightest line for the wavelength range covered at the galaxy redshift

(i.e., H$\alpha$ for $0 < z < 0.424$, [O III]$\lambda$5007 for $0.424 < z < 0.865$ and [O II]$\lambda$3729 for $0.865 < z < 1.507$). The line velocity for each spaxel is restricted to ± 600 km/s relative to the stellar continuum velocity of the nearest Voronoi bin. For each MAGPI field, Mendel et al. (in prep) empirically measure the line spread function (LSF), which will be adopted in the following fitting processes. The spectral line data products, including [O II]$\lambda\lambda$3726, 29, $D_{4000}$, H$\beta$ (4861Å), [O III]$\lambda$5007, H$\alpha$ (6563Å) and [N II]$\lambda$6584 used in this work, are made by the MAGPI team and will be publicly available in a forthcoming data release (Battisti et al. in prep).

### 2.3.2 Spaxel selection criteria

To achieve a reliable scientific analysis of SG1202 and SG1204, we apply SNR >3 limits (Fig 2.2) to H$\beta$ and H$\alpha$ emission lines before extinction correction. The spaxels with SNR below 3 are excluded from all the following analyses. To ensure sufficient spaxels and accurate analysis, we establish a $3\sigma$ lower limit by assigning three times the noise as the new signal for [O III]$\lambda$5007 and [N II]$\lambda$6584 where if the spaxels have a SNR less than 3 (see Sec 2.6 of Rosario et al. 2016). In face-on spiral galaxies, H II regions with low scale height destroy the dust within birth clouds and therefore are predominantly affected by dust in the foreground (Wild et al. 2011). Thus, in this work, we apply the Milky Way extinction curve from Fitzpatrick et al. (2019) as:

$$E(B-V) = 2.5 \times \left( \frac{\log_{10} \frac{(H\alpha/H\beta)_{\rm obs}}{(H\alpha/H\beta)_{\rm int}}}{k_{H\beta} - k_{H\alpha}} \right). \tag{2.1}$$

We adopt $R_v = 3.1$ to determine the $k$ value at each wavelength and measure the colour excess $E(B-V)$ for all spaxels with SNR (H$\alpha$ & H$\beta$) >3. The $E(B-V)$ values are then used to calculate the intrinsic emission line fluxes $F_{\rm int}$ from the observed fluxes $F_{\rm obs}$ as:

$$F_{\rm int} = F_{\rm obs} \times 10^{0.4 k_\lambda E(B-V)}. \tag{2.2}$$

The extinction-corrected fluxes are used in all the following analyses to measure the gas-phase metallicities (Sec 2.3.6).

To limit our analyses to spaxels that arise predominantly from star formation (i.e., photoionisation) and exclude spaxels excited mainly by hard components (e.g., shocks, active galactic nuclei; AGN), we use the Baldwin, Phillips & Terlevich diagram (BPT diagram; Baldwin et al. 1981) to separate spaxels based on different excitation mechanisms. Based on [N II]$\lambda$6584/H$\alpha$ versus [O III]$\lambda$5007/H$\beta$, low-ionisation nuclear emission-line regions (LINERs) and AGN are distinguished from the H II regions, which are powered primarily by photoionisation (Kewley et al. 2001; Jin et al. 2022). We separate AGN/shock spaxels

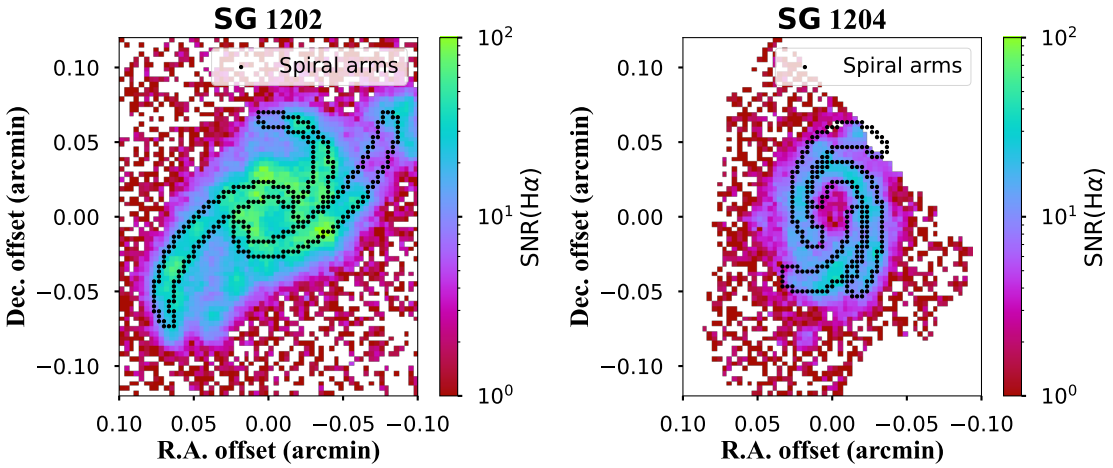


**Figure 2.2:** SNR maps of SG1202 and SG1204. Only spaxels with SNR >3 in H$\alpha$ and H$\beta$ are selected for all the following analyses. The defined spiral arms are over-plotted as black dots (see Sec 2.3.3). The spiral arms show a higher SNR of H$\alpha$ than the inter-arm regions.

from photoionisation by using the Kewley et al. (2001) demarcation line, which models the starburst galaxies with PEGASE v2.0 and STARBURST99 to derive the theoretical classification scheme for AGN and H II regions. Another work (Kauffmann et al. 2003b) presents an empirical demarcation line based on the properties of ~ 120,000 nearby galaxies with the Sloan Digital Sky Survey. The spaxels beneath the Kauffmann et al. (2003b) demarcation line are interpreted to be purely star-formation excited while data over the theoretical Kewley et al. (2001) demarcation line predominately arises by AGN or LINER emission sources. A total of 1.1% (0.8%) spaxels in SG1202 (SG1204) lie above the Kewley et al. (2001) line, which are excluded in the following analyses.

### 2.3.3 Defining the spiral arms

We identify the spiral arms of our two galaxies with a combination of computer algorithms and manual checks, using the automated tool SpArcFiRe (Davis & Hayes 2014), which was developed based on Galaxy Zoo data (Lintott et al. 2008, 2011). To highlight the spiral features of our two galaxies at $z \sim 0.3$, we employ `GALFIT` to determine the optimal Sérsic component and subtract it from the white-light images. Following the deprojection process in Sec 3.3 of Grasha et al. (2017), we deproject the galaxy images based on the inclination and P.A. in Tab 2.1 which are then set as the input of SpArcFiRe. The output of SpArcFiRe based on deprojected images is shown in Fig 2.12: red spiral arms are identified as having positive pitch angles (clockwise) while blue arms have negative pitch angles (counterclockwise). As three continuous spiral arms are vividly observable in both the white-light images (Fig 2.1), we only keep the three longest spiral arms from the output of SpArcFiRe for both spiral galaxies. As a secondary step, we fine-tune the starting and

ending radii of the spiral ridge lines to improve their alignment with the observed white-light images. The final adopted spiral arm ridge lines are presented in Fig 2.3, overplotted on the $\Delta\phi$ map, which represents the angular azimuthal distance to the nearest spiral arm at a constant galactocentric distance (Sec 2.3.4). The typical spiral arm width in the Milky Way is $\sim$ 1 kpc (Reid et al. 2014). We demarcate the width of spiral arms as 2 kpc in the MAGPI survey, taking the beam-smearing effects (0.6 – 0.8 arcsec; FWHM) into account. We show the boundary of the spiral arms as black dots in Fig 2.2.

### 2.3.4 Definition of azimuthal distance $\Delta\phi$

Depending on the physical mechanisms that assemble spiral arms, density wave theory or dynamic spirals, stellar populations and gas in the ISM between both sides of the spiral arms are expected to show different behaviours, which can be used to constrain the origin of the spiral features. The spatially resolved IFS data from our MAGPI observations allow us to compare the ISM properties between the spiral arm and inter-arm regions as well as differences between downstream and upstream in the inter-arm regions. To identify the different parts of inter-arms, we define $\Delta\phi$ which measures the azimuthal distance to the nearest spiral arm. We assign

$$\Delta\phi_i = -min(|\phi_j - \phi_i|) \tag{2.3}$$

when pixel $i$ is on the leading edge of the nearest spiral arm and assign

$$\Delta\phi_i = min(|\phi_j - \phi_i|) \tag{2.4}$$

when pixel $i$ is on the trailing edge of the nearest spiral arm. The pixel $i$ is the targeted pixel and the pixel $j$ is the pixel within the spiral regions at the same galactocentric distance (within 0.5 kpc uncertainty).

With the defined spiral arm ridge lines, the $\Delta\phi$ maps of SG1202 and SG1204 are presented in Fig 2.3. The inter-arm spaxels with negative (positive) $\Delta\phi$ are classified as downstream (upstream). In the following sections, we will analyse ISM properties and stellar populations as tests of the density wave theory.

### 2.3.5 Star formation rate

Star formation is one of the major drivers of galaxy evolution and is the process that enriches the ISM with metals. Young, massive stars produce copious amounts of ionising photons that are observed in emission nebular lines (e.g., H$\alpha$). Stars more massive than $\sim$ 10 $M_\odot$ produce a measurable ionising photon flux and only live $\sim$ 10 Myr, providing

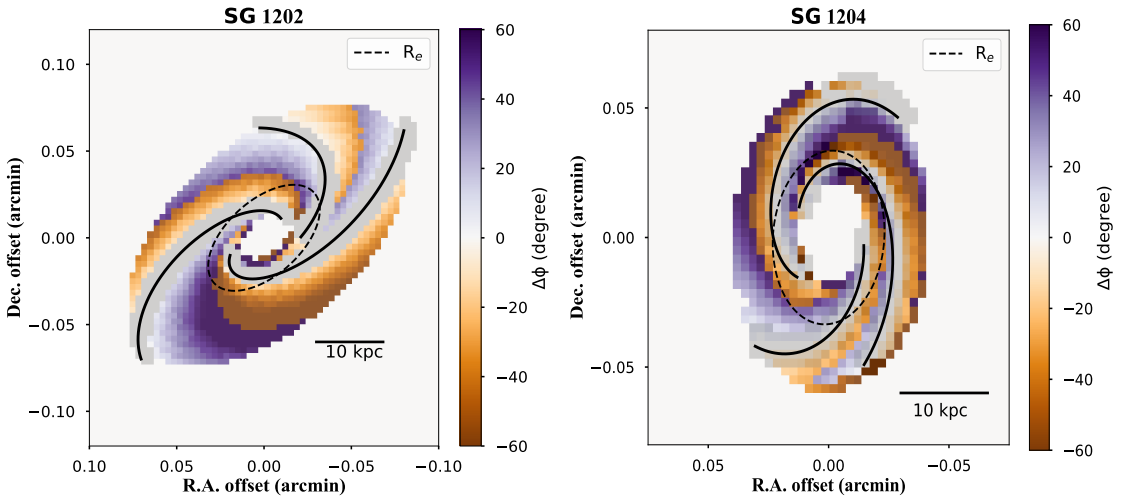


**Figure 2.3:** A measure of the angular azimuthal distance to the nearest spiral arm (grey pixels) at a constant galactocentric distance ($\Delta\phi$) of SG1202 (left) and SG1204 (right), over-plotted with the spiral arm ridge lines. We define $\Delta\phi$ only for the spaxels located at the galactocentric distance where three spiral arms are present, thus there is an absence of $\Delta\phi$ in the central region. Inter-arm spaxels with negative (positive) $\Delta\phi$ are classified as downstream (upstream), colour-coded as orange (purple). $1R_e$is shown as the dashed ellipse.

a sensitive indicator of young, massive stellar populations. In this work, we adopt the star formation rate (SFR) prescription from Kennicutt (1998) to measure the SFR for each spaxel:

$$\mathrm{SFR}(\mathrm{M_\odot yr^{-1}\ cm^{-2}}) = 7.9 \times 10^{-42} \times \mathrm{F_{H\alpha}(erg\ s^{-1}\ cm^{-2})}, \tag{2.5}$$

where $F_{\mathrm{H}\alpha}$ is the flux of H$\alpha$ per spaxel after dust-correction (Sec 2.3.2). For consistency with the MAGPI survey, we adopt the Chabrier (2003) IMF. Following Bernardi et al. (2010), the SFR is divided by $10^{0.25}$ to convert the IMF from the original Salpeter (1955) to our preferred Chabrier (2003) IMF.

We calculate the spatially resolved SFR surface density ($\Sigma_{\mathrm{SFR}}$) as follows:

$$\Sigma_{\mathrm{SFR}}(\mathrm{M_\odot yr^{-1}kpc^{-2}}) = \frac{\mathrm{SFR} \times\ 10^{-0.25}}{[\mathrm{D_A(kpc)} \times 0.2]^2}, \tag{2.6}$$

where $D_{\mathrm{A}}$ is the angular diameter distance of the galaxy and 0.2 arcsec pixel$^{-1}$ is the pixel scale of the MAGPI survey. The higher $\Sigma_{\mathrm{SFR}}$ in the spiral arms than in the inter-arm regions observed in both SG1202 and SG1204 shows that the enhanced star formation is occurring within the spiral arms (see derived $\Sigma_{\mathrm{SFR}}$ maps in Fig 2.4).

Fig 2.5 compares the radial profiles of $\Sigma_{\mathrm{SFR}}$ in the $\Delta\phi < 0$ (downstream; orange) and $\Delta\phi > 0$ (upstream; purple) regions as a function of deprojected radial distance. In SG1202 (left panel of Fig 2.5), we observe a generally higher $\Sigma_{\mathrm{SFR}}$ in the downstream (orange) than in the upstream (purple) between 1 and $2R_e$ ($\sim$ 10 kpc $-$ 20 kpc). The $\Sigma_{\mathrm{SFR}}$ in the

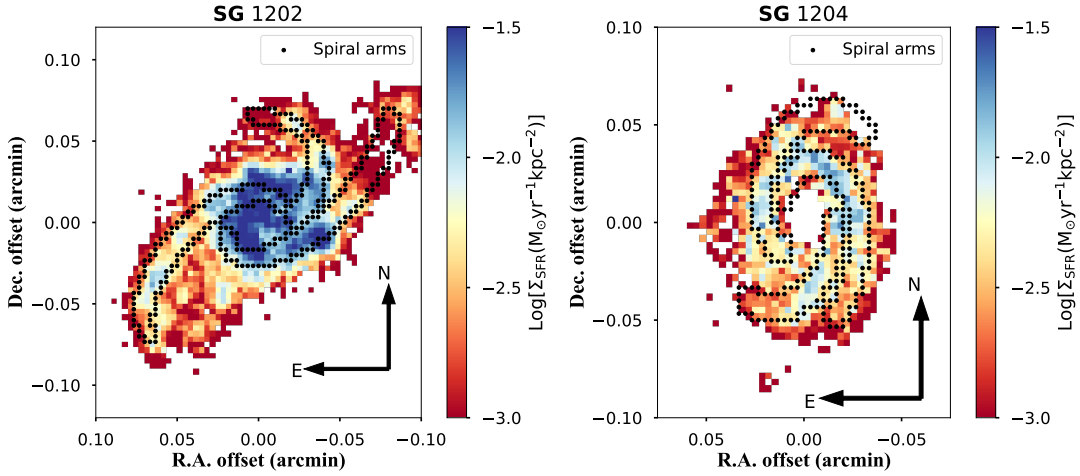


**Figure 2.4:** $\Sigma_{SFR}$ maps based on dust-corrected H$\alpha$ flux of SG1202 (left) and SG1204 (right), over-plotted with the boundary of defined spiral arm regions. Higher (blue) $\Sigma_{SFR}$ is predominantly located within the arm regions.

downstream ($\Delta\phi < 0$) of SG1204 (right panel of Fig 2.5) is indistinguishable from the upstream ($\Delta\phi > 0$) at all galactocentric distances and has no noticeable change at $1R_e$, unlike SG1202. The $\Sigma_{SFR}$ radial trends in different $\Delta\phi$ of SG1202 are consistent with the theoretical expectations from the quasi-stationary density wave theory (Sec 2.1). Our data indicate more intense star formation located on the leading side of the spiral arm, compared to the trailing side between 1 and $2R_e$. The absence of an offset in $\Sigma_{SFR}$ across all radii of SG1204 can be the consequence of the galaxy having a tighter pitch angle (last column in Tab 2.1) compared to SG1202. This scenario is further discussed in Sec 2.4 and requires a larger observational sample to investigate.

### 2.3.6 Gas-phase metallicity

The spatial distribution of gas-phase metallicities is a critical component for understanding the physical evolution of spiral galaxies, including their star formation history and mixing processes in the ISM (Maiolino & Mannucci 2019; Kewley et al. 2019; Li et al. 2021; Sharda et al. 2023). Oxygen is the most abundant metal element in the Universe, which is mostly produced on short timescales by Type II supernovae along with other $\alpha$-elements. In this work, we measure the oxygen abundances to represent the gas-phase metallicities of our galaxies utilising the N2O2 diagnostic (Kewley & Dopita 2002). The N2O2 diagnostic uses three bright optical lines: [N II]$\lambda$6584/[O II]$\lambda\lambda$3726,3729. The combination of [N II]$\lambda$6584 and [O II]$\lambda\lambda$3726,3729 requires an reliable extinction correction which is carried out in Sec 2.3.2. The N2O2 diagnostic is insensitive to the ionisation parameter or ionising spectrum hardness (Zhang et al. 2017a; Kewley et al. 2019). As such, it is also insensitive to the diffuse ionised gas that permeates outside of H II regions. It makes

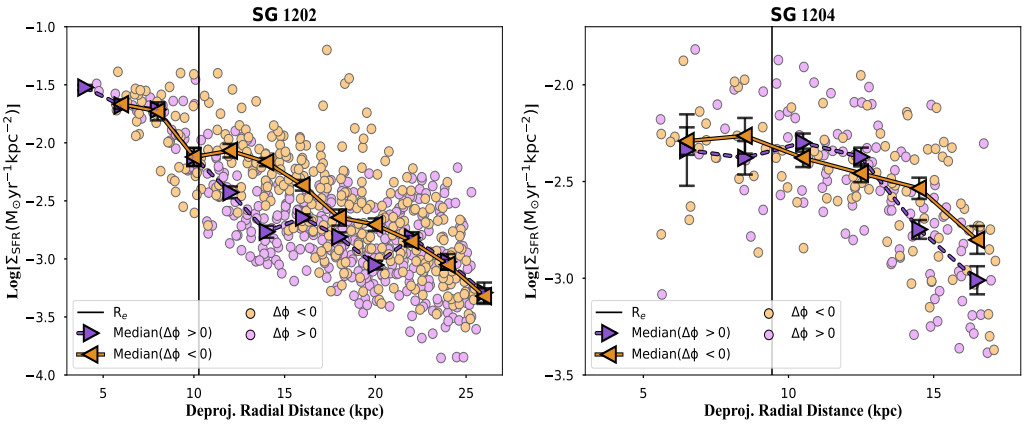


**Figure 2.5:** Radial profiles of $\Sigma_{\rm SFR}$ of SG1202 (left) and SG1204 (right), colour-coded by their location in the spiral galaxy: $\Delta\phi < 0$ (downstream; orange) and $\Delta\phi > 0$ (upstream; purple). The $x$-axis is the radial distance to the galaxy centre after deprojection (following Grasha et al. 2017). The medians of each 1 kpc elliptical bin are marked as triangles with 1 $\sigma$ error bars. The vertical solid line marks the location of $1R_e$ in each galaxy. Significantly higher $\Sigma_{\rm SFR}$ is observed in the downstream ($\Delta\phi < 0$; orange) of SG1202 than the upstream ($\Delta\phi > 0$; purple) between $1 <$ R/$R_e <$ 2, whereas SG1204 shows comparable $\Sigma_{\rm SFR}$ in the $\Delta\phi < 0$ (downstream) and $\Delta\phi > 0$ (upstream) regions across all galactocentric distances.

N2O2 an ideal metallicity diagnostic for our observations. We utilise the python package `PYMCZ` (Bianco et al. 2016) to measure the gas-phase metallicities and uncertainties with a Monte Carlo method.

We present the metallicity radial profiles, colour-coded by their $1\sigma$ uncertainty, in the left column of Fig 2.6. We show the 2D metallicity maps in the middle column of Fig 2.6. The observed negative radial gradient ($-0.069 \pm 0.002$ dex/$R_e$) in SG1202 is indicative of typical inside-out formation, commonly seen in local spiral galaxies (Sánchez-Menguiano et al. 2018; Chen et al. 2023) while the flat metallicity gradient ($-0.014 \pm 0.007$ dex/$R_e$) in SG1204 suggests strong gas mixing which could be induced by recent interactions or cosmic gas accretion (Kewley et al. 2010; Rupke et al. 2010a,b; Perez et al. 2011; Vollmer et al. 2012). The shallower gradient in the $\Sigma_{\rm SFR}$ profile of SG1204 compared to the one of SG1202 is also suggestive of a stronger mixing process, which can cause the absent azimuthal variation in the metallicity of SG1204 (further discussed in Sec 2.4).

From the 2D metallicity map of SG1202 (top middle panel of Fig 2.6), we observe significantly higher metallicities (redder colour) in the inner region which is consistent with the negative metallicity gradient. We notice bluer spaxels (low metallicities) concentrated within the spiral arms than the inter-arms. In the 2D metallicities map of SG1204 (bottom middle panel of Fig 2.6), we find comparable metallicity across the disc region which is in line with the observed shallow metallicity gradient. We do not find a distinctive difference in the metallicity between spiral arms and inter-arms which could be attributed to the

tighter spiral arms.

Azimuthal metallicity variation can inform us of how metals are mixed in with their neighbouring ISM when gas and stars are rotating in their orbits (Ho et al. 2017). The IFS data of MAGPI allow us to study small-scale variations (0.6 − 0.8 arcsec FWHM) present in the gas-phase metallicity, which is typically a much weaker trend than the global radial gradient. To calculate the residual metallicity maps $\Delta\log(\mathrm{O/H})$, we first calculate the weighted averages of each 1 kpc elliptical bin to represent the radial gradients and subtract that from the metallicity maps. Positive (negative) residual $\Delta\log(\mathrm{O/H})$ indicates higher (lower) 12 + log(O/H) compared to spaxels at the same galactocentric distance; this allows us to study the azimuthal variations, if present.

In SG1202 (top right panel of Fig 2.6), we find higher $\Delta\log(\mathrm{O/H})$ in the inner region of the northwest spiral arm while the north arm and east arm are systematically dominated by negative $\Delta\log(\mathrm{O/H})$. It is challenging to directly compare the metallicity between the arm and inter-arm regions based on the $\Delta\log(\mathrm{O/H})$ map of SG1204 (lower panel of Fig 2.6), since the scale of $\Delta\log(\mathrm{O/H})$ is comparable to the typical uncertainty of gas-phase metallicity (0.1 dex). We perform a Kolmogorov–Smirnov (KS) test to compare the distributions of $\Delta\log(\mathrm{O/H})$ in the arm and inter-arms. The results of the KS test and the $p$-values are shown in Table 2.2 and summarised below. The $p$-value measures the probability of the null hypothesis that the two samples are drawn from the same distribution for which a significance level of 1% is commonly used. It is worth mentioning that the $p$-values are an over-representation of how different the distributions truly are because the large sample size will cause the KS test to have very high power for discerning small differences in the distributions. In addition, the KS test does not take into account the error in the parameters (Lazariv & Lehmann 2018).

For SG1202, the $p$-value ($1.7 \times 10^{-4}$) of the KS test suggests that $\Delta\log(\mathrm{O/H})$ has a different distribution in the arms compared to the inter-arms. We find generally negative $\Delta\log(\mathrm{O/H})$ in the spiral arms with an error-weighted average of $-3.9 \pm 1.0 \times 10^{-3}$. This is lower than the inter-arms with an error-weighted average of $4.3 \pm 1.0 \times 10^{-3}$. SG1204 has spiral arms that are significantly tighter (with a smaller pitch angle) than SG1202. The KS test suggests that it is possible that the $\Delta\log(\mathrm{O/H})$ distributions in the arms and inter-arms are drawn from the same distribution (with a $p$-value of $6.8 \times 10^{-2}$; Tab 2.2). The difference in the $\Delta\log(\mathrm{O/H})$ of SG1202 and SG1204 is implied in the more wounded spiral arms of SG1204, coming along with stronger mixing processes. We discuss the physical mechanisms driving this difference in detail in Sec 2.4.

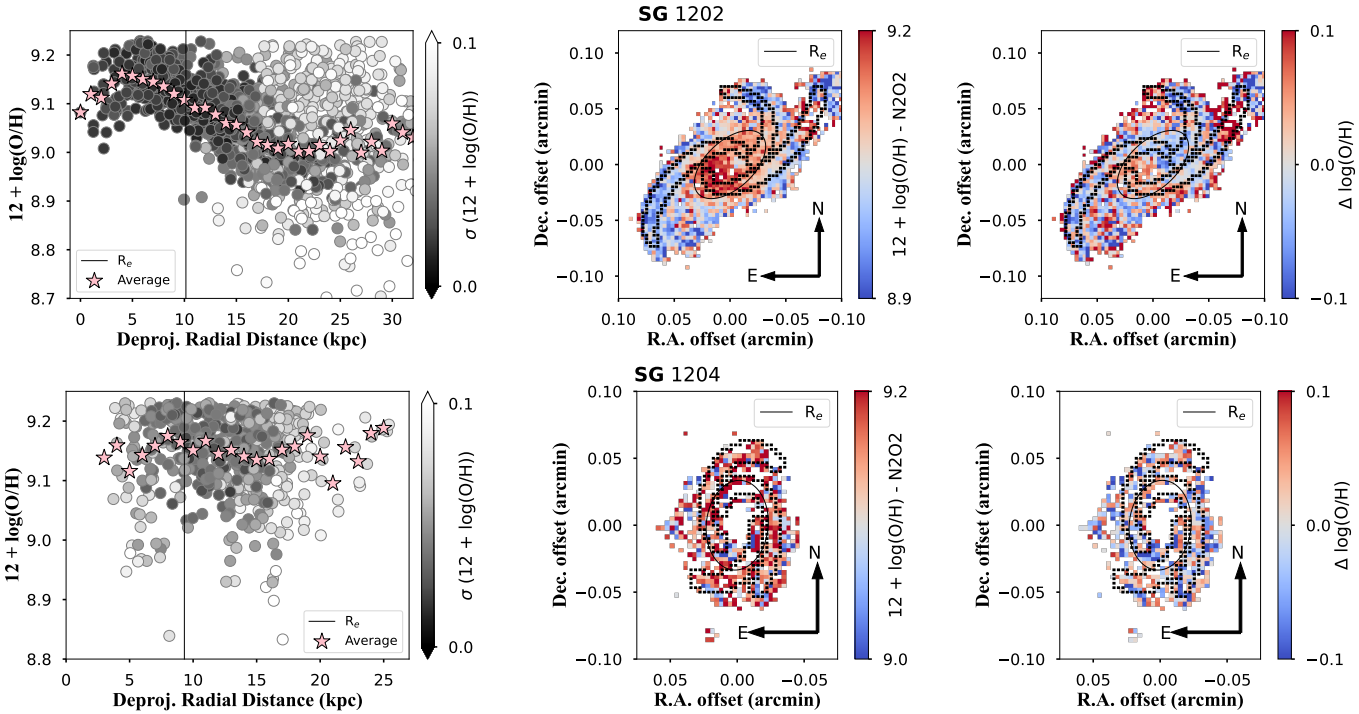


**Figure 2.6: Left panels:** Radial profiles of gas-phase metallicity of SG1202 (top) and SG1204 (bottom), color-coded by $1\sigma$ uncertainty. The vertical solid line delimits the $1R_e$. The pink star symbols are the weighted average of each 1 kpc elliptical bin. We observe a steep-shallow metallicity gradient in SG1202 which is consistent with the simulation in Garcia et al. (2022) and local observations in Grasha et al. (2022); Chen et al. (2023). We find a flat metallicity gradient in SG1204 which indicates strong mixing effects. **Middle panels:** gas-phase metallicity maps 12 + log(O/H) of SG1202 (top) and SG1204 (bottom), overplotted with the boundary of spiral arms and an ellipse at the location of $1R_e$. We find a concentration of blue spaxels with low metallicity within the spiral arms of SG1202 but no systematic difference between arms and inter-arms of SG1204. **Right panels:** residual metallicity maps $\Delta$log(O/H) of SG1202 (top) and SG1204 (bottom) obtained by subtracting the radial gradient (pink star symbols in the left column) from the metallicity maps (middle), overplotted with the boundary of spiral arms and ellipse at $1R_e$. We observe a lower $\Delta$log(O/H) in the arm regions of SG1202, but no significant azimuthal variation in SG1204. This difference can be a consequence of efficient mixing which is implied in the flat metallicity gradient of SG1204.

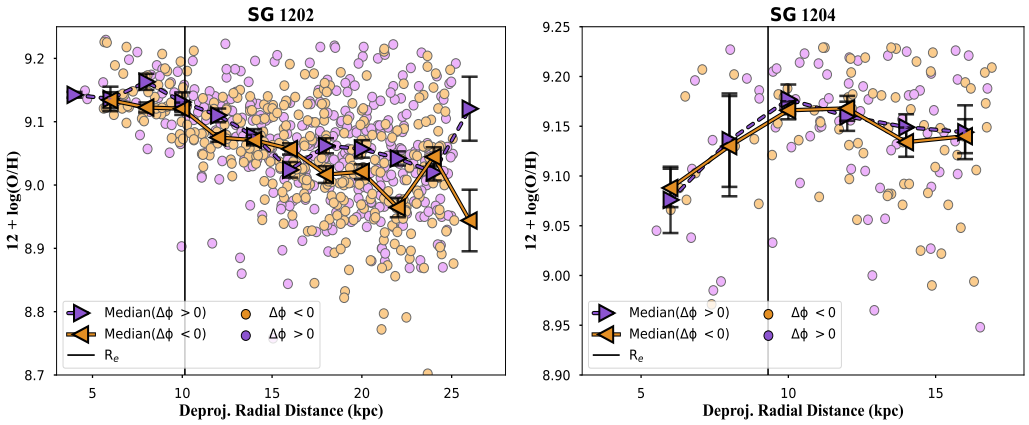


**Figure 2.7:** Comparison of metallicity in the $\Delta\phi < 0$ (downstream; orange) versus $\Delta\phi > 0$ (upstream; purple) spaxels in SG1202 (left) and SG1204 (right). The large solid triangles are the medians of each 1 kpc elliptical bin, with $1\sigma$ error bars. $1R_e$ is marked as vertical solid lines. The KS test suggests the 12 + log(O/H) in the downstream and upstream of SG1202 are possibly drawn from different distributions while agreeing that the 12 + log(O/H) on both sides of the spiral arms in SG1204 are possibly drawn from the same distribution.

Based on the measurement of $\Delta\phi$ (Sec 2.3.4), we compare the 12 + log(O/H) on different sides of the spiral arms across different radii (Fig 2.7). In SG1202, we observe marginally higher metallicities in the upstream (purple; $\Delta\phi > 0$) than in the downstream (orange; $\Delta\phi < 0$), outside $1\sigma$ uncertainty and within $3\sigma$ uncertainty. The $p$-value ($4.7 \times 10^{-3}$) from the KS test strongly rejects the null hypothesis that the 12 + log(O/H) in the downstream and upstream are drawn from the same distribution. The observed azimuthal variation in the metallicity of SG1202 suggests that the origin and development of spiral arms in this galaxy are consistent with the density wave theory. However, we find that the metals in the ISM are well mixed in the inter-arms of SG1204. The $p$-value ($4.1 \times 10^{-1}$) from the KS test supports the same distribution of 12 + log(O/H) on both sides of the spiral arms of SG1204. The absence of azimuthal metallicity variation in SG1204 is consistent with the dynamically-driven spiral arms. Besides, the different azimuthal metallicity distributions in the SG1202 and SG1204 can be attributed to the tighter pitch angle of SG1204 which implies a shorter (more efficient) mixing time scale and higher ISM mixing effects.

### 2.3.7 Stellar age

In addition to the distribution of the ISM gas, the distributions of stellar populations also hint at the origin and evolution of spiral galaxies. In this work, we constrain the stellar age with $D_{4000}$, which is a continuum feature that occurs around 4000Å due to the absorption in the atmosphere within older stellar populations (Noll et al. 2009). Due to our limited spectral quality, we are unable to operate spectrum energy distribution (SED) fitting on a spaxel scale. To get a sufficient SNR for SED fitting, we must bin the MAGPI data

into a coarser spatial resolution, rendering the spiral arms and inter-arm regions no longer distinguishable. Based on the GIST stellar continuum fits (Sec 2.3.1), we determine the $D_{4000}$ value on a spaxel level following:

$$D_{4000} = \frac{\mathrm{Flux}_{\mathrm{restframe}}(4050\text{Å} - 4250\text{Å})}{\mathrm{Flux}_{\mathrm{restframe}}(3750\text{Å} - 3950\text{Å})}. \tag{2.7}$$

We exclude spaxels with $D_{4000}$ uncertainty larger than 0.5 in the following analysis of stellar age.

Consistent with inside-out galaxy formation, we find negative gradients in the $D_{4000}$ of SG1202 and SG1204 (left panels of Fig 2.8), with a flattening trend outside $1R_e$. In the middle panels of Fig 2.8, we present the 2D maps of $D_{4000}$, overplotted with the boundary of the spiral arms. In SG1202, we observe slightly lower $D_{4000}$ (bluer spaxels) in the spiral arms compared to the inter-arms outside $1R_e$, which indicates younger stellar age in the arm regions than the inter-arms. These results are in agreement with the observed higher $\Sigma_{\mathrm{SFR}}$ within the arm regions of SG1202 (Sec 2.3.5). However, in SG1204, we have difficulty comparing the $D_{4000}$ within the arm regions and the close inter-arms based on the tight spiral features. We carry on our study of $D_{4000}$ by introducing the $D_{4000}$ residual in the next paragraph.

To explore the azimuthal variation of $D_{4000}$, we subtract the radial gradient from the original $D_{4000}$ maps (middle panels of Fig 2.8) to create the $D_{4000}$ residual maps ($\Delta D_{4000}$; right panels of Fig 2.8). The radial gradient is represented by the weighted average of each 1 kpc elliptical bin (light pink star symbols in the left panels of Fig 2.8). A positive $\Delta D_{4000}$ indicates an older stellar age than the average stellar age at the same galactocentric distance. Both SG1202 and SG1204 show a generally negative $\Delta D_{4000}$ (blue spaxels) within the spiral arms. The KS test results ($p$-value of $2.0 \times 10^{-6}$) indicate that the distribution of $\Delta D_{4000}$ in the spiral arms of SG1202 is significantly different from the distribution in the inter-arms. Similarly, SG1204 shows a $\Delta D_{4000}$ variation between arms and inter-arms, with a $p$-value of $3.6 \times 10^{-3}$. The concentration of negative $\Delta D_{4000}$ (younger stellar population) in the arm region of SG1202 and SG1204 is in line with the expectation from the observed higher $\Sigma_{\mathrm{SFR}}$ in the arms (Sec 2.3.5). We will further discuss the connection among different tracers in Sec 2.4.

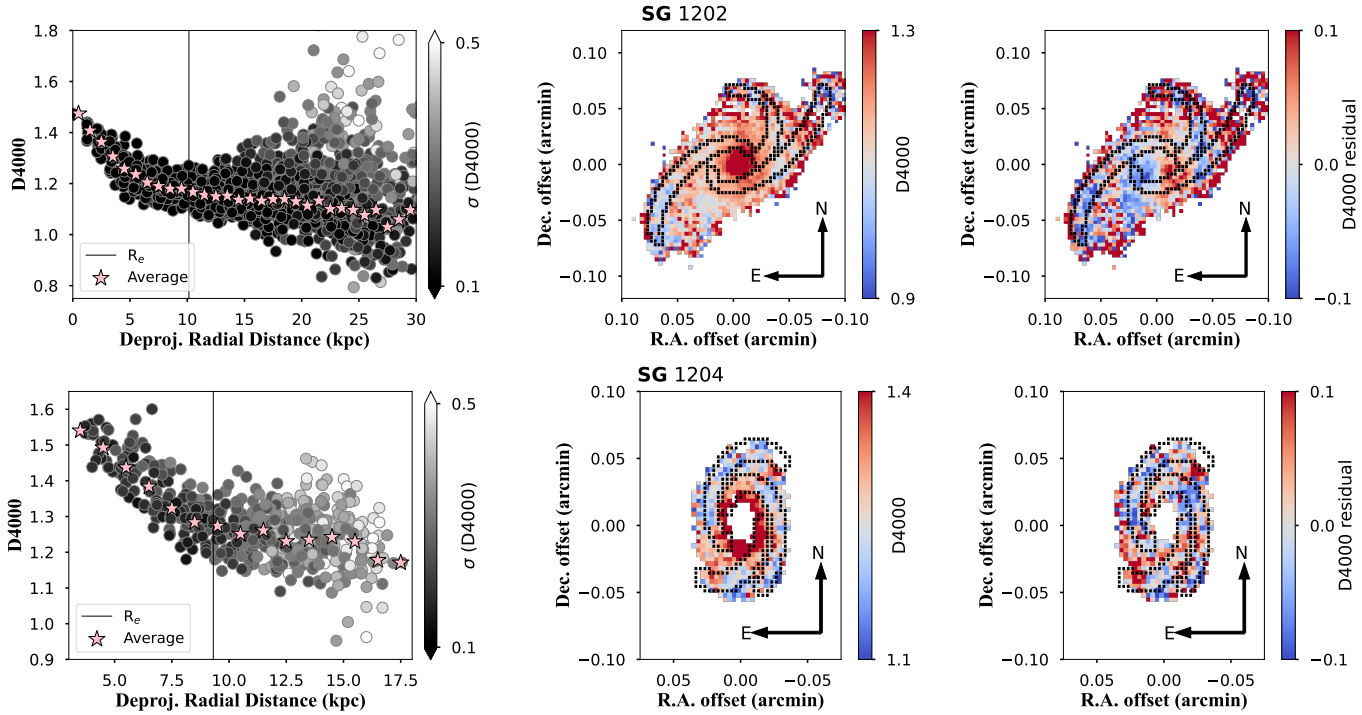


**Figure 2.8:** Radial profiles colour-coded by $1\sigma$ uncertainty (left), 2D maps (middle), and residual maps (right) of $D_{4000}$ in SG1202 (top) and SG1204 (bottom). The residual maps are calculated by subtracting the weighted average of each 1 kpc bin (light pink star symbols in the left panel) from the observed $D_{4000}$ maps (middle panel). The location of $R_e$ is shown as a vertical line in the left panel and as an ellipse in the middle and right panels. The boundary of the spiral arm regions is over-plotted as dashed lines on the $D_{4000}$ and residual maps. We find negative $D_{4000}$ radial gradients in both galaxies which support an inside-out formation scenario. Both $D_{4000}$ maps and residual maps indicate lower $D_{4000}$ (younger stellar populations) in the spiral arms of SG1202 and SG1204.

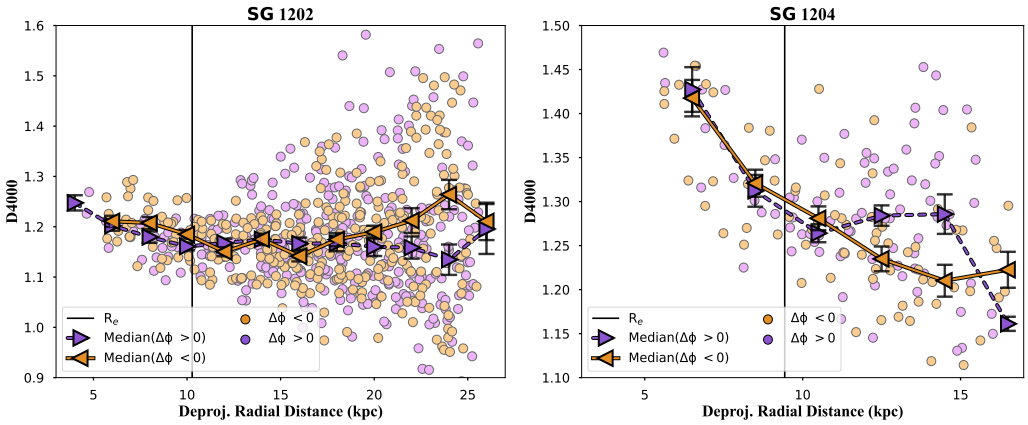


**Figure 2.9:** Similar to Fig 2.7 but with $D_{4000}$ on the $y$-axis. We find comparable $D_{4000}$ between $\Delta\phi > 0$ (upstream; purple) and $\Delta\phi < 0$ (downstream; orange) in both SG1202 and SG1204.

Taking advantage of the high spatial resolution of MUSE, we compare the $D_{4000}$ in the downstream and upstream across different radii (Fig 2.9). We observe no distinguishable $D_{4000}$ offset, within $1\sigma$ uncertainty, between downstream and upstream in SG1202 from the radial profiles (Fig 2.9). The $p$-values from the KS test on the $\Delta D_{4000}$ of downstream versus upstream ($1.4 \times 10^{-1}$ for SG1202 and $3.9 \times 10^{-1}$ for SG1204) indicate the $\Delta D_{4000}$ on both sides of the spiral arms are consistent with being drawn from the same distribution. The offset of the medians on the outskirt of SG1204 could be attributed to the limited number of available spaxels.

To summarise, the open-armed spiral galaxy SG1202 shows higher $\Sigma_{SFR}$ (left panel of Fig 2.5) and lower gas-phase metallicity (left panel of Fig 2.7) in the downstream ($\Delta\phi < 0$; orange) than the upstream ($\Delta\phi > 0$; purple). As a proxy for the stellar age within SG1202, $D_{4000}$ does not show a distinguishable offset between both sides of the arm regions (left panel of Fig 2.9). The tightly wounded spiral galaxy SG1204 presents no significant differences in the $\Sigma_{SFR}$ (right panel of Fig 2.5), 12 + log(O/H) (right panel of Fig 2.7) or $D_{4000}$ (right panel of Fig 2.9) between the downstream and the upstream. Observed differences in the azimuthal distributions of H$\alpha$, 12 + log(O/H) and $D_{4000}$ may arise due

| Galaxy | gas and stellar properties | Arms vs. Inter-arms | $\Delta\phi < 0$ vs. $\Delta\phi > 0$ |
|---|---|---|---|
| SG1202 | $\Delta\log(O/H)$ | $1.7\times10^{-4}$ | $4.7\times10^{-3}$ |
| | $\Delta D_{4000}$ | $2.0\times10^{-6}$ | $\mathbf{1.4\times10^{-1}}$ |
| SG1204 | $\Delta\log(O/H)$ | $\mathbf{6.8\times10^{-2}}$ | $\mathbf{4.1\times10^{-1}}$ |
| | $\Delta D_{4000}$ | $3.6\times10^{-3}$ | $\mathbf{3.9\times10^{-1}}$ |

**Table 2.2:** The $p$-values of KS-test on $\Delta\log(O/H)$ - first and third rows - and $\Delta D_{4000}$ - second and fourth rows - in the spiral arms versus inter-arms (column 3), $\Delta\phi < 0$ (downstream) versus $\Delta\phi > 0$ (upstream) in column 4. The populations whose $p$-values from the KS test are larger than 1% are highlighted in bold.

to the different stellar time scales for these tracers, which will be further discussed in Sec 2.4.

## 2.4 Discussion

In this section, we discuss the impacts of the boundary between downstream and upstream regions on the results of the MAGPI survey. We illustrate the differences among various ISM tracers and stellar population indicators. It reminds us of the importance of selecting an appropriate indicator when testing the density wave theory through observations. We also compare our observational results with the theoretical expectations derived from the density wave theory and the dynamical spiral theory. In the last subsection, we address the effects of gas flows, which can complicate our test of the density wave theory.

### 2.4.1 Impacts of the boundary between downstream and upstream regions

We find enhanced $\Sigma_{\rm SFR}$ in the downstream (orange) than the upstream (purple) in SG1202 but not in $D_{4000}$. It is important to note that the connection between downstream and upstream at the high $|\Delta\phi|$ end can possibly obscure the signals of offset. To address this, we conduct a test with SG1202 by employing a $|\Delta\phi|$ limit of $< 40^\circ$ (see Fig 2.10) and subsequently re-compare the downstream and upstream regions. Similarly, we detect a significant azimuthal variation in $\Sigma_{\rm SFR}$ but not in the 12+log(O/H) or $D_{4000}$ (Fig 2.11). The $p$-value ($1.6 \times 10^{-3}$) from the KS test suggests the 12+log(O/H) on both sides of the spiral arms are drawn from different distributions. On the other hand, the $p$-value ($7.3 \times 10^{-1}$) from the KS test indicates the $D_{4000}$ on both sides of the spiral arms are drawn from the same distribution. These results are consistent with our main findings, where we do not impose a limit on the $|\Delta\phi|$ (see Sec 2.3). Our tests suggest that the linkage between the downstream and the upstream has minimal impact on the azimuthal variation.

### 2.4.2 Difference in various tracers

The interpretation of the physics driving our observational trends is impacted by the different timescales associated with and traced by the ISM and stellar properties. Poggio et al. (2022) find the progressive disappearance of spiral structures in the global metallicity when they gradually include cooler and older stars. Their result hints at the importance of using tracers sensitive to appropriate time scales when observing spiral structures and material in the inter-arm regions. We compare and summarise what the different indicators (SFR, gas-phase metallicity and $D_{4000}$) trace and their different timescales in

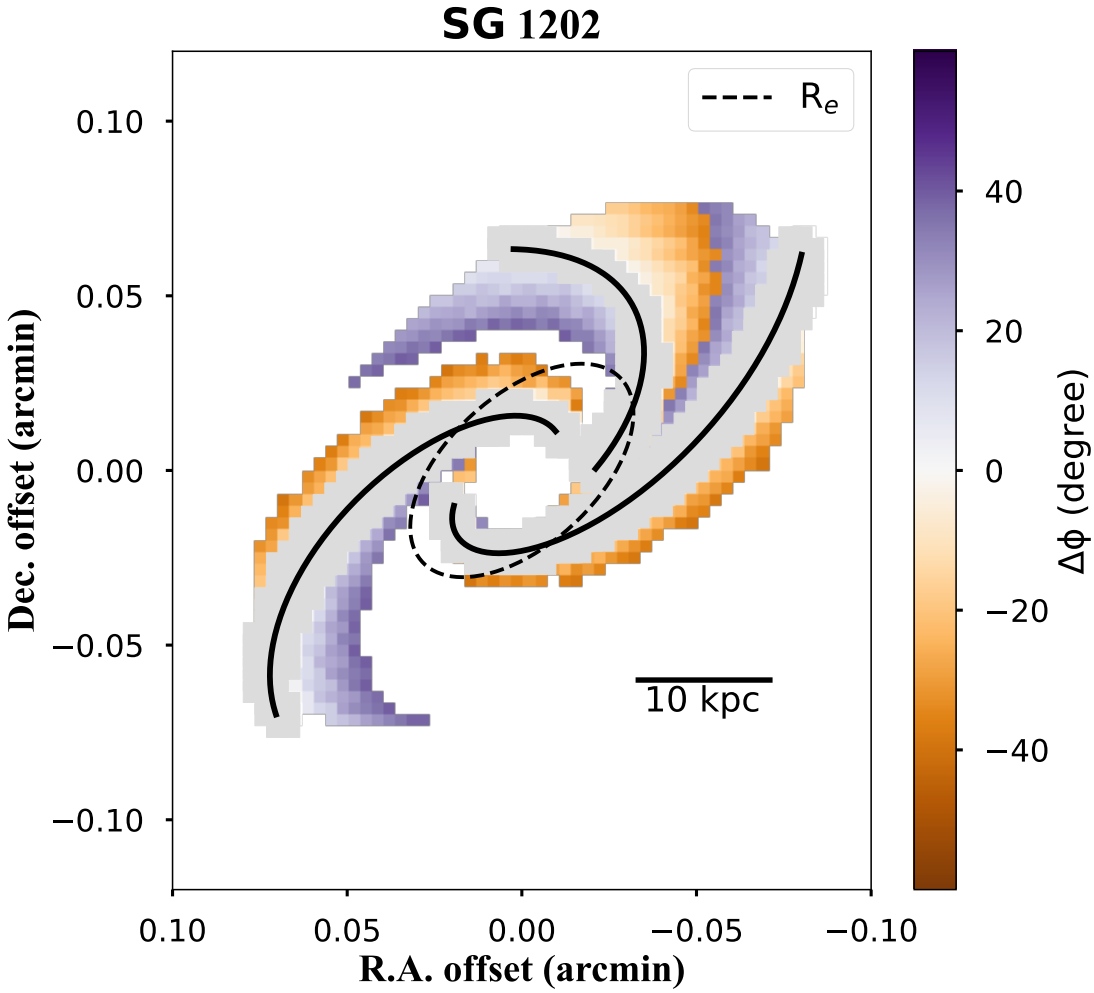


**Figure 2.10:** $\Delta\phi$ map after applying the limit of $|\Delta\phi| < 40°$. The grey regions are defined as the spiral arm regions. The limit of the color bar is matched with Fig 2.3 for better comparison.

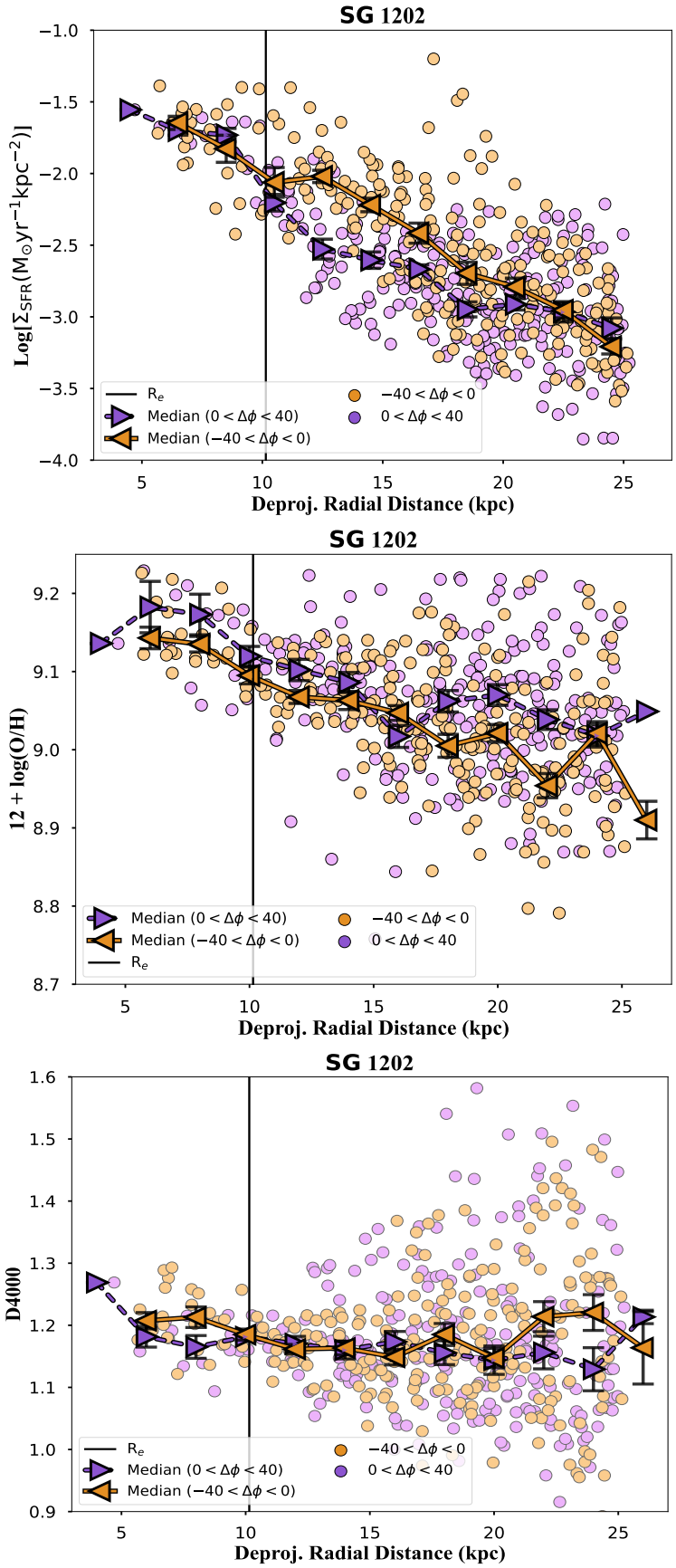


**Figure 2.11:** Radial profiles of $\Sigma_{SFR}$, 12+log(O/H), and $D_{4000}$, colour-coded by the downstream (orange) and upstream (purple). Only spaxels where $|\Delta\phi| < 40°$ are considered.

this section.

Only stars more massive than $\sim 20$ $M_\odot$ produce a measurable ionising photon flux. For recently formed stellar populations born through an instantaneous burst, the ionising photon flux decreases by two orders of magnitude between 5 Myr and 10 Myr after the burst. Thus, the H$\alpha$ emission is an instantaneous tracer ($\lesssim 30$ Myr; Calzetti 2013) of the youngest, most massive and short-lived rare stars.

Gas-phase metallicity traces metals produced by recent star formation, and it reaches equilibrium within a concise time (a few hundred Myr) compared to the depletion time (Davé et al. 2011, 2012; Lilly et al. 2013; Sharda et al. 2021). The emission lines we use to measure metallicity are mostly excited by O and B stars, which have formed within the past $\lesssim 10$ Myr, and the gas-phase metallicity measured in this way can therefore be treated as the current "instantaneous" metallicity of the gas out of which the stars have formed.

The $D_{4000}$ is tracing the stellar population ages while H$\alpha$ and gas-phase metallicity are indicators for gas ISM properties. The drop in intensity at the blue end of the spectrum is a result of (1) a relative lack of young, bright, blue stars in old stellar populations that dominate the light of a galaxy and (2) increased metal absorption in stellar atmospheres of old and metal-rich stellar populations. $D_{4000}$ is sensitive to starbursts in the past $1 \sim 2$ Gyr (Kauffmann et al. 2003a), which is tracing a timescale significantly longer than that of H$\alpha$ emission and gas-phase metallicity. The long timescale may allow the latest generation of stars to travel across the disc and reach the next spiral pattern. Due to their rarity and short-lived nature, the massive stars make up a small portion of all stars in a galaxy and thus have a small effect on the mean $D_{4000}$ in the IFS data as opposed to low-mass, cooler and longer-lived stars. Therefore, the influence of spiral structures on $D_{4000}$ is less significant, compared to H$\alpha$ as an emission line feature.

We estimate the upper limit of crossing time ($t$) between two spiral arms by assuming the spiral arms have an equal distance to each other at a radius of $2R_e$, using the following equations.

$$D_{\rm arm} = \frac{4\pi R_e}{3}, \tag{2.8}$$

where $D_{\rm arm}$ is simply the circumference at $2R_e$ divided by three (for a three spiral-arm galaxy),

$$t = \frac{D_{\rm arm}}{v_{\rm rot}}. \tag{2.9}$$

We adopt the gas rotational velocity ($v_{\rm rot}$) from Sharma et al. (in prep), which yields the beam-smearing corrected rotational curve based on their 3D modelling method of the ionised gas kinematics. They find that $v_{\rm rot}$ at $2R_e$ is 225 km/s and 305 km/s in SG1202 and

SG1204, respectively. The galactocentric distance of $2R_e$ is 20 kpc for SG1202 and 18 kpc for SG1204. The estimated crossing time of SG1202 (SG1204) is ~0.18 Gyr (~0.12 Gyr), which is shorter than the timescale to which $D_{4000}$ is sensitive ($1 \sim 2$ Gyr). Thus the absent azimuthal variation in the $D_{4000}$ of SG1202 as well as SG1204 is not unreasonable. Both estimated crossing times are longer than the timescale to which H$\alpha$ is sensitive (i.e., $\lesssim 30$ Myr). Therefore, the observed azimuthal variation in H$\alpha$ of SG1202 is reasonable.

Our work reveals the underlying differences in timescales traced by gas ISM properties (H$\alpha$ and gas-phase metallicity) and stellar populations ($D_{4000}$). When investigating the mechanisms driving spiral features, selecting an indicator sensitive to a timescale shorter than the crossing time $t$ is crucial. Our pilot sample suggests that an instantaneous or short-time-scale tracer (e.g., SFR and gas-phase metallicity) is better suited for testing the density wave theory, compared to $D_{4000}$.

### 2.4.3 Testing the density wave theory

Recently, there has been a growing number of observational tests on the density wave theory and dynamic spiral theory, which are mostly regarding the pattern speed of spiral arms and the differentiation of gas and stellar motion. Due to the challenges in measuring the pattern speed, an indirect method to constrain the origin of spiral features is to determine the location of spiral shocks. The density wave theory expects an offset between the spiral shocks and the spiral pattern while there is no observable offset expected by the dynamic spirals. In SG1202, we find significantly higher ($\sim$ 0.25 dex) $\Sigma_{\rm SFR}$ in the leading edge of the spiral arms (downstream; orange). The azimuthal variation in $\Sigma_{\rm SFR}$ suggests that the origin and development of the spiral arms in SG1202 can be explained by the density wave theory.

Based on the density wave theory, Edmunds (1990) and Ho et al. (2017) construct chemical evolution models which predict an azimuthal variation in the gas-phase metallicity. NGC1365 (Ho et al. 2017) is observed to show azimuthal variation in the gas-phase metallicity which is consistent with the enhancement effects of spiral arms when material flows across the density waves. However, there are some nearby spiral galaxies showing no azimuthal variation in metallicity (Kreckel et al. 2019).

In this work, we do not observe a significant azimuthal variation in metallicity in SG1202, unlike NGC 1365 ($\sim$ 0.2 dex; Ho et al. 2017). The KS-test (Sec 2.3.6) shows that the gas-phase metallicities in the downstream and upstream regions of SG1202 are drawn from different distributions, which is consistent with the chemical evolution models based on the density wave theory.

Dobbs et al. (2010) suggest an indirect method to examine the density wave theory through

the observed age distribution of stellar clusters. Based on the density wave theory (Lin & Shu 1964), star formation occurs when the gas is compressed and shocked as it periodically passes through the spiral density wave. Due to the differential rotation between material and density wave, the newborn stars move out of the spiral pattern, where the stellar populations inside the co-rotation radius overtake the spirals while the stellar populations outside the co-rotation radius are left behind. This is observable as a red spiral arm with an older stellar population that shows a smaller pitch angle than a blue spiral arm with young stellar ages (Martínez-García et al. 2009b; Pour-Imani et al. 2016). The density wave theory would thus be observable through an offset between different cluster ages azimuthally across the spiral, whereas dynamic spirals predict no age pattern as material falls into the minimal potential from both sides of the spiral arms, resulting in stars at similar ages lying on both sides of the spirals. This method is widely applied to spatially resolved data (Martínez-García et al. 2009b; Sánchez-Gil et al. 2011; Shabani et al. 2018; Abdeen et al. 2022), supporting the density wave theory. On the other hand, there are studies that show no age pattern (Choi et al. 2015; Shabani et al. 2018), in agreement with dynamic spirals.

The limited SNR of the continuum in the MAGPI data hinders our ability to determine reliable and resolved stellar ages through SED fitting. In this study, we employ $D_{4000}$ as a stellar age proxy with the necessary spatial resolution. In both SG1202 and SG1204, we do not find a statistically significant offset of $D_{4000}$ between the downstream and upstream regions. As detailed in Sec 2.4.2, $D_{4000}$ is not an ideal indicator for testing the density wave theory due to its long timescale ($1 - 2$ Gyr). Thus, it remains inconclusive to compare the observations and theories regarding stellar ages in the context of density wave theory in this work.

Some of our observations provide evidence that challenges the validity of the density wave theory. In SG1204, we observe no azimuthal variation in either $\Sigma_{\rm SFR}$ or gas-phase metallicity, which shows a preference for the dynamic spiral theory. It is a caveat that the lack of azimuthal offset results from the combination of i) more pronounced beam-smearing effects than SG1202, and ii) a shorter mixing timescale in SG1204, which features tighter pitch angles. We need to expand our study to more MAGPI spiral galaxies to have a better understanding of how pitch angles impact our test of the density wave theory.

### 2.4.4 Radial gas flows complicate the comparison between observations and theories

Previous simulations (Di Matteo et al. 2013; Grand et al. 2016; Carr et al. 2022; Orr et al. 2023) have discussed the impact of radial stellar migration and gas flows, induced by asymmetric structures such as spiral arms and stellar bars, on the radial and azimuthal variations of metals. In the Feedback In Realistic Environments (FIRE-2) simulation, Orr et al. (2023) find that the spiral arms act as highways to transfer enriched gas outward, flattening the metallicity radial gradients. The FIRE-2 simulated galaxies show no bias of gas-phase metallicity between the arm and inter-arm regions when the sub-grid turbulent diffusion of metals is considered. Simulations by Khoperskov et al. (2023) reveal that the peak of ISM metal-rich material varies depending on the initial radial ISM metallicity gradient. Specifically, the metal-rich gas is concentrated as a spiral feature in the trailing side of the stellar spiral arm when a radial gradient is present in the simulation. Their simulation does not see large-scale azimuthal variation in metallicity in a spiral galaxy set with no radial gradient. The radial gas flows are important and non-negligible as they potentially impact and complicate the observed metallicity gradient and azimuthal variation. Consequently, they obscure potential observational signatures of density waves and affect our interpretation of the origin of spiral features.

We detect a negative gas-phase metallicity radial gradient in both SG1202 ($-0.069 \pm 0.002$ dex/$R_e$) and SG1204 ($-0.014 \pm 0.007$ dex/$R_e$), consistent with an inside-out galaxy formation. The gradients we measure for these two galaxies are relatively shallow compared to those typically seen in local spiral galaxies in the CALIFA survey ($-0.1$ dex/$R_e$; Sánchez et al. 2015), and in the MaNGA survey ($-0.14$ dex/$R_e$; Belfiore et al. 2017). This scenario could be indicative of radial gas flows dispersing and flattening the metal distribution.

The higher gas-phase metallicity observed in the trailing edge of SG1202 (Fig 2.6) is consistent with the simulated galaxy with an initial radial gradient in Khoperskov et al. (2023) The metallicity distribution in SG1202 could be driven by the density wave theory and/or radial gas flows. In SG1204, the azimuthal variation of metallicity is non-observable with a flat metallicity radial gradient. This scenario is in line with Khoperskov et al. (2023) where the presence of radial metallicity gradient is essential for azimuthal variation. The dynamic spirals can also result in no azimuthal variation in metallicity. Our current observations are insufficient to discern the dominant physical mechanisms driving the spiral features in SG1202 and SG1204.

## 2.5 Conclusions

We study the two-dimensional distributions of $\Sigma_{\rm SFR}$ (H$\alpha$), gas-phase metallicity, and $D_{4000}$ in two three-armed spiral galaxies, SG1202 and SG1204, at $z \sim 0.3$ (3 – 4 Gyr ago) from the MAGPI survey (Foster et al. 2021). The goal of our study is to investigate the driving physics of spiral arm formation and how the different physical mechanisms impact and vary the ISM and stellar properties within and up/down stream from the spiral arms. Specifically, we compare our findings with the expectations from two spiral arm formation mechanisms: density wave theory and dynamic spirals.

In SG1202, we observe higher $\Sigma_{\rm SFR}$ (Fig 2.4), systematically lower metallicity (Fig 2.6), and younger stellar age (Fig 2.8) in the spiral arms than the inter-arms. In SG1204, we do not find a statistically significant difference in metallicity (Fig 2.6) or $D_{4000}$ (Fig 2.8) between the arms and inter-arms. We do, however, recover higher $\Sigma_{\rm SFR}$ (Fig 2.4) in the arms of SG1204. These results support the enhancement of star formation within the arm regions. The diversity in the metallicity and stellar age azimuthal trends between SG1202 and SG1204 may be a result of a combination of beam-smearing effects and/or shorter mixing timescale, likely due to the tighter pitch angles in SG1204 compared to SG1202.

We find higher $\Sigma_{\rm SFR}$ in the leading edge of spiral arms ($\Delta\phi < 0$; downstream) in SG1202 (Fig 2.5). This matches the expectation of the density wave theory. The observed higher metallicity in the trailing edge of the spiral arms of SG1202 (Fig 2.7) is consistent with the expectations of radial gas flows driven by spiral arms (Khoperskov et al. 2023). SG1204, on the other hand, does not show a statistically significant offset in the $\Sigma_{\rm SFR}$ (Fig 2.5) or metallicity (Fig 2.7) between both sides of the spiral arms. Our findings for SG1204 are consistent with the dynamic spiral theory. This could also be impacted by radial gas flows, which is consistent with the simulated spiral galaxies with no radial gradients in Khoperskov et al. (2023). We are however unable to determine the dominant mechanism driving the observations based on the current data.

Neither galaxy shows an azimuthal variation in the $D_{4000}$ (Fig 2.9), which may be a consequence of the long timescale (1 – 2 Gyr) traced by $D_{4000}$. This reflects the importance of choosing an indicator sensitive to changes in star formation on time scales shorter than the travel time between two spiral arms.

The effects of spiral arms on the ISM are a complex question requiring further high-resolved observational data across cosmic time. This work is a pilot project with two spiral galaxies at $z \sim 0.3$, with a plan to expand the data to the entire MAGPI survey.

# Acknowledgements

We thank the anonymous referee for their constructive and detailed comments that improved the quality of this work. We thank Paul Torrey for his constructive and enlightening comments and suggestions on this work.

We wish to thank the ESO staff, and in particular the staff at Paranal Observatory, for carrying out the MAGPI observations. MAGPI targets were selected from GAMA. GAMA is a joint European-Australasian project based around a spectroscopic campaign using the Anglo-Australian Telescope. GAMA is funded by the STFC (UK), the ARC (Australia), the AAO, and the participating institutions. GAMA photometry is based on observations made with ESO Telescopes at the La Silla Paranal Observatory under programme ID 179.A-2004, ID 177.A-3016. Parts of this work are supported by the Australian Research Council Centre of Excellence for All Sky Astrophysics in 3 Dimensions (ASTRO 3D), through project number CE170100013. KG is supported by the Australian Research Council through the Discovery Early Career Researcher Award (DECRA) Fellowship (project number DE220100766) funded by the Australian Government. PS is supported by Leiden University Oort Fellowship and the IAU Gruber Foundation Fellowship. CF is the recipient of an Australian Research Council Future Fellowship (project number FT210100168) funded by the Australian Government. CL, JTM and CF are the recipients of ARC Discovery Project DP210101945. GS thanks SARAO postdoctoral fellowship (Grant no.: 97882). LMV acknowledges support by the German Academic Scholarship Foundation (Studienstiftung des deutschen Volkes), the Marianne-Plehn-Program of the Elite Network of Bavaria, and the COMPLEX project from the European Research Council (ERC) under the European Union's Horizon 2020 research and innovation program grant agreement ERC-2019-AdG 882679.

This research has made use of NASA's Astrophysics Data System Bibliographic Services (ADS). This research made use of ASTROPY,[4] a community-developed core Python package for Astronomy (Astropy Collaboration et al. 2013, 2018). This research has made use of the NASA/IPAC Extragalactic Database (NED) which is operated by the Jet Propulsion Laboratory, California Institute of Technology, under contract with NASA. Parts of the results in this work make use of the colormaps in the CMasher package (van der Velden 2020).

[4] http://www.astropy.org

## Data availability

The data used in this article are available under the MAGPI survey on the ESO public archive (1104.B-0536). The reduced MAGPI MUSE datacubes and emission line data products will be made publicly available in forthcoming papers by Medel et al. (in prep.) and Battisti et al. (in prep), respectively. Additional data generated by the analyses in this work are available upon request to the corresponding author.

# 2.6 Appendix: Identified spiral arms from SpArcFiRe

In Sec 2.3.3, we introduce our method of defining the spiral arm ridge lines. The initially defined spiral arms from SpArcFiRe is overplotted on the deprojected white-light images of our galaxies in the left column of Fig 2.12. We fine-tune the starting and ending radii of the spiral ridge lines to improve their alignment with the observed white-light images, shown in the right column of Fig 2.12. The red spiral arms are clockwise with positive pitch angles while the blue ones are counter-clockwise with negative pitch angles.

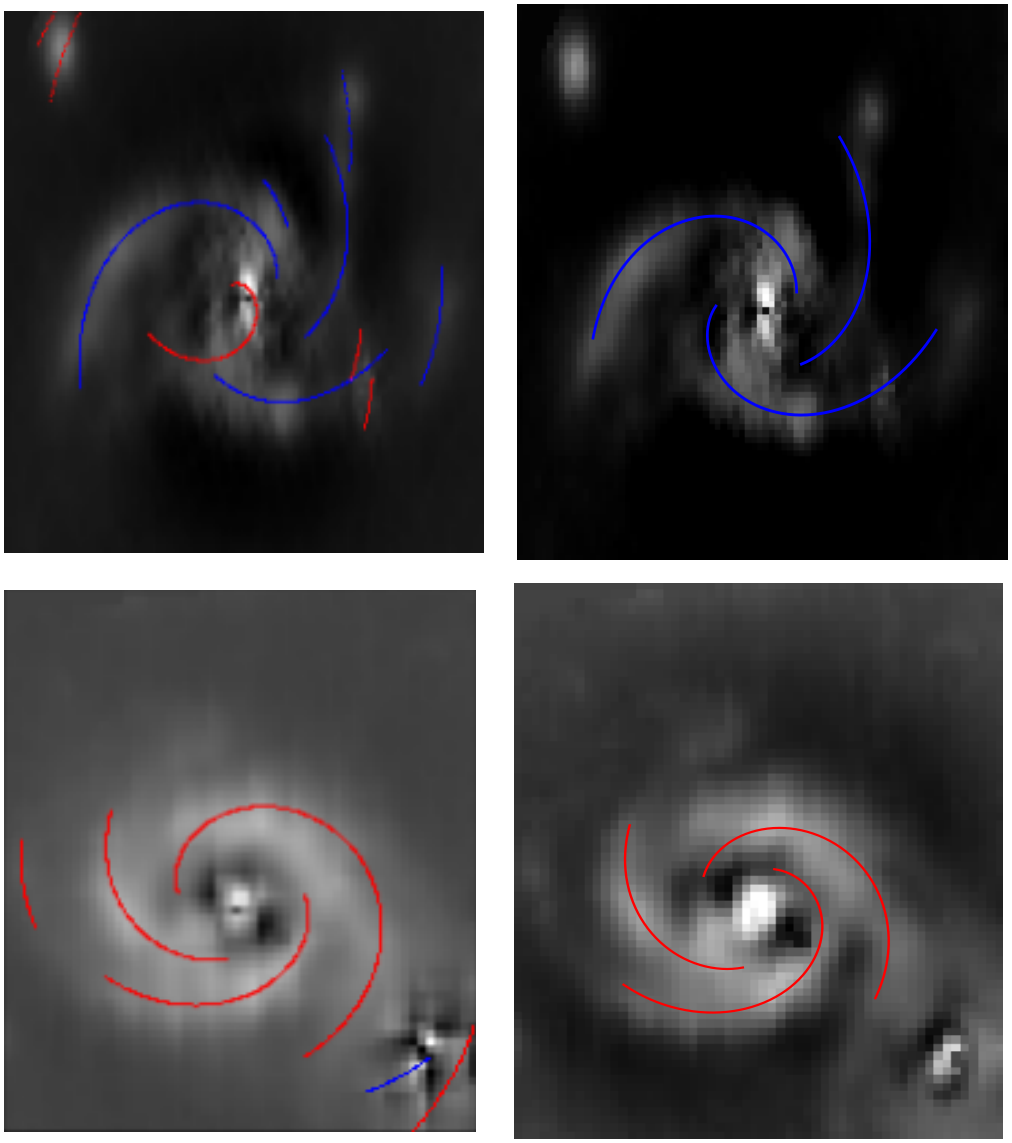

**Figure 2.12: Left Column**: The spiral arm ridge initially defined by SpArcFiRe, overplotted on the deprojected white-light images after subtracted by the Sérsic profile. The red spiral arms are clockwise while the blue ones are counter-clockwise. **Right Column**: The final accepted spiral arm ridge after we fine-tune the starting and ending radii of the spiral arms to improve their alignment with the observed white-light images. The top panels show the SG1202 while the bottom panels show the SG1204.

Chapter 3

# Quantifying azimuthal variations within the interstellar medium of $z \sim 0$ spiral galaxies with the TYPHOON survey

## *Context and Contribution*

*This chapter has been previously published as* ***Quantifying azimuthal variations within the interstellar medium of z ∼0 spiral galaxies with the TYPHOON survey****, by* ***Qian-Hui Chen, Kathryn Grasha, Andrew J. Battisti, Emily Wisnioski, Zefeng Li, Hye-Jin Park, Brent Groves, Paul Torrey, Trevor Mendel, Barry F. Madore, Mark Seibert, Eva Sextl, Alex M. Garcia, Jeff A. Rich, Rachael L. Beaton, and Lisa J. Kewley, 2024, MNRAS, 534, 883–901****. The work is slightly revised based on the thesis examiners' comments, compared to the published version. I have analysed the observation data. I have written the majority of the paper, with inputs and suggestions from co-authors.*

**Abstract**

Most star formation in the local Universe occurs in spiral galaxies, but their origin remains an unanswered question. Various theories have been proposed to explain the development of spiral arms, each predicting different spatial distributions of the interstellar medium. This study maps the star formation rate (SFR) and gas-phase metallicity of nine spiral galaxies with the TYPHOON survey to test two dominating theories: *density wave theory* and *dynamic spiral theory*. We discuss the environmental effects on our galaxies, considering reported environments and merging events. Taking advantage of the large field of view covering the entire optical disk, we quantify the fluctuation of SFR and metallicity relative to the azimuthal distance from the spiral arms. We find higher SFR and metallicity in the trailing edge of NGC 1365 (by 0.117 dex and 0.068 dex, respectively) and NGC 1566 (by 0.119 dex and 0.037 dex, respectively), which is in line with density wave theory. NGC 2442 shows a different result with higher metallicity (0.093 dex) in

the leading edge, possibly attributed to an ongoing merging. The other six spiral galaxies show no statistically significant offset in SFR or metallicity, consistent with dynamic spiral theory. We also compare the behaviour of metallicity inside and outside the co-rotation radius ($R_{CR}$) of NGC 1365 and NGC 1566. We find comparable metallicity fluctuations near and beyond the $R_{CR}$of NGC 1365, indicating gravitational perturbation. NGC 1566 shows the greatest fluctuation near the $R_{CR}$, in line with the analytic spiral arms. Our work highlights that a combination of mechanisms explains the origin of spiral features in the local Universe.

## 3.1 Introduction

Spiral galaxies constitute approximately two-thirds of all massive galaxies in the local Universe (Lintott et al. 2008; Willett et al. 2013) and are the primary hosts for most star formation (Brinchmann et al. 2004). Despite their ubiquity, the underlying physics that drives the origin of spiral features remains a topic of ongoing debate. Numerous previous studies over the past decades have endeavoured to explain the formation of spiral arms through various theoretical frameworks (Lin & Shu 1964; Toomre 1977; Athanassoula 1992; Binney & Tremaine 2008).

Among all the proposed theories, the three most widely accepted ones are the density wave theory, dynamic spiral theory, and tidal-induced spiral arms. While the proposed mechanisms may potentially all contribute to the formation and evolution of spiral features in a galaxy, each has specific characteristics that we detail below:

*(Quasi-stationary) density wave theory*: Proposed by Lin & Shu (1964), later improved and popularised by Toomre (1977), Bertin & Lin (1996) and Shu (2016), the density wave theory envisages long-lived spiral arms and solves the winding problem[1]. This theory proposes that spiral features are areas of greater density that rotate at a specific pattern speed across the disc, and the differential gravitational pull leads to a logarithmic spiral with a constant pitch angle (Athanassoula et al. 2010; Martínez-García 2012; Davis et al. 2015). As the pattern speed of the spiral arms is constant, while the rotational velocity of the stars varies radially, differential rotation occurs (right panel of Fig 3.1). Only at the co-rotation radius ($R_{CR}$) are the stars and the arms expected to rotate synchronously. Due to differential rotation, the new-borne stars rotate faster than the spiral pattern within the $R_{CR}$ while falling behind outside the $R_{CR}$, which has been observed in previous works (Pour-Imani et al. 2016; Peterken et al. 2019). Thus in this theory, the interstellar medium (ISM) properties and stellar populations differ on the leading edge and trailing edge of the

[1]The winding problem: in other theories, the pitch angle of the spiral features is expected to decrease to 0 over time, which is in disagreement with observations of long-lived spirals.

spiral arms (Gittins & Clarke 2004). Ho et al. (2017) observe lower gas-phase metallicity in the leading edge than the trailing edge in NGC 1365, which can be explained by their toy model.

*Dynamic spiral theory*: Sellwood & Carlberg (1984) suggests that spiral arms are short-lived and recurrent features. In numerical simulations, dynamic spiral arms arise rapidly from gravitational instability due to swing amplification (Fujii et al. 2011; Grand et al. 2012a; D'Onghia et al. 2013). However, this kind of spiral arms fades quickly because of the particle scattering and increased velocity dispersion of stars in the simulations. The spiral arms heat the disc kinematically and undergo a cycle of breaking up into small segments of kpc in size. The segments possibly will reconnect to form new, large-scale spiral patterns, which makes the spiral features "recurrent". While the dynamic spiral arms may appear globally cohesive, the assemblies of segments can form at distinct times and later merge with the arms. This contrasts with density wave theory, where the spiral arms arise as an entity. A kinematically cold population of stars help maintain the dynamic spiral arms while gas dissipation and accretion introduce instabilities. There is no significant difference in rotation between the disc and the dynamic spiral arms. Thus, the stars do not flow across the spiral features but stay still in the arm regions due to gravitational potential. This means no coherent azimuthal variations are expected between the gas and stars in dynamical spiral theory (left panel of Fig 3.1).

*Tidal-induced spiral arms*: Tidal interactions are common and give rise to tails, bridges and spiral features (Pfleiderer & Siedentopf 1961; Pikel'Ner 1965; Toomre & Toomre 1972). Toomre (1969) predict that the outer arms and tidal tails are material arms, rotating at a similar angular velocity with the disc, which is observed in M51 (Meidt et al. 2013). However, some simulations (Sundelius et al. 1987) and observations (Rots & Shane 1975) argue that tidal-induced spiral arms are density waves. Interestingly, the density wave spiral arms from tidal interactions can be quasi-stationary or kinematic — the gas and stars do flow through the spiral arms but the spiral pattern speed decreases with radii (Donner & Thomasson 1994; Oh et al. 2015). Simulations (Pettitt et al. 2016, 2017) report that azimuthal offsets do exist in different media in a tidal-induced spiral galaxy, in agreement with observations (Schinnerer et al. 2013; Egusa et al. 2017).

The fundamental physics that drives the formation of spiral features remains a topic of debate, given the various observational results among different spiral galaxies in our Universe. One of the practical methods to discern the dominant theory is to detect the azimuthal variation across the spiral arms — as the density wave theory predicts an observable azimuthal offset in ISM properties such as gas-phase metallicity and stellar ages while dynamic spiral theory predicts no offset. However, existing observational evidence is conflicted with clear azimuthal variations in metallicities seen in some galaxy

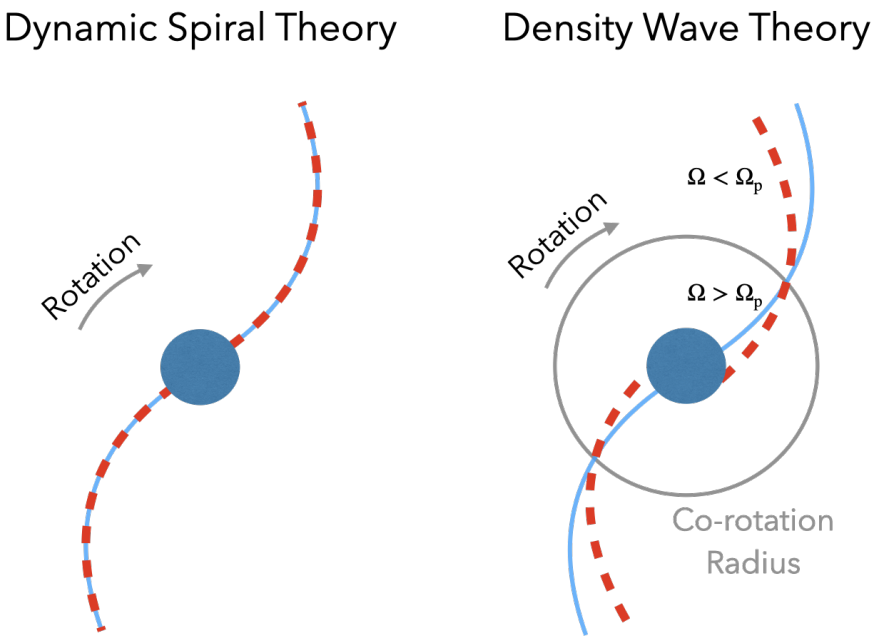


**Figure 3.1:** Theoretical expectations from the dynamic spiral theory (left) and density wave theory (right) regarding the location of young (blue) and old (red) stellar populations. The azimuthal offset between young and old stars is predicted by density wave theory but not by dynamic spiral theory, also see Fig 1 in Puerari & Dottori (1997) and Martínez-García et al. (2009b). The rotation direction is based on the assumption that the observed spiral arms are trailing features, which will be applied to all spiral galaxies in this work. $\Omega$ refers to the rotational velocity of material while $\Omega_p$ denotes the rotational velocity of the spiral pattern.

samples (Sánchez-Menguiano et al. 2016; Ho et al. 2017; Vogt et al. 2017; Ho et al. 2018) but not in others (e.g. Foyle et al. 2011; Kreckel et al. 2019; Chen et al. 2024b). The discrepancy also occurs in stellar ages with some galaxies showing azimuthal variation (Martínez-García et al. 2009b; Sánchez-Gil et al. 2011; Abdeen et al. 2022) and others not (Choi et al. 2015; Shabani et al. 2018). More studies using multi-wavelength imaging data report the offset between the young and old stellar populations (Egusa et al. 2004, 2009; Pour-Imani et al. 2016; Yu & Ho 2019; Savchenko et al. 2020; Abdeen et al. 2020), in line with density wave theory.

For isolated spiral galaxies, density wave and dynamic spiral theory are two widely accepted mechanisms driving the spiral features. However, tidal forces from interactions with passing or nearby companions can also give rise to spiral arms with an offset between the gas and the stars (Pettitt et al. 2017), making it more difficult to test density wave theory or dynamic spiral theory. Conversely, tidal-induced spiral galaxies show distinct behaviours in their tail and bridge arms. Gravity perturbations from the interaction can create two armed spiral galaxies (Toomre & Toomre 1972; Pettitt & Wadsley 2018), which is likely the case in M51 (Dobbs et al. 2010). Spiral features created in tidal interactions are more likely to be kinematic density waves (Chapter 6 in Binney & Tremaine 1987) that will wind up faster than quasi-stationary density waves. However, the gas moves through the spiral arms from the trailing edge to the leading edge, similar to the quasi-stationary density waves (Oh et al. 2008; Struck et al. 2011). These findings indicate that the ISM and stellar distributions in spiral galaxies may be under the impact of more than one physical mechanism.

With three common theories briefly explained, we summarise the expectations of star formation surface density ($\Sigma_{SFR}$) and gas-phase metallicity in observation from the different mechanisms. In density wave theory, the spiral arms observed in shorter wavelengths, where the most recent star formation event has occurred, should exhibit a looser pitch angle (blue arms in the right panel of Fig 3.1) than the spiral arms observed in redder wavelengths, dominated by the old stars (Pour-Imani et al. 2016). If star formation occurs after gas clouds pass through the minimum potential of density waves (left spiral arm in Fig 1 of Pour-Imani et al. 2016), the peaks of $\Sigma_{SFR}$ are predicted in the leading edge inside the $R_{CR}$ (Martínez-García et al. 2009b) . If star formation starts as the gas clouds approach the density wave (right spiral arm in Fig 1 of Pour-Imani et al. 2016), $\Sigma_{SFR}$ should be higher in the trailing edge inside the $R_{CR}$. In contrast, the dynamic spiral theory predicts a symmetrical $\Sigma_{SFR}$ distribution to the spiral arms. Tidal induced-spiral structures will lead to kinematic density waves which result in azimuthal variations, exhibiting a decreasing pattern speed with increasing radii. The comparison of $\Sigma_{SFR}$ between the leading and trailing edge, combined with the reported environmental factors, will help to disentangle

the origin of spiral features.

For gas-phase metallicity, spiral arms driven by density wave theory will lead to higher metallicity in the trailing edge than the leading edge, within the $R_{CR}$. This scenario is modelled in (Ho et al. 2017) as 1) self-enrichment in the trailing edge before the material reaches the spiral arms, and 2) metal mixing in the leading edge. In dynamic spiral theory, gas-phase metallicity is expected to be symmetric on both sides of the spiral arms, as there is no differential rotation between the spiral arms and the disc.

Although many spiral galaxies in the local Universe and at higher redshift have been studied, most researches i) focus on HII regions (e.g., Rozas et al. 1996; Santoro et al. 2022); ii) examined azimuthal variations through visual comparison on 2D maps (Kreckel et al. 2019), or by binning the spaxels into leading and trailing sections (Ho et al. 2018; Chen et al. 2024b). These previous studies offer limited quantitative analysis of the behaviour of the gas and stars as they move away from the spiral arms. In this work, we present the azimuthal distributions of star formation rate (SFR) and gas-phase metallicity and test the toy model in Ho et al. (2017), with a sample of nine nearby spiral galaxies. Our motivation is to quantitatively track the fluctuation in the ISM properties when moving in/out of the spiral arms.

We introduce our observations and sample in Sec 3.2. We present our analysis including spiral arm definition and mapping the ISM properties in Sec 3.3. We report the fluctuation of the ISM properties when moving through the spiral arms in Sec 3.4. In Sec 3.5, we will discuss the effects of $R_{CR}$ on our results and the dominant mechanism(s) responsible for driving the spiral features in these galaxies. Luminosity distances are adopted from Leroy et al. (2019), assuming $H_0 = 70$ km s$^{-1}$Mpc$^{-1}$ and a flat cosmology with $\Omega_m = 0.27$.

## 3.2 Observations and sample selection

### 3.2.1 Observations

TYPHOON[2] is a pseudo-IFU survey of 44 galaxies observable in the southern hemisphere. TYPHOON uses the Wide Field CCD (WFCCD) imaging spectrograph ($18' \times 1.65$") on the 2.5m du Pont telescope at the Las Campanas Observatory in Chile. The TYPHOON survey builds up a dispersed image data cube by applying the Progressive Integral Step Method (PrISM), also known as the "step-and-stare" technique. The large field of view (FoV) of TYPHOON, ranging from 2.3' × 18' to 6.5' × 18' in our selected spiral galaxies, allows us to observe the entire optical disc of nearby star-forming galaxies in an IFU-like manner. The spectrograph is configured to have a resolving power of approximately R

[2]https://typhoon.datacentral.org.au/

$\approx$ 850 at 7000 Å and R $\approx$ 960 at 5577 Å. Our spectra cover the wavelength range of 3650−8150 Å with a flux calibration accuracy of 2% (Ho et al. 2017). The observations are conducted only when the seeing is smaller than the slit width of 1.65" (to prevent slit loss; Grasha et al. 2022). More detailed information about the TYPHOON/PrISM survey is in Ho et al. (2017), Chen et al. (2023), and Seibert et al. (In prep.). The raw data are reduced into 3D data cubes using a standard long-slit data reduction procedure (Seibert et al. In prep.). The reduced 2D spectra are later tiled together to form 3D data cubes with spectral and spatial samplings of 1.5Å and 1.65", respectively. The astrometric solutions are made for combined slit steps of individual nights independently and they are tied to the Gaia reference system (Gaia Collaboration et al. 2016).

### 3.2.2 Sample selection

Our work includes bright ($M_{\rm v}$ < -20 mag) spiral galaxies that have three spiral arms or fewer. We exclude flocculent galaxies with poorly defined arms to allow for better comparison between leading and trailing regions. We exclude one galaxy (NGC 1068) with more than 20% spaxels impacted by harder-component ionisation (e.g., active galactic nuclei, AGN; Lamastra et al. 2016; D'Agostino et al. 2018), based on the Baldwin, Phillips & Terlevich diagram (BPT diagram; Baldwin et al. 1981). The remaining spiral galaxies in our sample show < 2% of their spaxels dominated by AGN (column 12 of Table 3.1). These selection criteria reduce the total sample to nine well-defined, star-forming galaxies available in this work. Two galaxies have a strong bar (Hubble type of SB) and seven galaxies exhibit a weak bar (Hubble type of SAB). We constrain our analysis of azimuthal variation starting from/beyond the end of bars (Sec 3.3.3) to focus on the study of spiral arms. The detailed physical parameters are listed in Table 3.1.

The large FoV allows us to cover the disc regions extending beyond $R_{25}$ for our entire sample. Our sample spans a resolution of 52 – 170 parsec per pixel (1.65" per pixel), enabling us to 1) identify the central ridge line of each spiral arm, and 2) measure changes in the ISM when moving azimuthally from the spiral arms on a spaxel level. These azimuthal distributions are key observables to distinguish between competing spiral theories.

## 3.3 Data analysis

In this section, we introduce our analyses on the TYPHOON data, starting with the emission line fitting process using LZIFU (Sec 3.3.1). We select reliable spaxels with signal-to-noise ratio (SNR) limits and subsequently identify star-forming spaxels with the BPT diagram, described in Sec 3.3.2. Sec 3.3.3 introduces the methodology to define the ridge lines of the spiral arms. Sec 3.3.4 outlines how we measure the ISM properties

($\Sigma_{\rm SFR}$ and gas-phase metallicity).

### 3.3.1 Emission line fitting

We measure the 2D emission line maps using the tool LZIFU (Ho 2016; Ho et al. 2016). The reduced emission line maps of all galaxies in the TYPHOON survey are described in Battisti et al. (in prep.). We briefly introduce the emission line fitting process of LZIFU below that is relevant to this work.

Firstly, LZIFU uses PPXF (Cappellari & Emsellem 2004b; Cappellari 2017b) to fit and subtract the continuum on a spaxel-to-spaxel basis. This continuum modelling is based on the MIUSCAT simple stellar population models (Vazdekis et al. 2012). The principle goal of LZIFU is to derive emission lines from continuum-free spectra, rather than constraining stellar parameters from continuum measurements (Sec 2.2 in Ho 2016) [3]. For this work, we only adopt the emission line fits from LZIFU. Secondly, LZIFU fits each emission line as a single Gaussian component using the Levenberg-Marquardt least-square method. In this study, we fit the following emission lines simultaneously: H$\beta$ (4861Å), [O III]$\lambda$5007, [N II]$\lambda$6583, H$\alpha$ (6563Å), and [S II]$\lambda\lambda$6716,31. We tie together the velocity and velocity dispersion of all the lines. The flux ratios of [O III]$\lambda$5007/[O III]$\lambda$4959 and [N II]$\lambda$6583/[N II]$\lambda$6548 are constrained to their theoretical values predicted by quantum mechanics (3.1; Gurzadyan 1997). Finally, LZIFU returns the outputs of emission line fluxes with corresponding error maps.

[3] A detailed analysis of stellar populations based on the TYPHOON data is published in Sextl et al. (2024). In this work, continuum fits are conducted at the spaxel level. H$\beta$ absorption line is the only stellar absorption feature that can impact the emission flux. However, H$\beta$ will not be used in our measurements of SFR or 12 + log(O/H).

| Galaxy | T-type | Morphology | R.A | Dec. | Inclination (degrees) | P.A. (degrees) | Distance (Mpc) | $\log M_*$ ($M_\odot$) | $R_{25}$ (arcmin) | Number of spiral arms | Fraction of excluded spaxels |
|---|---|---|---|---|---|---|---|---|---|---|---|
| (1) | (2) | (3) | (4) | (5) | (6) | (7) | (8) | (9) | (10) | (11) | (12) |
| NGC 1365 | 3.2 ± 0.7 | SB(s)b | 03h33m36.371s | -36d08m25.45s | 35.7 | 49.5 | 18.1 ± 0.04 | 10.75 ± 0.10 | 5.61 | 2 | 1.11% |
| NGC 1566 | 4.0 ± 0.2 | SAB(s)bc | 04h20m00.42s | -54d56m16.1s | 49.1 | 44.2 | 18.0 ± 0.12 | 10.67 ± 0.10 | 4.16 | 2 | 1.14% |
| NGC 2442 | 3.7 ± 0.6 | SAB(s)bc | 07h36m23.84s | -69d31m51.0s | 50.3 | 12.3 | 21.2 ± 2.0 | 10.56 ± 0.12[a] | 2.75 | 2 | 0.81% |
| NGC 2835 | 5.0 ± 0.4 | SB(rs)c | 09h17m52.91s | -22d21m16.8s | 56.2 | 1.3 | 10.1 ± 0.12 | 9.67 ± 0.10 | 3.30 | 3 | 0.05% |
| NGC 2997 | 5.1 ± 0.5 | SAB(rs)c | 09h45m38.79s | -31d11m27.9s | 53.7 | 98.9 | 11.3 ± 0.12 | 10.46 ± 0.10 | 4.46 | 3 | 0.19% |
| NGC 4536 | 4.3 ± 0.7 | SAB(rs)bc | 12h34m27.050s | +02d11m17.29s | 73.1 | 120.7 | 15.2 ± 0.06 | 10.19 ± 0.10 | 3.80 | 3 | 0.60% |
| NGC 5236 | 5.0 ± 0.3 | SAB(s)c | 13h37m00.950s | -29d51m55.50s | 15.3 | 44.9 | 4.9 ± 0.04 | 10.41 ± 0.10 | 6.44 | 2 | 0.18% |
| NGC 5643 | 5.0 ± 0.3 | SAB(rs)c | 14h32m40.743s | -44d10m27.86s | 29.6 | 98.1 | 11.8 ± 0.12 | 10.06 ± 0.10 | 2.29 | 2 | 3.58% |
| NGC 6744 | 4.0 ± 0.2 | SAB(r)bc | 19h09m46.10s | -63d51m27.1s | 53.5 | 13.7 | 11.6 ± 0.12 | 10.87 ± 0.10 | 9.98 | 3 | 0.66% |

**Table 3.1:** Physical parameters of the spiral galaxies in this study. **Column 1:** Galaxy name. **Column 2:** RC3 morphological T-types from Hyperleda (http://atlas.obs-hp.fr/hyperleda/). **Column 3 – 5:** Morphology and J2000 Coordinates from NASA extragalactic database (NED). **Column 6:** Inclination between the line of sight and polar axis from Hyperleda. **Column 7:** Position angle of the major axis in the B-band, northeastward [b]. **Column 8 & 9:** Distance and stellar mass from Leroy et al. (2019). **Column 10:** $R_{25}$, defined as the 25 mag arcsec$^2$ $B$-band isophote from NED. **Column 11:** Number of spiral arms in each galaxy (Sec 3.3.3). **Column 12:** Fraction of spaxels excluded from BPT constraints. (Sec 3.3.2).

**Note.**

[a] The stellar mass and the uncertainty of NGC 2442 are from Pan et al. (2020).

[b] The position angle of NGC 1365 comes from the 2MASS survey (Jarrett et al. 2003), for consistency with Ho et al. (2017).

### 3.3.2 Spaxel selection criteria

We apply an SNR limit of 3 to H$\alpha$ and H$\beta$ to obtain a reliable analysis. The spaxels with SNR (H$\alpha$ & H$\beta$) below 3 are excluded from all the following analyses. If an SNR less than 3 is detected in a spaxel for any of the following three doublet lines: [O III]$\lambda$5007, [N II]$\lambda\lambda$6548,83 and [S II]$\lambda\lambda$6716,31, we adopt a limiting value of 3$\sigma$ for the corresponding emission line(s), where $\sigma$ is the uncertainty in the line measurement (see Sec 2.6 of Rosario et al. 2016).

We correct for dust extinction using the Milky Way extinction curve from Fitzpatrick et al. (2019) as:

$$E(B-V) = 2.5 \times \left( \frac{\log_{10} \frac{(H\alpha/H\beta)_{\rm obs}}{(H\alpha/H\beta)_{\rm int}}}{k_{H\beta} - k_{H\alpha}} \right), \tag{3.1}$$

where $E(B-V)$ is the colour excess, $(H\alpha/H\beta)_{\rm obs}$ is the observed flux ratio measured from the data. We adopt the intrinsic flux ratio $(H\alpha/H\beta)_{\rm int}$ of 2.86 by assuming case B recombination at the electron temperature of 10,000 K and electron density of 100 cm$^{-3}$ (Osterbrock 1989). We use $R_v$ = 3.1 to determine the $k$ value at each wavelength. For spaxels with negative $E(B-V)$ values, we assign a value of 0 to colour excess. The $E(B-V)$ values are then used to calculate the intrinsic emission line fluxes $F_{\rm int}$ from the observed fluxes $F_{\rm obs}$, following Calzetti (2001):

$$F_{\rm int} = F_{\rm obs} \times 10^{0.4 k_\lambda E(B-V)}. \tag{3.2}$$

The extinction-corrected fluxes are used in all the following analyses to measure the $\Sigma_{\rm SFR}$ and gas-phase metallicities (Sec 3.3.4).

We further exclude the spaxels ionised by hard components and limit our study to the photoionised spaxels by star formation by using the BPT diagram. Based on [N II]$\lambda$6584/H$\alpha$ versus [O III]$\lambda$5007/H$\beta$, the spaxels dominantly ionised by star formation (H II regions) are distinguished from the low-ionisation nuclear emission-line regions (LINERs) and AGN.

There are two common demarcation lines to separate AGN/LINERs and H II regions based on optical emission lines. Kauffmann et al. (2003b) presents an empirical demarcation line based on the properties of $\sim$ 120,000 nearby galaxies with the Sloan Digital Sky Survey. Kewley et al. (2001) models the starburst galaxies with PEGASE v2.0 and STARBURST99 to derive the theoretical classification scheme for AGN and H II regions. All spaxels over the Kewley et al. (2001) demarcation line are excluded in the following analysis in this work. The fraction of excluded spaxels due to BPT constraints is below 4% in all cases, as shown in the last column in Table 3.1.

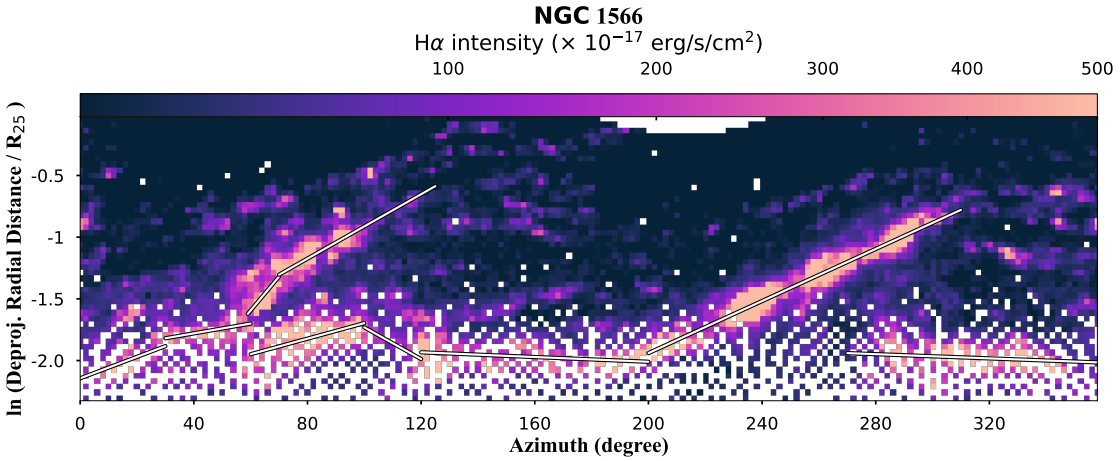


**Figure 3.2:** Deprojected radial distance in a logarithm scale versus the azimuth, colour-coded by the H$\alpha$ intensity of NGC 1566. The best fits of the H$\alpha$-bright (intensity >100 $\times 10^{-17}$ erg/s/cm$^2$) regions are shown as the black solid lines. The pixelation at the central region results from the reduced area as the radial distance decreases.

### 3.3.3 Spiral arm definition and $\Delta\phi$ definition

We follow the method of Ho et al. (2018) to identify our spiral arm ridge lines:

$$r(\phi) = r_0 e^{\tan\theta_{\rm p}(\phi-\phi_0)} \tag{3.3}$$

where $\theta_{\rm p}$ is the pitch angle, $r_0$ is the initial radius and $\phi_0$ is the initial azimuth of the spiral arm. The spiral arms are recovered as straight lines in a plot of logarithm-scale deprojected radial distance versus azimuth (Fig 3.2). Eq 3.3 is transformed into a linear function:

$$\ln r(\phi) = \ln r_0 + \tan\theta_{\rm p}(\phi - \phi_0) \tag{3.4}$$

We fit the spiral arms with Eq 3.4 using a non-linear least squares method[4] using the H$\alpha$-bright regions as the input of the fitting process. The best-fit line is the defined spiral arm ridge line, represented as the black solid line in Fig 3.2. We present the phase diagram of only NGC 1566 in this paper for demonstration.

We aim to quantitatively trace the behaviour of star formation activities as stars and gas move in and out of the spiral arms. We adopt the parameter $\Delta\phi$, which quantifies the azimuthal distance to the nearest spiral arm at a constant galactocentric distance (Chen et al. 2024b). Given a pixel $T$ as the targeted pixel and pixel $arm1$, $arm2$, ..., $armN$ as pixels within the spiral regions at the same galactocentric distance, the $\Delta\phi$ is defined as,

$$\Delta\phi_T = -\min(|\phi_{arm1} - \phi_T|, |\phi_{arm2} - \phi_T|, ..., |\phi_{armN} - \phi_T|) \tag{3.5}$$

[4]We use the curve_fit module in python to carry out the fitting process.

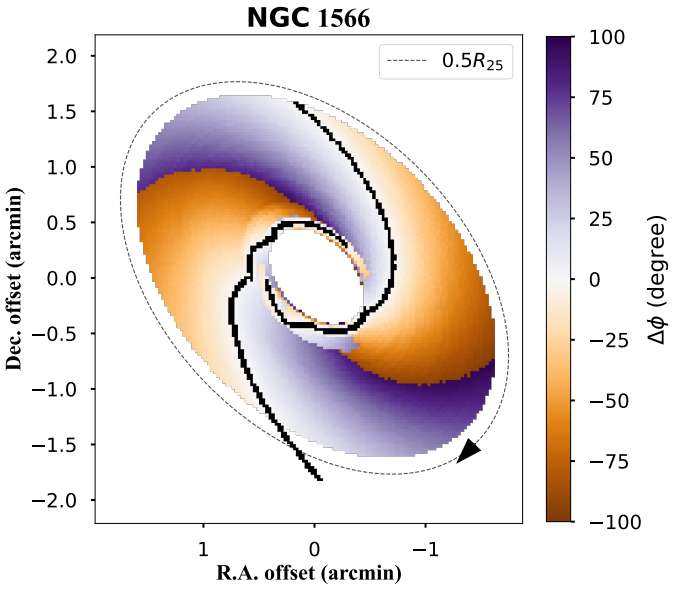


**Figure 3.3:** A measure of the angular azimuthal distance to the nearest spiral arm at a constant galactocentric distance ($\Delta\phi$), taking NGC 1566 as an example, over-plotted with the spiral arm ridge lines. The solid ellipse shows the location of 0.5 $R_{25}$, with the circular flow indicated by the arrow. The orange spaxels on the leading edge are assigned negative values while the spaxels on the trailing edge are given positive values, color-coded as purple. The deeper colour the spaxel has, the further its azimuth is from the spiral arm.

when pixel $T$ is on the leading edge of the nearest spiral arm while

$$\Delta\phi_T = \min(|\phi_{arm1} - \phi_T|, |\phi_{arm2} - \phi_T|, ..., |\phi_{armN} - \phi_T|) \tag{3.6}$$

when pixel $T$ is on the trailing edge of the nearest spiral arm. The $\Delta\phi$ map of NGC 1566 is presented in Fig 3.3, overplotted with the spiral arm ridge lines.

We calculate the angular distance $\theta$ that stars will travel in 10 Myr, a typical life span of O-type stars, as:

$$\begin{aligned} t &= \frac{2\pi R}{V_{\rm circ}}, \\ \theta &= \frac{10\ {\rm Myr}}{t} \times 360^\circ. \end{aligned} \tag{3.7}$$

Here, $V_{\rm circ}$ is the circular velocity and $R$ is the radial distance to the galaxy centre. Using a typical rotational velocity of 200 km s$^{-1}$ (8 kpc to the centre of Milky Way; Honma et al. 2015), we get $\theta = 17^\circ$. For a conservative analysis, we classify spaxels with $|\Delta\phi| < 20^\circ$ as spiral arm regions, which will be applied to our statistic test (Sec 3.4.2 and Fig 3.8).

### 3.3.4 Mapping the ISM: SFR and gas-phase metallicity

**Mapping $\Sigma_{\rm SFR}$ and $\Delta\Sigma_{\rm SFR}$**

The spatial distribution of star formation and gas-phase metallicities are critical components for understanding the physical evolution of spiral galaxies, including their ongoing star formation, star formation history and mixing processes in the ISM (Maiolino & Mannucci 2019; Li et al. 2021; Sharda et al. 2023; Garcia et al. 2023). In this section, we introduce our method to map the SFR and the gas-phase metallicity, used to investigate the effects of the spiral arms on the SFR and metallicity distribution.

We measure the SFR by converting the extinction-corrected (i.e., intrinsic) H$\alpha$ intensity to a SFR indicator. Stars with masses exceeding $\sim 10$ M$_\odot$ produce a detectable flux of ionizing photons and have a short lifespan of $\lesssim 30$ million years (Calzetti 2013). The H$\alpha$ nebular emission line is thus a direct tracer of the ionizing photons powered by young, massive stars. Following the SFR prescription in Kennicutt (1998), we measure the SFR as:

$$\mathrm{SFR}(\mathrm{M_\odot yr^{-1}}) = 7.9 \times 10^{-42} \times\ 4\pi D_{\rm L}^2 F_{\rm H\alpha}(\mathrm{erg\ s^{-1}\ cm^{-2}}), \tag{3.8}$$

where $F_{\rm H\alpha}$ is the flux of H$\alpha$ per spaxel and $D_{\rm L}$ is the luminosity distance in Table 3.1. We calculate the $\Sigma_{\rm SFR}$ as follows:

$$\Sigma_{\rm SFR}(\mathrm{M_\odot yr^{-1} kpc^{-2}}) = \frac{\mathrm{SFR}}{[D_{\rm A}(\mathrm{kpc}) \times 1.65''/180^\circ \times \pi]^2}, \tag{3.9}$$

where 1.65" is the spaxel size of the TYPHOON data and $D_{\rm A}$ is the angular distance of the observed galaxy. The measured $\Sigma_{\rm SFR}$ map of NGC 1566 is shown in the left column of Fig 3.4, with the remaining galaxies shown in Fig 3.11 and Fig 3.12.

We find higher $\Sigma_{\rm SFR}$ (bluer spaxels) predominantly concentrated in the central regions in most of our galaxies. To remove the radial dependence on the $\Sigma_{\rm SFR}$, we subtract the radial gradient, represented by a piecewise linear function, from $\Sigma_{\rm SFR}$ to get the offset $\Delta\Sigma_{\rm SFR}$ value, which indicates the azimuthal variation. The residual $\Delta\Sigma_{\rm SFR}$ map of NGC 1365 is shown in the right column of Fig 3.4, with the rest of the sample presented in Fig 3.11 and Fig 3.12.

We observe positive $\Delta\Sigma_{\rm SFR}$ (i.e., higher $\Sigma_{\rm SFR}$) along the spiral arm ridge lines of NGC 1566 which is expected from our definition of spiral arms (Sec 3.3.3). This scenario is observed in all our galaxies (Fig 3.7). With $\Delta\Sigma_{\rm SFR}$ we can better compare both sides of the spiral arms, with generally negative $\Delta\Sigma_{\rm SFR}$ in the leading edge (orange; $\Delta\phi < 0$) and positive $\Delta\Sigma_{\rm SFR}$ in the trailing edge. The $\Delta\Sigma_{\rm SFR}$ maps of other spiral galaxies can be found in Appendix 3.7 and we will further discuss the azimuthal variation in Section 3.4.1.

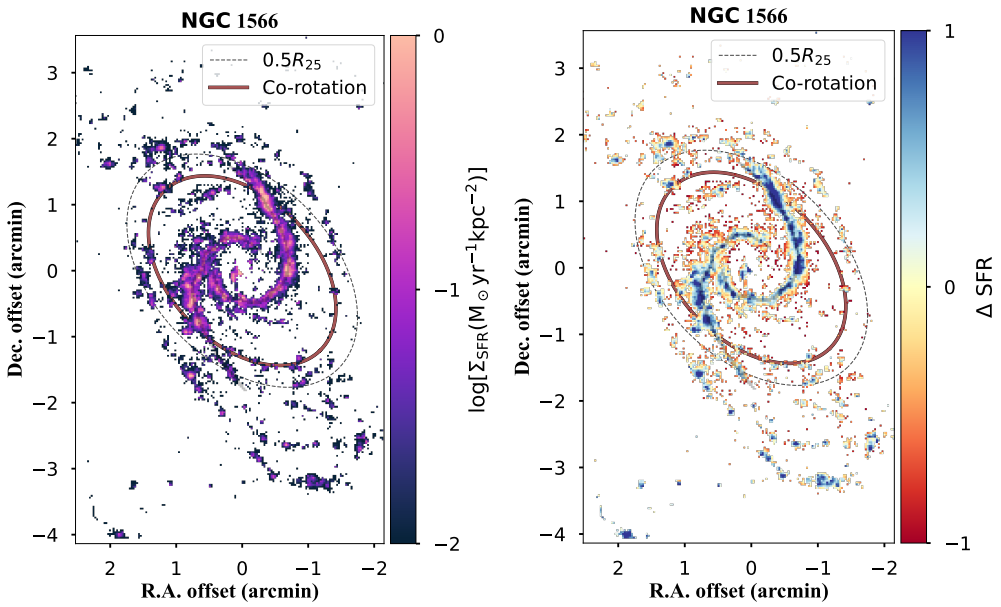


**Figure 3.4:** 2D maps of derived $\Sigma_{SFR}$ and $\Delta\Sigma_{SFR}$ of NGC 1566 after SNR limit and spaxel selection based on BPT diagram, overplotted with the defined spiral arms from Sec 3.3.3. The dashed ellipse marks the location of half $R_{25}$ and the red ellipse denotes the co-rotation radius reported in previous publications (see Sec 3.5.3). Fig 3.11 shows the SFR maps for the remaining galaxies in this work.

### Mapping 12 + log(O/H) and $\Delta$log(O/H)

Stars produce heavy metals during their lifetimes, which are subsequently released into the interstellar medium upon their death, enhancing the metal content of the ISM for subsequent generations of stars. Consequently, gas-phase metallicity serves as a marker for preceding stellar generations, influenced by gas inflows, outflows, and depletion mechanisms. The spatial distribution of the gas-phase metallicity represents a snapshot in time of the production history and mixing processes. Deviations in the azimuthal direction of the metal distribution offer insights into the mixing process of metals with the surrounding ISM as both gas and stars orbit within the galactic potential. As oxygen is the most abundant metal in the gas-phase ISM, we measure the oxygen abundance through collisionally excited lines in the optical spectrum as an indicator of the gas-phase metallicity.

We adopt the N2S2-N2H$\alpha$ diagnostic from Dopita et al. (2016, hereafter D16) to measure the gas-phase metallicity. The D16 diagnostic uses the H$\alpha$, [NII]$\lambda$6484 and [SII]$\lambda\lambda$6717,31 emission lines. All four emission lines above are well-detected by the TYPHOON survey. With the inclusion of [SII]$\lambda\lambda$6717,31 doublet lines, the D16 diagnostic is subject to contamination from diffuse ionised gas (DIG; Zhang et al. 2017b; Shapley et al. 2019; Kumari et al. 2019). Poetrodjojo et al. (2019) find that DIG has less impact on the calibrated metallicity at the resolution of the TYPHOON data, compared to MaNGA and SAMI. Appendix 3.9 further discusses the impacts of DIG with metallicity variation

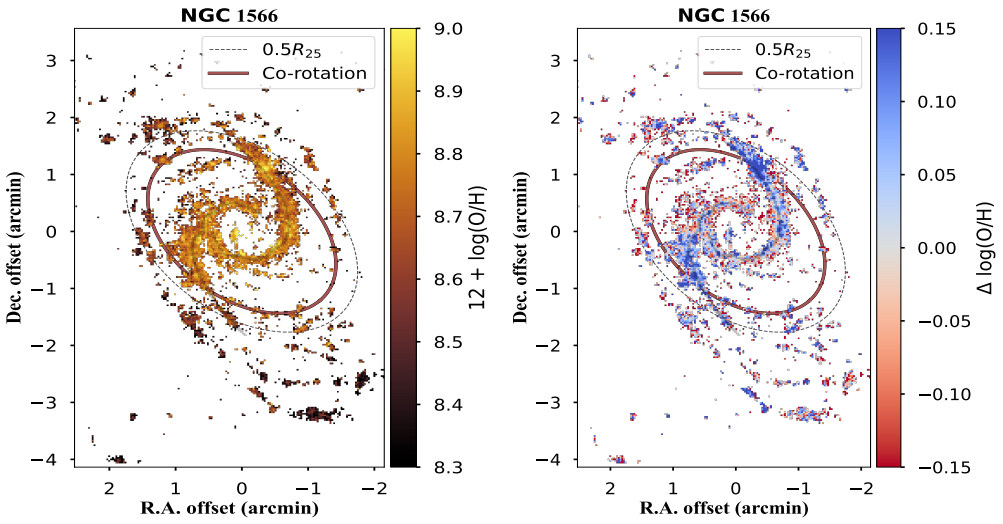


**Figure 3.5:** 2D maps of derived 12 + log(O/H) and $\Delta$log(O/H) of NGC 1566, overplotted with the defined spiral arms from Sec 3.3.3. The half $R_{25}$ radius is shown as a dashed ellipse while the $R_{CR}$ is shown as a solid ellipse. The 12 + log(O/H) and $\Delta$log(O/H) maps for the remaining sample are presented in Fig 3.13 and Fig 3.14.

calculated by S-calibration (Pilyugin & Grebel 2016) diagnostic. Similarly, we find higher $\Delta$log(O/H) in the trailing edge of NGC 1566, although the magnitude of the azimuthal variation (0.017 dex) is smaller than the one found in N2S2-N2H$\alpha$ (0.037 dex).

We present the metallicity maps in the left panel of Fig 3.5 (NGC 1566) and Fig 3.13, Fig 3.14 for the remaining sample, overplotted with the defined spiral arms (Sec 3.3.3). We find higher 12 + log(O/H) values in the central region (bluer spaxels) and lower 12 + log(O/H) measurements in the outskirts (redder spaxels) in all galaxies. The negative radial metallicity gradient is indicative of inside-out galaxy formation (Tinsley & Larson 1978; Prantzos & Boissier 2000).

Similar to the methodology applied to $\Sigma_{SFR}$, we derive the $\Delta$log(O/H) value for each spaxel by subtracting the radial gradient, measured through the best fit of a piecewise linear function. The residual $\Delta$log(O/H) maps are shown in the right panel of Fig 3.13 and the second and fourth column of Fig 3.14. We observe generally positive $\Delta$log(O/H) (blue pixels) along the spiral arms in all galaxies. To quantitatively compare the metallicity in the downstream versus upstream, we investigate the correlation between $\Delta\phi$ and $\Delta$log(O/H) in the spiral galaxies in Sec 3.4.2.

## 3.4 Results

### 3.4.1 SFR

We examine the behaviour in SFR when moving into or out of the spiral arms by exploring the relation between $\Delta\Sigma_{SFR}$ and $\Delta\phi$ (Fig 3.6). $\Delta\Sigma_{SFR}$ denotes a higher/lower SFR within the measured spaxel compared to those at the same galactocentric distance (Sec 3.3.4) and $\Delta\phi$ quantifies the angular distance to the nearest spiral arm (Sec 3.3.3). Gas flows from the trailing edge ($\Delta\phi$ >0) into the spiral arms, and then passes to the leading edge ($\Delta\phi$ <0). We measure the moving medians of each 20° (solid lines in Fig 3.6), with blue shadow representing 25% and 75% quantiles. The fluctuation of $\Delta\Sigma_{SFR}$ across different $\Delta\phi$ ranges from $-1.5$ dex to 1.5 dex.

In density wave theory, star formation may occur either i) after gas clouds pass through density waves or ii) as they approach density waves, resulting in various distributions of old stars, young stars, and gas (Pour-Imani et al. 2016). In scenario i/ii, it is expected to observe a gaseous blue arm with young stars on the leading/trailing edge of a stellar arm inside the $R_{CR}$. Our work finds generally higher $\Delta\Sigma_{SFR}$ on the trailing side ($\Delta\phi > 0$), with the highest $\Delta\Sigma_{SFR}$ near the spiral arms and lower $\Delta\Sigma_{SFR}$ on the leading edge ($\Delta\phi < 0$) of NGC 1365 and NGC 1566. This observation is consistent with density wave theory in the latter scenario, when star formation occurs as gas clouds approach the potential minimum (right spiral arms in Fig 1 of Pour-Imani et al. 2016). In NGC 2442, we find decreasing $\Delta\Sigma_{SFR}$ in the trailing edge and increasing $\Delta\Sigma_{SFR}$ in the leading edge ($\Delta\phi < 0$). Between $\Delta\phi$ of -20° and -50°, the trailing edge shows higher $\Delta\Sigma_{SFR}$ than the corresponding leading edge, which is likely contributed by the interaction affecting this galaxy (further discussed in Sec 3.5.4). In NGC 2835, NGC 2997, NGC 4536, NGC 5236, NGC 5643 and NGC 6744, we do not observe significant differences on either side of the spiral arms. This indicates that the $\Sigma_{SFR}$ is comparable in these six galaxies and this finding aligns with the predicted symmetrical $\Sigma_{SFR}$ from dynamic spiral theory. We do note that there is a large scatter in the $\Delta\Sigma_{SFR}$-$\Delta\phi$ trend and it is possible that the non-detected offset in $\Sigma_{SFR}$ could be due to noise obscuring the trend.

The varying motions of material inside and outside the $R_{CR}$ might obscure and even eliminate the azimuthal offset. To address the potential obscuration of detecting azimuthal offset, separate analyses of $\Delta\phi$-$\Delta\Sigma_{SFR}$ (Fig 3.6) inside versus outside the $R_{CR}$ or at various radial regions (if $R_{CR}$ is unknown) are necessary. Among our sample, only three spiral galaxies have $R_{CR}$ reported from the literature (see Sec 3.5.3). To ensure consistency in our analyses, we examine the $\Delta\phi$-$\Delta\Sigma_{SFR}$ trend at various radii for all galaxies, without using the reported $R_{CR}$ for three of our samples. We divide each galaxy disc into two

radial ranges, with an equal number of spaxels in each section[5]. The fluctuation of $\Delta\Sigma_{\rm SFR}$ along $\Delta\phi$ in the inner (outer) radial bin is presented as dotted (dashed) lines in Fig 3.6. We observe the same $\Delta\Sigma_{\rm SFR}$ - $\Delta\phi$ trend between the inner and outer regions in the eight of our spiral galaxies. NGC 4536 is the only spiral galaxy exhibiting an opposite $\Delta\Sigma_{\rm SFR}$ trend between the inner and outer regions, which still fluctuates in between 25% and 75% quantiles (blue shadow).

[5]The radial cut for each galaxy is: NGC 1365−10.98 kpc ($0.37R_{25}$), NGC 1566−8.80 kpc ($0.41R_{25}$), NGC 2442−10.35 kpc ($0.61R_{25}$), NGC 2835−5.81 kpc ($0.58R_{25}$), NGC 2997−7.95 kpc ($0.54R_{25}$), NGC 4536−7.43 kpc ($0.50R_{25}$), NGC 5236−4.66 kpc ($0.38R_{25}$), NGC 5643−4.76 kpc ($0.42R_{25}$), NGC 6744−10.54 kpc ($0.35R_{25}$). This is also applied to the separation of inner and outer regions in Sec 3.4.2 and Fig 3.7.

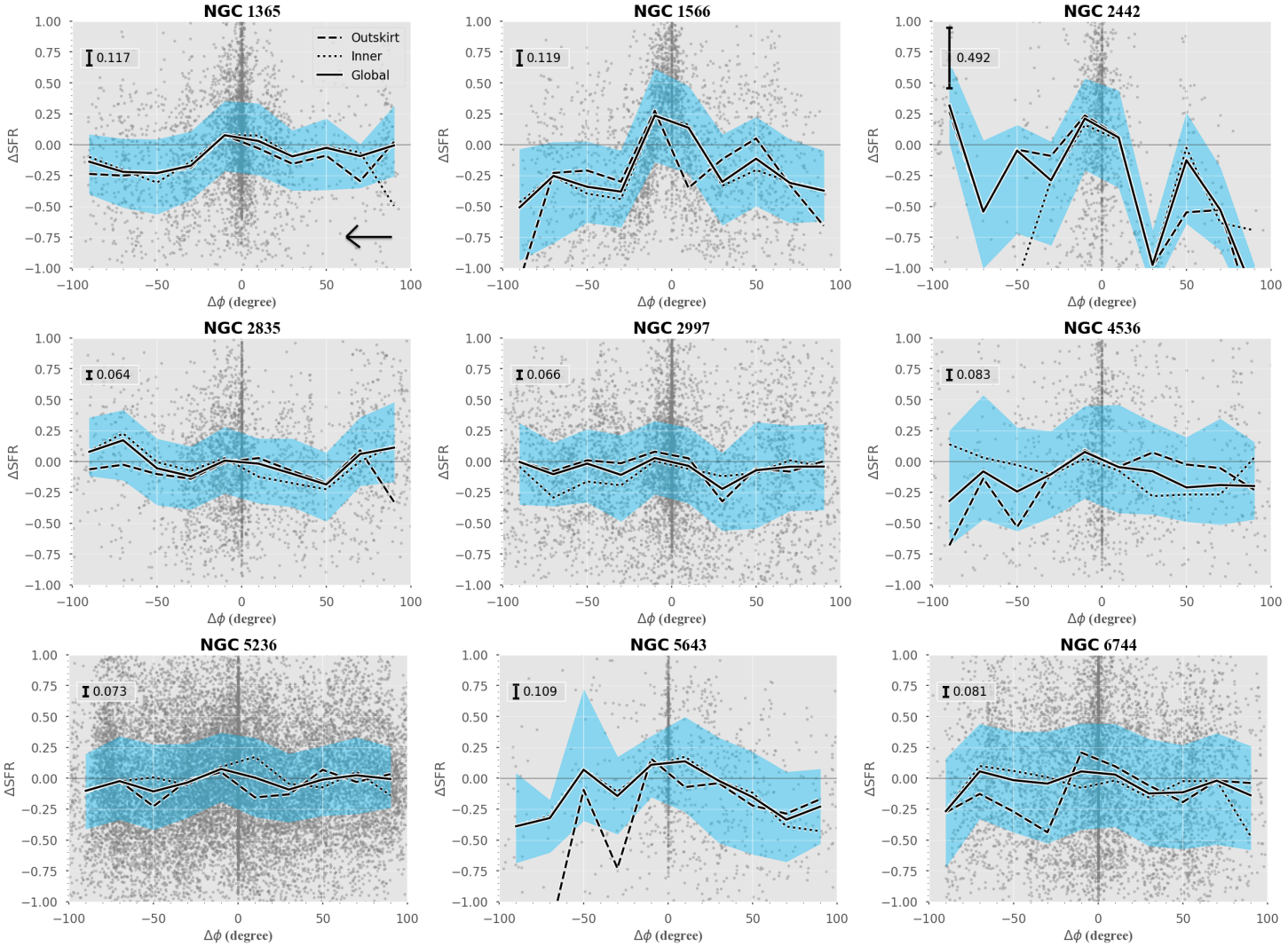


**Figure 3.6**: (Caption next page.)

**Figure 3.6:** The fluctuation of $\Delta\Sigma_{SFR}$ along $\Delta\phi$. The gas flows (shown as an arrow at the bottom right) from $\Delta\phi$ >0 (trailing) to $\Delta\phi$ <0 (leading). The solid black line marks the moving medians of each 20° $\Delta\phi$ bin, with 25% and 75% quartiles represented as the blue shadows. The average offset between $\Delta\Sigma_{SFR}$ in the trailing and the leading edge is shown as a scale bar. We find subtly higher $\Delta\Sigma_{SFR}$ in the trailing edge ($\Delta\phi$> 0) in NGC 1365 and NGC 1566. NGC 2442 shows higher $\Delta\Sigma_{SFR}$ from -20° to -50°, compared to the trailing edge. We do not find a significant global azimuthal offset in $\Delta\Sigma_{SFR}$ in the other six galaxy samples. We find an opposite trend of $\Delta\Sigma_{SFR}$-$\Delta\phi$ in the inner region versus the outskirts only in NGC 4536, with large uncertainty and limited spaxels. We divide the galaxy disc into two regions: the inner region and the outskirts, with each region including half of the spaxels. We trace the fluctuation of $\Delta\Sigma_{SFR}$ in the inner region using dotted lines and in the outskirts using dashed lines and eight out of nine galaxies (except for NGC 4536) show the same $\Delta\Sigma_{SFR}$ trend in both inner and outer regions.

### 3.4.2 12 + log(O/H)

As introduced in Sec 3.1, spiral arms driven by density wave theory will lead to higher metallicity in the trailing edge than the leading edge, while dynamic spiral arms will not show azimuthal variations. Similar to $\Sigma_{SFR}$ (Sec 3.4.1), we will quantify the metallicity offsets on each side of the spiral arms.

Fig 3.7 shows $\Delta\log(O/H)$ versus $\Delta\phi$, showing the azimuthal fluctuation of the relative metal content once the global radial trend has been removed (Sec 3.3.4). The spaxels with positive $\Delta\log(O/H)$ represent regions of enriched gas, while spaxels with negative $\Delta\log(O/H)$ values have less enriched gas. Similar to Sec 3.4.1 with $\Sigma_{SFR}$, we measure the moving medians of each 20° $\Delta\phi$ (solid black lines in Fig 3.7). The 25% and 75% quantiles are shown as a blue-shaded region.

In NGC 1365, we observe increasing $\Delta\log(O/H)$ from 100° to 20° and a drop of $\Delta\log(O/H)$ from $-20°$ to $-50°$. Both NGC 1365 and NGC 1566 show higher $\Delta\log(O/H)$ in the trailing edge ($\Delta\phi$>0) than in the leading edge ($\Delta\phi$<0). This finding is consistent with the toy model in Ho et al. (2017), which predicts i) a build-up of metal-rich gas in the trailing edge when the material rotates forward to the spiral arms; ii) a decrease in metallicity due to the mixing and diluting process when the material passes the spiral arms. We remind the readers that the model in Ho et al. (2017) assumes that gas overtakes the spiral patterns (i.e., inside the $R_{CR}$). In NGC 2442, we observe decreasing metallicity from $\Delta\phi \sim 70°$ to $\Delta\phi \sim 20°$ and increasing metallicity at $\Delta\phi$ <-20 °. This does not align with either dynamic spiral theory or density wave theory. We attribute the azimuthal variation in NGC 2442 to the ongoing merging event (Sec 3.5.4). In NGC 2835, NGC 2997, NGC 4536, NGC 5236, NGC 5643 and NGC 6744, we find no offset on both sides of the spiral arms, indicating no observed azimuthal variation in metallicity. This lack of azimuthal variation aligns with the prediction from the dynamic spiral theory. However, the uncertainty of gas-phase metallicity and detection limit might also be attributed to the

absent azimuthal variation. Further statistical analysis is carried out to test the reliability of the observed azimuthal variation in gas-phase metallicity (below).

The density wave theory predicts material to show opposite kinematics inside and outside the $R_{CR}$. The opposite motion leaves a caveat to interpreting the azimuthal variation without analysis of different radial ranges. Similar to Fig 3.6, we divide the disc into two sections: inner region and outskirt, with an equal number of spaxels in each section. We present the azimuthal trend in $\Delta\log(O/H)$ separately with dashed (outskirts) and dotted (inner) lines in Fig 3.7. We do not observe a significant difference between the inner and outer regions in eight of our samples, except for NGC 2835. This divergence is evidence of the gas accretion from the circumgalactic medium of NGC 2835, which was detected in the flattened metallicity radial profile (Chen et al. 2023). The higher $\Delta\log(O/H)$ near the spiral arms in the outskirts, compared to the inner region, supports the notion that spiral arms facilitate gas radial migration (Sec 3.5.2).

To assess whether the metallicity on both sides of the spiral arms is drawn from the same parent distribution, we present histograms and cumulative distribution functions (CDFs) in Fig 3.8, colour-coded by their location in their spiral arms: trailing (purple), leading (orange) and spiral arm (black) region. We conduct KS tests and Anderson–Darling (AD) tests, with $p$-values from both tests presented in Fig 3.8. The $D$-value, representing the maximum absolute difference between the CDFs of metallicity on both sides, assesses whether metallicity distributions deviate from each other.

We test the detection limit of the statistical framework with the bootstrap resampling method. For each pixel in the galaxy, we calculate the error ($\sigma_Z$) through error propagation. In each bootstrapping trail, we generate a random metallicity map from a Gaussian distribution with a mean value of observed metallicity and standard deviation of $\sigma_Z$. After repeating the procedure 1000 times, we compute the mean values of $D$-values, $p$-values and significance level, as well as the standard deviation. We summarise the $D$-values, KD/AD test results and their uncertainty in Tab 3.2.

Fig 3.8 shows that the trailing edge (purple) of NGC 1365 and NGC 1566 exhibit systematically higher metallicity than the leading edge (orange), with a $p$-value[6] of $1\times10^{-3}$ and $1.52\pm2.51 \times 10^{-3}$ from the AD test, respectively. The $D$-values of 0.171 and 0.114 also suggest the azimuthal variation in the metallicity of NGC 1365 and NGC 1566. Combined with the observed azimuthal variation seen in $\Sigma_{SFR}$(Fig 3.6), this suggests that density wave theory drives the spiral features in both NGC 1365 and NGC 1566. In NGC 2442, the $D$-value of 0.142 and the $p$-value of $4.80\pm5.57 \times 10^{-2}$ from AD test indicate that the metallicity on both sides of the spiral arms is drawn from different parent distributions. However, NGC 2442 shows higher metallicity values in the leading edge (orange) instead

[6]There is a lower limit of $1\times10^{-3}$ for $p$-value from the AD test.

of the trailing edge (purple), the opposite of what was observed in both NGC 1365 and NGC 1566. The kinematic and star-forming properties of NGC 2442 are indicative of what is expected from a typical interacting system shortly after the initial collision (Mihos & Bothun 1997). We thus attribute the opposite azimuthal variation trends present in metallicity to the ongoing merger.

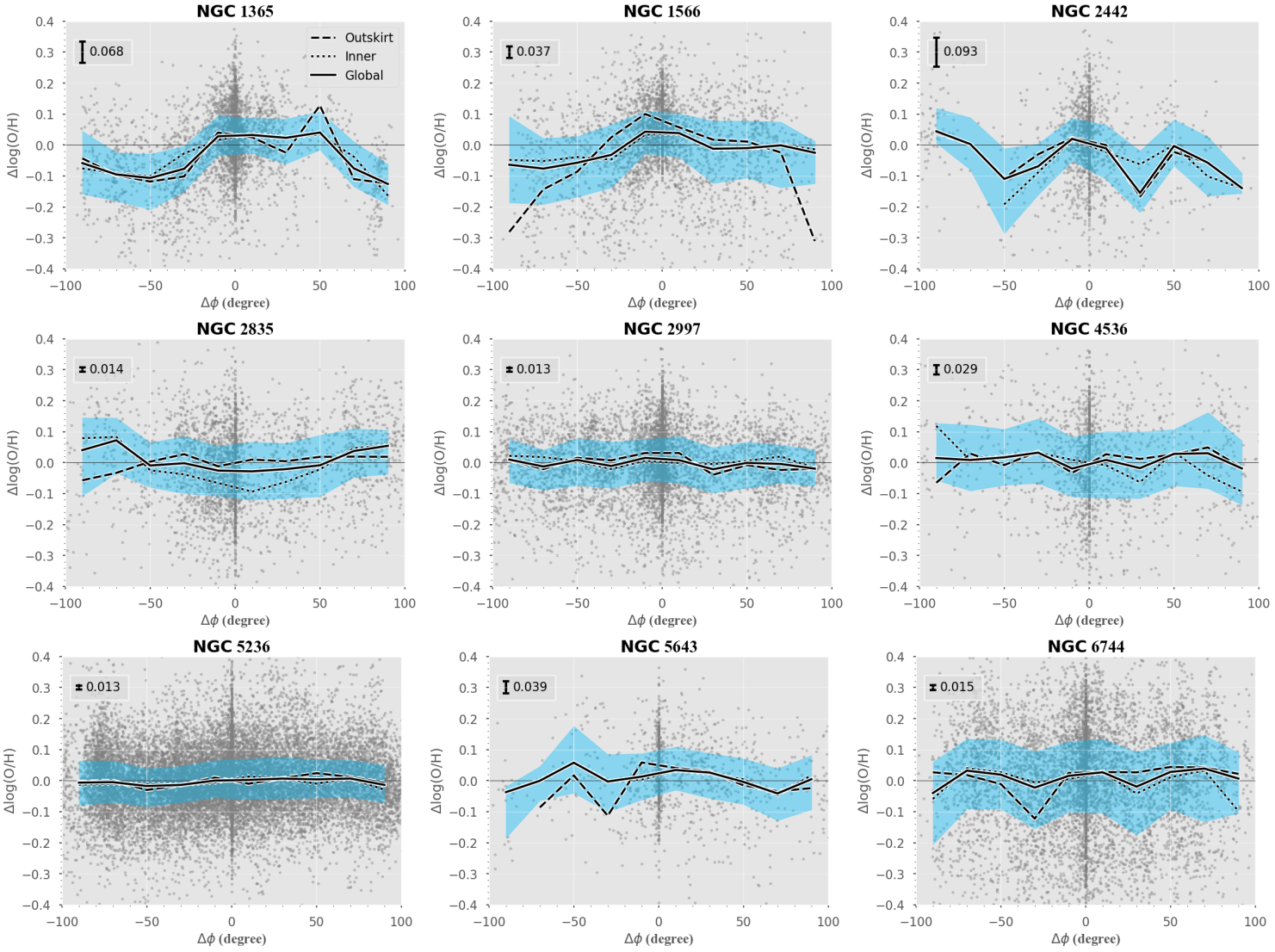


**Figure 3.7**: (Caption next page.)

**Figure 3.7:** Similar to Fig 3.6 but for $\Delta\log(O/H)$. The gas flows (leftward) from 100° to 0° then towards -100°. The higher the $\Delta\log(O/H)$ is, the more metal-rich the spaxel is, compared to other spaxels at the same galactocentric distance. We find significant offsets (> 0.1 dex) in the metallicity of NGC 1365 and NGC 1566 and NGC 2442 ($\Delta\phi$> 50). We find no significant azimuthal variation in the other six spiral galaxies. We do not find any opposite trend of $\Delta\log(O/H)$-$\Delta\phi$ in the inner region versus the outskirt. The $\Delta\log(O/H)$ in the inner region of NGC 2835 is significantly different from the $\Delta\log(O/H)$ in the outskirt, indicative of environmental effects in the outskirt.

In NGC 2835, NGC 2997, and NGC 5236, the AD test returns a $p$-value of $(1.11\pm0.72) \times 10^{-3}$, $(1.15\pm0.87) \times 10^{-3}$, and $1\times10^{-3}$, rejecting the hypothesis that the metallicities distributions are drawn from the same parent distribution. Interestingly, the metallicity offset between $\Delta\phi > 0$ and $\Delta\phi < 0$ is absent in Fig 3.7 and absent in the CDFs with a $D$-value of 0.084 ± 0.010, 0.075 ± 0.008, and 0.043 ± 0.003, respectively. The small $D$-value in the metallicity of NGC 2835, NGC 2997 and NGC 5236 aligns with the prediction from dynamic spiral theory. The small $p$-value can be driven by 1) the tail of the distribution, as the mean values of the metallicity on both sides of the spiral arms are not distinguishable, and/or 2) the environmental effects such as gas accretion (Sec 3.5.4) enhancing the metallicity asymmetry. We notice that NGC 2835 has surprisingly metal-poor spiral arms, compared to the interarm regions. One possible mechanism is the accretion of metal-poor gas from the circumgalactic medium (CGM), which may be funnelled along spiral arms(e.g., Werk et al. 2010; Orr et al. 2023).

The substantial scatter observed in both $\Sigma_{SFR}$ and metallicity can obscure the detection of azimuthal offset, leading to a discrepancy between the absence of an azimuthal offset and the statistical tests of NGC 2835, NGC 2997, and NGC 5236. Previous studies on star clusters in NGC 5236 have reported: i) a small fraction of higher $\Sigma_{SFR}$ in the leading edge of one arm (Silva-Villa & Larsen 2012), and ii) an azimuthal age gradient (Bialopetravičius & Narbutis 2020; Abdeen et al. 2022). These observational results, different from our work, may be attributed to the various analyses performed on star clusters and on spaxel levels. Measuring metallicity with less uncertainty and conducting deeper observations in fainter inter-arm regions could provide more evidence. In this paper, using the TYPHOON survey, we will maintain our discussion of the non-detected azimuthal variation in these three galaxies as a preference for dynamic spiral theory.

NGC 4536, NGC 5643 and NGC 6744 show highly similar metallicity CDF between the leading edge and trailing edge, with a $p$-value larger than 0.05. These symmetrical distributions in metallicity show a preference for the dynamic spiral theory when explaining the formation of spiral features in these five galaxies. We test our detection limit with 1000 times bootstrapping within the metallicity measurement uncertainty. The lower than 0.05 $p$-values, even with the uncertainty, suggest the absent azimuthal variation in NGC 4536,

NGC 5643 and NGC 6744 are not obscured by the detection limit.

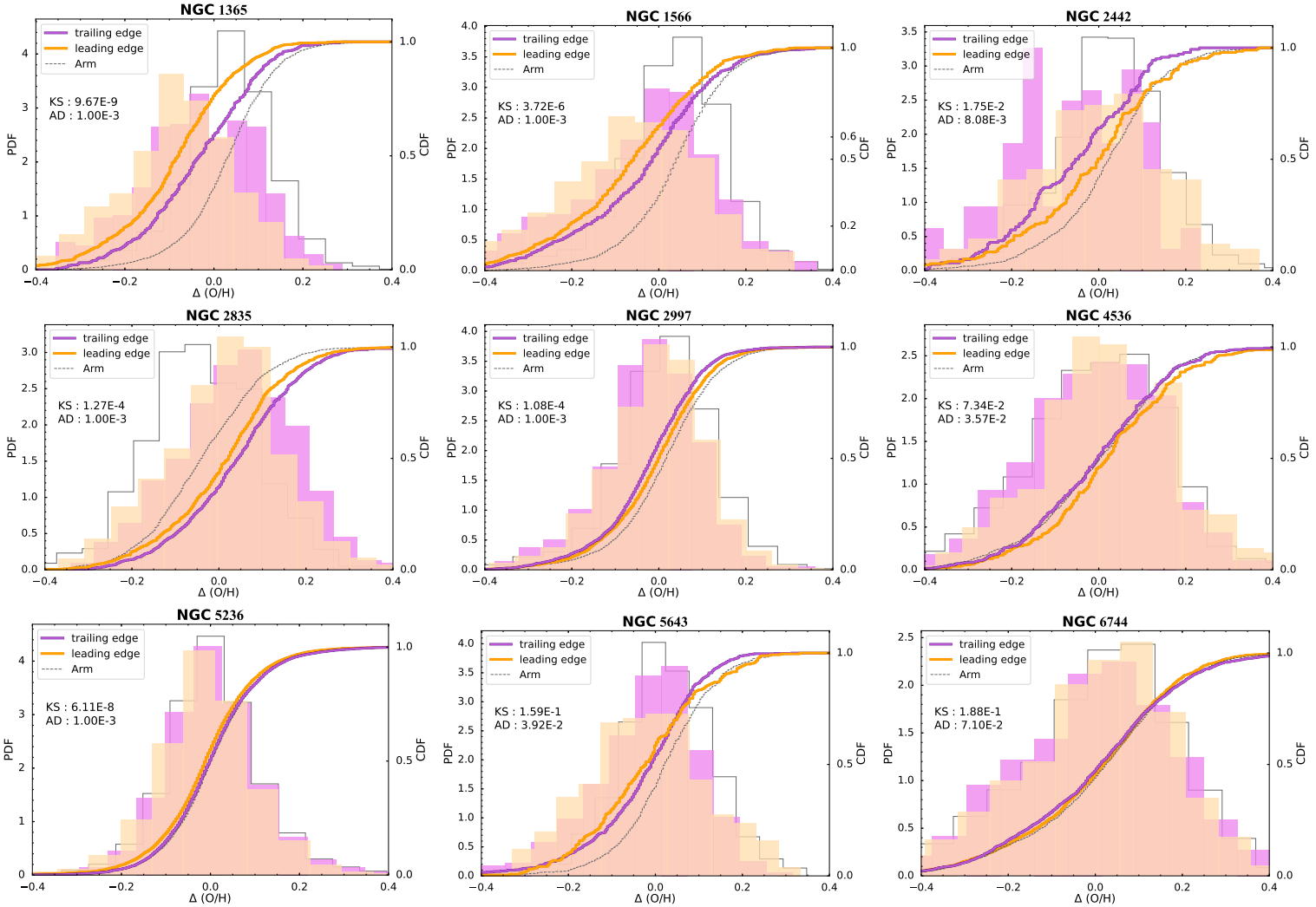


**Figure 3.8:** Histograms and CDF diagrams of $\Delta\log(O/H)$, colour-coded by their location to the spiral arms: purple marks the trailing edge of the spiral arms and orange marks the leading edge. We leave the gap within $-20° < \Delta\phi < 20°$ as the spiral arm region (black hollow histograms and black CDFs), which are not included in the leading/trailing edge regions. NGC 1365 and NGC 1566 show higher $\Delta\log(O/H)$ in the trailing edge (purple) than the leading edge (orange), while NGC 2442 presents higher $\Delta\log(O/H)$ in the leading edge. The other six galaxies show similar metallicity CDFs on both sides of the spiral arms.

| Galaxy | $D$-value | $z$-score | $p$-value (KS) | Significance level (AD) |
|---|---|---|---|---|
| **NGC 1365** | $0.171 \pm 0.013$ | $4.70\sigma$ | $(1.33 \pm 5.41) \times 10^{-6}$* | $1.00 \times 10^{-3}$* |
| **NGC 1566** | $0.114 \pm 0.015$ | $2.92\sigma$ | $(1.18 \pm 3.27) \times 10^{-3}$* | $(1.51 \pm 2.51) \times 10^{-3}$* |
| NGC 2442 | $0.142 \pm 0.025$ | $1.25\sigma$ | $(1.05 \pm 1.12) \times 10^{-1}$ | $(4.80 \pm 5.57) \times 10^{-2}$* |
| **NGC 2835** | $0.084 \pm 0.010$ | $2.56\sigma$ | $(0.52 \pm 1.05) \times 10^{-2}$* | $(1.11 \pm 0.72) \times 10^{-3}$* |
| **NGC 2997** | $0.075 \pm 0.008$ | $3.43\sigma$ | $(2.99 \pm 7.78) \times 10^{-4}$* | $(1.15 \pm 0.87) \times 10^{-3}$* |
| NGC 4536 | $0.070 \pm 0.017$ | $0.31\sigma$ | $(3.78 \pm 2.48) \times 10^{-1}$ | $(9.82 \pm 8.18) \times 10^{-2}$ |
| **NGC 5236** | $0.043 \pm 0.003$ | $4.30\sigma$ | $(0.85 \pm 2.05) \times 10^{-5}$* | $1.00 \times 10^{-3}$* |
| NGC 5643 | $0.073 \pm 0.012$ | $0.55\sigma$ | $(2.92 \pm 1.60) \times 10^{-1}$ | $(1.30 \pm 0.67) \times 10^{-1}$ |
| NGC 6744 | $0.030 \pm 0.005$ | $0.60\sigma$ | $(2.74 \pm 1.47) \times 10^{-1}$ | $(8.49 \pm 5.33) \times 10^{-2}$ |

**Table 3.2:** $D$-values, $z$-scores, $p$-values from the KS tests, significance level from AD tests and their uncertainty. The $D$-value indicates the largest vertical distance between the CDFs of the leading and trailing edge $\Delta\log(\mathrm{O/H})$. The $z$-scores quantify how significant the $p$-values (KS) are. A $z$-score of 1 corresponds to being 1 standard deviation away from the mean in a Gaussian distribution. The $1\sigma$ uncertainty in $D$-values, $p$-values and significance level is the standard deviation of 1000 iterations of bootstrap resampling. We use asterisks to highlight $p$-values and significance levels below 0.05. Galaxies with both $p$-values and significance levels below 0.05 are highlighted in bold.

## 3.5 Discussion

### 3.5.1 Global galaxy properties and azimuthal variations

In this work, three of our nine galaxies (NGC 1365, NGC 1566, NGC 2442) show statistically significant azimuthal variation in metallicity. Similarly, Kreckel et al. (2019) found subtle azimuthal variation in half of their galaxy samples but not always associated with the spiral features. It is important to study the correlation between the global properties of spiral galaxies and the presence of azimuthal variation in the gas-phase metallicity. This will bring us hints on which type of spiral galaxies tend to exhibit observable azimuthal variation in metallicity.

In Fig 3.9, we show the correlation between $D$-values calculated from metallicity CDFs (Fig 3.8) and global galaxy properties, including the tightness of spiral arms (T-type), disk size, stellar mass, global SFR, the presence of a bar, amplitude of spiral arms and metallicity gradient. The points are colour-coded by their dominant mechanism that drives the spiral features (Sec 3.4.2 and further discussed in Sec 3.5.4). In Fig 3.9, we find that more open-armed galaxies (large T-type) tend to have low $D$-values while less open-armed galaxies (small T-type) exhibit large $D$-values. There is a weak but positive correlation between $R_{25}$ and $D$-values, with one outlier galaxy, NGC 6744. Our finding suggests that more extended galaxies tend to have stronger azimuthal variation in metallicity compared to compact galaxies. We present the strength of spiral arms using the H$\alpha$ luminosity

ratio between the spiral arm regions ($|\Delta\phi|$ <20°) and the inter-arm regions. Our galaxies show larger $D$-values with stronger spiral arms, which suggests that galaxies with more pronounced spiral arms tend to have greater metallicity offset on both sides of spiral arms. Similarly, Sánchez-Menguiano et al. (2020) find the metallicity difference of arm versus interarm is larger ($\sim$ 0.015 dex) in grand-design than in flocculent galaxies. More studies on nearby galaxies can fill up the gap between strong spiral arms ($\frac{L_{\rm arm}}{L_{\rm inter-arm}} > 4$) and weak spiral arms ($\frac{L_{\rm arm}}{L_{\rm inter-arm}} < 3$) and provide more constraints. The galaxies in our sample do not show a clear correlation between the $D$-values and the stellar mass, global SFR, and the presence of a bar. A larger sample of spiral galaxies will improve the study of the correlation between azimuthal variations and global galaxy properties.

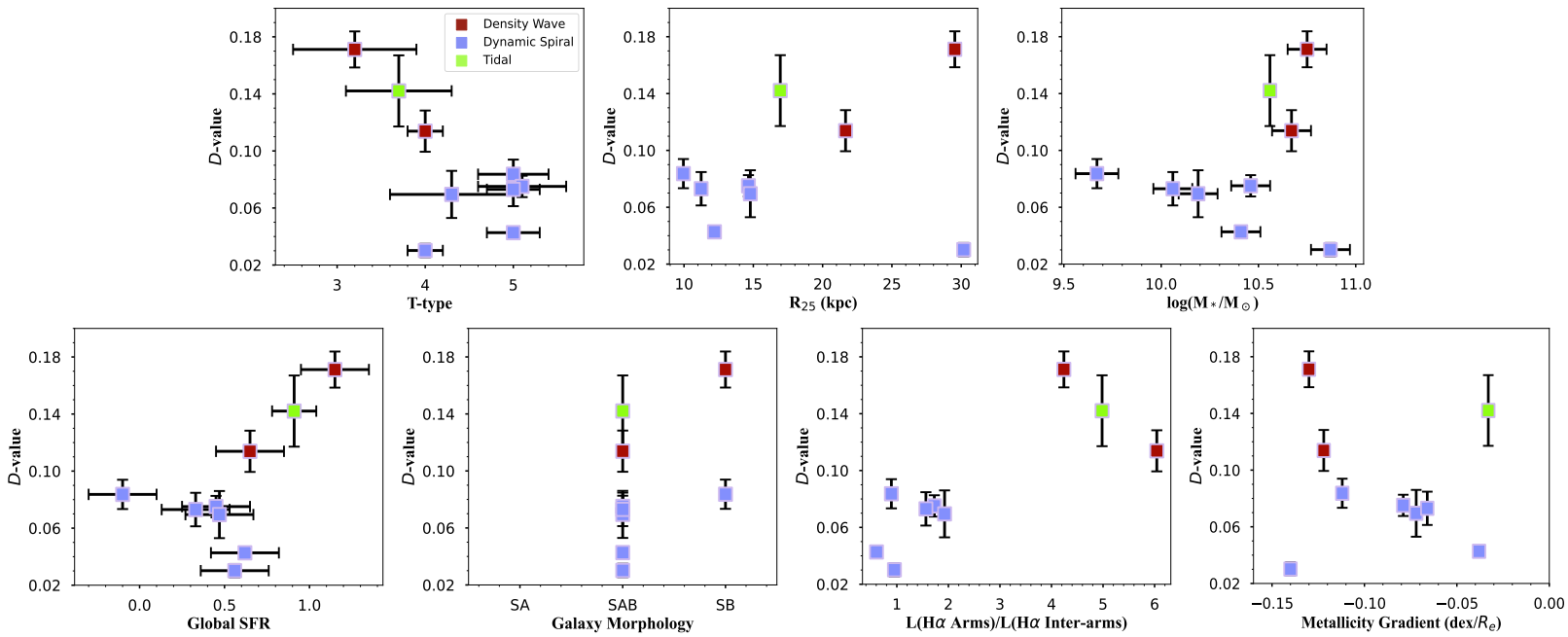


**Figure 3.9:** The relation between global properties and $D$-value drawn from metallicity CDFs (Fig 3.8 and Tab 3.2). The higher the $D$-value is, the greater the metallicity azimuthal variation is. All galaxies are colour-coded by their dominant mechanism that drives the origin of spiral arms. T-type is the numerical morphological type adopted from http://atlas.obs-hp.fr/hyperleda/, with 3 referring to Sb, 4 referring to Sbc and 5 referring to Sc in the de Vaucouleurs (1959) morphological classification. We use $R_{25}$ to represent the size of the galaxy disc, taken from Tab 3.1. The stellar mass is the same as Tab 3.1. The global SFR are taken from Leroy et al. (2019) [a]. The presence of a bar is taken from the morphological information in Tab 3.1. The H$\alpha$ luminosity ratios between the spiral arms ($|\Delta\phi|$ <20°) and the inter-arm regions describe the strength of spiral features. The radial gradient of metallicity is defined as the slope of the best linear fit on spaxels, in dex kpc$^{-1}$ (further discussed in Sec 3.5.2).

**Note.**

[a]: the global SFR of NGC 2442 is taken from Pancoast et al. (2010) as it is not included in Leroy et al. (2019).

### 3.5.2 Impacts of radial streams and radial migration

Previous simulations have discussed the impacts of radial streams and radial migration on azimuthal variations of gas and stars (e.g., Sellwood & Binney 2002; Grand et al. 2015; Grand & Kawata 2016; Orr et al. 2023). Radial stellar migration can move metal-rich star particles outward along the trailing edge, while bringing metal-poor star particles inward along the leading edge (e.g., Grand et al. 2016). Radial gas streams can lead to azimuthal variations of gas-phase metallicity distribution, with metal-rich gas concentrated in the trailing side of the stellar spiral arm (e.g., Khoperskov et al. 2023). Sánchez-Menguiano et al. (2016) found azimuthal variations of gas metallicity in NGC 6754, where large-scale gas radial migration is also detected. Radial migration is expected to be stronger in a bar-spiral coupled system (Minchev & Famaey 2010). Given the varying bar strength in our sample, ranging from strong to weak, it is important to discuss the impacts of radial migration in our study of azimuthal variation.

Measuring and modelling the velocity field to investigate the radial gas migration is out of the scope of this paper. Instead, we adopt the radial metallicity gradient as an indicator for radial gas migration. We measure the radial metallicity gradient with a single linear function, listed in Tab 3.3, each showing a negative metallicity gradient. The negative metallicity gradients are consistent with an inside-out galaxy formation. Seven of our galaxies (except for NGC 2442 and NGC 5236) have comparable radial metallicity gradients with those reported in previous studies, such as the CALIFA survey ($-0.1$ dex/$R_e$; Sánchez et al. 2015), and the MaNGA survey ($-0.14$ dex/$R_e$; Belfiore et al. 2017). The shallow metallicity gradients in NGC 2442 and NGC 5236 could be indicative of large-scale radial gas flows dispersing and flattening the metal distribution. A large sample of spiral galaxies is needed to establish a stronger relation between metallicity gradients and azimuthal variations.

The final panel in Fig 3.9 compares the radial metallicity gradients of our sample and their $D$-values from metallicity CDF in the leading and trailing edge. We cannot draw a conclusive correlation between the metallicity radial gradient and $D$-values. In the shallow radial gradient regime ($\lesssim -0.05$dex/$R_e$), where strong and large-scale radial gas flows are expected to exist, we find both galaxies with high (NGC 2442) and low (NGC 5236) $D$-values. This result suggests that large-scale radial gas flow does not necessarily lead to strong azimuthal offset in metallicity.

| Galaxy | NGC 1365 | NGC 1566 | NGC 2442 | NGC 2835 | NGC 2997 |
|---|---|---|---|---|---|
| Single linear (dex/$R_e$) | −0.136 | −0.144 | −0.014 | −0.119 | −0.077 |
| Piecewise fits (dex/$R_e$) | **−0.664, −0.093** | −0.118, −0.156 | **−0.816, −0.00** | **−0.152, −0.078** | −0.037, −0.097 |
| Break radius (kpc) | 4.82 | 8.00 | 1.93 | 6.00 | 6.73 |
| Galaxy | NGC 4536 | NGC 5236 | NGC 5643 | NGC 6744 | |
| Single linear (dex/$R_e$) | −0.086 | −0.038 | −0.066 | −0.132 | |
| Piecewise fits (dex/$R_e$) | **−0.281, −0.068** | **−0.075, 0.038** | **−0.262, −0.061** | 0.030, −0.160 | |
| Break radius (kpc) | 2.77 | 5.37 | 1.85 | 7.65 | |

**Table 3.3:** This table shows the metallicity gradient fitted by a single linear function and piecewise linear function, with both the inner gradient and outer gradient listed sequentially. The break radius of the piecewise fits is listed in the last row. All of the observed spiral galaxies show a negative metallicity gradient, consistent with an inside-out galaxy formation. The galaxies showing a flattening metallicity gradient truncated outside 2 kpc are in bold.

A truncated metallicity radial gradient, especially a flattening gradient in the outer parts, is possibly a phenomenon driven by radial gas mixing (Minchev et al. 2011; Sánchez-Menguiano et al. 2018; Garcia et al. 2023, Kewley et al. In Preparation). We summarise the best fit of a piecewise linear function on gas-phase metallicity (Sec 3.3.4) in Table 3.3. We find a shallow-steep metallicity radial profile in NGC 1566, NGC 2997 and NGC 6744. In NGC 1365, NGC 2442, NGC 2835, NGC 4536, NGC 5236 and NGC 5643, we observe a flattening of the metallicity radial gradient, i.e., the outer gradient is less than half as steep as the inner gradient. This phenomenon could be indicative of radial gas migration outside the break radius (Minchev et al. 2011) and/or satellite accretion (Qu et al. 2011). Among the six spiral galaxies with a flattening metallicity radial gradient, an azimuthal offset is observed in NGC 1365 and NGC 2442. In NGC 1365, we cannot distinguish the dominant mechanisms driving the azimuthal variation, with the potential involvement of both density wave theory and radial gas motion. The merging event in NGC 2442 can be attributed to the strong radial gas mixing and meanwhile azimuthal variations in metallicity.

### 3.5.3 Inside and outside the co-rotation radius

The asymmetric distributions of $\Sigma_{SFR}$ and gas-phase metallicity in NGC 1365 and NGC 1566 (Sec 3.4.1 and Sec 3.4.2) suggest that the density wave theory explains the origin of their spiral features. According to the density wave theory, the material surpasses the spiral density wave inside the $R_{CR}$ while lagging behind the density wave outside the $R_{CR}$. A simulation by Spitoni et al. (2019) shows that the density perturbation of a disc model can result in stronger oxygen abundance fluctuations in the outer region compared to the inner regions of a galaxy. When an analytic spiral arm[7] is included in the simulation, and the fluctuations near the co-rotation resonance are enhanced. To further compare the observations and simulations, it is essential to assess the behaviour of ISM inside/outside the $R_{CR}$.

Although it is challenging to measure the $R_{CR}$, astronomers have devoted numerous efforts to measuring the $R_{CR}$ of nearby spiral galaxies with various methods. Three of our observed spiral galaxies (NGC 1365, NGC 1566, and NGC 5236) have their $R_{CR}$ reported in previous works and collected in Tab 3.4.

With the location of $R_{CR}$, we divide the spiral galaxies into three sections: inside the $R_{CR}$, near the $R_{CR}$, and outside the $R_{CR}$. We exclude NGC 5236 in the following discussion since the $R_{CR}$ of NGC 5236 is more than 3 kpc beyond the observed optical disc in the TYPHOON survey. Fig 3.10 compares the behaviour of metallicities at different azimuths

[7] Analytic spiral arms show regular gravitational perturbation with a fixed pattern speed. The surface arm density can be described by the radial distance and the azimuth.

| Galaxy | $R_{CR}$ (kpc) | References |
|---|---|---|
| NGC 1365 | 13.8 | Lindblad et al. (1996); Elmegreen et al. (2009) |
| NGC 1566 | 8.8 | Scarano & Lépine (2013); Abdeen et al. (2020) |
| NGC 5236 | 8.5 | Scarano & Lépine (2013); Abdeen et al. (2020) |

**Table 3.4:** The $R_{CR}$ of NGC 1365, NGC 1566 and NGC 5236 reported in previous publications. We take the mean values as the $R_{CR}$ in the analysis in this work.

and radii, indicated by colours. The azimuth starts from the position angle in Table 3.1 and increases counter-clockwise to 360°.

We observe the smallest azimuthal fluctuation (0.13 dex for NGC 1365; 0.07 dex for NGC 1566) of metallicity in the inner region (grey line in Fig 3.10), in agreement with the observations of NGC 6754 (Fig 7 in Sánchez et al. 2015). In NGC 1365, we find that the fluctuations in metallicity with azimuth are comparable when near (0.24 dex) and outside the $R_{CR}$ (0.25 dex), which is significantly larger than those within the $R_{CR}$. As an analytic spiral arm (Spitoni et al. 2019) predicts the largest metallicity fluctuation near the $R_{CR}$, our observation indicates the presence of a density perturbation in NGC 1365, resulting in a greater metallicity fluctuation beyond the $R_{CR}$. Additionally, we notice that the $\Delta\log(O/H)$ offset between the leading and trailing edge (Fig 3.7) is slightly larger in the outskirts (R >10.98 kpc) than in the inner region (R <10.98 kpc). The absent opposing behaviour inside versus outside the $R_{CR}$ (13.8 kpc) does not align with the prediction of density wave theory. However, there is a large uncertainty in the detection of $R_{CR}$. In Ho et al. (2017), they adopt a larger $R_{CR}$ where all observed spaxels in the TYPHOON field are within the $R_{CR}$. In this case, the consistent $\Delta\log(O/H)$-$\Delta\phi$ trend at different radii (dashed and dotted lines in Fig 3.7) aligns with the prediction of density wave theory within the $R_{CR}$.

In NGC 1566, the metallicity shows the highest fluctuation near the $R_{CR}$ (0.21 dex) when compared with the metallicity fluctuation outside the $R_{CR}$ (0.12 dex) and within the $R_{CR}$ (0.07 dex). This is in line with the predictions from Spitoni et al. (2019), indicating that the spiral arms in NGC 1566 are also analytic.

Inside the $R_{CR}$, the metallicity fluctuation can be decreased or wiped out by the rotation of material, due to the decreased travel distance between spiral arms. We calculate the timescale required to travel between spiral arms, in order to assess the reliability of the small-scale metallicity fluctuations we measured. We calculate the angular distance that stars will travel in 10 Myr, a typical life span of O-type stars, using equation 3.3.3. The $V_{\rm circ}$ of NGC 1365 is $\sim$ 300 km s$^{-1}$ at $\sim$ 100" ($\sim$ 8 kpc; Jorsater & van Moorsel 1995), while NGC 1566 has a $V_{\rm circ}$ of $\sim$ 180 km s$^{-1}$ at 6 kpc (Elagali et al. 2019). Following equation 3.7, we find the rotation angle within 10 Myr is $\lesssim 20°$ inside the $R_{CR}$ for both

NGC 1365 and NGC 1566, which is smaller than the azimuthal distance between two spiral arms. Considering the flattening of the rotation curve, we find that the rotation angle is >20° outside the $R_{CR}$ of NGC 1365 and NGC 1566. Hence, the fluctuation of metallicity cannot be wiped out by the rotational motion of the material, even inside the $R_{CR}$. Therefore, the observed smaller metallicity fluctuation within the $R_{CR}$ can be considered reliable and meaningful.

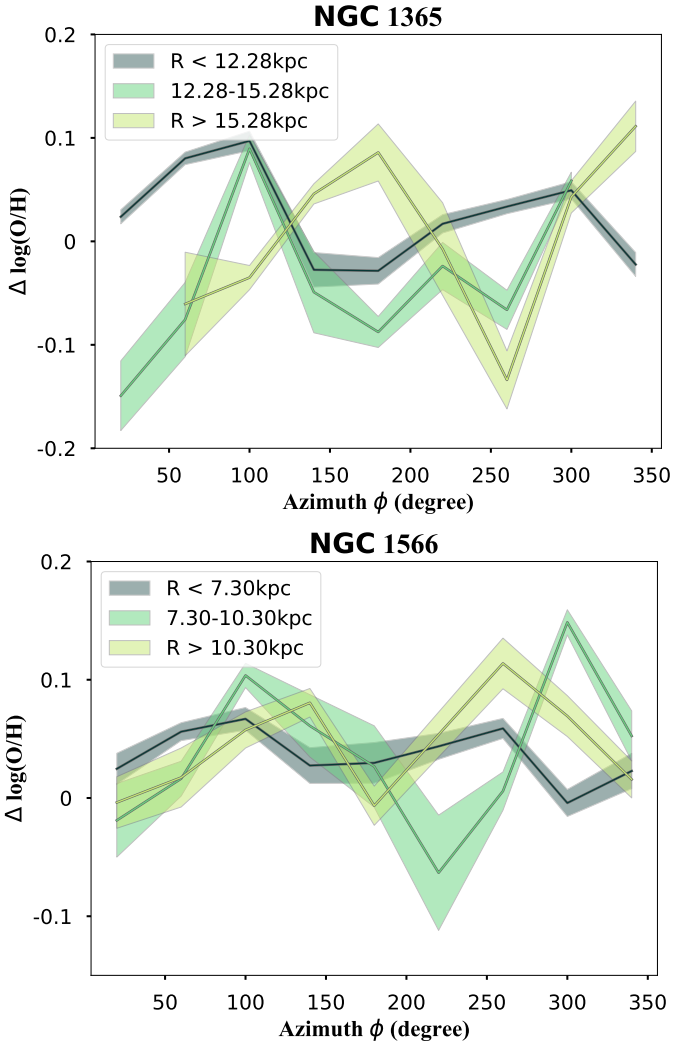


**Figure 3.10:** Residual of gas-phase metallicity as a function of azimuth inside the $R_{CR}$ (grey), near the $R_{CR}$ (green), and beyond the $R_{CR}$ (lime). The azimuth starts from the position angle (Table 3.1) and increases counter-clockwise. We apply bootstrapping for 500 iterations and show the medians with $1\sigma$ uncertainty in the figure. The shadow of the lines indicates $1\sigma$ of the medians.

### 3.5.4 Dominant mechanisms driving spiral features of each galaxy

In this section, we discuss the underlying mechanisms driving the formation of spiral arms in our galaxies, taking into account the distributions of $\Sigma_{\rm SFR}$, 12 + log(O/H) from the TYPHOON survey, as well as the environmental factors reported in previous works.

NGC 1365 is a grand-design spiral galaxy in the Fornax cluster. The small fragments near the two prominent spiral arms infer that NGC 1365 has undergone tidal interaction. In this work, we find slightly higher $\Sigma_{\rm SFR}$ (Sec 3.4.1) and generally higher metallicity (Sec 3.4.2) in the trailing edge ($\Delta\phi > 0$) of the spiral arms. These scenarios are supportive evidence for density wave spiral arms. However, the radial gas motion, indicated by the flattening metallicity gradient (Sec 3.5.2), can also result in the azimuthal variation in $\Sigma_{\rm SFR}$ and $\Delta\log({\rm O/H})$. We notice a comparable fluctuation in metallicity near (0.24 dex) and beyond (0.25 dex) the $R_{\rm CR}$, which is twice as pronounced as the fluctuation within the $R_{\rm CR}$ (13.8 kpc). This observation supports the influence of tidal interactions, by comparison with the simulated model in Spitoni et al. (2019).

According to the asymmetric HI distribution (Elagali et al. 2019), NGC 1566 is possibly experiencing ram-pressure interaction with the intergalactic medium (IGM) in the Dorado cluster. Slater et al. (2019) report the strong outflows observed in ionised and molecular gas in the central kpc along the bar and the spiral arms. Our observations show generally higher $\Sigma_{\rm SFR}$ and higher metallicity in the trailing edge ($\Delta\phi > 0$) of the spiral arms. This evidence supports that the spiral arms in NGC 1566 follow the density wave theory. The strongest metallicity fluctuations near the $R_{\rm CR}$ (Fig 3.10) are consistent with the simulated galaxy with an analytic spiral arm.

NGC 2442 is a system undergoing a merger (Mihos & Bothun 1997; Pancoast et al. 2010) and the south and north spiral arms are distorted fragments from the same galaxy (NGC 2442 and NGC 2443 respectively). Our observations find significantly lower $\Sigma_{\rm SFR}$ and lower metallicity in the trailing edge ($\Delta\phi > 0$) of the spiral arms, which is unexpected by either density wave theory or dynamic spiral theory. The spiral features in NGC 2442 are dominated by the gravity perturbation from the ongoing tidal interactions and the induced strong gas radial migration (Sec 3.5.2).

NGC 2835 is a multi-armed spiral galaxy in a small galaxy group (Anand et al. 2021), with ESO 497-035 and ESO 565-001. The flattened metallicity radial profile, happening at $\sim$ 7 kpc, indicates the gas accretion from the circumgalactic medium to the outskirts of the galaxy (Chen et al. 2023; Garcia et al. 2023). We observe negligible offset in $\Sigma_{\rm SFR}$ and 12 + log(O/H), given the scatters of the spaxels. The $D$-value is not significant while the KS test and AD test suggest the metallicity on both sides of the spiral arms are drawn

from different distributions. This result suggests the spiral arms in NGC 2835 follow the dynamical spiral theory, potentially under the density perturbation from the accreted gas, flattening the metallicity gradient in the outskirts (Table 3.3).

NGC 2997 belongs to a loose galaxy group and has undergone tidal interaction according to the anomalous HI distribution (Hess et al. 2009). We observe generally no offset between both sides of the spiral arms, either in $\Sigma_{SFR}$ or 12 + log(O/H). This suggests that tidal interaction does not necessarily lead to azimuthal variation in $\Sigma_{SFR}$ and 12 + log(O/H). The tidal-induced spiral arms in NGC 2997 behave similarly to dynamic spiral arms, instead of density-wave-like structures.

NGC 4536 is located in the Virgo cluster without evident hints of tidal interaction. The only kinematic perturbation is the bar-induced inflows observed in the HI map (Davies et al. 1997). We observe slightly lower $\Sigma_{SFR}$ and lower metallicity in the trailing edge ($\Delta\phi > 0$). However, the CDF diagram shows no offset between the downstream and upstream. The $p$-value ($3.78 \times 10^{-1}$) from the KS test suggests that the metallicity on both sides of the spiral arms is drawn from the same parent distribution. Therefore, we conclude that the current TYPHOON data suggest NGC 4536 follows the dynamic spiral theory, with insufficient spaxels to discern the azimuthal variations.

NGC 5236 (M83) is the largest member in its galaxy group. There is a large optically detected tidal stream to the north of M83 (Malin & Hadley 1997; Pohlen et al. 2004; Jarrett et al. 2013), tracing the disruption of a dwarf galaxy in the strong gravitational field of M83. The penetrating gas stream may be attributed to the flattening metallicity gradient beyond 5.37 kpc (Table 3.3). Unlike studies on star clusters (Silva-Villa & Larsen 2012; Bialopetravičius & Narbutis 2020; Abdeen et al. 2022) and full-spectral fitting (Sextl et al. 2025), we observe no significant offset in either $\Sigma_{SFR}$ or 12 + log(O/H) between the two sides of the spiral arms. Our observations do not support the density wave theory but rather show a preference for the dynamic spiral theory.

As a type-II Seyfert galaxy (Simpson et al. 1997), NGC 5643 is in a small galaxy group with NGC 5530 and has a dwarf satellite ESO 273-014. After excluding the hard component contaminated spaxels, we find slightly higher $\Sigma_{SFR}$ in part of the trailing edge ($\Delta\phi > 70°$) and lower metallicity in the trailing edge ($\Delta\phi > 0$). However, the CDF diagram shows no offset and the KS test agrees that the metallicity in the downstream and upstream is drawn from the same distribution. This finding implies that no statistical offset is found in NGC 5643 based on the TYPHOON data, due to the limited spaxel in the inter-arm regions (especially $\Delta\phi < 0$). We agree that NGC 5643 follows the dynamic spiral theory, instead of the density wave theory.

NGC 6744 is a spiral galaxy in the Virgo supercluster. The HI in NGC 6744 is possibly connected to a companion galaxy, ESO 104−g44 (Ryder et al. 1999). We observe a slightly

increasing trend in $\Sigma_{SFR}$ and $\Delta\log(O/H)$ when crossing the spiral arms from the trailing edge ($\Delta\phi > 0$) to the leading edge ($\Delta\phi < 0$). However, the difference in $\Delta\log(O/H)$ is not statistically evident in the CDF and the KS test. Our findings suggest that under environmental influences, NGC 6744 shows a preference for dynamic spiral theory with absent azimuthal variation.

## 3.6 Summary

We map the 2D ISM properties, $\Sigma_{SFR}$ and gas-phase metallicity, of nine spiral galaxies in the TYPHOON survey. The 3D dataset and wide FoV, covering most of the star-forming disc of each galaxy, allows us to constrain spaxel-by-spaxel fluctuations in ISM properties as a function of azimuthal distance from the spiral arms in each galaxy. These azimuthal distributions constrain the dominant mechanism driving the spiral arms, which can assess the density wave theory.

Considering the azimuthal ISM distribution observed in TYPHOON and the environment reported in previous works (Sec 3.5.4), we discuss the dominant theory/theories that drive the spiral features in our samples. We find higher $\Sigma_{SFR}$ (Fig 3.6) and higher gas-phase metallicity (Fig 3.7) in the trailing edge of NGC 1365 and NGC 1566, which is in line with expectations from density wave theory driving the observed spiral features in these two galaxies. Additionally, the higher $\Sigma_{SFR}$ in the trailing edge indicates that star formation occurs when gas clouds approach the density wave (right spiral arms in Fig 1 of Pour-Imani et al. 2016) in NGC 1365 and NGC 1566. The interacting galaxy, NGC 2442, presents significantly lower metallicity in part of the trailing edge ($\Delta\phi < 50^\circ$), opposite to the expectation of density wave theory, which can be attributed to the ongoing merging event. We do not observe statistically significant offset in the inter-arm regions of the remaining six galaxies, in line with the prediction of dynamic spiral theory.

We investigate the global properties of galaxies and the $D$-values from metallicity CDFs, indicating the significance of azimuthal variations. We find that more prominent spiral arms, more open-armed galaxies and more extended galaxies tend to show stronger azimuthal variations in metallicity.

We collect the co-rotation radius ($R_{CR}$) from the earlier works and compare the azimuthal variation in metallicity within and beyond the $R_{CR}$ (Sec 3.5.3). In NGC 1365, we find the smallest metallicity fluctuation inside the $R_{CR}$ and comparable fluctuation near and outside the $R_{CR}$. This is consistent with a simulated density wave spiral galaxy under gravity perturbation in the outer region (Spitoni et al. 2019). In NGC 1566, we observe the greatest metallicity fluctuation near the $R_{CR}$, aligning with an analytic spiral arm where gravity perturbation is regular.

Our work highlights the importance of azimuthal variations in ISM, which constrain the dominant mechanism driving spiral features. Different theories, including the density wave theory, dynamic spiral theory and tidal interactions, can explain the formation of spiral arms in various galaxies in the local Universe. Despite our handful of galaxy samples, we observe a positive relation between azimuthal metallicity variation and T-type, galaxy size, and arm strength. A larger sample of observations and a comparison between simulations and observations are essential for more constraints on the dominant mechanism driving spiral arms.

## Acknowledgements

We gratefully acknowledge the anonymous referee for their highly constructive and valuable comments, which have significantly improved the scientific quality of this paper. This paper includes data obtained with the du Pont Telescope at the Las Campanas Observatory, Chile, as part of the TYPHOON programme, which has been obtaining optical data cubes for the largest angular-sized galaxies in the Southern Hemisphere. We thank past and present Directors of The Observatories and the numerous time assignment committees for their generous and unfailing support of this long-term programme.

This research has made use of NASA's Astrophysics Data System Bibliographic Services (ADS). This research made use of Astropy[8], a community-developed core Python package for Astronomy (Astropy Collaboration et al. 2013, 2018). This research has made use of the NASA/IPAC Extragalactic Database (NED) which is operated by the Jet Propulsion Laboratory, California Institute of Technology, under contract with NASA.

KG is supported by the Australian Research Council through the Discovery Early Career Researcher Award (DECRA) Fellowship DE220100766 funded by the Australian Government. KG is supported by the Australian Research Council Centre of Excellence for All Sky Astrophysics in 3 Dimensions (ASTRO 3D), through project number CE170100013.

ES acknowledges support by the Munich Excellence Cluster Origins funded by the Deutsche Forschungsgemeinschaft (DFG, German Research Foundation) under Germany's Excellence Strategy EXC-2094 390783311.

## Data Availability

The TYPHOON team is planning for a public data release on Data Central[9] once the observation is complete. The TYPHOON data and the code in this article will be shared

[8] http://www.astropy.org
[9] https://datacentral.org.au/

on reasonable request to the corresponding author.

## 3.7 Appendix: $\Sigma_{SFR}$ maps and $\Delta\Sigma_{SFR}$ maps

The maps of $\Sigma_{SFR}$ and $\Delta\Sigma_{SFR}$ are shown in Fig 3.11 and Fig 3.12.

## 3.8 Appendix: 12 + log(O/H) maps and $\Delta\log(\mathrm{O/H})$ maps

The maps of 12 + log(O/H) and $\Delta\log(\mathrm{O/H})$ are shown in Fig 3.13 and Fig 3.14.

## 3.9 Appendix: Gas-phase metallicity with S-cal calibration

In the main text, we use N2S2-N2H$\alpha$ diagnostic from D16 to determine the gas-phase metallicity of our spiral galaxies. As the physical resolution of our sample ranges from 145 pc to 39 pc, comparable to the typical size of H II region, it is a caveat that the metallicities of some spaxels are contaminated by DIG. Poetrodjojo et al. (2019) find that all diagnostics are affected by the inclusion of DIG. As the current knowledge about modelling metallicity in DIG is still limited (Kewley et al. 2019), we cannot separately derive the metallicity in the DIG.

Emission lines in DIG are excited by ionized photons leaked from H II regions and low-mass evolved stars. To test the impact of DIG in our results, we adopt S-calibration (Scal) from Pilyugin & Grebel (2016) which relies on three standard diagnostic lines:

$$\begin{aligned} R_2 &= I_{[OIII]\lambda 4959+\lambda 5007}/I_{H\beta}, \\ N_2 &= I_{[NII]\lambda\lambda 6548,84}/I_{H\beta}, \\ S_2 &= I_{[SII]\lambda\lambda 6717,31}/I_{H\beta}. \end{aligned} \tag{3.10}$$

The inclusion of three emission line ratios allows Scal to be corrected for the dependence on ionization parameter (Pilyugin & Grebel 2016).

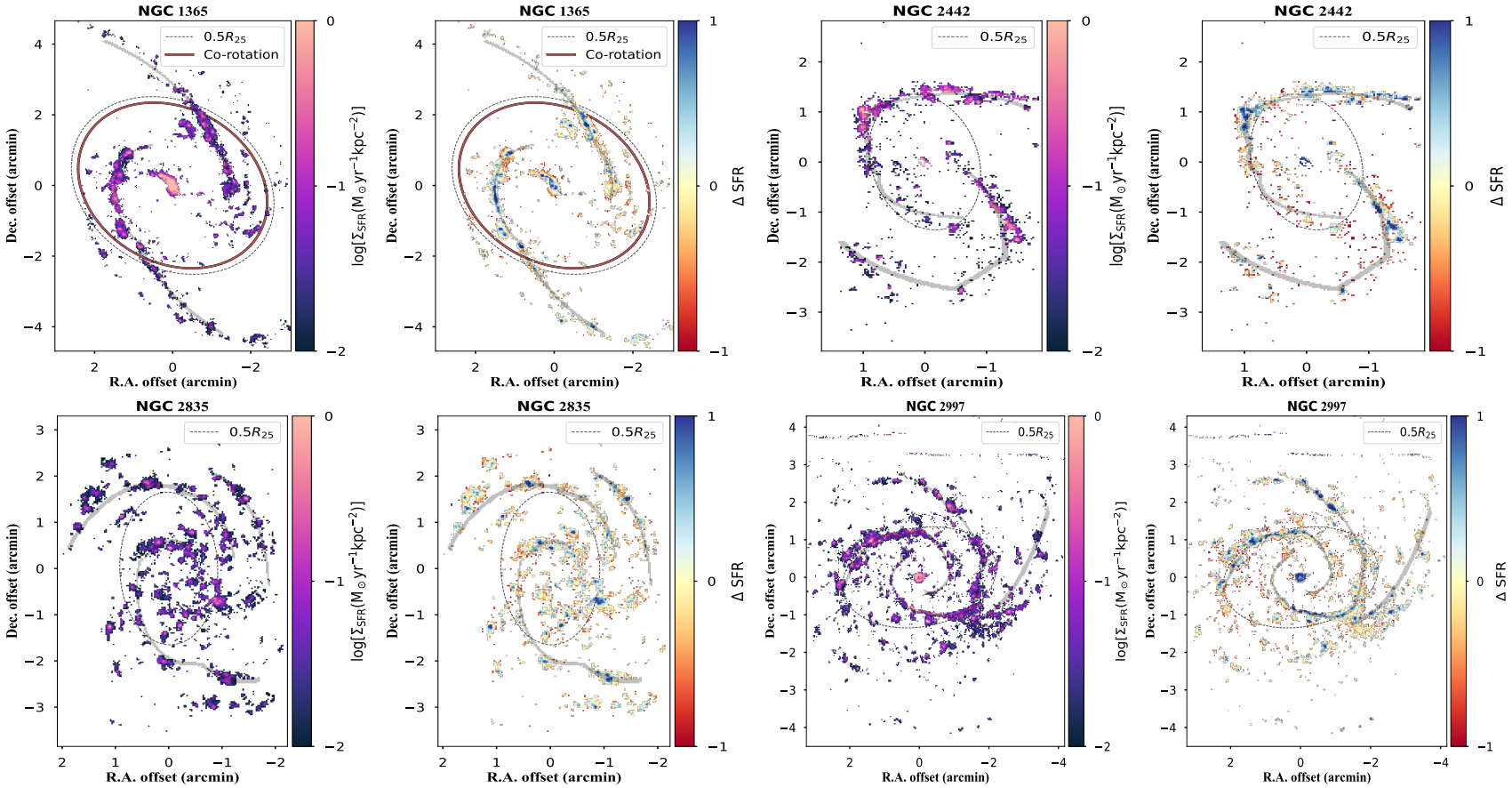


**Figure 3.11: Column 1 & 3**: 2D $\Sigma_{SFR}$ maps of our galaxies, except for NGC 1566 (Fig 3.4). **Column 2 & 4**: Residual of $\Sigma_{SFR}$ by subtracting the radial gradients. More detail on this analysis is in Sec 3.3.4. The dashed ellipse marks the location of half $R_{25}$ and the red ellipse denotes the $R_{CR}$, if applicable.

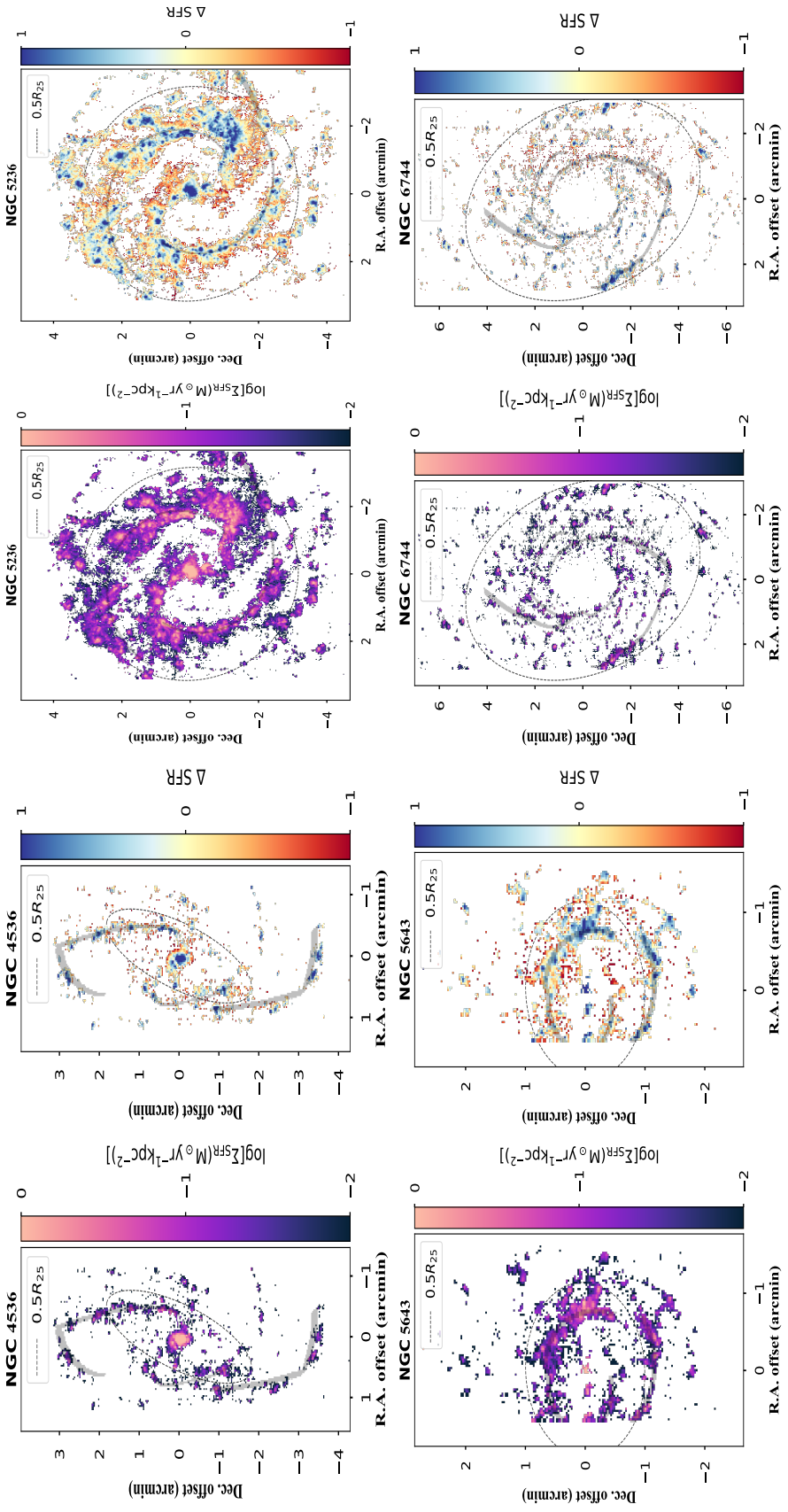


**Figure 3.12**: Continute to Fig 3.11.

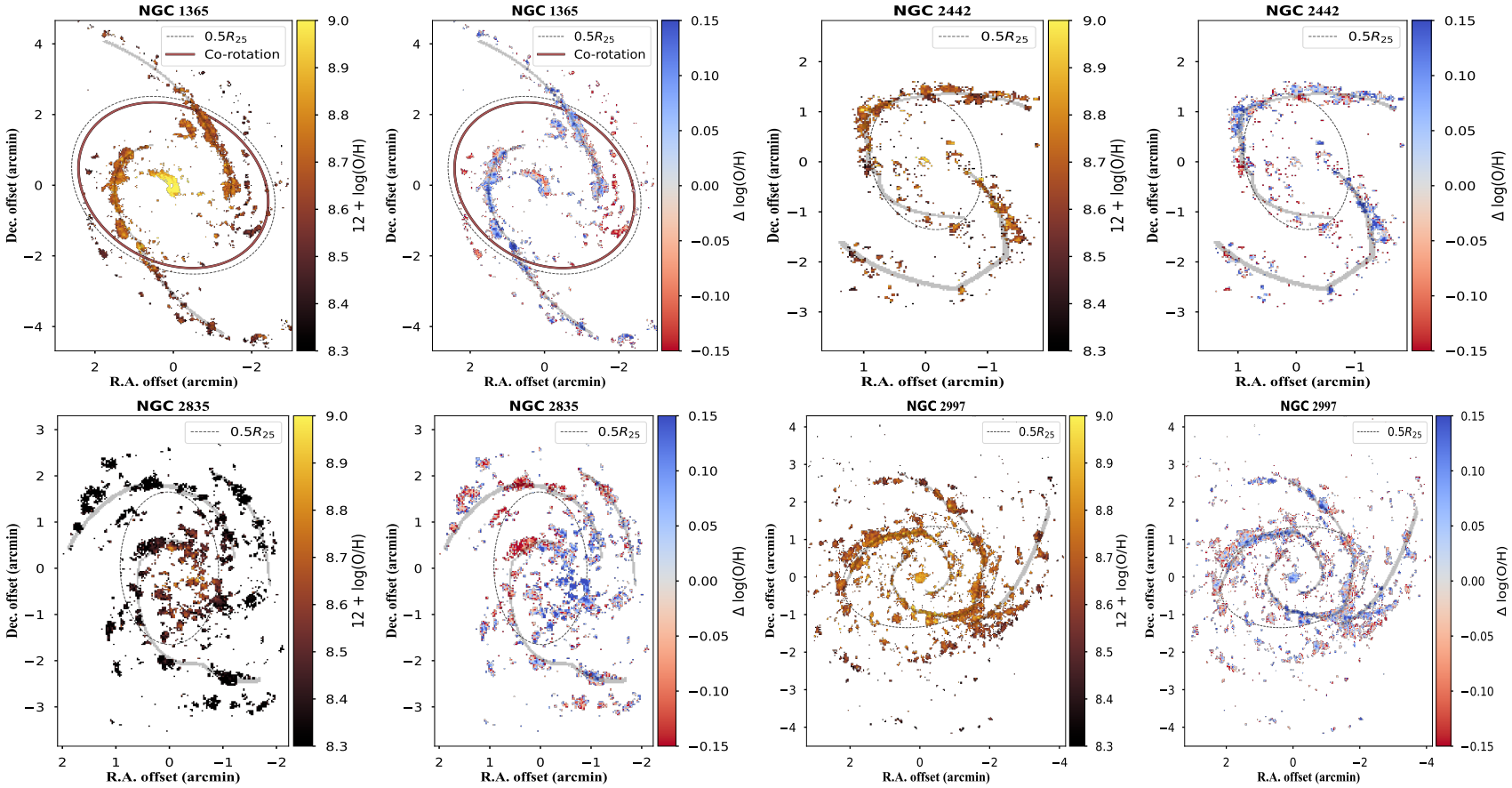


**Figure 3.13: Column 1 & 3**: 2D 12 + log(O/H) maps of our galaxies, except for NGC 1566 (Fig 3.5). **Column 2 & 4**: Residual of metallicity ($\Delta\log(O/H)$) by subtracting the radial gradients. The dashed ellipse marks the location of half $R_{25}$ and the red ellipse denotes the $R_{CR}$, if applicable. More detail on this analysis is in Sec 3.3.4.

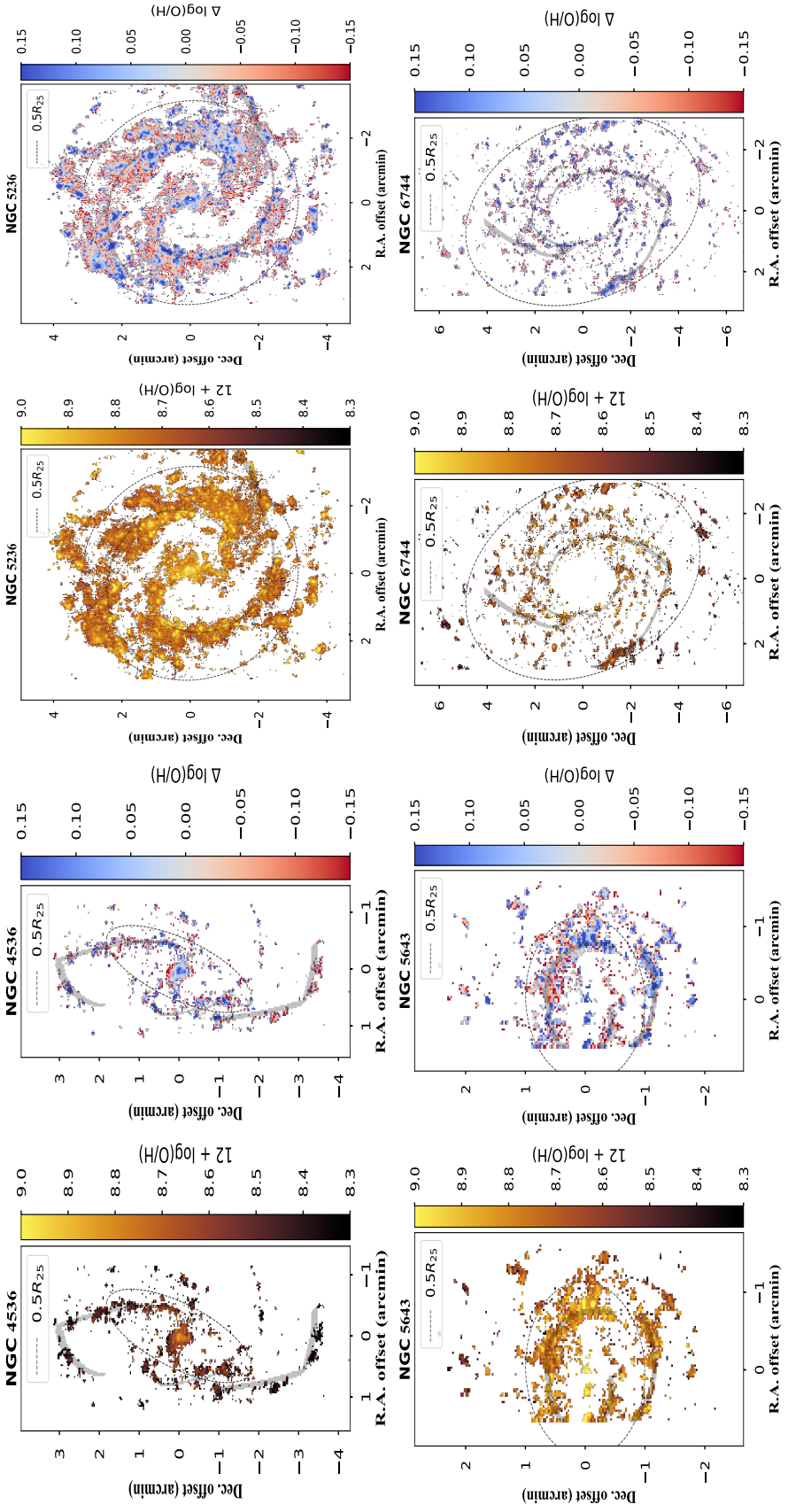


**Figure 3.14**: Continue to Fig 3.13.

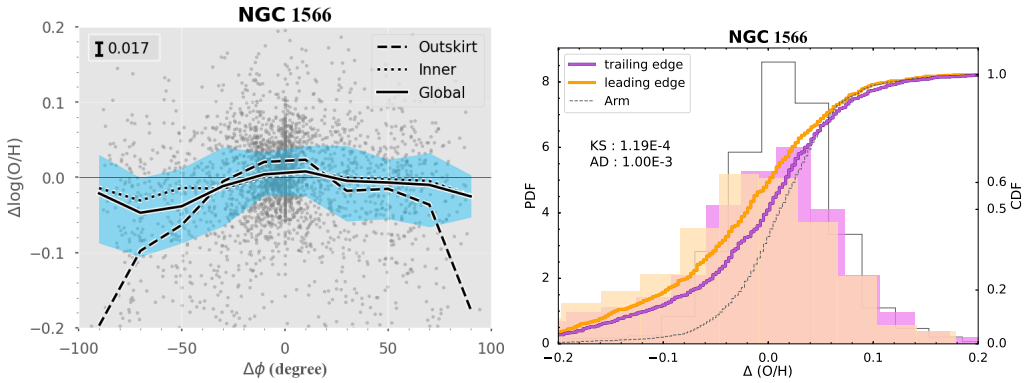


**Figure 3.15: Left**: density scatter plot of metallicity residual $\Delta\log(\mathrm{O/H})$ versus azimuthal distance to the spiral arms $\Delta\phi$. $\Delta\log(\mathrm{O/H})$ is calculated by subtracting the radial gradient from the S-cal metallicity. $\Delta\phi$ is the same as Fig 3.3, described in Sec 3.3.3. We find slightly higher $\Delta\log(\mathrm{O/H})$ in the trailing edge ($\Delta\phi > 0$) than the leading edge ($\Delta\phi < 0$), similar with the main results using N2S2-N2H$\alpha$ diagnostic (Fig 3.7). **right**: comparing the CDFs of $\Delta\log(\mathrm{O/H})$ from Scal among the trailing edge, leading edge and spiral arms. The $p$-value from the KS test and AD test are shown in the upper left. We find higher $\Delta\log(\mathrm{O/H})$ in the trailing edge, with a $p$-value of $1.19\times10^{-4}$, suggesting that the metallicity on both sides of the spiral arms are drawn from different distributions.

We take NGC 1566 for an explanation in this section. The left panel of Fig 3.15 shows the fluctuation of metallicity residual $\Delta\log(\mathrm{O/H})$ when crossing the spiral arms, with positive $\Delta\phi$ indicating the trailing edge. We use the same definition of $\Delta\phi$ in the main test, shown in Fig 3.3 and described in Sec 3.3.3. The moving medians of each 20° $\Delta\phi$ are shown as a solid black line, with 25% and 75% quantiles as blue shadows. We repeat the calculation of moving medians to the inner region and outer region, with each region containing half of the spaxels. Similar to the result from N2S2-N2H$\alpha$ (Fig 3.7), we find slightly lower metallicity in the leading edge ($\Delta\phi < 0$) in NGC 1566 using Scal (Fig 3.15). The magnitude of the azimuthal variation and the metallicity scattering from Scal are smaller than those from N2S2-N2H$\alpha$, which is expected (Pilyugin & Grebel 2016; Kreckel et al. 2019).

We further compare the metallicity distributions on both sides of the spiral arms by applying the KS-test and AD-test to their CDFs. Both tests reject that the metallicity distribution in the leading and trailing edges are drawn from the same parental distribution. Although Scal brings in a smaller intrinsic scatter, we obtain a $D$-value of 0.127 from the Scal CDFs, comparable to the $D$-value from N2S2-N2H$\alpha$. We observe azimuthal variation in the metallicity of NGC 1566 in both Scal and N2S2-N2H$\alpha$ diagnostics. The highly similar trend of $\Delta\log(\mathrm{O/H})$ along $\Delta\phi$ suggests the limited impacts of DIG on our TYPHOON data.

Chapter 4

# How Mergers and Flybys Shape Azimuthal Age Patterns in Spiral Galaxies

## *Context and Contribution*

*This chapter has been submitted as* ***How Mergers and Flybys Shape Azimuthal Age Patterns in Spiral Galaxies****, by* ***Qian-Hui Chen, Alex M. Garcia, Zefeng Li, Emily Wisnioski, Kathryn Grasha, Paul Torrey, Rhea-Silvia Remus, Lucas C. Kimmig, Andrew J. Battisti and Sven Buder*** *to Monthly Notices of the Royal Astronomical Society. The work is slightly revised based on the thesis examiners' comments, compared to the submitted version. I have analysed the simulation data. I have written the majority of the paper, with inputs and suggestions from co-authors.*

**Abstract**

Spiral structures are one of the most common features in galaxies, yet their origins and evolution remain debated. Stellar age distributions offer crucial insights into galaxy evolution and star formation, though environmental effects can obscure the intrinsic age patterns. Using the Auriga cosmological gravo-magnetohydrodynamical zoom-in simulations, we investigate the azimuthal age distribution of young stars (< 2 Gyr) in five Milky Way-mass spiral galaxies over the past 5 Gyr. We quantify the age gradients across spiral arms using the mean age offset ($\Delta\tau$) and the non-overlap fraction ($f_{\rm non-overlap}$). We further analyse the impact of mergers and fly-by events on the age gradients. Our results show that the spiral arms in Auriga spiral galaxies generally feature younger stars in their leading edges compared to the trailing edges, with a typical $\Delta\tau$ between 30 and 80 Myr. However, gas-rich interactions can disrupt this age offset, resulting in similar age distributions on each side of the spiral arms. In three snapshots, we observe similar mean ages on both sides of spiral arms but differing age distribution broadness, coinciding with satellite interactions

crossing the host galaxy's disc plane. A comparison with observational studies reveals consistent trends, showing a lack of azimuthal variations in galaxies impacted by mergers or tidal interactions. Our simulation data suggest that the typical azimuthal age variation recovers within ~600 Myr after galaxy interactions. This work highlights the transient role of environmental interactions in shaping spiral arm age patterns.

## 4.1 Introduction

The morphological structures of galaxies provide a direct window into their assembly and evolution histories. Galaxies are broadly classified into three groups based on the Hubble sequence: elliptical galaxies, spiral galaxies, and irregular (Hubble 1926). Large image-based surveys (e.g., Sloan Digital Sky Survey, hereafter SDSS; York et al. 2000) – along with extensive analyses by collaborations such as Galaxy Zoo (Lintott et al. 2011) – have revealed that approximately two-thirds of massive galaxies in the local Universe display spiral structures. Spiral galaxies typically exhibit higher star formation rates (SFRs) than elliptical galaxies, making them the primary hosts of star formation in the local Universe (Martig et al. 2013). At higher redshifts ($0.5 \leq z \leq 4$), Kuhn et al. (2024) find that a quarter of galaxies ($M > 10^{10} M_{\odot}$) already display spiral-like structures. Understanding the origin of spiral arms and their relations to star formation is thus crucial to unravelling how galaxies have evolved from high redshifts to their present-day forms.

Spiral arms are fundamental in organising the distribution and dynamics of gas and stars within galactic discs. Various theories propose differing predictions regarding the effects of spiral arms (Dobbs & Baba 2014; Sellwood & Masters 2022), with the *density wave theory* (Lin & Shu 1966) standing as one of the most well-known frameworks. This theory proposes that long-lived spiral density waves propagate through a galaxy disc, rotating at a constant angular speed. As molecular gas clouds enter density wave potentials, cloud-cloud collisions are triggered, which subsequently enhances SFRs (Silva-Villa & Larsen 2012; Cedrés et al. 2013; Choi et al. 2015). Since material in the disc rotates at decreasing angular velocities with increasing radii, newly formed stars move ahead of the density waves inside the co-rotation radius, where the disc materials and the spiral pattern rotate at the same rate. This differential rotation hypothesis predicts an age gradient across spiral arms, with young stars concentrated near the density waves and progressively older stars found further away (Martínez-García et al. 2009a; Sánchez-Gil et al. 2011; Shabani et al. 2018; Vallée 2022; Martínez-García et al. 2023). Under this framework, the leading edge of a spiral arm is expected to host an intermediate-age stellar population, while the trailing edge of the following spiral pattern harbours the oldest stellar populations.

In contrast, the *dynamic spiral theory* offers a different perspective of stellar distributions

in spiral galaxies (Goldreich & Lynden-Bell 1965; Julian & Toomre 1966). According to this theory, spiral arms are short-lived and transient features that arise from local gravitational instabilities (Marchuk & Sotnikova 2018). Galactic shear stretches and disrupts the spiral arms locally, while self-gravity works to hold the segments together. This tug-of-war between shear and self-gravity causes the arms to fragment into structures that are a few kpc in size, which then reconnect to form larger-scale patterns (Fujii et al. 2011; Benhaiem et al. 2019). Unlike the density wave theory, the dynamic spiral theory posits that gas flows into the potential wells of the spiral arms from both sides, resulting in no differential rotation between the spiral arms and the surrounding disc material. Consequently, the dynamic spiral theory does not predict a systematic age gradient across the spiral arms.

Both the density wave theory and dynamic spiral theory effectively explain the formation of spiral structures in isolated galaxies, as supported by observations and simulations (Fujii et al. 2011; Grand et al. 2012a; Baba et al. 2013; D'Onghia et al. 2013; Khrapov et al. 2021). However, spiral structures are not exclusive to isolated galaxies and can also arise due to galaxy interactions, leading to the formation of tidally induced spiral arms. When a satellite galaxy passes by, tidal forces can create a bridge-and-tail structure that subsequently evolves into grand-design spiral patterns in the host galaxy. These tidal-driven spiral arms have been observed in the local Universe (Darg et al. 2010; Di Teodoro & Fraternali 2014), at $z \sim 0.3$ (e.g., G12-J120759 in Foster et al. 2021) and near cosmic noon ($1 < z < 3$; Law et al. 2012; Margalef-Bentabol et al. 2022) in galaxies undergoing minor or major mergers. Tidal-induced spiral arms can be distinguished from those formed by density wave or dynamic spiral theories through the presence of a companion galaxy (Semczuk et al. 2017; Antoja et al. 2022). Furthermore, bridge and tail structures associated with tidal interactions exhibit distinct kinematic properties, which differ from the predictions of both density wave and dynamic spiral theories (Pettitt et al. 2016, 2017).

Measuring azimuthal variations in stellar age and the interstellar medium (ISM) provides a straightforward approach to studying the influence of spiral arms on star formation propagation, though it comes with significant challenges. Some observational studies, e.g., Tamburro et al. (2008) and Egusa et al. (2009), have reported spatial offsets between ionized and molecular gas, consistent with density wave theory. Similarly, azimuthal offsets are found in stellar age (Sánchez-Gil et al., 2011 and Shabani et al.2018). In contrast, other studies (Scheepmaker et al. 2009; Kaleida & Scowen 2010; Shabani et al. 2018) report no systematic trend of age gradients across spiral arms, and Foyle et al. (2011) found no consistent azimuthal offsets between different tracers in 12 nearby spiral galaxies. More recently, Chen et al. (2024b) examined two spiral galaxies at $z \sim 0.3$ and

found no offset in $D_{4000}$, an age proxy measured from the spectral continuum, between the leading and trailing edges of the arms across various radii. Chen et al. (2024b) suggest that the $D_{4000}$, with a sensitivity timescale of 1 Gyr, is not suitable for testing density wave theory since 1 Gyr is long enough to allow stars to travel between two spiral arms. Overall, while numerous studies have explored age gradients in nearby galaxies, the conflicting results suggest that no single theory can fully explain the formation and evolution of all spiral features in the local Universe.

Spiral arms are not solely responsible for the azimuthal distributions observed in galaxies. Gas and stellar migration also contribute significantly to shaping these variations. For instance, Sánchez-Menguiano et al. (2016) directly measure streaming motion in NGC 6754, revealing metal-rich gas moving outward along the trailing edge of the spiral arms, which induces azimuthal variations in metallicity. Additionally, environmental effects – accretion of gas and stars from fly-by satellites and/or mini-mergers – can perturb the gravitational potential of the disc, redistributing gas and stars both radially and azimuthally without destroying the spiral structures (Block et al. 2002; Fraternali & Binney 2008; Eliche-Moral et al. 2011).

Measuring the radial migrations (Roškar et al. 2012; Sánchez-Menguiano et al. 2016; Ruiz-Lara et al. 2017), classifying fly-by satellites (van Dokkum et al. 2023; Zaritsky et al. 2023), and identifying past merging events in galaxies (George et al. 2018; Ristea et al. 2022; Kelkar et al. 2023) remain a significant observational challenge. Simulations provide a complementary avenue to address these limitations, with many successfully reproduced spiral structures (Sellwood 2011; Fujii et al. 2011; Grand et al. 2012a; D'Onghia et al. 2013; Grand et al. 2014). Several studies on simulations (e.g., Baba et al. 2013; Grand et al. 2016) find large-scale radial migrations in star particles driven by spiral arms in isolated disk galaxies. Using the FIRE-2 hydrodynamic simulation model, Orr et al. (2023) further demonstrate that spiral arms act as highways for radial migration of gas and metals. Khoperskov et al. (2018) on the other hand conclude from $N$-body simulations that vertical metallicity gradients may play a more important role in shaping the azimuthal variations in stellar metallicities compared with radial gradients. Simulations offer comprehensive insights into a host galaxy's environment by constructing merger trees using subhaloes (Tweed et al. 2009; Robles et al. 2022). These allow us to track the timing of merger events, the trajectories of fly-by satellites, and the properties of companions, such as their gas masses ($M_{\rm gas}$). This environmental context allows the comparison of spiral galaxies across diverse environments, as well as within a single galaxy before and after a merger event. For one example, Pettitt et al. (2017) simulate a multi-arm spiral galaxy that evolves into a two-arm spiral galaxy 400 Myr after introducing a perturbation by a companion satellite. Their study highlights distinct behaviours in the bridge and tail, focusing on the

spatial offset between gas and stellar arms, an outcome misaligned with predictions from both density wave theory and dynamic spiral theory.

The connection between spiral features and the azimuthal distribution of gas and stars remains a topic of debate, with one of the least explored questions being the long-term evolution of these distributions in spiral galaxies. The motivation of this work is to investigate the long-term fluctuations of azimuthal variation in stellar age using the Auriga simulations. Building on the work of Grand et al. (2016), we use a higher mass resolution dataset spanning a longer period. We specifically focus on the role of environmental effects, such as mergers and fly-bys, in driving changes to azimuthal variations. We begin by introducing the Auriga simulations (Sec. 4.2.1) and our method to define the spiral arms in each snapshot (Sec. 4.2.2). We quantify the azimuthal variation at each snapshot (Sec. 4.3.1), as well as explore the environment of the host galaxy from merger tree data (Sec. 4.3.2). In Sec. 4.4, we discuss the connection between fluctuation in age gradient across spiral arms and potential ongoing mergers and fly-bys and compare our findings with observational results from the literature. In Sec. 4.5, we summarise our conclusions of this work. This work assumes a Hubble constant of $H_0 = 100\ h$ km s$^{-1}$ Mpc$^{-1}$, where $h = 0.6777$, and adopts cosmological parameters of $\Omega_\mathrm{m} = 0.307, \Omega_\mathrm{b} = 0.048, \Omega_\Lambda = 0.693$ (Planck Collaboration et al. 2014).

## 4.2 Methods

### 4.2.1 Auriga simulations

#### Auriga Level 3 dataset

In this work, we use data products from the Auriga cosmological zoom-in simulations (Grand et al. 2017). Auriga is a follow-up to the "Aquarius" project of zoom-in simulations (Marinacci et al. 2014) and is run on the moving mesh magneto-hydrodynamics code AREPO (Springel 2005; Pakmor et al. 2016). The complete Auriga suite is comprised of several haloes selected from the "Evolution and Assembly of GaLaxies in their Environment" (EAGLE; Schaye et al. 2015) parent $(67.8\ \mathrm{Mpc}/h)^3$ volume[1]. These haloes were selected to be approximately Milky Way mass – $1\times10^{12}\mathrm{M}_\odot < M_{200} < 2\times10^{12}\mathrm{M}_\odot$ – at $z = 0$ as well as similar in their environments, which are relatively isolated at $z = 0$ (for computational reasons). Once these targets were selected, particles within the radius of $4R_{200}$ (where $R_{200}$ is the radius at which the mean enclosed mass volume density becomes 200 times

[1]We note that the original EAGLE simulation was run using a heavily modified version of GADGET-3 called ANARCHY (see Schaye et al. 2015). The resimulation of the Auriga haloes, however, was done in AREPO (see Grand et al. 2017, for complete details on this process).

the critical density) were resimulated at higher resolution using the method outlined in Jenkins (2010).

The Auriga galaxy evolutionary model builds upon the Illustris model (Vogelsberger et al. 2014a,b; Genel et al. 2014; Torrey et al. 2014) and implements a wide range of (astro-)physical processes including, but not limited to: gravity, star formation, stellar feedback, magnetic fields, chemical enrichment, as well as black hole growth and feedback. Briefly, the ISM's behaviour is described by the Springel & Hernquist (2003) effective equation of state. This (and, indeed, all) equation(s) of state provide a physically motivated prescription for the dense, unresolved ISM. In the Springel & Hernquist (2003) model, new star particles form stochastically beyond a threshold density of $n_{\rm H} \geq 0.13$ cm$^{-3}$. The star particles are treated as a single stellar population drawn from a Chabrier (2003) initial mass function and adopt the metallicity from the gas in which they form. As they evolve, star particles return their mass and metals to the ISM via asymptotic giant branch winds as well as type Ia and II supernovae, with the metal yields from these events taken from Karakas (2010), Thielemann et al. (2003), and Portinari et al. (1998), respectively.

Our analyses are carried out on the public data release of Auriga[2] (Grand et al. 2024). The data release of the Auriga simulations contains several haloes simulated at two different resolution levels: "level 4" (L4) with baryon mass resolution of $5 \times 10^4$ M$_\odot$ and temporal resolution of ∼160 Myr; and "level 3" (L3) with baryon mass resolution of $6 \times 10^3$ M$_\odot$ and temporal resolution of ∼300 Myr. Table 4.1 summarises all L3 haloes from the "original" sample in the public data release (we refer the reader to Table 2 of Grand et al. 2024 for the complete details of 30 haloes in Auriga simulations). This work is carried out on the L3 dataset since the higher mass resolution allows us to study the stellar populations in the interarm regions with higher fidelity and obtain a more accurate definition of the spiral arms. Appendix 4.6 provides a detailed comparison between spiral structures at L3 and L4 resolutions. The public L3 dataset includes six halos: Halo 6, 16, 21, 23, 24, and 27.

To visualise the particle data, we rotate the galaxy face-on by calculating the unit vectors of angular momentum of star particles within $0.1R_{200}$ of the main halo. We rotate the galaxy such that this angular momentum vector points in the $+\hat{z}$ direction to construct face-on images of galaxies. Our analysis only involves star particles in the main halo disc within a box size of $20 \times 20 \times 5$ kpc$^3$, excluding halo stars (Li et al. 2024). Furthermore, we limit the $z$-direction velocity to within ±20 km/s, removing halo stars that may transiently appear on the disc plane during specific snapshots. To create "images" of the system, we first map the discrete particle distributions of Auriga onto a 3D grid using a traditional smoothing method with a cubic spline kernel. We convert this 3D grid into a 2D projection

[2]https://wwwmpa.mpa-garching.mpg.de/auriga/data.html.

| (1) Halo | (2) $\log(M_{200}/M_\odot)$ | (3) $R_{200}$ (kpc) | (4) $\log(M_*/M_\odot)$ | (5) Morphology |
|---|---|---|---|---|
| 6 | 12.006 | 211.834 | 10.806 | Barred |
| 16 | 12.177 | 241.530 | 10.959 | Large disc, barred |
| 21 | 12.151 | 246.688 | 10.944 | Unbarred |
| 23 | 12.177 | 241.501 | 10.954 | Large disc, barred |
| 24 | 12.167 | 239.568 | 10.939 | Large disc, unbarred |
| 27 | 12.230 | 251.400 | 10.995 | Large disc, barred |

**Table 4.1:** Summary information of six haloes in the Original Milky Way-mass Auriga L3 simulations. The columns list: (1) the halo name; (2) the total mass inside $R_{200}$; (3) $R_{200}$ is the radius at which the density becomes 200 times the critical density; (4) the stellar mass of the central galaxy; (5) a summary of the morphology of each halo.

by integrating over the $\hat{z}$ direction (as defined by the angular momentum vector, see above) on a $300 \times 300$ pixel grid in the $xy$ plane. Following this method, we construct the young star mass map in Sec.4.2.2 and the mass-weighted age map in Sec.4.3.1.

#### Merger Trees

Gravitationally-bound structures in the Auriga simulations are identified using SUBFIND (Springel et al. 2001), a friends-of-friends nearest neighbour algorithm (Davis et al. 1985). Merger trees are built on top of the SUBFIND haloes using the procedure outlined in Springel, Di Matteo, & Hernquist (2005). These merger trees identify structures across different snapshots and enable direct tracking of galaxies over cosmic time. The merger tree properties are also a part of the Auriga public data release. We refer the reader to Grand et al. (2024) for complete details regarding the implementation and structure of merger trees.

### 4.2.2 Classification of spiral arms, leading and trailing edge

We design an automated algorithm, named *"ridgeline walking"*[3], to identify the spiral arms in the Auriga L3 data. Our algorithm aims to identify all pixels on the spiral arm ridge lines. Although analytic spiral arms can be expressed as a formula (Ho et al. 2017; Chen et al. 2024a):

$$r(\phi) = r_0 e^{\tan\theta_{\rm p}(\phi-\phi_0)}, \tag{4.1}$$

the ridgeline walking algorithm does not parameterise the spiral arms, as the spiral arms may not follow the analytic formula (Eq. 4.1) during interaction/merger events (e.g., 2.97 Gyr snapshot in Fig. 4.16). Since spiral arms are regions with concentrations of young stars, we identify the spiral arms by searching for the mass peaks in the young star

[3]This algorithm is available on GitHub https://github.com/Qian-HuiChen/ridgeline_walking.

mass ($M_{\rm young}$; age < 2 Gyr) maps, e.g., Halo 23 at $z = 0$ in Fig. 4.1. The algorithm is carried out in four steps (Fig. 4.2 and Fig. 4.3):

- Firstly, we convert the face-on young star mass map to a phase diagram (azimuth versus distance; Fig. 4.2). To increase the contrast between spiral arms and inter-arms, we subtract the $M_{\rm young}$ by the radial gradient, represented by a moving mean value in every 3 pixels (0.4 kpc). Fig. 4.2 is colour-coded by the $M_{\rm young}$ residuals, where the spiral arms are highlighted as positive values.
- Now, we locate the brightest pixel ($\phi_0$, $R_0$) within 9 kpc < $R$ < 11 kpc on the phase diagram, which works as the starting anchor for the ridgeline walking. We apply the SCIPY.SIGNAL.FIND_PEAKS module [4] on a small region of the phase diagram, $\phi_0$ to $\phi_0 + 2^\circ$ and $R_0 \pm 2$ kpc, to detect a localised peak ($\phi_1$, $R_1$). The algorithm extends the ridgeline to this new point ($\phi_1$, $R_1$) and detects the next localised peak within the region of $\phi_1$ to $\phi_1 + 2^\circ$ and $R_1 \pm 2$ kpc. By continuously extending the ridgeline from $\phi_0$ to 360° and then from 0° to 360°, the algorithm classifies the inner ridgeline of the brightest spiral arm.
- To identify the outer ridgeline of the brightest spiral arm, the algorithm returns to the starting anchor ($\phi_0$, $R_0$). Peak detection is operated in a new region of $\phi_0 - 2^\circ$ to $\phi_0$ and $R_0 \pm 2$ kpc, and continues in the direction of decreasing $\phi$. The algorithm completes the outer ridgeline of the brightness spiral arm by walking from $\phi_0$ to 0° and then from 360° to 0°.
- The previous process identifies pixels on the brightest spiral arm and any connected spiral arms. To locate spiral arms that are not connected to the brightest one, we mask out the spiral pixels identified in steps (ii) through (iii), spanning 2 kpc along the $y$-axis and 10° along the $x$-axis on the phase diagram. The algorithm then repeats steps (ii) and (iii) and ultimately returns pixels on all spiral arm ridgelines.

An example of the outcome of the ridgeline walking algorithm is shown as purple lines in the right panel of Fig. 4.1 (Halo 23 at snapshot $z = 0$) and Fig. 4.2.

The main science goal of this work is to study the impact of environmental interactions on azimuthal variations in stellar age. It is necessary to quantitatively separate the disc region into the leading and trailing edges, after identifying the spiral arm pixels. Following Chen et al. (2024b), we measure the parameter $\Delta\phi$, i.e., azimuthal distance to the nearest spiral arm at the same galactocentric distance. Given a pixel $T$,

$$|\Delta\phi_T| = \min(|\phi_T - \phi_{arm1}|, |\phi_T - \phi_{arm2}|, ..., |\phi_T - \phi_{armN}|), \tag{4.2}$$

[4]The detection threshold for peak detection is set to half of the median value of all points in the phase diagram. If the first signal detection fails, the algorithm will attempt a second threshold, set to half of the 25th percentile of all values in the phase diagram.

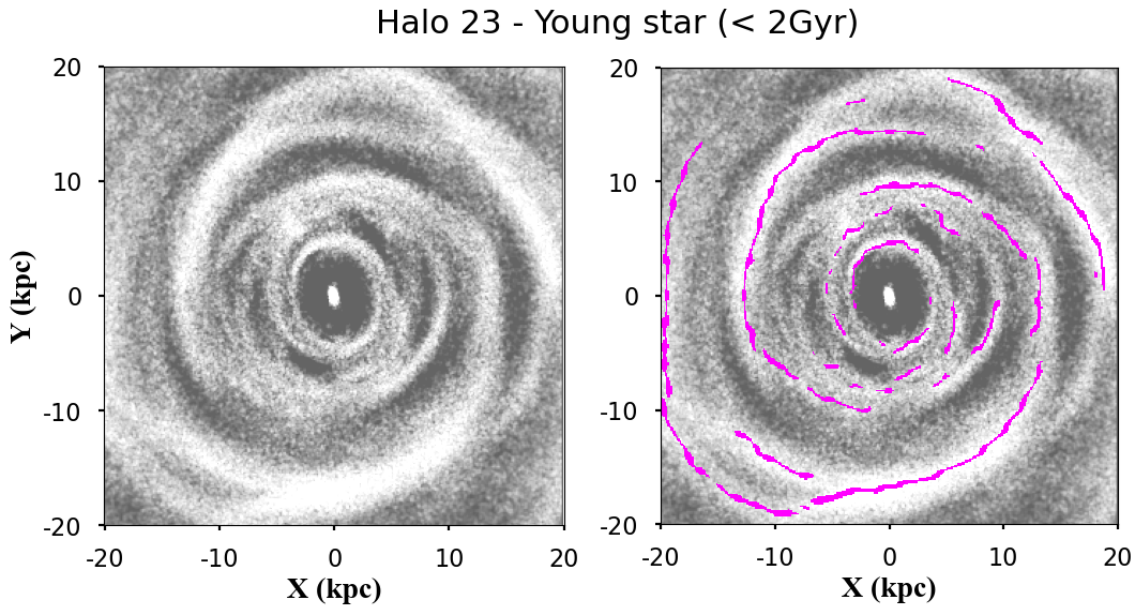


**Figure 4.1:** Young star (age < 2 Gyr) mass map of Halo 23 at $z = 0$. The spiral arms identified by the algorithm (Sec. 4.2.2) are presented as purple pixels in the right panel.

where pixel $arm1$, $arm2$, ..., and $armN$ are on the spiral arm ridgelines and at the same galactocentric distance as pixel $T$. We assign a positive (negative) $\Delta\phi$ when the targeted pixel is on the trailing (leading) edge of the nearest spiral arm. We perform the spiral arm identification algorithm, followed by the $\Delta\phi$ measurement, to snapshots from $z = 0$ back to $z = 0.46$ (lookback time of 5 Gyr) when the disc became stable and spiral arms became prominent. We find that in Halo 6, the spiral features are tightly wound, nearly ring-like and not prominent in the disc (Fig. 4.13). Consequently, we focus our analysis on the other five L3 halos and exclude Halo 6. Appendix 4.8 presents the young star maps of all our samples over the past 5 Gyr, overlaid with the defined spiral arms.

We note that there are various other methods by which spiral arms are identified in simulations and observations. Some observational work (Ho et al. 2018; Querejeta et al. 2021) identify spiral arms by visual inspection on images or phase diagrams. Other studies first select the main spiral arm regions by eye and then fit the areas with the analytic formula (Eq. 4.1). The large number of snapshots in our sample, however, makes it impractical to classify the spiral arms manually, necessitating an automatic identification procedure. Davis & Hayes (2014) developed an automated detection of spiral arm segments based on over 600,000 objects in the SDSS – SpArcFiRe. This algorithm is successfully applied to two spiral galaxies at $z \sim 0.3$ (Chen et al. 2024b). However, designed for observation images, SpArcFiRe does not perform well on the Auriga-simulated galaxy images, potentially due to the absence of observational effects such as the point spread function.

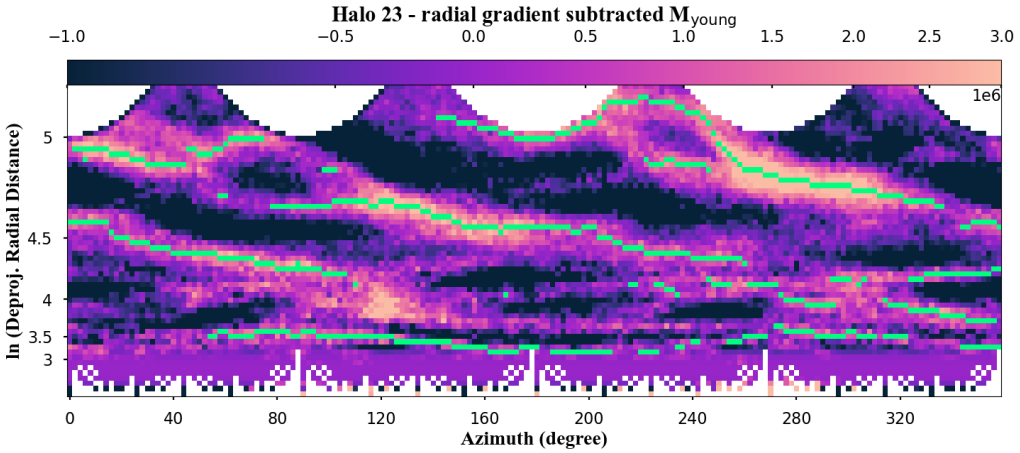


**Figure 4.2:** Phase diagram of Halo 23 at $z = 0$, colour-code by the young star (< 2 Gyr) mass after subtracting the radial gradient. We use the moving average of each 3-pixel bin to represent the radial gradient. The x-axis is the azimuth while the y-axis is the radial distance to the galaxy centre after taking the natural logarithm. An ideal spiral arm following Eq. 4.1 is a straight line in the phase diagram. We use an automatic algorithm, ridgeline walking, to identify pixels on the spiral arms, shown as green lines.

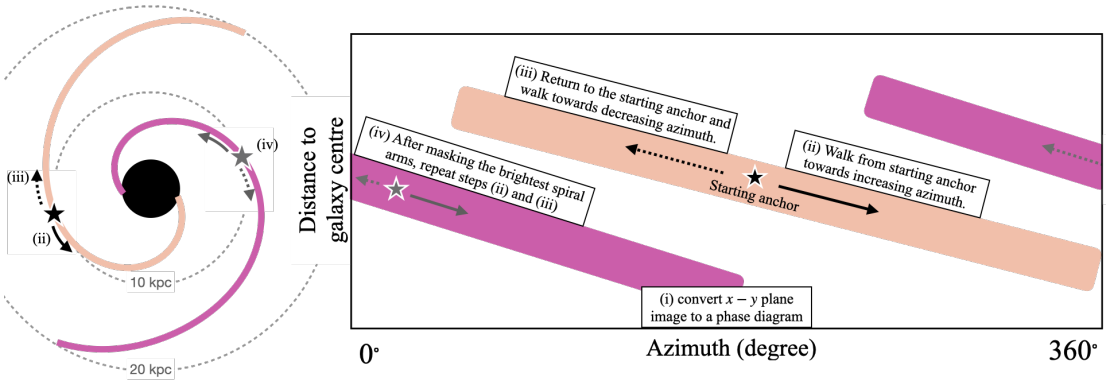


**Figure 4.3:** This schematic illustrates the four-step process of the ridgeline walking algorithm used to automatically identify spiral arms. The algorithm locates spiral arms on an azimuth − radial distance diagram, where colour represents the young star mass after subtracting the radial gradient. The starting anchor, marked by a black star symbol, is set at the brightest pixel in the middle radius (10kpc ± 1kpc). From this anchor, the algorithm searches for the next localized maximum and moves toward increasing azimuth, then returns to the anchor to walk towards decreasing azimuth, outlining the brightest spiral arm pixels. After masking out the brightest spiral arm, the algorithm repeats this process to identify the second brightest spiral arm. Appendix 4.8 presents the young star maps for all five halos over the past 5Gyr, with spiral arm definitions overlaid (red lines).

Another software by Forgan et al. (2018) classifies the spiral structures in a protostellar disc in hydrodynamic simulations. The tensor classification in Forgan et al. (2018) is designed to operate on smooth continuous fields. However, the spiral arms are disrupted and do not follow the analytic formula during environmental interactions. Since one of our science goals is to compare the spiral galaxies before and after interactions with satellites, we do not adopt the algorithm from Forgan et al. (2018) in this work.

## 4.3 Analysis and results

### 4.3.1 Quantifying the azimuthal variation in stellar age

Generally, the distribution of young stars is expected to exhibit a closer association with spiral arms, whereas older stars tend to be more diffusely spread across the disc (Grasha et al. 2017). To highlight the impact of spiral arms on stellar age, the following analysis focuses exclusively on young stars (< 2 Gyr) in each snapshot. In observed galaxies, stellar age varies in both radial and azimuthal directions simultaneously, with the radial gradient (Parikh et al. 2021) generally being more prominent than the azimuthal variation (Shabani et al. 2018). To remove the radial trend of the stellar age, we subtract the average age of a moving 3-pixel (0.4 kpc) wide ring from the stellar age. We denote the age residual as Δage. Fig. 4.4 compares the Δage in the leading edge ($\Delta\phi < 0°$) and the trailing edge ($\Delta\phi > 0°$) of the spiral arms in Halo 23 at $z = 0$. We present the moving medians of Δage of each 20° as a silver solid line in Fig. 4.4. We find lower Δage in the leading edge ($\Delta\phi < 0°$), indicating more young stars in the leading edge than the trailing edge. The younger leading edge is consistent with observations in the local Universe (e.g., NGC 1566 in Shabani et al. 2018) and also aligns with the prediction of density wave theory, within the co-rotation radius.

We quantify the age gradient across spiral arms at each snapshot. This analysis allows us to trace azimuthal variations over cosmic time, especially before and after mergers. We focus on star particles near the spiral arms ($|\Delta\phi| < 25°$), where the spiral arms' influence is expected to be the primary factor (shown as coloured data in Fig. 4.4). Fig. 4.5 shows the distribution of Δage in the trailing (purple; $0° < \Delta\phi < 25°$) and leading edge (orange; $-25° < \Delta\phi < 0°$). We fit these histograms with Gaussian distributions separately. The azimuthal variations are quantified at each snapshot using two parameters: $\Delta\tau$ and $f_{\mathrm{non-overlap}}$. The first parameter, $\Delta\tau$, is defined as the difference between the average ages of the two Gaussian distributions,

$$\Delta\tau = |\overline{\Delta\mathrm{age}}_{\mathrm{trailing}} - \overline{\Delta\mathrm{age}}_{\mathrm{leading}}|. \tag{4.3}$$

The second parameter, $f_{\rm non-overlap}$, is the non-overlap fraction between the two Gaussian distributions, calculated as

$$f_{\rm non-overlap} = \begin{cases} (1 - \frac{\text{overlap area}}{\text{total area}}) \times 100\%, & \overline{\Delta\text{age}}_{\rm trailing} < \overline{\Delta\text{age}}_{\rm leading} \\ -(1 - \frac{\text{overlap area}}{\text{total area}}) \times 100\%, & \overline{\Delta\text{age}}_{\rm trailing} > \overline{\Delta\text{age}}_{\rm leading} \end{cases} \tag{4.4}$$

We assign a negative $f_{\rm non-overlap}$ when the leading edge has a younger average $\Delta$age ($\Delta\tau > 0$), otherwise, a positive $f_{\rm non-overlap}$ is assigned.

In terms of the relative relations of $\Delta\tau$ and $f_{\rm non-overlap}$, we identify the following three cases in Auriga L3 simulations.

- Case I: A significant age gradient across the spiral arms is expected to result in a large magnitude of $|f_{\rm non-overlap}|$ and $|\Delta\tau|$ in a given snapshot.
- Case II: A low magnitude of $|f_{\rm non-overlap}|$ with $|\Delta\tau|$ close to zero indicates no or little age azimuthal variation in the galaxy.
- Case III: A notable case is that a large $|f_{\rm non-overlap}|$ is observed but along with $|\Delta\tau|$ close to zero. In this case, the average $\Delta$age remains similar for both populations, but the different broadness is responsible for the large $|f_{\rm non-overlap}|$ (no matter what sign it has).

Together, $\Delta\tau$ and $f_{\rm non-overlap}$ robustly quantify the azimuthal age variations at each redshift. We will discuss our findings of azimuthal age azimuthal in detail in Sec. 4.3.3.

### 4.3.2 Merging and interaction time

Mergers and interactions can impact the azimuthal distribution of stars and gas in spiral galaxies, which may even induce or reshape the spiral arms (Villalobos & Helmi 2008). In this section, we introduce our determination of merging events and fly-by companions by analysing the merger trees (see Sec. 4.2.1 and Grand et al. 2024).

We track the stellar mass ($M_*$) of the main halo over the past 6 Gyr with solid lines and its gas mass with dotted lines in the left upper panel of Fig. 4.6, Fig. 4.7, Fig. 4.8, Fig. 4.9 and Fig. 4.10. We also show the mass of all satellites within $R_{200}$ and with a stellar mass over 1% of the main halo. The bottom sub-panels demonstrate the distance from the satellites to the main halo ($D_{\rm sat}$). When a subhalo is approaching the main halo (i.e., $D_{\rm sat}$ is decreasing) and finally disappears at a snapshot, we determine that the merger happens at that snapshot, as highlighted by the dashed vertical lines. The $D_{\rm sat}$ is essential to distinguish merged satellites from those that move outside $R_{200}$, which shows an increasing $D_{\rm sat}$. We can also identify fly-by events, when a satellite approaches and moves away from the main halo, based on the U-shape in $D_{\rm sat}$.

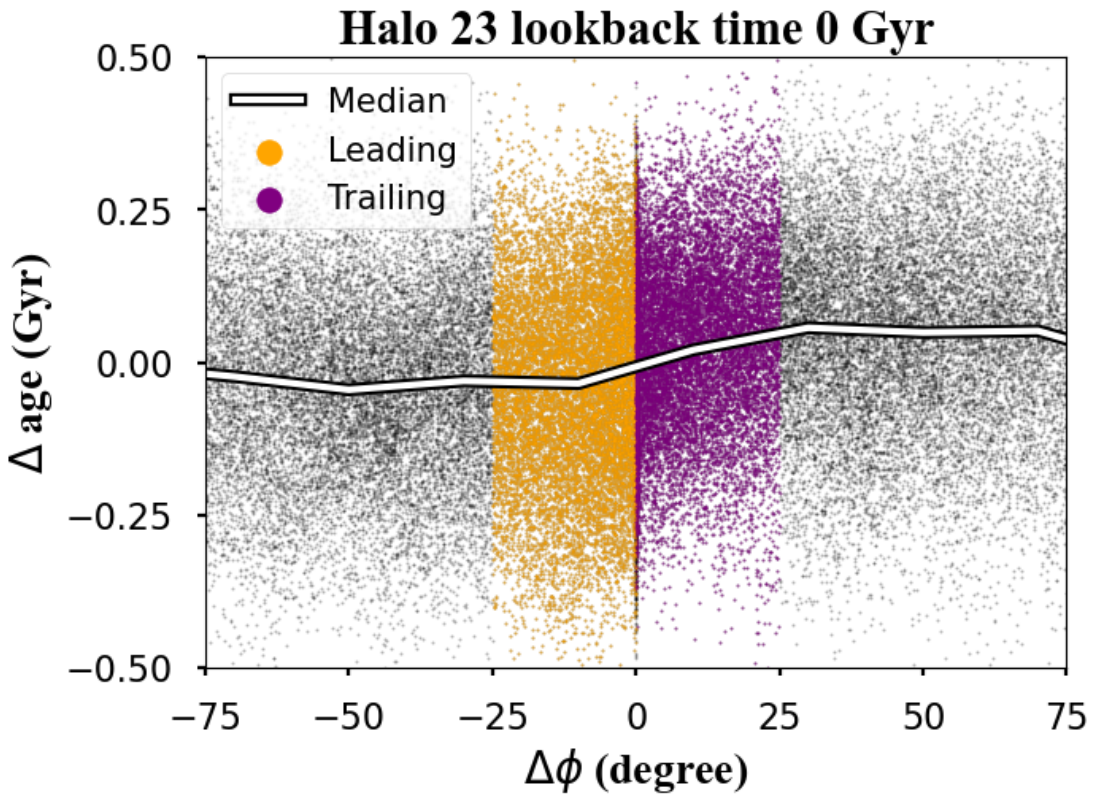


**Figure 4.4:** The parameter Δage (stellar age with the radial gradient subtracted) varies with the azimuthal distance $\Delta\phi$ to the spiral arms. Spaxels on the leading (trailing) edge are assigned with negative (positive) $\Delta\phi$. The region $-25^\circ < \Delta\phi < 25^\circ$ is highlighted, where the influence of the spiral arms on the age pattern is most significant. Only the coloured pixels within this range are used to quantify azimuthal variations at each snapshot (Fig. 4.5). The solid white line represents the median value within each moving 20° bin.

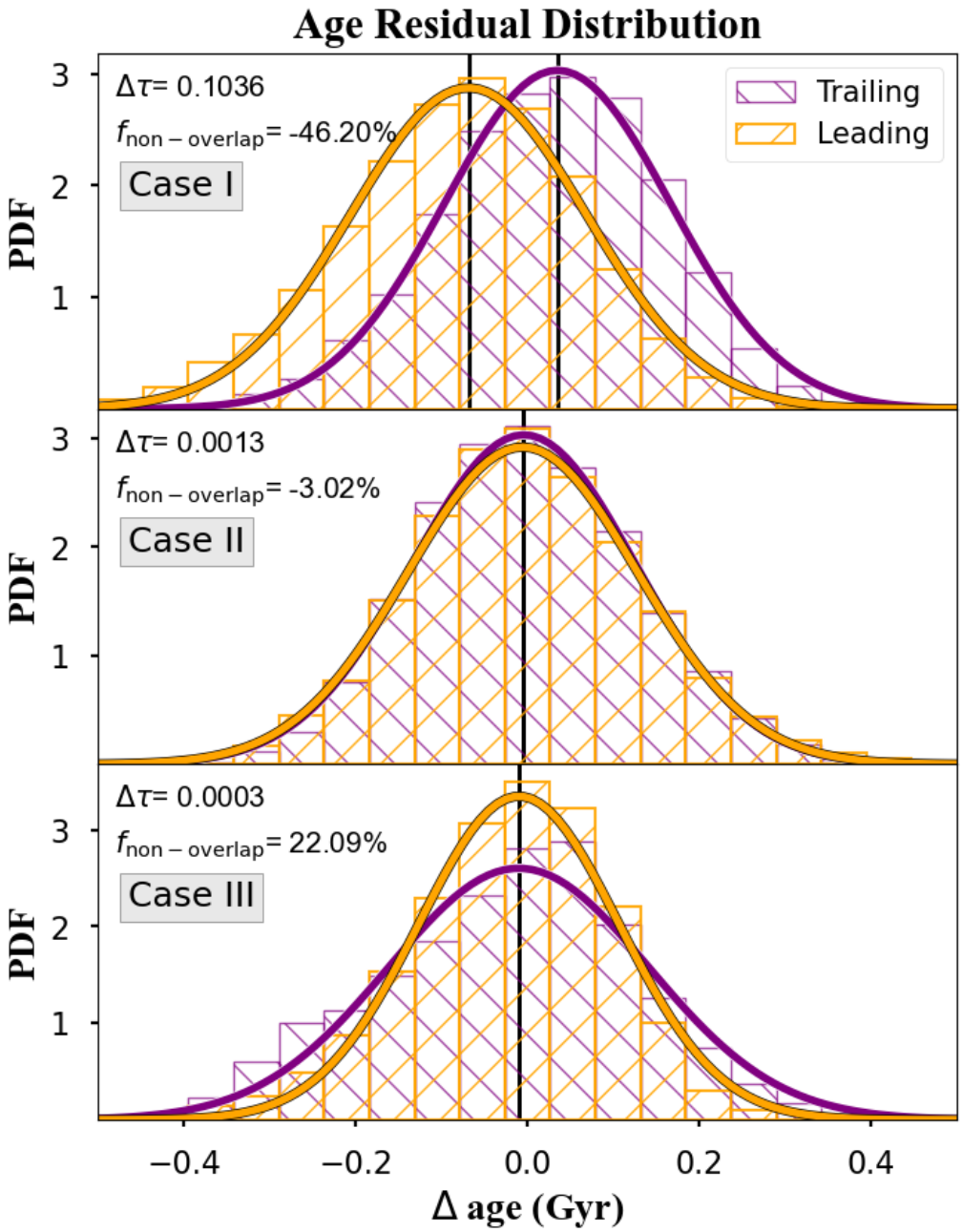


**Figure 4.5:** Three cases of Δage distributions at the leading and trailing edges. **Case I**: The $f_{\text{non-overlap}}$ is large with a significant $\Delta\tau$, indicating an evident age gradient across the spiral arms. **Case II**: Both $f_{\text{non-overlap}}$ and $\Delta\tau$ are small, suggesting little to no azimuthal age variation. **Case III**: The $f_{\text{non-overlap}}$ is large, but the $\Delta\tau$ is near zero, indicating distinct age distributions on each side of the spiral arms, with the difference mainly laying in the tail of the distribution.

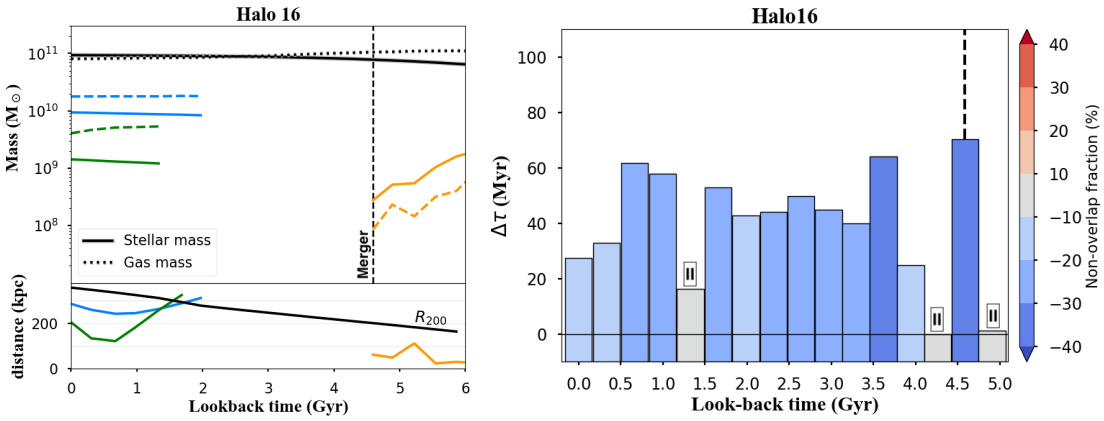


**Figure 4.6: Left:** Stellar mass (solid lines) and gas mass (dashed lines) of the main halo (black lines) and the nearby satellites (blue/green/orange/brown lines, if they exist) from the lookback time of 6 Gyr. We only present satellites within $R_{200}$ of the main haloes and with a stellar mass larger than 1% of the main halo. Dashed vertical lines indicate merging events. The bottom panel presents the distance between the main halo and the satellites, with their corresponding colours. **Right:** The evolution of $f_{\rm non-overlap}$ and $\Delta\tau$ over the past 5 Gyr, with merger events marked by dashed vertical lines. The histogram is colour-coded by $f_{\rm non-overlap}$ for better comparison with Fig4.11, and the bar height represents $\Delta\tau$. Values of $\Delta\tau$ between $-10$ and 0 Myr are shown at all times solely for visualisation, allowing the colour of small (near zero) $\Delta\tau$ to be seen. The snapshots aligning with case II and case III are highlighted with a II symbol or III symbol on the top. Most snapshots exhibit a negative $f_{\rm non-overlap}$ and a large $\Delta\tau$ (case I), indicating a younger leading edge compared to the trailing edge, a trend consistent across our entire sample. We identify a fly-by satellite (green line on the left) approaching Halo 16 around 1 Gyr ago, coinciding with a case II snapshot 1.33 Gyr ago. A satellite (orange line in the left) merged into Halo 16 at a lookback time of ~4.5 Gyr, along with two case II snapshots observed around the merging time.

Halo 23 and Halo 27 live in relatively quiet environments, with only two companions within $R_{200}$ over the past 5 Gyr. Halo 16, 21, and 24, however, have encountered three or more sub-haloes within their $R_{200}$. We find that most galaxies in our sample (except for Halo 21) experienced mergers over the past 5 Gyr, with stellar mass ratios between the merging galaxy and the main halo of $\sim 1:10$ to $1:100$, classified as minor and mini-mergers, respectively (Remus & Forbes 2022; Bottrell et al. 2024). We notice that $M_{\rm gas}$ decreases along with $M_*$ before merging, reflecting that the satellite's gas is being stripped by the main halo. Fly-by events are also detected in all galaxies (except Halo 23), with stellar mass ratios in a similar range of $\sim 1:10$ to $1:100$. We will discuss the influences from both merger and fly-by events on the azimuthal variations in Sec. 4.4.

### 4.3.3 Age patterns before and after merging

We apply the analyses of measuring age offset (Sec. 4.3.1) and merging time (Sec. 4.3.2) to snapshots from $z = 0$ back to $z = 0.46$ (lookback time of 5 Gyr), covering snapshots 63

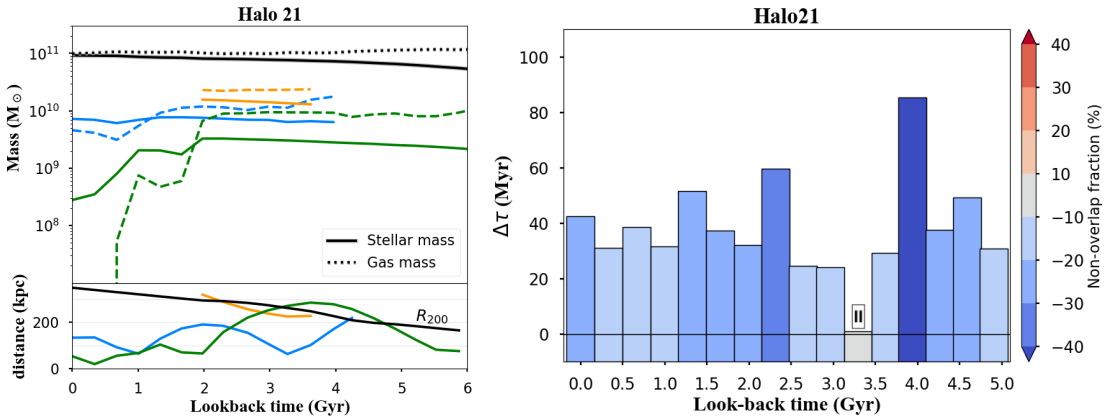


**Figure 4.7:** Same as Fig. 4.6 but for Halo 21. We observe one case II snapshot at a lookback time of 3.3 Gyr, coinciding with a fly-by satellite (blue line in the left panel).

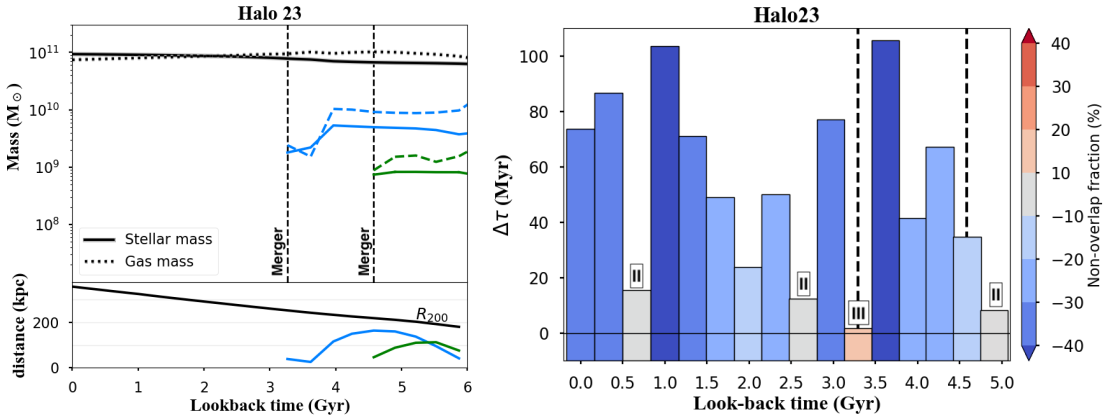


**Figure 4.8:** Same as Fig. 4.6 but for Halo 23. We observe a case II snapshot ∼ 5 Gyr ago, with a satellite (green line in the left panel) merging in ∼ 300 Myr. At around 3 Gyr ago, a case II snapshot and a case III snapshot are observed, coinciding with a merging event (blue line in the left panel). We find a case II snapshot at ∼0.6Gyr ago, with no sign of any satellite over 1% stellar mass of Halo 23 within $R_{200}$.

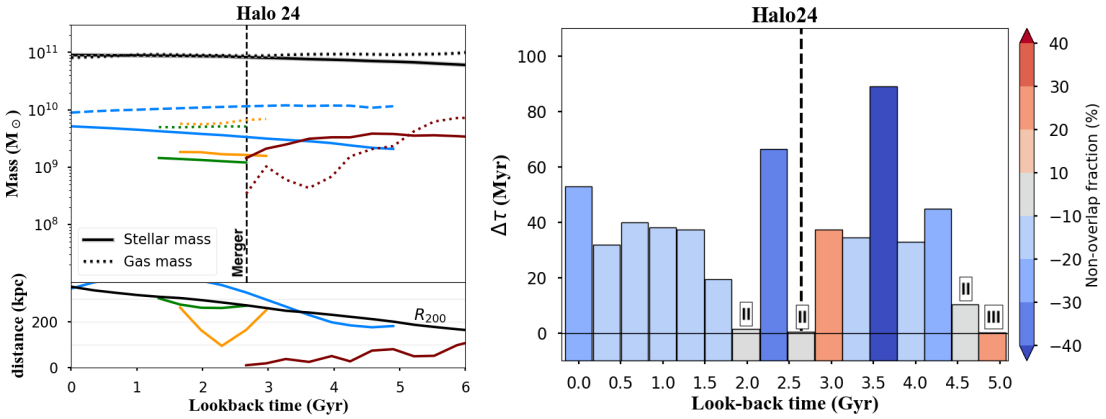


**Figure 4.9:** Same as Fig. 4.6 but for Halo 24. Around 5 Gyr, we find one case II snapshot and one case III snapshot, when the gas of a satellite (dark red line in the left panel) got stripped into Halo 24. When this satellite merged in, a case II snapshot is found at a lookback time of ~ 2.6 Gyr. Another case II snapshot is identified at a lookback time of 2 Gyr, with a fly-by event happening (orange line in the left panel).

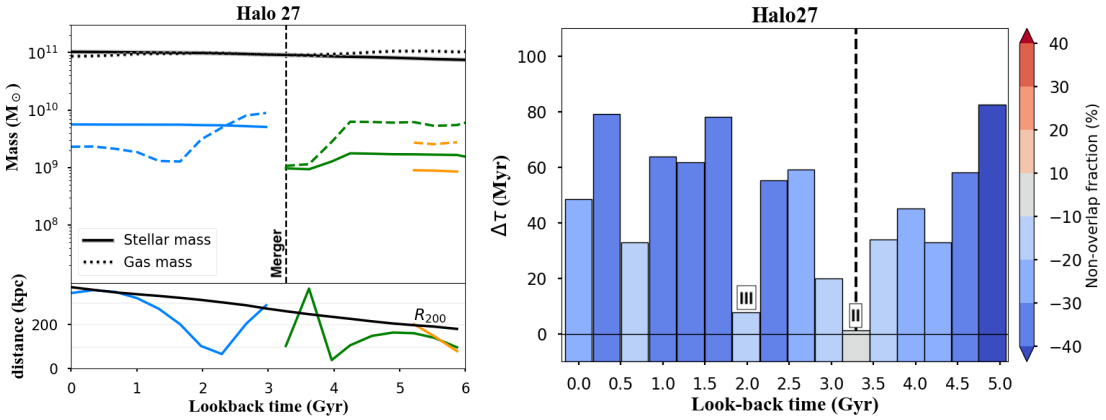


**Figure 4.10:** Same as Fig. 4.6 but for Halo 27. Around 3.3 Gyr, we find a case II snapshot, when a satellite (green line in the left panel) merged into Halo 27. A case III snapshot is found at a lookback time of ~ 2 Gyr with a fly-by event happening (blue line in the left panel).

to 48, respectively. The right panel of Fig. 4.6, Fig. 4.7, Fig. 4.8, Fig. 4.9 and Fig. 4.10 presents the age azimuthal variation over the past 5 Gyr of all haloes, with the dashed vertical lines indicating the timing of merger events. To quantify the significance of the non-overlap fractions, we draw random samples of two identical Gaussian distributions, with a $10^4$ sample size, 1000 times. The average $f_{\mathrm{non-overlap}}$ from the random sampling is 9.98%, represented by the grey regime in the colour bar. When a galaxy's $f_{\mathrm{non-overlap}}$ falls within the grey regime, the age distributions on either side of the spiral arms can be considered statistically indistinguishable, therefore, no age azimuthal variation is present in this galaxy.

In the past 5 Gyr, our haloes, at most redshifts, follow case I and show a negative $f_{\mathrm{non-overlap}}$ (tall blue histograms), referring to a younger leading edge than the trailing edge. This situation aligns with the prediction of density wave theory when the new-borne stars overtake the density waves inside the co-rotation radius (Sec. 4.1). One snapshot (Halo 24 at 3 Gyr ago) is detected to follow case I but a positive $f_{\mathrm{non-overlap}}$ (tall orange histogram in the bottom middle panel), indicating age azimuthal variation but a younger trailing edge. During this time, there was a satellite (dark red line in Fig. 4.9) approaching Halo 24 and continuously losing a substantial fraction of its gas mass. At a lookback time of 3 Gyr, 300 Myr (one snapshot) before this satellite fully merges with Halo 24, the spiral structure is highly disturbed, showing pronounced tidal features, including a strong stream surrounding the right side of the galaxy (Fig. 4.17). This snapshot stands out from other redshifts of Halo 24 and is most likely driven by the prominent bridge structure and tidal disruptions caused by the merger.

We also find that a few snapshots of our galaxies follow case II (short grey histograms), indicating little or no age azimuthal variation. Around 50% of case II (including lookback times of $\sim$ 4.3 Gyr and $\sim$ 5 Gyr in Halo 16, $\sim$ 5 Gyr in Halo 23, $\sim$ 2.6 Gyr in Halo 24, and $\sim$ 3.3 Gyr in Halo 27) takes place near or at the snapshot that a merger happens (dashed vertical lines in Fig. 4.6, Fig. 4.7, Fig. 4.8, Fig. 4.9 and Fig. 4.10). This finding suggests that gravitational perturbation and merged-in stars from the satellites destroy the age azimuthal variation in the main halo. We notice that some merging events, i.e., $\sim$ 4.6 Gyr in Halo 16, $\sim$ 2.6 Gyr in Halo 24, and $\sim$ 3.3 Gyr in Halo 27, lead to more open (larger pitch angle) spiral structures and reduce the number of spiral arms, see Fig. 4.14, Fig. 4.17 and Fig. 4.18, respectively. This supports the hypothesis that mergers reset the density wave potential in the disc, eliminating the age gradient across the spiral arms during the rebuilding process.

Interestingly, we observe a small difference in average age $\Delta\tau$ but a large non-overlap fraction $f_{\mathrm{non-overlap}}$ (short coloured histogram) at a lookback time of $\sim$ 3.3 Gyr in Halo 23, 5 Gyr in Halo 24, and 2 Gyr in Halo 27, consistent with case III. It is important to note

that the sign of $f_{\rm non-overlap}$ is determined by whether the leading edge has a higher $\mu$ than the trailing edge. However, when $\Delta\tau$ is close to zero, the sign of $f_{\rm non-overlap}$ can be highly uncertain. The combination of small $\Delta\tau$ and large $f_{\rm non-overlap}$ (case III) suggests that the age distribution differs between the leading and trailing edges, primarily driven by the distribution's broadness, while the average age remains similar on both sides of the spiral arms. We find all three snapshots coincide with significant gas loss in the companion galaxy within 300 Myr (one snapshot).

After a merger, the $f_{\rm non-overlap}$ spends $\sim$ 600 Myr ($\sim$1-2 snapshots) decreasing to around $-20\%$ to $-40\%$, along with a larger $\Delta\tau$ compared to the merger snapshots, suggesting a recovery of azimuthal variations and the reformation of a younger leading edge. A higher temporal resolution simulation can impose more constraints on the timescale required for rebuilding the age gradient across spiral arms. We will further discuss the three cases and possible impacts from the environment (mergers and fly-bys) in Sec. 4.4.

## 4.4 Discussion

In this section, we discuss the snapshots corresponding to three cases: case I (high $f_{\rm non-overlap}$ and $\Delta\tau$; Sec. 4.4.1), case II (low $f_{\rm non-overlap}$ and $\Delta\tau$; Sec. 4.4.2), and case III (high $f_{\rm non-overlap}$ and low $\Delta\tau$; Sec. 4.4.3), with a focus on the environmental impacts of mergers and fly-by events. We also compare our findings from the Auriga simulations with observational findings reported in the literature (Sec. 4.4.4).

### 4.4.1 Case I: Consistency with density wave theory and caveats

A subset of snapshots from the Auriga simulations, particularly those not during merging events, exhibit spiral arm features with a younger leading edge. This age pattern is apparently consistent with the quasi-stationary density wave theory prediction inside the co-rotation radius. In these cases, we measure a large negative $f_{\rm non-overlap}$ with $\Delta\tau$ $>$ 10 Myr, indicating a statistically younger stellar population within the leading edge than the trailing edge.

In density wave theory, spiral arms are long-lived, rigidly rotating patterns (Lin & Shu 1966). Star formation is triggered when gas clouds enter these stationary density waves. The newly formed stars then orbit faster than the pattern inside the co-rotation radius, leading to a secondary concentration of young stars on the leading edge of the arm (Martínez-García et al. 2009a). Our method of statistically comparing stellar age on each side of the spiral arms (Section 4.3.1) is designed to capture such a spatial offset in star-forming regions.

However, we note a significant caveat in directly attributing this simulated age offset solely to a quasi-stationary density wave. It is difficult to create and maintain a steady, global density wave in controlled, isolated N-body discs, let alone isolate one in a highly dynamic, cosmological environment like Auriga (Grand et al. 2024). High-resolution studies of isolated discs (e.g., Fujii et al. 2011), with a resolution of nearing star-by-star, still struggle to find clear, long-lived signatures of density waves. This density wave features do emerge but are frequently transient and co-rotating (Sellwood 2011). The Auriga simulations, while excellent models of galactic formation in a cosmological context, have a resolution that is coarse-grained compared to these tailored simulations. This makes the identification of density wave dynamics challenging.

Therefore, while the observed age asymmetry is consistent with a density wave, it is not conclusive proof of one. Alternative mechanisms must be considered, with radial migration being a plausible candidate. For instance, in Auriga L4, Grand et al. (2016) found that Halo 25 exhibits a faster peculiar azimuthal velocity and an inward radial velocity at the leading edge. Given the observed negative metallicity radial gradient, this inward migration of metal-poor stars from the outer disc could contribute to chemical. This radial migration can potentially lead to age—differences across the arm. The stellar velocity data in Auriga L3 will be crucial for quantifying the role of radial migration in the observed azimuthal age variation, a topic reserved for a separate publication.

### 4.4.2 Case II: Implications on gas-rich interactions

We observe case II with small $f_{\mathrm{non-overlap}}$ and small $\Delta\tau$ (Fig. 4.6, 4.7, 4.8, 4.9 and 4.10) in all five haloes. Most case II snapshots occur near a fly-by or merger event, except for Halo 23 at 0.7 Gyr ago.

If a given snapshot is aligned with case II or case III and this snapshot occurs within 300 Myr (one snapshot) of a merging event, we trace the orbital history of the merged satellite in the previous ∼1.2 Gyr (four snapshots). Similarly, if case II or case III occurs during a satellite fly-by of the main halo, we track the satellite's orbit to two snapshots (∼ 600 Myr) before and after case II and case III appears. Fig. 4.11a summarizes the evolution of the satellites' height ($z$-component) relative to the main halo in the past 5 Gyr. The dashed lines represent the plane of the main halo's disc, i.e., height $h_z = 0$. Fig. 4.11b presents the projected 2D radial distance ($r$) between the satellites and the main halo centre at each snapshot, traced back to 5 Gyr ago. The top and middle panels provide comprehensive satellite orbital history data. When a satellite's orbit crosses the dashed lines in the top panel and $r$ is relatively small ($\lesssim$ 100 kpc for a conservative evaluation), the satellite has passed through the main halo's disc. Fig. 4.11c summarises the gas (dashed) and stellar (solid) mass ratio between the satellites and their main haloes over cosmic time.

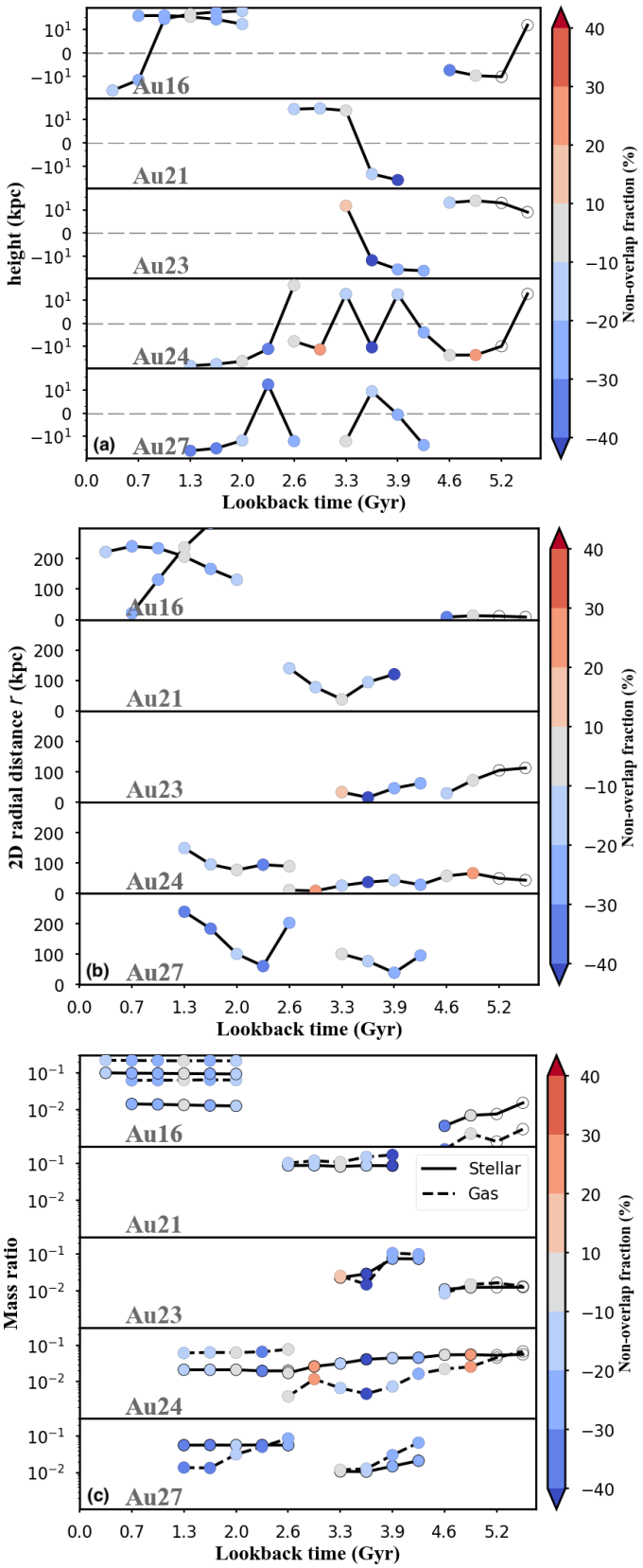


**Figure 4.11:** Height (top) and 2D radial distance (middle) of satellites to their main haloes are presented. The bottom panel shows the gas (dashed) and stellar (solid) mass ratio. Only satellites from snapshots corresponding to case II and case III are included, with data points colour-coded by $f_{\mathrm{non-overlap}}$ as derived in Sec. 4.3.1. We extensively present the orbital history and mass ratios beyond 5Gyr (hollow points) if a case II or case III event occurs within three snapshots (1Gyr).

We will discuss the presence of case II in each halo in detail below. The findings summarise that when an azimuthal age variation is absent, we observe a gas loss in companion galaxies or the presence of fly-by satellites with gas masses of ∼10% of the main halo's mass. Near the case II snapshots, some satellites punch through the main halo's disc, while others do not. Therefore, our results do not suggest a direct correlation between orbital history and the disappearance of the age gradient. Instead, our data indicates that gas-rich interactions are the primary mechanism responsible for the similar age distribution on each side of the spiral arms.

### Case II in Halo 16

At a lookback time of ∼ 5 Gyr, a satellite with a stellar mass ratio of ∼1:100 and a gas mass ratio of $\sim 1:150$ (orange line in the left panel of Fig. 4.6) crossed the main Halo 16's disc plane at small $r$ ($\lesssim$ 20 kpc) and merged. This satellite shows a continuous decrease in gas mass before merging into the main halo (Fig. 4.6 and Fig. 4.11c). The process of gas stripping may explain the absence of an azimuthal age distribution just before the merger event. Later, case II is observed again in Halo 16 at a lookback time of ∼ 1.3Gyr, with no recent satellite crossings through the main halo's disc. Near this snapshot, two satellites are orbiting around Halo 16, one of which (blue line in the left panel of Fig. 4.6) has a stellar (gas) mass ratio of ∼ 1:10 (1:9). The comparable gravitational potential in the satellite may give rise to the absence of azimuthal age distribution in the main halo.

### Case II in Halo 21

In Halo 21, at a lookback time of 3.3 Gyr, a satellite (blue line in the left panel of Fig. 4.7) flies by and passes through the main halo's disc just before the case II snapshot. The satellite has a high gas (stellar) mass ratio of ∼ 1:9 (1:10), with evidence of gas stripping between 3.3 and 4 Gyr ago. This interaction may have disturbed the density wave, leading to the absence of an age gradient across the spiral arms.

### Case II in Halo 23

We find Halo 23 showing case II at a lookback time of ∼ 4.9 Gyr. Near this case II snapshot, there is a satellite with a stellar and gas mass ratio of ∼1:90 (green line in Fig. 4.8) orbiting above the mid-plane of the disc and eventually merging into Halo 23. Similar to Halo 16, we observe a significant gas loss in the satellite before the merging event. The absence of azimuthal variation in the stellar age can be attributed to the gas stripping process.

**Case II in Halo 24**

Halo 24 has encountered most satellites over the past 5 Gyr, with merger trees indicating that four satellites with stellar mass ratios >1:100 have entered $R_{200}$. We identify three snapshots showing case II at lookback times of around 2 Gyr, 2.6 Gyr and 4.6 Gyr. A fly-by satellite (orange line in the left panel of Fig. 4.9) crossed the main halo's disc 2.5 Gyr ago, and 500 Myr later, an absence of an age gradient across the spiral arms in the main halo. This satellite has a gas-mass ratio of ∼1:45 and a stellar mass ratio of ∼1:90, compared to Halo 24. Another satellite (dark red line in the left panel of Fig. 4.9) approached and orbited Halo 24 starting 6 Gyr ago, merging around 2.6 Gyr ago. This satellite crossed the main halo's disc multiple times before the merger and is accompanied by significant gas loss lasting for over 2 Gyr during the interaction. The complex orbital history, involving multiple interactions and the final merger, likely contributed to the fluctuating $f_{\mathrm{non-overlap}}$ and $\Delta\tau$ in Halo 24 between 2.6 and 5 Gyr ago.

**Case II in Halo 27**

Halo 27 exhibits a younger leading edge in all snapshots during the past 5 Gyr, with a single exception at a lookback time of 3.3 Gyr, coinciding when a satellite galaxy merged (green line in the left panel of Fig. 4.10). The satellite crosses the main halo's disc and undergoes a significant decrease in gas mass right before the merger, with a gas (stellar) mass ratio of ∼ 1:45 (1:90). This satellite's transverse orbit likely facilitates gas stripping, transferring material to the main halo and subsequently erasing the younger leading edge signature.

### 4.4.3 Case III: Differences in the broadness of the age distributions

In Halo 23, Halo 24, and Halo 27, we observe snapshots with noticeable discrepancies in the broadness of the age distributions between the leading and trailing edges, despite comparable mean ages (case III, bottom panel of Fig. 4.5). Notably, one side of the spiral arms displays a broader age distribution (with a larger $\sigma$). This suggests that while the mean age offset across the spiral arms is minimised, age asymmetry between the two sides remains. In this section, we discuss the orbital history and satellite properties of galaxy interactions near case III snapshots.

In Halo 23, we observe case III at a lookback time of 3.3 Gyr, coinciding with the merger of a satellite (blue line in the left panel of Fig. 4.8) with a stellar mass ratio of ∼ 1:30. This satellite crossed the main halo's disc just before the onset of case III (Fig. 4.11), with significant gas loss occurring around 600 Myr before the merger. Similarly, 2 Gyr ago

in Halo 27, a satellite (blue line in the left panel of Fig. 4.10) experienced gas stripping while crossing the disc, potentially linked to the disappearance of age gradients (small $\Delta\tau$) across spiral arms. In Halo 24, at a lookback time of 5.3 Gyr, a satellite (dark red line in Fig. 4.9) approached the main halo, passing through the disc plane, and started showing a significant and continuous gas loss. Around 600Myr (two snapshots) later, we observe very little age gradient (small $\Delta\tau$) across the spiral arms, while age asymmetry persists as age distributions differ on either side of the spiral arms (large $f_{\mathrm{non-overlap}}$). This satellite merged into Halo 24 at the lookback time of 2.6 Gyr, after a few interactions.

All three case III snapshots occur under a common scenario: gas-rich merging or fly-by satellites traversing the main halo's disc. These results indicate that this specific type of galaxy interaction disrupts the age distribution, erasing out the signal of the younger leading edge. The variation in the broadness of the age distributions corresponds to a larger $\sigma$ on one side of the spiral arms, which means a more diverse stellar population on that side (leading edge for Halo 23 and 27 and trailing edge for Halo 24).

We note, however, that case III is not observed after every gas-rich interaction with a traversing orbital history. This includes Halo16 at 5 Gyr ago, Halo21 at 3.3 Gyr ago, and Halo 27 at 2 Gyr ago. In these cases, the age distributions on both sides of the spiral arms overlap greatly, showing negligible differences in both mean age and broadness.

### 4.4.4 Comparing spiral galaxies in observations and the Auriga simulation

Comparison between simulations and observational data is crucial for testing theoretical frameworks and allowing us to identify the inside physical mechanisms needed in simulations. In this section, we collect the azimuthal distributions of spiral galaxies from observational studies and compare them with the results from the Auriga simulations.

Observations have found azimuthal variations in stellar age in several nearby spiral galaxies including M 74 (Sánchez-Gil et al. 2011), NGC 1566 (Shabani et al. 2018), NGC 628, NGC 3726, NGC 6946 (Sakhibov et al. 2021) and M 101 (Garner et al. 2024). These observations are consistent with the prediction of density wave theory, showing azimuthal propagation in stellar age. Some observational studies (Yu & Ho 2018; Abdeen et al. 2022) also measure the pitch angle of spiral arms with multi-wavelength data, providing another vantage point as density wave theory predicts a looser spiral arm in the older stellar population (traced by redder wavelengths). Indeed, some spiral galaxies in the local Universe (Yu & Ho 2018; Abdeen et al. 2022) and at higher redshift (up to 8 Gyr ago; Martínez-García et al. 2023) do show colour jump across the spiral arms. To examine

these phenomena in simulations, mock observations across multiple wavelengths (e.g., TNG; Lan et al. 2024) or mapping 2D distributions of multi-phase ISM structures, such as CO and H$\alpha$ (e.g., FIRE-2; Hopkins et al. 2018), could provide valuable insights for future work.

The gas-phase ISM properties provide additional insight for examining spiral arm theories. Ho et al. (2017) presents a chemical model in a spiral galaxy driven by density waves, which leads to a lower metallicity – 12+log(O/H) – in the leading edge. Observational evidence for such metallicity offsets have been reported in NGC 1365 (Ho et al. 2017), NGC 1087, NGC 1672 (Kreckel et al. 2019) and NGC 1566 (Chen et al. 2024a). Other gas-phase properties, including electron temperature (Ho et al. 2019) and SFR (Chen et al. 2024b), also exhibit azimuthal offsets. These findings indicate azimuthal star formation propagation across spiral arms, consistent with density wave theory. In the Auriga simulation, we observe a younger stellar population along the leading edge in most snapshots, even recovering a younger leading edge after a merger or fly-by event. The age azimuthal variations align with some observed spiral galaxies, consistent with the prediction of density wave theory.

In contrast to density wave theory expectations, some spiral galaxies are observed to have older stellar populations in the leading edge, such as M 51 (Sánchez-Gil et al. 2011) [5] and NGC 2442 (Chen et al. 2024a). Both M 51 and NGC 2442 are grand-design spiral galaxies, interacting with their companion (M 51b and NGC 2443, respectively). In this work, Halo 24 displays an older leading edge at a lookback time of 3 Gyr, ~300 Myr before a satellite merges in. This snapshot presents grand-design spiral structures and prominent tidal features (Fig. 4.17), resembling the characteristics seen in M 51 and NGC 2442. This suggests that the merging event is likely a primary factor contributing to the age azimuthal variation observed in M 51 and NGC 2442.

Some spiral galaxies in the local Universe do not exhibit age gradients across their spiral arms. The interacting systems M 51b (Sánchez-Gil et al. 2011) are reported to have no age pattern associated with spiral arms. Choi et al. (2015) find no age azimuthal variation in M 81, which experiences hydrogen gas stripping toward M 82 and NGC 3077. Weżgowiec et al. (2022) find no age azimuthal variation in NGC 628, with hot magnetic gas suggesting a possible tidal interaction. We find little age azimuthal variation, i.e., case II, in the snapshots undergoing gas stripping or gas-rich interactions (Sec. 4.4.2). Our findings in Auriga are consistent with these observations. More importantly, this work highlights the potential role of gas-rich mini- and minor mergers in erasing detectable age

[5] We note that Sánchez-Gil et al. (2011) observed azimuthal age variation in M 51, whereas Shabani et al. (2018) reported little to no variation. The discrepancy may result from the difference in spatial resolution, as the Sánchez-Gil et al. (2011) analysis is done on a pixel level whereas the Shabani et al. (2018) study is done using the age of unresolved star clusters.

gradients. Karademir et al. (2019) discuss that mini-mergers frequently occur without disrupting the galactic disc. However, the detection of mini-mergers remains challenging due to the low surface brightness of the satellites. Our study provides a novel indirect diagnostic for identifying mini-mergers based on azimuthal age variations.

In a comparison of the gas-phase metallicity in NGC 2835, NGC 2997 and M 83, Chen et al. (2024a) find negligible offsets in the median $\Delta$(O/H) – radial gradient subtracted metallicity – while the Kolmogorov–Smirnov test and Anderson-Darling tests suggest $\Delta$(O/H) on each side of the spiral arms support the distributions arising from different parent distributions. NGC 2835 presents a flattening radial profile (Chen et al. 2023), indicating accreted gas in the outskirts (which is also seen in simulations; Garcia et al. 2023). Tidal features are observed in the H I in both NGC 2997 and NGC 5236. Similarly, in the Auriga simulation, we identify three case III snapshots where the leading and trailing edges have comparable average ages, but their broadness differs. Our analysis of the merger tree (Sec. 4.3.2) and orbital history (Sec. 4.4.3) suggests that a gas-rich satellite passes through the main halo disc before case III snapshots. The azimuthal distribution, similar to case III, along with the asymmetric gas distribution, suggests that NGC2835, NGC2997, and NGC 5236 may have undergone gas-rich interactions involving a crossing of the galaxy disc plane. However, it is important to note that Chen et al. (2024a) derives gas-phase metallicities from emission lines on a spaxel-by-spaxel basis. Potential offsets between leading and trailing edges may be obscured by significant scatters in gas-phase metallicities. Additionally, we emphasise that the analysis presented here focuses on stellar variations, whereas some prior observational studies have primarily examined variations in the gas phase. Nevertheless, while this study focuses on star particles rather than gas cells, we expect both simulations and observations to capture the same underlying physical mechanisms.

## 4.5 Conclusions

We analyse five spiral galaxies from the Auriga L3 simulation dataset to investigate the long-term evolution of stellar age azimuthal distributions over the past 5 Gyr, focusing on environmental effects from mergers and fly-bys. To identify spaxels on spiral arms in each snapshot, we develop an automated "ridgeline walking" algorithm and divide the disc region into leading and trailing edges, following Chen et al. (2024b).

To measure azimuthal variations relative to the spiral arms, we compare the age distributions of young stars on each side of the spiral arms using two metrics: $f_{\mathrm{non-overlap}}$ (non-overlap fraction) and $\Delta\tau$ (mean age difference). These metrics quantify the differences in age distribution between the leading and trailing edges, providing insights into

the impact of environmental interactions on spiral arm evolution.

We track fluctuations in both $f_{\mathrm{non-overlap}}$ and $\Delta\tau$ over the past 5Gyr. Our results indicate that spiral galaxies in the Auriga simulations generally have younger leading edges compared to trailing edges, supporting density wave theory as the primary mechanism driving distribution in isolated spiral galaxies. However, gas-rich interactions (mini-mergers or fly-bys) can erase azimuthal age offsets. We identify three snapshots where the mean age difference between the two sides of the spiral arms is negligible, yet significant differences appear in the age distribution tails. All of these snapshots coincide with gas-rich interactions involving satellites crossing the main halo's disc plane.

Comparing our results with observational data from previous studies, we find a consistent trend where galaxy interactions erase azimuthal variations. While ~70% snapshots in our study a younger leading edge, only $\lesssim$30% of nearby galaxies exhibit azimuthal variations in metallicity and/or age gradient across spiral arms.

For future study, simulations with multi-phase ISM (e.g., FIRE; Wetzel et al. 2016) enable a more direct and detailed comparison with observations. Simulations with a high temporal resolution (e.g., NIHAO; Buck et al. 2020, Buder et al. 2024) can also provide more constraints on the recovery timescale of age patterns.

# Acknowledgements

QHC sincerely acknowledges Caroline Foster for her insightful suggestions and valuable support in this work.

Parts of this work are supported by the Australian Research Council Centre of Excellence for All Sky Astrophysics in 3 Dimensions (ASTRO 3D), through project number CE170100013. KG is supported by the Australian Research Council through the Discovery Early Career Researcher Award (DECRA) Fellowship (project number DE220100766) funded by the Australian Government. LCK acknowledges support by the DFG project nr. 516355818. RSR and LCK acknowledge support from the ASTRO 3D visitor programme. SB acknowledges support by DECRA funding through DE240100150.

This research has made use of NASA's Astrophysics Data System Bibliographic Services (ADS). This research made use of ASTROPY,[6] a community-developed core Python package for Astronomy (Astropy Collaboration et al. 2013, 2018). This research has made use of the NASA/IPAC Extragalactic Database (NED) which is operated by the Jet Propulsion Laboratory, California Institute of Technology, under contract with NASA. Parts of the

[6] http://www.astropy.org

results in this work make use of the colormaps in the CMASHER package (van der Velden 2020).

## Data Availability

The data used in this article are available on the Auriga simulation website https://wwwmpa.mpa-garching.mpg.de/auriga/index.html. The products of this work are available upon request. The "ridgeline walking" algorithm is available on GitHub https://github.com/Qian-HuiChen/ridgeline_walking.

## 4.6 Appendix: Comparison of L3 and L4 dataset

The Auriga simulations release L3 and L4 datasets, which differ in baryon mass resolution (Grand et al. 2024). In our main analysis, we utilise the L3 dataset, which has a higher baryon mass resolution of $6 \times 10^3 M_\odot$, allowing for a more detailed representation of spiral structures.

The formation and evolution of spiral galaxies in simulations are resolution-dependent, with different resolutions yielding distinct spiral structures. In the lower-resolution L4 simulation (Fig. 4.12), spiral arms appear smoother and less prominent compared to the inter-arm regions, and tightly wound inner spirals transition into a ring-like structure. As a result, the identification of spiral arms and the measurement of age gradients are inherently influenced by the baryon mass resolution. While L4 provides a larger sample of halos, this study focuses on the higher-resolution L3 simulations to minimise resolution effects and ensure more robust structural analysis.

## 4.7 Appendix: Halo 6 exhibits tightly wound and non-prominent spiral arms

Fig. 4.13 presents young star maps of Halo6 at lookback times of 0, 1, and 2 Gyr. Halo 6 features spiral arms with very small pitch angles, approaching a ring-like structure. We find a gas-rich satellite (gas mass ratio of 1:5) within $R_{200}$ of Halo 16 over the past 4 Gyr, which could attribute to the appearance of the ring structure. These tightly wounded spiral arms make it challenging to distinguish the disc's leading and trailing edges. The spiral arms are non-prominent, blending smoothly with other young stars in the disc, making them difficult to locate visually or with the "ridgeline walking" algorithm (Sec. 4.2.2). To maintain accuracy in defining spiral arms and comparing stellar ages on both sides of the

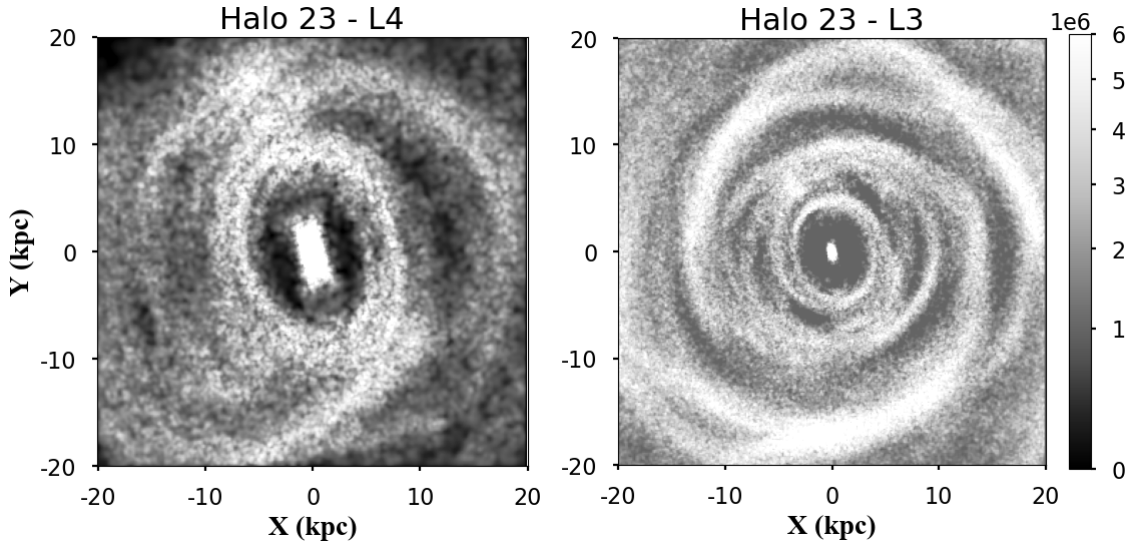


**Figure 4.12:** Young stars (< 2 Gyr) mass map of Halo 23, simulated at L4 (left) and L3 (right) resolutions. The visualisation process is described in detail in Sec.4.2.1. The higher-resolution L3 dataset reveals more prominent and detailed spiral structures compared to L4. Notably, the lower-left spiral arm in the outer region, observed in L3, become absent in L4.

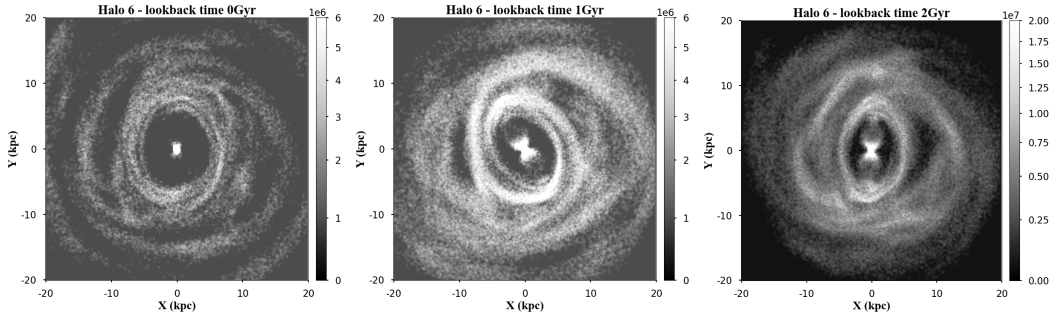


**Figure 4.13:** Young star (< 2 Gyr) map of Halo 6 at the lookback time of 0 Gyr (left), 1 Gyr (middle) and 2 Gyr (right).

arms, we exclude this halo from our analysis.

## 4.8 Appendix: Young star maps of each snapshot

In this appendix, we present the young star (< 2 Gyr) mass maps of all five halos in our sample over the past 5 Gyr, using the visualisation method described in Sec. 4.2.1. Spiral arms identified by the ridgeline walking algorithm (see Sec. 4.2.2) are marked in red.

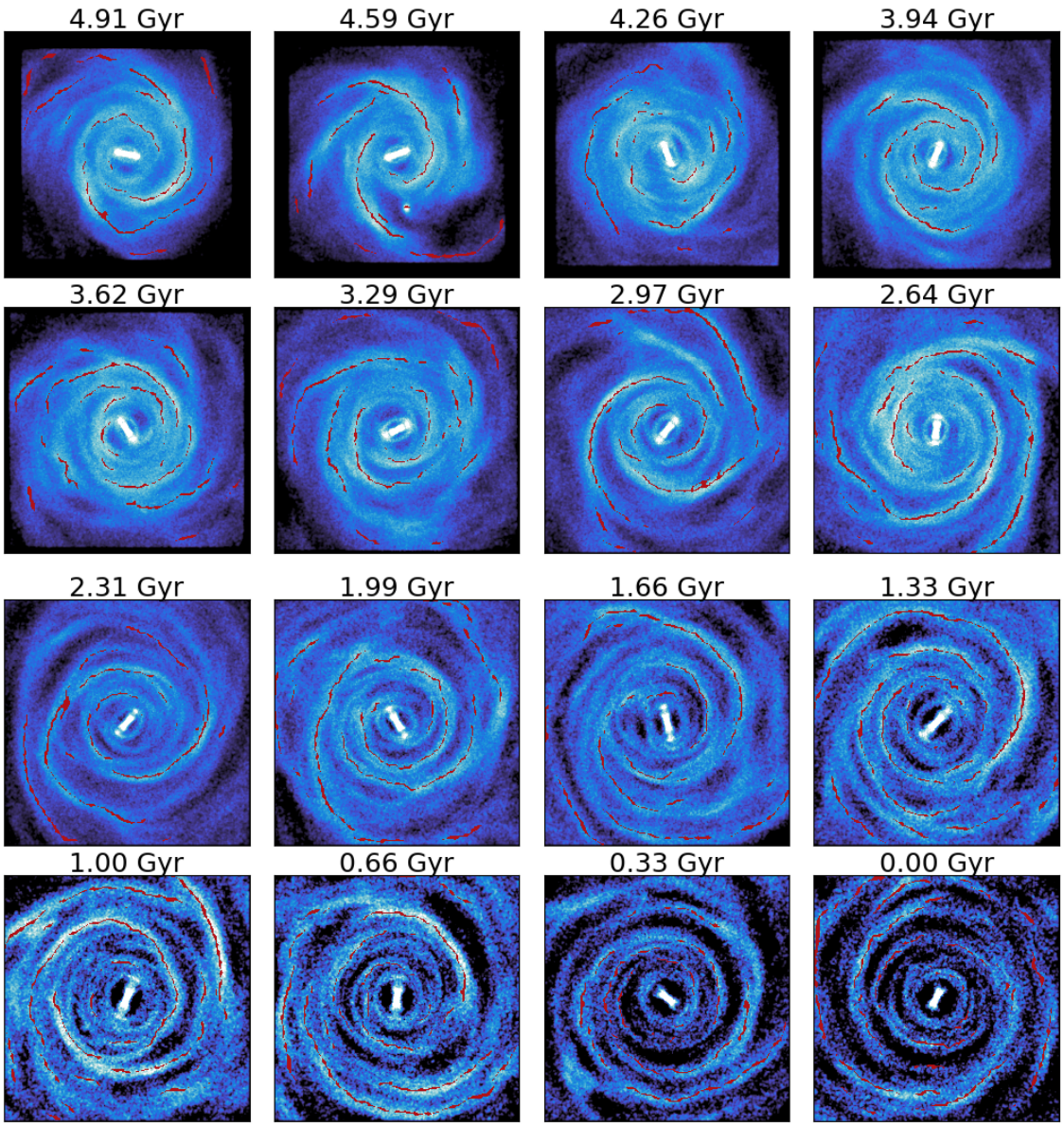


**Figure 4.14:** Young star (age < 2 Gyr) mass map of Halo 16 over the past 5 Gyr, overlaid the definition of spiral arms found by ridgeline walking algorithm (Sec. 4.2.2).

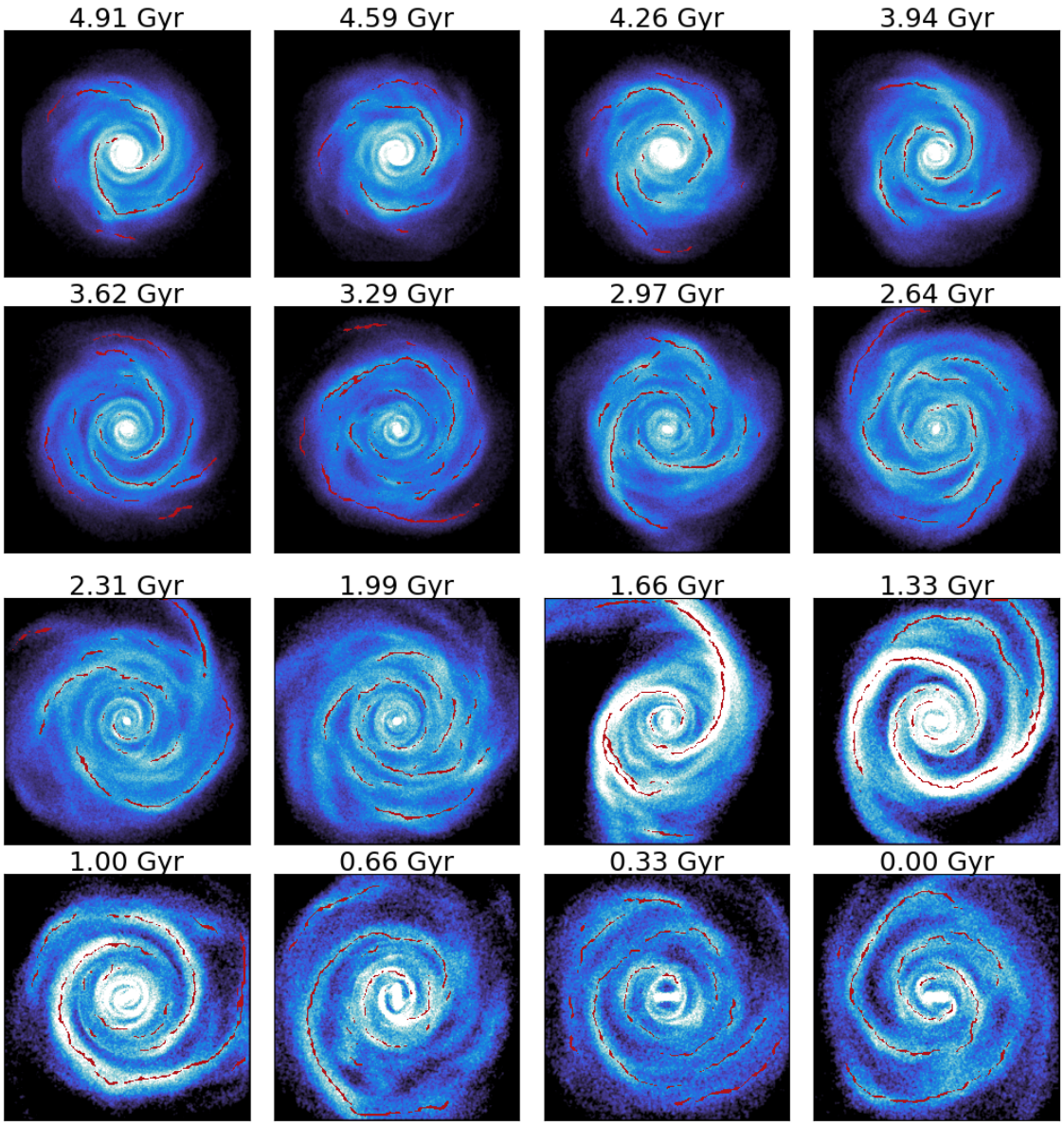


**Figure 4.15**: Similar to Fig. 4.14 but for Halo 21.

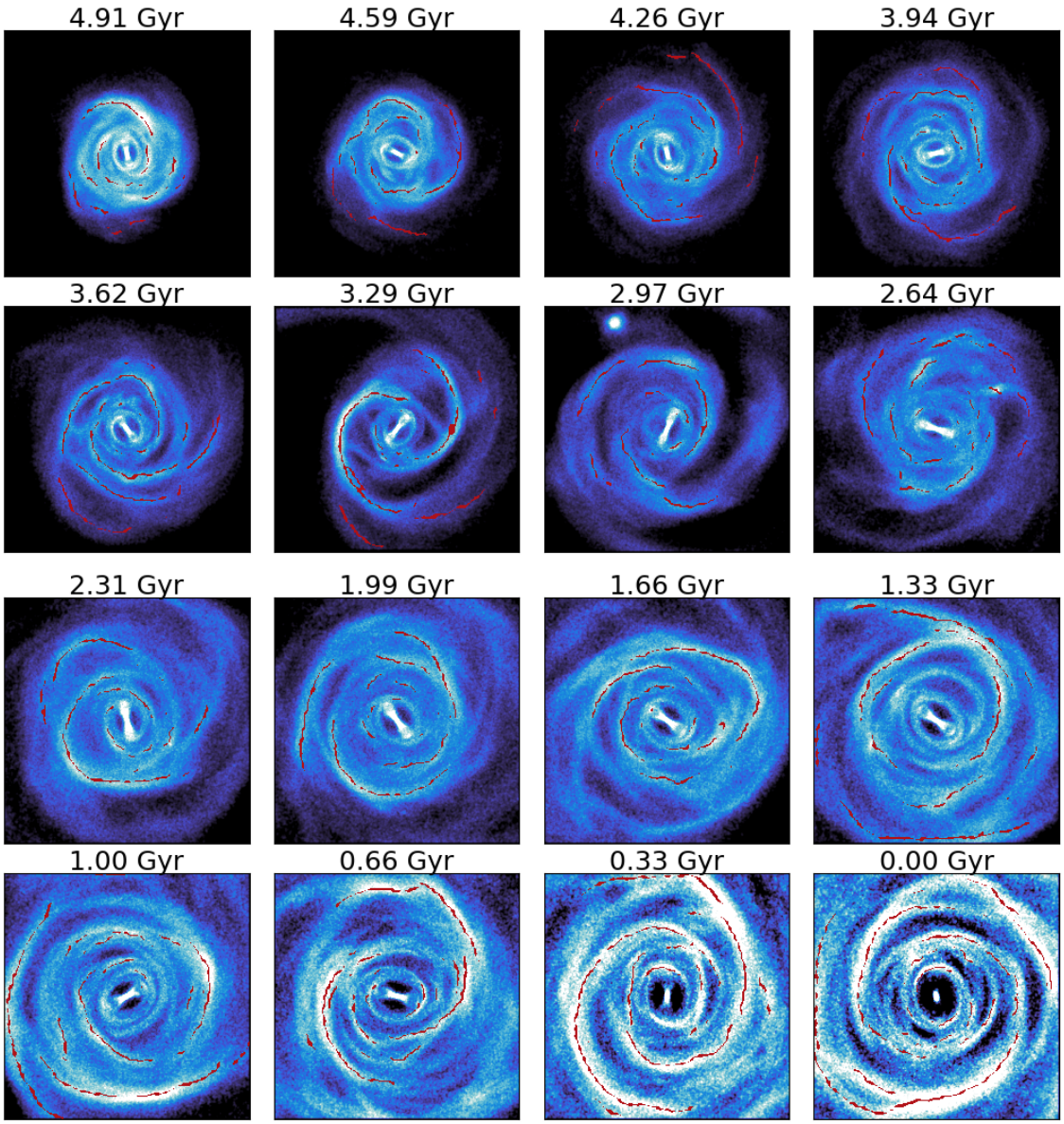


**Figure 4.16**: Similar to Fig. 4.14 but for Halo 23.

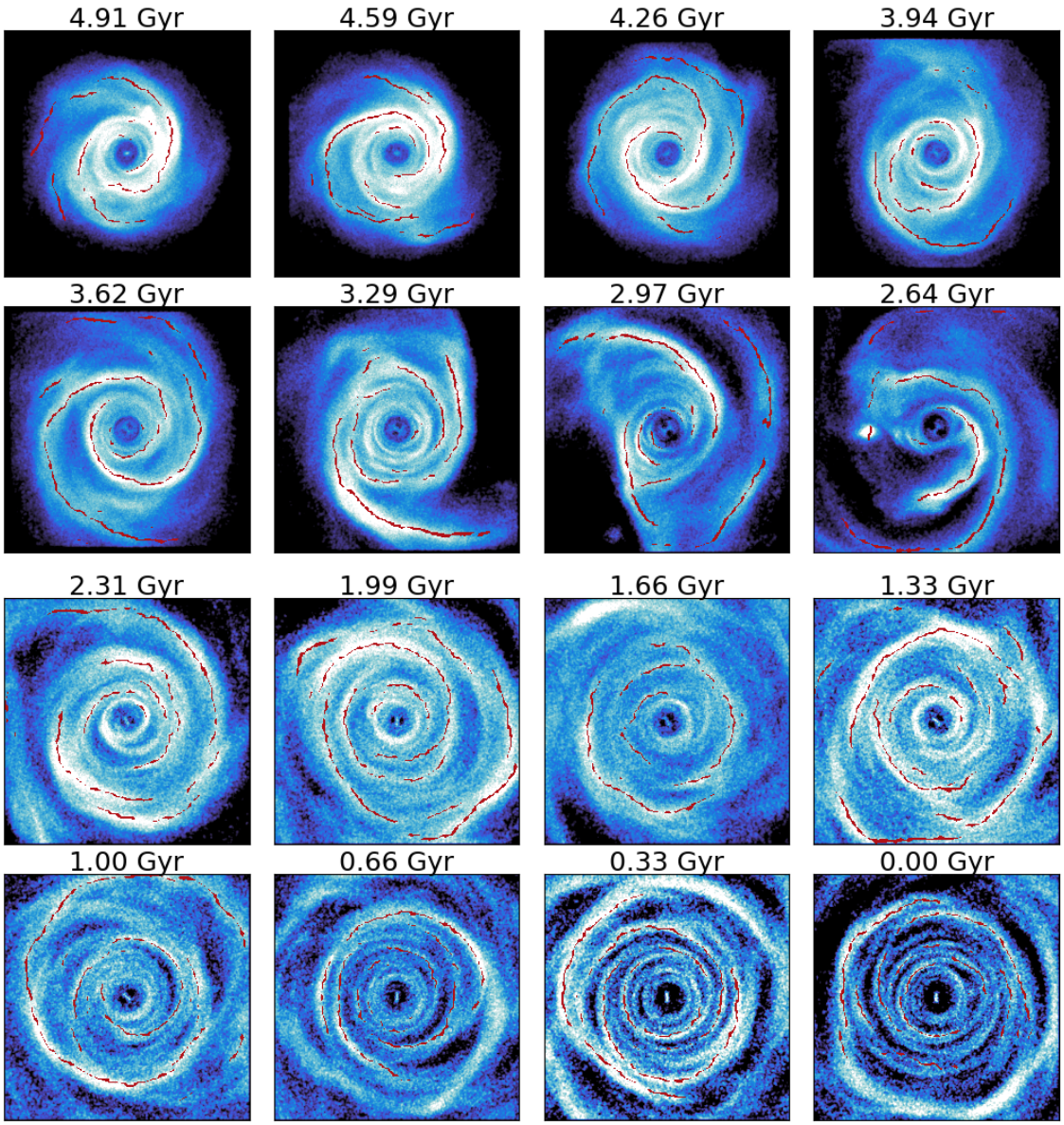


**Figure 4.17**: Similar to Fig. 4.14 but for Halo 24.

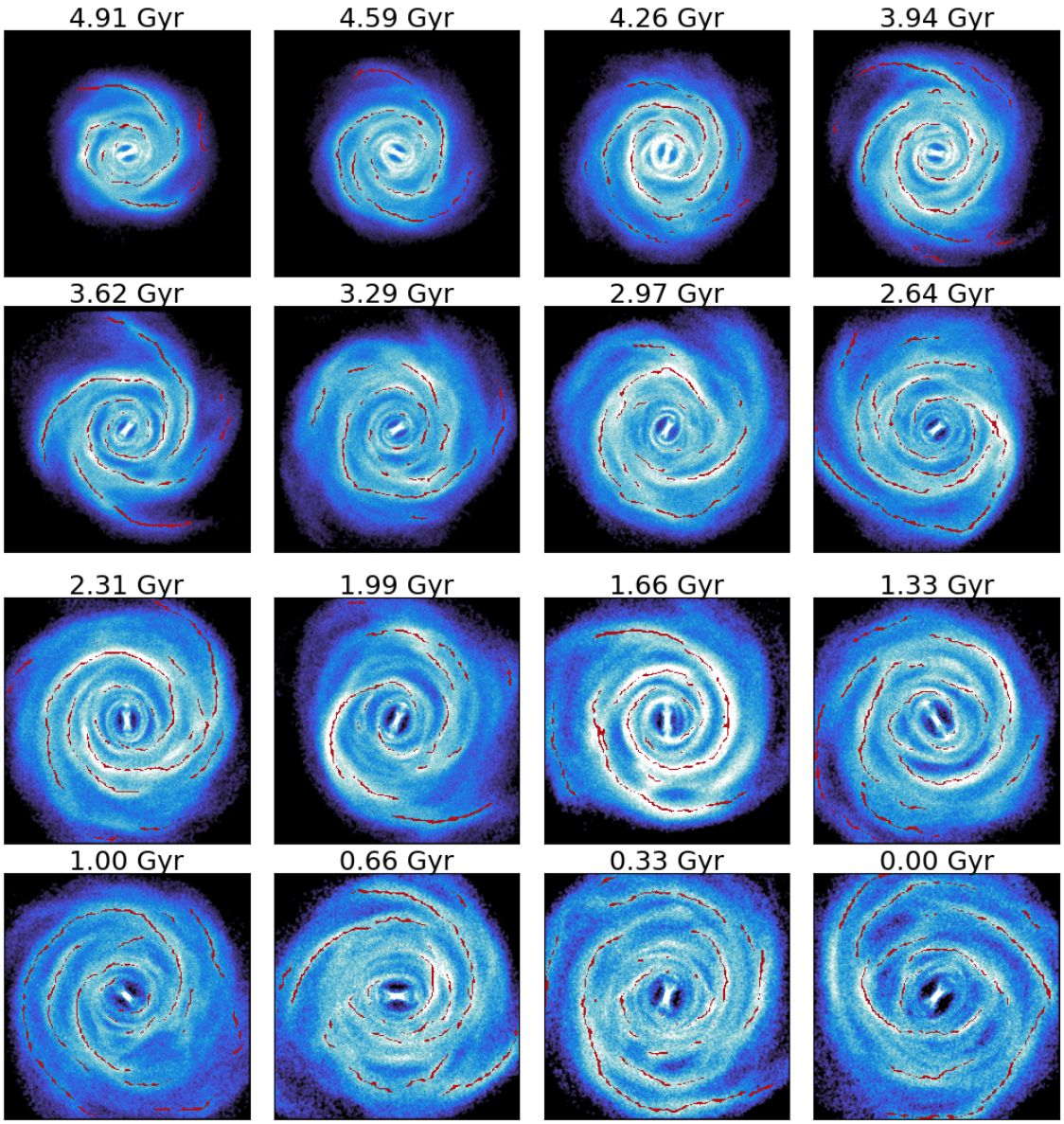


**Figure 4.18**: Similar to Fig. 4.14 but for Halo 27.

Chapter 5

# Conclusions

## 5.1 Summary of this thesis

This thesis has analysed multi-wavelength observations of spiral galaxies across cosmic time, combined with cosmological simulations, to test fundamental theories of spiral structure. Our investigation into the azimuthal distributions of star formation rate, gas-phase metallicity, and stellar age reveals that no single theory can universally explain the origin and evolution of spiral arms. Instead, we find that stellar and gaseous distributions in spiral galaxies are observably governed by a complex interplay between internal dynamical mechanisms and external environmental influences. The collective findings from this work challenge a monolithic view of spiral structure and argue for a more unified framework.

The chapters of this thesis form a coherent argument, moving from observations to simulations to build a complete picture. Chapter 4 established a critical theoretical baseline using the Auriga cosmological simulations. It demonstrated that long-lived spiral patterns can produce younger stellar populations on the leading edge, validating the core mechanic of the density wave theory. However, a pivotal finding was that these coherent age patterns, while fragile enough to be systematically erased during gas-rich minor mergers or fly-by events, are also highly resilient. The Auriga simulations show that this environmentally-induced disruption is temporary, with the pattern recovering within ~600 Myr, illustrating the dynamic competition between internal and external forces.

When this framework is compared with the findings from our observations (Chapters 2 and 3), the observational results robustly confirm the dual nature of spiral structure. We developed and applied tailored methods (SPARCFIRE for $z \sim 0.3$ and the phase-diagram method for $z \sim 0$) to accurately identify spiral arms despite varying spatial resolutions. We find:

- **Evidence for Density Waves**: We observe clear, statistically significant azimuthal offsets in $\Sigma_{\rm SFR}$ and gas-phase metallicity between the leading and trailing edges in one galaxy at $z \sim 0.3$ and two galaxies at $z \sim 0$. These results are a direct match

to the predictions of density wave theory, indicating that long-lived spiral arms can regulate star formation and chemical enrichment in isolated systems.

- **Evidence for Dynamic Spirals**: Conversely, a significant population of spirals at both redshifts, including SG 1204 at $z \sim 0.3$, NGC 2835, NGC 5236 and NGC 6744 at $z \sim 0.3$, show no statistically significant azimuthal trends. This absence is a key signature predicted by dynamic spiral theory, which posits that transient, locally-driven arms do not generate large-scale, coherent offsets.

Our most critical contribution lies in highlighting the significant role of the environment, which shows consistent trends in both observations and simulations. The case study of the merging system NGC 2442 is particularly illuminating: it exhibits lower $\Sigma_{\rm SFR}$ and lower metallicity on the trailing edge of its spiral arms – a pattern that is directly opposite to the prediction of density wave theory and cannot be explained by dynamic theory. This misalignment powerfully demonstrates that tidal forces during a major interaction can establish an entirely new azimuthal pattern, dominating the galaxy's evolution.

In Auriga simulations, we similarly find a older stellar population in the leading edge (opposite to the prediction of density wave theory) in Halo 24 at a lookback time of 3 Gyr, coinciding with a merger event. In general, the finding from observations is powerfully corroborated by our simulation results in Chapter 4, which showed that environmental perturbations can erase intrinsic patterns. The absence of azimuthal offsets in galaxies like NGC 2835 and NGC 6744 may therefore not solely be evidence for dynamic arms, but could also be attributed to past perturbations caused by their environmental history.

Furthermore, our work provides a crucial methodological insight: we determined that $D_{4000}$ is not an effective tracer for resolving azimuthal age offsets across spiral arms (Chapter 2). Its sensitive timescale of $1-2$ Gyr allows stars to orbit significantly, blurring the age contrast between the leading and trailing edges. This finding guides future studies towards tracers with shorter age sensitivities or more direct dynamical mapping.

Collectively, these three chapters argue that the question "How do spiral arms form?" leads to more questions, as no single theory can universally explain all observed spiral arms. Our thesis provides a preliminary answer:

- Long-lived density waves require stable, isolated conditions to develop, maintain their coherence, and generate observable azimuthal offsets in stellar and gaseous properties.
- Dynamic spiral arms appear to be a common alternative in undisturbed disks, producing spiral structures without large-scale stellar or gaseous offsets.
- Environmental interactions are a dominant force that can overwrite the imprints of both internal mechanisms by temporarily erasing their patterns.

The presence, absence, or anomalous nature of azimuthal patterns in star formation and metallicity thus serves as a powerful diagnostic for a galaxy's dynamical state and interaction history.

In conclusion, this thesis demonstrates that the diversity of spiral structure directly reflects the diversity of galactic formation paths and evolutionary histories. A galaxy's observed state is the combined result of internal and environmental forces. Our understanding is greatly advanced by rejecting a single-theory paradigm and embracing a multi-faceted framework where internal dynamics and environment conspire to shape these iconic structures. We have provided a set of observational diagnostics to decode this history and laid the groundwork for a more complete model of spiral structure formation.

## 5.2 Future work

This thesis provides insights into the mechanisms driving spiral features by combining low-$z$ ($z < 0.3$) observations with simulations. However, it remains uncertain whether spiral galaxies at higher redshifts, such as cosmic noon, follow the same physical processes as those at low redshifts. Spiral galaxies at cosmic noon appear more clumpy and reside in denser environments, which also make their spiral arms more challenging to resolve.

Additionally, while simulations reveal that azimuthal age patterns can be interrupted by galaxy interactions, the recovery timescales is dependent on the temporal resolution of the simulations. Higher temporal resolution simulations are needed to accurately capture the dynamical evolution of spiral structures and provide more details on the motion of star particles across spiral arms.

Furthermore, the ISM properties analysed in this thesis focus primarily on ionised gas. A direct comparison between multiple gas phases, such as molecular versus ionised gas, would provide stronger and more direct constraints on how spiral structures regulate star formation.

### 5.2.1 Resolving spiral galaxies at cosmic noon

Quantitative analyses of azimuthal distributions in spiral galaxy discs have predominantly focused on low redshifts ($z < 0.3$), leaving higher-redshift spiral galaxies largely unexplored. Gravitational lensing offers a powerful tool for resolving spiral structures at much earlier epochs, such as the remarkable case of a spiral galaxy resolved at $z = 4.41$ (Tsukui & Iguchi 2021). Projects like the Planck All-Sky Survey to Analyze Gravitationally-lensed Extreme Starbursts (PASSAGES) will expand the sample of resolved spiral galaxies at cosmic noon ($z = 1.1 - 3.3$) using the magnifying effects of gravitational lensing.

The current near IR and radio facilities (e.g., the JWST and Atacama Large Millimeter/submillimeter Array; ALMA) and future instrumentations (Extremely Large Telescope; ELT, ALMA upgrades) will enable us to resolve the interarm regions of spiral galaxies at $1 < z < 3$ without the need for gravitational lensing (Sharp et al. 2016; Thatte et al. 2021; Agapito et al. 2022; Ju et al. 2025). These observations will enable the identification of spiral structures and comparison of ISM properties (such as $\Sigma_{\rm SFR}$ and gas-phase metallicity) among leading edge, arm regions and trailing edge of spiral galaxies at cosmic noon.

By combining these studies with existing research at low redshifts, we can address a critical question in the field: do spiral structures follow the same physical processes across different cosmic time? This comprehensive approach will deepen our understanding of the evolution of spiral galaxies and the long-term effects of spiral structures in shaping star formation and organising the ISM over time.

### 5.2.2 Spiral galaxies in simulations with a high temporal resolution

This thesis demonstrates that fly-bys and merger events can erase azimuthal age variations in spiral galaxies. However, the temporal resolution of simulations might impact the results derived from the simulations (Benson et al. 2012), including the timescales needed for the age patterns to recover. Higher temporal-resolution simulations can provide a more precise estimate of the number of snapshots needed for the age patterns to re-emerge after a merger or fly-by event. Therefore, it offers a clearer insight on the timescale for spiral potentials to re-establish stellar age distributions.

Such simulations can also be used to examine spiral galaxies in the absence of galaxy interactions, to gain a clearer understanding of the intrinsic dynamics of stars (Hunt & Kawata 2013). By simulating an isolated spiral galaxy (Bottema 2003; Shimizu et al. 2019), we can directly trace how spiral structures regulate star formation and organise stellar populations (Dubois et al. 2021) over time. A particularly promising approach is the statistical analysis of star particle orbits (Röttgers et al. 2014), which can reveal how spiral arms influence stellar motions and age distributions. To achieve this, simulations must have sufficiently high temporal resolution to accurately track star particle trajectories between spiral arms.

High time-resolution simulations, such as those from the Feedback In Realistic Environments-2 (FIRE-2) project, offer a transformative opportunity. FIRE-2 achieves a time resolution of $\Delta t = 2.2$ Myr at $0 < z < 0.1$ (Wetzel et al. 2023), enabling us to track young stars as they are borne within spiral arms and migrate over time. By assigning

unique IDs to individual particles, we can directly track star particles and quantify how stellar age patterns are gradually shaped by the spiral arm potential wells.

This method provides a direct test of the spiral arm potential governing star particles and gas particles in simulations. Moreover, by combining these high time-resolution simulations with spatially resolved observations, we can gain a more comprehensive understanding for the observed and absent stellar age patterns, linking the short-term galaxy interactions with the long-term evolution of spiral galaxies.

### 5.2.3 Determining co-rotation radius with CO and H$\alpha$ observation at z $\sim$ 0.3

In density wave theory, differential rotation leads to a spatial offset ($\theta$) between newly formed massive stars (traced by H$\alpha$) and molecular gas (traced by CO), with $\theta$ close to zero near the $R_{CR}$. Mapping the spatial distributions of H$\alpha$ and CO thus provides a direct test of whether a given spiral galaxy follows density wave theory (see Fig. 5.1).

This offset $\theta$ is theoretically correlated with the angular velocities of CO ($\Omega_{CO}$) and H$\alpha$ ($\Omega_{H\alpha}$), as well as the star formation timescale ($t_{SF}$) by (Egusa et al. 2009):

$$\theta = 0.586\,|\Omega_{H\alpha} - \Omega_{CO}| \times \frac{t_{SF}}{10^7\ \mathrm{yr}}\ \mathrm{degree}. \tag{5.1}$$

We can measure $\theta$ by comparing optical and radio imaging, which must cover a wide range of radii. Additionally, optical and radio spectroscopic observations are required to obtain rotational curves for both tracers, yielding the rotational velocity ($V_{rot}$) at different radii. From these measurements, we determine $\Omega_{CO}$ and $\Omega_{H\alpha}$, ultimately allowing us to estimate the co-rotation radius ($R_{CR}$), where $\theta = 0$, and derive $t_{SF}$ from Eq. 5.1, thereby directly examining the density wave theory.

Previous studies (Egusa et al. 2004, 2017) have used this method to measure the $R_{CR}$, $t_{SF}$, and pattern speed in nearby spiral galaxies. Expanding this analysis to higher-redshift galaxies remains an exciting frontier. For example, with the ionised gas maps from MAGPI already in hand, we can apply for CO observations with the ALMA survey to analyse spiral galaxies at $z \sim 0.3$. To extend this study to galaxies at cosmic noon, we can combine optical observations from JWST with radio observations from ALMA. These multi-wavelength observations across $z = 0 - 2$ will enable us to assess whether star formation timescales ($t_{SF}$) remain comparable or shorten as we trace spiral galaxies from the local universe back to cosmic noon, where the global star formation rate peaks. This research will offer crucial insights into the physics shaping spiral structures over cosmic time and across diverse environmental conditions.

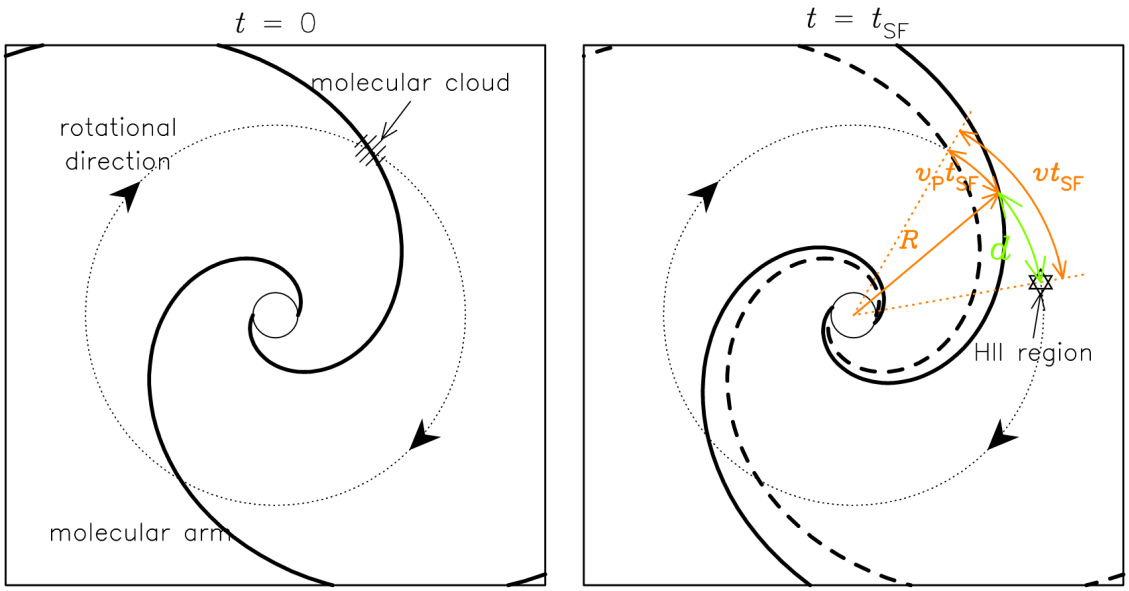


**Figure 5.1: Left**: Spiral arm locations traced by molecular gas clouds at time $t = 0$. **Right**: After the star formation timescale $t_{SF}$, the molecular gas spiral arms are expected to orbit from the dashed line to the solid line. Meanwhile, young massive stars overtake the molecular arms and reach the star symbol, traced as the H II regions.

# Bibliography


Aarseth, S. J. 1963, Monthly Notice of the Royal Astronomical Society, 126, 223 (ADS entry)

Abdeen, S., Kennefick, D., Kennefick, J., Miller, R., Shields, D. W., Monson, E. B., & Davis, B. L. 2020, Monthly Notice of the Royal Astronomical Society, 496, 1610 (ADS entry)

Abdeen, S., et al. 2022, Monthly Notice of the Royal Astronomical Society, 512, 366 (ADS entry)

Adelman-McCarthy, J. K., et al. 2008, Astrophysical Journal Supplement, 175, 297 (ADS entry)

Agapito, G., Vassallo, D., Plantet, C., Cranney, J., Zhang, H., Viotto, V., Pinna, E., & Rigaut, F. 2022, in Society of Photo-Optical Instrumentation Engineers (SPIE) Conference Series, Vol. 12185, Adaptive Optics Systems VIII, ed. L. Schreiber, D. Schmidt, & E. Vernet, 121853L (ADS entry)

Agertz, O., et al. 2021, Monthly Notice of the Royal Astronomical Society, 503, 5826 (ADS entry)

Anand, G. S., et al. 2021, Monthly Notice of the Royal Astronomical Society, 501, 3621 (ADS entry)

Antoja, T., Ramos, P., López-Guitart, F., Anders, F., Bernet, M., & Laporte, C. F. P. 2022, Astronomy and Astrophysics, 668, A61 (ADS entry)

Aouad, C. J., James, P. A., & Chilingarian, I. V. 2020, Monthly Notice of the Royal Astronomical Society, 496, 5211 (ADS entry)

Ardèvol, J., Semczuk, M., Antoja, T., Debattista, V. P., Bernet, M., & Pettitt, A. 2025, arXiv e-prints, arXiv:2507.15473 (ADS entry)

Astropy Collaboration et al. 2013, Astronomy and Astrophysics, 558, A33 (ADS entry)

—. 2018, Astronomical Journal, 156, 123 (ADS entry)

Athanassoula, E. 1992, Monthly Notice of the Royal Astronomical Society, 259, 345 (ADS entry)

Athanassoula, E., Romero-Gómez, M., Bosma, A., & Masdemont, J. J. 2010, Monthly Notice of the Royal Astronomical Society, 407, 1433 (ADS entry)

Baba, J. 2015, Monthly Notice of the Royal Astronomical Society, 454, 2954 (ADS entry)

Baba, J., Asaki, Y., Makino, J., Miyoshi, M., Saitoh, T. R., & Wada, K. 2009, Astrophysical Journal, 706, 471 (ADS entry)

Baba, J., Morokuma-Matsui, K., & Saitoh, T. R. 2017, Monthly Notice of the Royal Astronomical Society, 464, 246 (ADS entry)

Baba, J., Saitoh, T. R., & Wada, K. 2013, Astrophysical Journal, 763, 46 (ADS entry)

Bagla, J. S. 2005, Current Science, 88, 1088 (ADS entry)

Baldwin, J. A., Phillips, M. M., & Terlevich, R. 1981, Publications of the Astronomical Society of the Pacific, 93, 5 (ADS entry)

Belfiore, F., et al. 2017, Monthly Notices of the Royal Astronomical Society, 469, 151 (Link)

Benhaiem, D., Sylos Labini, F., & Joyce, M. 2019, Physical Review E, 99, 022125 (ADS entry)

Benson, A. J., Borgani, S., De Lucia, G., Boylan-Kolchin, M., & Monaco, P. 2012, Monthly Notice of the Royal Astronomical Society, 419, 3590 (ADS entry)

Bernardi, M., Shankar, F., Hyde, J. B., Mei, S., Marulli, F., & Sheth, R. K. 2010, Monthly Notice of the Royal Astronomical Society, 404, 2087 (ADS entry)

Bertin, G., & Lin, C. C. 1996, Spiral structure in galaxies a density wave theory (Cambridge, MA MIT Press) (ADS entry)

Bialopetravičius, J., & Narbutis, D. 2020, Astronomical Journal, 160, 264 (ADS entry)

Bianco, F., Modjaz, M., Oh, S., Fierroz, D., Liu, Y., Kewley, L., & Graur, O. 2016, Astronomy and Computing, 16, 54 (Link)

Binney, J., & Tremaine, S. 1987, Galactic dynamics (Princeton University Press) (ADS entry)

—. 2008, Galactic Dynamics: Second Edition (Princeton University Press) (ADS entry)

Bittner, A., Gadotti, D. A., Elmegreen, B. G., Athanassoula, E., Elmegreen, D. M., Bosma, A., & Muñoz-Mateos, J.-C. 2017, Monthly Notice of the Royal Astronomical Society, 471, 1070 (ADS entry)

Bittner, A., et al. 2019, Astronomy and Astrophysics, 628, A117 (ADS entry)

Block, D. L., Bournaud, F., Combes, F., Puerari, I., & Buta, R. 2002, Astronomy and Astrophysics, 394, L35 (ADS entry)

Block, D. L., Buta, R., Knapen, J. H., Elmegreen, D. M., Elmegreen, B. G., & Puerari, I. 2004, Astronomical Journal, 128, 183 (ADS entry)

Bocquet, S., Saro, A., Dolag, K., & Mohr, J. J. 2016, Monthly Notice of the Royal Astronomical Society, 456, 2361 (ADS entry)

Bonnell, I. A., Dobbs, C. L., Robitaille, T. P., & Pringle, J. E. 2006, Monthly Notice of the Royal Astronomical Society, 365, 37 (ADS entry)

Bottema, R. 2003, Monthly Notice of the Royal Astronomical Society, 344, 358 (ADS entry)

Bottrell, C., et al. 2024, Monthly Notice of the Royal Astronomical Society, 527, 6506 (ADS entry)

Brinchmann, J., Charlot, S., White, S. D. M., Tremonti, C., Kauffmann, G., Heckman, T., & Brinkmann, J. 2004, Monthly Notice of the Royal Astronomical Society, 351, 1151 (ADS entry)

Brown, J. S., Martini, P., & Andrews, B. H. 2016, Monthly Notice of the Royal Astronomical Society, 458, 1529 (ADS entry)

Buck, T., Obreja, A., Macciò, A. V., Minchev, I., Dutton, A. A., & Ostriker, J. P. 2020, Monthly Notice of the Royal Astronomical Society, 491, 3461 (ADS entry)

Buder, S., Buck, T., Chen, Q.-H., & Grasha, K. 2024, arXiv e-prints, arXiv:2412.01157 (ADS entry)

Bundy, K., et al. 2015, Astrophysical Journal, 798, 7 (ADS entry)

Buta, R., Vasylyev, S., Salo, H., & Laurikainen, E. 2005, Astronomical Journal, 130, 506 (ADS entry)

Buta, R. J., Knapen, J. H., Elmegreen, B. G., Salo, H., Laurikainen, E., Elmegreen, D. M., Puerari, I., & Block, D. L. 2009, Astronomical Journal, 137, 4487 (ADS entry)

Calzetti, D. 2001, Publications of the Astronomical Society of the Pacific, 113, 1449 (ADS entry)

—. 2013, in Secular Evolution of Galaxies, ed. J. Falcón-Barroso & J. H. Knapen, 419 (ADS entry)

Cano-Díaz, M., Ávila-Reese, V., Sánchez, S. F., Hernández-Toledo, H. M., Rodríguez-

Puebla, A., Boquien, M., & Ibarra-Medel, H. 2019, Monthly Notice of the Royal Astronomical Society, 488, 3929 (ADS entry)

Cantalupo, S., et al. 2019, Monthly Notice of the Royal Astronomical Society, 483, 5188 (ADS entry)

Canzian, B. 1993, Astrophysical Journal, 414, 487 (ADS entry)

Capozziello, S., & Lattanzi, A. 2006, Astrophysics and Space Science, 301, 189 (ADS entry)

Cappellari, M. 2017a, Monthly Notice of the Royal Astronomical Society, 466, 798 (ADS entry)

—. 2017b, Monthly Notice of the Royal Astronomical Society, 466, 798 (ADS entry)

Cappellari, M., & Copin, Y. 2012, VorBin: Voronoi binning method, Astrophysics Source Code Library, record ascl:1211.006 (ADS entry)

Cappellari, M., & Emsellem, E. 2004a, Publications of the Astronomical Society of the Pacific, 116, 138 (ADS entry)

—. 2004b, Publications of the Astronomical Society of the Pacific, 116, 138 (ADS entry)

Carr, C., Johnston, K. V., Laporte, C. F. P., & Ness, M. K. 2022, Monthly Notice of the Royal Astronomical Society, 516, 5067 (ADS entry)

Cedrés, B., Cepa, J., Bongiovanni, Á., Castañeda, H., Sánchez-Portal, M., & Tomita, A. 2013, Astronomy and Astrophysics, 560, A59 (ADS entry)

Chabrier, G. 2003, Publications of the Astronomical Society of the Pacific, 115, 763 (ADS entry)

Chandrasekhar, S. 1931, Astrophysical Journal, 74, 81 (ADS entry)

Chang, P., & Chakrabarti, S. 2011, Monthly Notice of the Royal Astronomical Society, 416, 618 (ADS entry)

Chen, Q.-H., Grasha, K., Battisti, A. J., Kewley, L. J., Madore, B. F., Seibert, M., Rich, J. A., & Beaton, R. L. 2023, Monthly Notice of the Royal Astronomical Society, 519, 4801 (ADS entry)

Chen, Q.-H., et al. 2024a, Monthly Notice of the Royal Astronomical Society, 534, 883 (ADS entry)

—. 2024b, Monthly Notice of the Royal Astronomical Society, 527, 2991 (ADS entry)

Chevance, M., Krumholz, M. R., McLeod, A. F., Ostriker, E. C., Rosolowsky, E. W., & Sternberg, A. 2023, in Astronomical Society of the Pacific Conference Series, Vol. 534, Protostars and Planets VII, ed. S. Inutsuka, Y. Aikawa, T. Muto, K. Tomida, & M. Tamura, 1 (ADS entry)

Chevance, M., et al. 2020, Monthly Notice of the Royal Astronomical Society, 493, 2872 (ADS entry)

Choi, Y., Dalcanton, J. J., Williams, B. F., Weisz, D. R., Skillman, E. D., Fouesneau, M., & Dolphin, A. E. 2015, Astrophysical Journal, 810, 9 (ADS entry)

Cid Fernandes, R., Mateus, A., Sodré, L., Stasińska, G., & Gomes, J. M. 2005, Monthly Notice of the Royal Astronomical Society, 358, 363 (ADS entry)

Cluver, M. E., Jarrett, T. H., Dale, D. A., Smith, J. D. T., August, T., & Brown, M. J. I. 2017, Astrophysical Journal, 850, 68 (ADS entry)

Conselice, C. J. 2014, Annual Review of Astronomy and Astrophysics, 52, 291 (ADS entry)

Crain, R. A., et al. 2015, Monthly Notice of the Royal Astronomical Society, 450, 1937 (ADS entry)

Croom, S. M., et al. 2021, Monthly Notice of the Royal Astronomical Society, 505, 991 (ADS entry)

da Silva, R. L., Fumagalli, M., & Krumholz, M. 2012, Astrophysical Journal, 745, 145 (ADS entry)

D'Agostino, J. J., Poetrodjojo, H., Ho, I. T., Groves, B., Kewley, L., Madore, B. F., Rich, J., & Seibert, M. 2018, Monthly Notice of the Royal Astronomical Society, 479, 4907 (ADS entry)

Darg, D. W., et al. 2010, Monthly Notice of the Royal Astronomical Society, 401, 1552 (ADS entry)

Davé, R., Anglés-Alcázar, D., Narayanan, D., Li, Q., Rafieferantsoa, M. H., & Appleby, S. 2019, Monthly Notice of the Royal Astronomical Society, 486, 2827 (ADS entry)

Davé, R., Finlator, K., & Oppenheimer, B. D. 2011, Monthly Notice of the Royal Astronomical Society, 416, 1354 (ADS entry)

—. 2012, Monthly Notice of the Royal Astronomical Society, 421, 98 (ADS entry)

Davies, R. I., Sugai, H., & Ward, M. J. 1997, Molecular Hydrogen Emission in NGC 4536, Technical Report, OUAST/97/15 Astrophysics Dept. (ADS entry)

Davis, B. L., et al. 2015, Astrophysical Journal Letter, 802, L13 (ADS entry)

Davis, D. R., & Hayes, W. B. 2014, Astrophysical Journal, 790, 87 (ADS entry)

Davis, M., Efstathiou, G., Frenk, C. S., & White, S. D. M. 1985, ApJ, 292, 371

de Vaucouleurs, G. 1959, Handbuch der Physik, 53, 275 (ADS entry)

Denicoló, G., Terlevich, R., & Terlevich, E. 2002, Monthly Notice of the Royal Astronomical Society, 330, 69 (ADS entry)

Di Matteo, P., Haywood, M., Combes, F., Semelin, B., & Snaith, O. N. 2013, Astronomy and Astrophysics, 553, A102 (ADS entry)

Di Teodoro, E. M., & Fraternali, F. 2014, Astronomy and Astrophysics, 567, A68 (ADS entry)

Dobbs, C., & Baba, J. 2014, Publications of the Astronomical Society of Australia, 31, e035 (ADS entry)

Dobbs, C., & Pettitt, A. 2015, in Lessons from the Local Group: A Conference in honor of David Block and Bruce Elmegreen, ed. K. Freeman, B. Elmegreen, D. Block, & M. Woolway, 147–156 (ADS entry)

Dobbs, C. L., & Bonnell, I. A. 2008, Monthly Notice of the Royal Astronomical Society, 385, 1893 (ADS entry)

Dobbs, C. L., Pringle, J. E., & Naylor, T. 2014, Monthly Notice of the Royal Astronomical Society, 437, L31 (ADS entry)

Dobbs, C. L., Theis, C., Pringle, J. E., & Bate, M. R. 2010, Monthly Notice of the Royal Astronomical Society, 403, 625 (ADS entry)

Dobbs, C. L., et al. 2017, Monthly Notice of the Royal Astronomical Society, 464, 3580 (ADS entry)

D'Onghia, E., Vogelsberger, M., & Hernquist, L. 2013, Astrophysical Journal, 766, 34 (ADS entry)

Donner, K. J., & Thomasson, M. 1994, Astronomy and Astrophysics, 290, 785 (ADS entry)

Dopita, M. A., & Evans, I. N. 1986, Astrophysical Journal, 307, 431 (ADS entry)

Dopita, M. A., Kewley, L. J., Heisler, C. A., & Sutherland, R. S. 2000, Astrophysical Journal, 542, 224 (ADS entry)

Dopita, M. A., Kewley, L. J., Sutherland, R. S., & Nicholls, D. C. 2016, Astrophysics and Space Science, 361, 61 (ADS entry)

Draine, B. T. 2011, Physics of the Interstellar and Intergalactic Medium (ADS entry)

Dubois, Y., et al. 2014, Monthly Notice of the Royal Astronomical Society, 444, 1453 (ADS entry)

—. 2021, Astronomy and Astrophysics, 651, A109 (ADS entry)

Durbala, A., Buta, R., Sulentic, J. W., & Verdes-Montenegro, L. 2009, Monthly Notice of the Royal Astronomical Society, 397, 1756 (ADS entry)

Edmunds, M. G. 1990, Monthly Notice of the Royal Astronomical Society, 246, 678 (ADS entry)

Egusa, F., Kohno, K., Sofue, Y., Nakanishi, H., & Komugi, S. 2009, Astrophysical Journal, 697, 1870 (ADS entry)

Egusa, F., Mentuch Cooper, E., Koda, J., & Baba, J. 2017, Monthly Notice of the Royal Astronomical Society, 465, 460 (ADS entry)

Egusa, F., Sofue, Y., & Nakanishi, H. 2004, Publications of the Astronomical Society of Japan, 56, L45 (ADS entry)

Elagali, A., et al. 2019, Monthly Notice of the Royal Astronomical Society, 487, 2797 (ADS entry)

Eldridge, J. J., Stanway, E. R., Xiao, L., McClelland, L. A. S., Taylor, G., Ng, M., Greis, S. M. L., & Bray, J. C. 2017, Publications of the Astronomical Society of Australia, 34, e058 (ADS entry)

Eliche-Moral, M. C., González-García, A. C., Balcells, M., Aguerri, J. A. L., Gallego, J., Zamorano, J., & Prieto, M. 2011, Astronomy and Astrophysics, 533, A104 (ADS entry)

Elmegreen, B. G., Elmegreen, D. M., Knapen, J. H., Buta, R. J., Block, D. L., & Puerari, I. 2007, Astrophysical Journal Letter, 670, L97 (ADS entry)

Elmegreen, B. G., Elmegreen, D. M., & Seiden, P. E. 1989, Astrophysical Journal, 343, 602 (ADS entry)

Elmegreen, B. G., Galliano, E., & Alloin, D. 2009, Astrophysical Journal, 703, 1297 (ADS entry)

Elmegreen, D. M., & Elmegreen, B. G. 1982, Monthly Notice of the Royal Astronomical Society, 201, 1021 (ADS entry)

Falcón-Barroso, J., et al. 2006, Monthly Notice of the Royal Astronomical Society, 369, 529 (ADS entry)

Ferland, G. J., et al. 2013, Revista Mexicana de Astronomía y Astrofísica, 49, 137 (ADS entry)

Fitzpatrick, E. L., Massa, D., Gordon, K. D., Bohlin, R., & Clayton, G. C. 2019, Astrophysical Journal, 886, 108 (ADS entry)

Forgan, D. H., Ramón-Fox, F. G., & Bonnell, I. A. 2018, Monthly Notice of the Royal Astronomical Society, 476, 2384 (ADS entry)

Foster, C., et al. 2021, Publications of the Astronomical Society of Australia, 38, e031 (ADS entry)

Foyle, K., Rix, H. W., Dobbs, C. L., Leroy, A. K., & Walter, F. 2011, Astrophysical Journal, 735, 101 (ADS entry)

Fraternali, F., & Binney, J. J. 2008, Monthly Notice of the Royal Astronomical Society, 386, 935 (ADS entry)

Fuchs, B. 2001, Astronomy and Astrophysics, 368, 107 (ADS entry)

Fujii, M. S., Baba, J., Saitoh, T. R., Makino, J., Kokubo, E., & Wada, K. 2011, Astrophysical Journal, 730, 109 (ADS entry)

Fujimoto, M. 1968, Astrophysical Journal, 152, 391 (ADS entry)

Gaia Collaboration et al. 2016, Astronomy and Astrophysics, 595, A1 (ADS entry)

Gallazzi, A., Charlot, S., Brinchmann, J., White, S. D. M., & Tremonti, C. A. 2005, Monthly Notice of the Royal Astronomical Society, 362, 41 (ADS entry)

Garcia, A. M., et al. 2022, arXiv e-prints, arXiv:2212.03326 (ADS entry)

—. 2023, Monthly Notice of the Royal Astronomical Society, 519, 4716 (ADS entry)

—. 2024, Monthly Notice of the Royal Astronomical Society, 529, 3342 (ADS entry)

Garner, R., Mihos, J. C., Harding, P., & Garner, C. R. 2024, Astrophysical Journal, 961, 217 (ADS entry)

Garrison-Kimmel, S., Boylan-Kolchin, M., Bullock, J. S., & Lee, K. 2014, Monthly Notice of the Royal Astronomical Society, 438, 2578 (ADS entry)

Genel, S., et al. 2014, Monthly Notice of the Royal Astronomical Society, 445, 175 (ADS entry)

George, K., et al. 2018, Astronomy and Astrophysics, 614, A130 (ADS entry)

Gerola, H., & Seiden, P. E. 1978, Astrophysical Journal, 223, 129 (ADS entry)

Ghosh, S., & Jog, C. J. 2016, Monthly Notice of the Royal Astronomical Society, 459, 4057 (ADS entry)

Gittins, D. M., & Clarke, C. J. 2004, Monthly Notice of the Royal Astronomical Society, 349, 909 (ADS entry)

Goldreich, P., & Lynden-Bell, D. 1965, Monthly Notice of the Royal Astronomical Society, 130, 125 (ADS entry)

Goodwin, S. P., & Pagel, B. E. J. 2005, Monthly Notices of the Royal Astronomical Society, 359, 707 (Link)

Grand, R. J. J., Fragkoudi, F., Gómez, F. A., Jenkins, A., Marinacci, F., Pakmor, R., & Springel, V. 2024, Monthly Notice of the Royal Astronomical Society, 532, 1814 (ADS entry)

Grand, R. J. J., & Kawata, D. 2016, Astronomische Nachrichten, 337, 957 (ADS entry)

Grand, R. J. J., Kawata, D., & Cropper, M. 2012a, Monthly Notice of the Royal Astronomical Society, 426, 167 (ADS entry)

—. 2012b, Monthly Notice of the Royal Astronomical Society, 421, 1529 (ADS entry)

—. 2014, Monthly Notice of the Royal Astronomical Society, 439, 623 (ADS entry)

—. 2015, Monthly Notice of the Royal Astronomical Society, 447, 4018 (ADS entry)

Grand, R. J. J., et al. 2016, Monthly Notice of the Royal Astronomical Society, 460, L94 (ADS entry)

—. 2017, Monthly Notice of the Royal Astronomical Society, 467, 179 (ADS entry)

Grasha, K., et al. 2017, Astrophysical Journal, 842, 25 (ADS entry)

—. 2022, Astrophysical Journal, 929, 118 (ADS entry)

Grohs, E., & Fuller, G. M. 2022, in Handbook of Nuclear Physics, 127 (ADS entry)

Gurzadyan, G. A. 1997, The Physics and Dynamics of Planetary Nebulae (Springer-Verlag Berlin Heidelberg New York) (ADS entry)

Hess, K. M., Pisano, D. J., Wilcots, E. M., & Chengalur, J. N. 2009, Astrophysical Journal, 699, 76 (ADS entry)

Ho, I. T. 2016, LZIFU: IDL emission line fitting pipeline for integral field spectroscopy data (ADS entry)

Ho, I.-T., et al. 2016, Astrophysics and Space Science, 361 (Link)

Ho, I. T., et al. 2017, Astrophysical Journal, 846, 39 (ADS entry)

—. 2018, Astronomy and Astrophysics, 618, A64 (ADS entry)

—. 2019, Astrophysical Journal Letter, 885, L31 (ADS entry)

Hockney, R. W., & Brownrigg, D. R. K. 1974, Monthly Notice of the Royal Astronomical Society, 167, 351 (ADS entry)

Hohl, F. 1971, Astrophysical Journal, 168, 343 (ADS entry)

Holmberg, E. 1941, Astrophysical Journal, 94, 385 (ADS entry)

Honma, M., Nagayama, T., & Sakai, N. 2015, Publications of the Astronomical Society of Japan, 67, 70 (ADS entry)

Hopkins, P. F., et al. 2018, Monthly Notice of the Royal Astronomical Society, 480, 800 (ADS entry)

Horie, S., Okamoto, T., & Habe, A. 2024, Monthly Notice of the Royal Astronomical Society, 527, 10077 (ADS entry)

Hsu, C.-J., Tan, J. C., Christie, D., Cheng, Y., & O'Neill, T. J. 2023, Monthly Notice of the Royal Astronomical Society, 522, 700 (ADS entry)

Hubble, E. P. 1926, Astrophysical Journal, 64, 321 (ADS entry)

Hunt, J. A. S., & Kawata, D. 2013, Monthly Notice of the Royal Astronomical Society, 430, 1928 (ADS entry)

Hunter, G. H., Clark, P. C., Glover, S. C. O., & Klessen, R. S. 2023, Monthly Notice of the Royal Astronomical Society, 519, 4152 (ADS entry)

Jacoby, G. H., Hunter, D. A., & Christian, C. A. 1984, Astrophysical Journal Supplement, 56, 257 (ADS entry)

Jarrett, T. H., Chester, T., Cutri, R., Schneider, S. E., & Huchra, J. P. 2003, Astronomical Journal, 125, 525 (ADS entry)

Jarrett, T. H., et al. 2013, Astronomical Journal, 145, 6 (ADS entry)

Jenkins, A. 2010, Monthly Notice of the Royal Astronomical Society, 403, 1859 (ADS entry)

Jensen, E. B., Strom, K. M., & Strom, S. E. 1976, Astrophysical Journal, 209, 748 (ADS entry)

Jin, Y., Kewley, L. J., & Sutherland, R. S. 2022, Astrophysical Journal Letter, 934, L8 (ADS entry)

Jorsater, S., & van Moorsel, G. A. 1995, Astronomical Journal, 110, 2037 (ADS entry)

Ju, M., et al. 2025, Astrophysical Journal Letter, 978, L39 (ADS entry)

Julian, W. H., & Toomre, A. 1966, Astrophysical Journal, 146, 810 (ADS entry)

Kaleida, C., & Scowen, P. A. 2010, Astronomical Journal, 140, 379 (ADS entry)

Karademir, G. S., Remus, R.-S., Burkert, A., Dolag, K., Hoffmann, T. L., Moster, B. P., Steinwandel, U. P., & Zhang, J. 2019, Monthly Notice of the Royal Astronomical Society, 487, 318 (ADS entry)

Karakas, A. I. 2010, Monthly Notice of the Royal Astronomical Society, 403, 1413 (ADS entry)

Kauffmann, G., et al. 2003a, Monthly Notice of the Royal Astronomical Society, 341, 33 (ADS entry)

—. 2003b, Monthly Notice of the Royal Astronomical Society, 346, 1055 (ADS entry)

Kelkar, K., et al. 2023, Astronomy and Astrophysics, 680, A54 (ADS entry)

Kennicutt, Jr., R. C. 1998, Astrophysical Journal, 498, 541 (ADS entry)

Kewley, L. J., & Dopita, M. A. 2002, Astrophysical Journal Supplement, 142, 35 (ADS entry)

Kewley, L. J., Dopita, M. A., Sutherland, R. S., Heisler, C. A., & Trevena, J. 2001, Astrophysical Journal, 556, 121 (ADS entry)

Kewley, L. J., & Ellison, S. L. 2008, Astrophysical Journal, 681, 1183 (ADS entry)

Kewley, L. J., Geller, M. J., & Barton, E. J. 2006, Astronomical Journal, 131, 2004 (ADS entry)

Kewley, L. J., Nicholls, D. C., & Sutherland, R. S. 2019, Annual Review of Astronomy and Astrophysics, 57, 511 (ADS entry)

Kewley, L. J., Rupke, D., Zahid, H. J., Geller, M. J., & Barton, E. J. 2010, Astrophysical Journal Letter, 721, L48 (ADS entry)

Khoperskov, A. V., Khoperskov, S. A., Zasov, A. V., Bizyaev, D. V., & Khrapov, S. S. 2013, Monthly Notice of the Royal Astronomical Society, 431, 1230 (ADS entry)

Khoperskov, S., Di Matteo, P., Haywood, M., & Combes, F. 2018, Astronomy and Astrophysics, 611, L2 (ADS entry)

Khoperskov, S., Sivkova, E., Saburova, A., Vasiliev, E., Shustov, B., Minchev, I., & Walcher, C. J. 2023, Astronomy and Astrophysics, 671, A56 (ADS entry)

Khrapov, S., Khoperskov, A., & Korchagin, V. 2021, Galaxies, 9, 29 (ADS entry)

Kim, W., Kim, C., & Ostriker, E. 2021, in American Astronomical Society Meeting Abstracts, Vol. 237, American Astronomical Society Meeting Abstracts, 148.08 (ADS entry)

Kobulnicky, H. A., & Kewley, L. J. 2004, Astrophysical Journal, 617, 240 (ADS entry)

Kreckel, K., et al. 2019, Astrophysical Journal, 887, 80 (ADS entry)

Kroupa, P. 2001, Monthly Notice of the Royal Astronomical Society, 322, 231 (ADS entry)

Krumholz, M. R., Burkhart, B., Forbes, J. C., & Crocker, R. M. 2018, Monthly Notice of the Royal Astronomical Society, 477, 2716 (ADS entry)

Kuhn, V., Guo, Y., Martin, A., Bayless, J., Gates, E., & Puleo, A. 2024, Astrophysical Journal Letter, 968, L15 (ADS entry)

Kumari, N., Maiolino, R., Belfiore, F., & Curti, M. 2019, Monthly Notices of the Royal Astronomical Society, 485, 367–381 (Link)

Lamastra, A., et al. 2016, Astronomy and Astrophysics, 596, A68 (ADS entry)

Lan, Y., Tang, L., Lin, W., & Gong, J. 2024, Astrophysical Journal, 974, 40 (ADS entry)

Law, D. R., Shapley, A. E., Steidel, C. C., Reddy, N. A., Christensen, C. R., & Erb, D. K. 2012, Nature, 487, 338 (ADS entry)

Lazariv, T., & Lehmann, C. 2018, arXiv e-prints, arXiv:1810.09753 (ADS entry)

Leroy, A. K., et al. 2019, The Astrophysical Journal Supplement Series, 244, 24 (Link)

Li, Z., Krumholz, M. R., Wisnioski, E., Mendel, J. T., Kewley, L. J., Sánchez, S. F., & Galbany, L. 2021, Monthly Notice of the Royal Astronomical Society, 504, 5496 (ADS entry)

Li, Z., et al. 2024, Monthly Notice of the Royal Astronomical Society, 528, 7103 (ADS entry)

Lilly, S. J., Carollo, C. M., Pipino, A., Renzini, A., & Peng, Y. 2013, Astrophysical Journal, 772, 119 (ADS entry)

Lin, C. C., & Shu, F. H. 1964, Astrophysical Journal, 140, 646 (ADS entry)

—. 1966, Proceedings of the National Academy of Science, 55, 229 (ADS entry)

Lindblad, P. A. B., Lindblad, P. O., & Athanassoula, E. 1996, Astronomy and Astrophysics, 313, 65 (ADS entry)

Lindblad, P. O. 1960, Stockholms Observatoriums Annaler, 4, 4 (ADS entry)

Lintott, C., et al. 2011, Monthly Notice of the Royal Astronomical Society, 410, 166 (ADS entry)

Lintott, C. J., et al. 2008, Monthly Notice of the Royal Astronomical Society, 389, 1179 (ADS entry)

Maiolino, R., & Mannucci, F. 2019, The Astronomy and Astrophysics Review, 27, 3 (ADS entry)

Malin, D., & Hadley, B. 1997, Publications of the Astronomical Society of Australia, 14, 52 (ADS entry)

Marchuk, A. A., & Sotnikova, N. Y. 2018, Monthly Notice of the Royal Astronomical Society, 475, 4891 (ADS entry)

Margalef-Bentabol, B., Conselice, C. J., Haeussler, B., Casteels, K., Lintott, C., Masters, K., & Simmons, B. 2022, Monthly Notice of the Royal Astronomical Society, 511, 1502 (ADS entry)

Marinacci, F., Pakmor, R., & Springel, V. 2014, Monthly Notice of the Royal Astronomical Society, 437, 1750 (ADS entry)

Marino, R. A., et al. 2012, Astrophysical Journal, 754, 61 (ADS entry)

—. 2016, Astronomy and Astrophysics, 585, A47 (ADS entry)

Martig, M., Bournaud, F., Croton, D. J., Dekel, A., & Teyssier, R. 2012, Astrophysical Journal, 756, 26 (ADS entry)

Martig, M., et al. 2013, Monthly Notice of the Royal Astronomical Society, 432, 1914 (ADS entry)

Martínez-García, E. E. 2012, Astrophysical Journal, 744, 92 (ADS entry)

Martínez-García, E. E., González-López lira, R. A., & Bruzual-A, G. 2009a, Astrophysical Journal, 694, 512 (ADS entry)

—. 2009b, Astrophysical Journal, 694, 512 (ADS entry)

Martínez-García, E. E., González-López lira, R. A., & Puerari, I. 2023, Monthly Notice of the Royal Astronomical Society, 524, 18 (ADS entry)

Matteucci, F., Panagia, N., Pipino, A., Mannucci, F., Recchi, S., & Della e, M. 2006, Monthly Notices of the Royal Astronomical Society, 372, 265 (Link)

Medling, A. M., et al. 2018, Monthly Notice of the Royal Astronomical Society, 475, 5194 (ADS entry)

Meidt, S. E., et al. 2013, Astrophysical Journal, 779, 45 (ADS entry)

Michikoshi, S., & Kokubo, E. 2016, Astrophysical Journal, 821, 35 (ADS entry)

Mihos, J. C., & Bothun, G. D. 1997, Astrophysical Journal, 481, 741 (ADS entry)

Miller, R. H., Prendergast, K. H., & Quirk, W. J. 1970, Astrophysical Journal, 161, 903 (ADS entry)

Minchev, I., & Famaey, B. 2010, Astrophysical Journal, 722, 112 (ADS entry)

Minchev, I., Famaey, B., Combes, F., Di Matteo, P., Mouhcine, M., & Wozniak, H. 2011, Astronomy and Astrophysics, 527, A147 (ADS entry)

Mo, H., van den Bosch, F. C., & White, S. 2010, Galaxy Formation and Evolution (ADS entry)

Mueller, M. W., & Arnett, W. D. 1976, Astrophysical Journal, 210, 670 (ADS entry)

Nelson, D., et al. 2015, Astronomy and Computing, 13, 12 (ADS entry)

Noll, S., Burgarella, D., Giovannoli, E., Buat, V., Marcillac, D., & Muñoz-Mateos, J. C. 2009, Astronomy and Astrophysics, 507, 1793 (ADS entry)

Oh, S. H., Kim, W.-T., & Lee, H. M. 2015, Astrophysical Journal, 807, 73 (ADS entry)

Oh, S. H., Kim, W.-T., Lee, H. M., & Kim, J. 2008, Astrophysical Journal, 683, 94 (ADS entry)

Orr, M. E., et al. 2023, Monthly Notice of the Royal Astronomical Society, 521, 3708 (ADS entry)

Osterbrock, D. E. 1989, Astrophysics of gaseous nebulae and active galactic nuclei (University Science Book) (ADS entry)

Pagel, B. E. J., Edmunds, M. G., Blackwell, D. E., Chun, M. S., & Smith, G. 1979, Monthly Notice of the Royal Astronomical Society, 189, 95 (ADS entry)

Pakmor, R., Springel, V., Bauer, A., Mocz, P., Munoz, D. J., Ohlmann, S. T., Schaal, K., & Zhu, C. 2016, Monthly Notice of the Royal Astronomical Society, 455, 1134 (ADS entry)

Palicio, P. A., et al. 2025, Astronomy and Astrophysics, 695, A193 (ADS entry)

Pan, Y. C., Foley, R. J., Jones, D. O., Filippenko, A. V., & Kuin, N. P. M. 2020, Monthly Notice of the Royal Astronomical Society, 491, 5897 (ADS entry)

Pancoast, A., Sajina, A., Lacy, M., Noriega-Crespo, A., & Rho, J. 2010, Astrophysical Journal, 723, 530 (ADS entry)

Parikh, T., Thomas, D., Maraston, C., Westfall, K. B., Andrews, B. H., Boardman, N. F., Drory, N., & Oyarzun, G. 2021, Monthly Notice of the Royal Astronomical Society, 502, 5508 (ADS entry)

Perez, J., Michel-Dansac, L., & Tissera, P. B. 2011, Monthly Notice of the Royal Astronomical Society, 417, 580 (ADS entry)

Pérez-Montero, E., & Contini, T. 2009, Monthly Notice of the Royal Astronomical Society, 398, 949 (ADS entry)

Peterken, T. G., Merrifield, M. R., Aragón-Salamanca, A., Drory, N., Krawczyk, C. M., Masters, K. L., Weijmans, A.-M., & Westfall, K. B. 2019, Nature Astronomy, 3, 178 (ADS entry)

Pettini, M., & Pagel, B. E. J. 2004, Monthly Notice of the Royal Astronomical Society, 348, L59 (ADS entry)

Pettitt, A. R., Dobbs, C. L., Baba, J., Colombo, D., Duarte-Cabral, A., Egusa, F., & Habe, A. 2020, Monthly Notice of the Royal Astronomical Society, 498, 1159 (ADS entry)

Pettitt, A. R., Tasker, E. J., & Wadsley, J. W. 2016, Monthly Notice of the Royal Astronomical Society, 458, 3990 (ADS entry)

Pettitt, A. R., Tasker, E. J., Wadsley, J. W., Keller, B. W., & Benincasa, S. M. 2017, Monthly Notice of the Royal Astronomical Society, 468, 4189 (ADS entry)

Pettitt, A. R., & Wadsley, J. W. 2018, Monthly Notice of the Royal Astronomical Society, 474, 5645 (ADS entry)

Pfleiderer, J., & Siedentopf, H. 1961, Zeitschrift für Astrophysik, 51, 201 (ADS entry)

Pickles, A. J. 1998, Publications of the Astronomical Society of the Pacific, 110, 863 (ADS entry)

Pikel'Ner, S. B. 1965, Soviet Astronomy, 9, 408 (ADS entry)

Pilyugin, L. S., Ferrini, F., & Shkvarun, R. V. 2003, Astronomy and Astrophysics, 401, 557 (ADS entry)

Pilyugin, L. S., & Grebel, E. K. 2016, Monthly Notice of the Royal Astronomical Society, 457, 3678 (ADS entry)

Planck Collaboration et al. 2014, Astronomy and Astrophysics, 571, A16 (ADS entry)

Poetrodjojo, H., D'Agostino, J. J., Groves, B., Kewley, L., Ho, I. T., Rich, J., Madore, B. F., & Seibert, M. 2019, Monthly Notice of the Royal Astronomical Society, 487, 79 (ADS entry)

Poggio, E., et al. 2022, Astronomy and Astrophysics, 666, L4 (ADS entry)

Pohlen, M., Martínez-Delgado, D., Majewski, S., Palma, C., Prada, F., & Balcells, M. 2004, in Astronomical Society of the Pacific Conference Series, Vol. 327, Satellites and Tidal Streams, ed. F. Prada, D. Martinez Delgado, & T. J. Mahoney, 288 (ADS entry)

Portinari, L., Chiosi, C., & Bressan, A. 1998, Astronomy and Astrophysics, 334, 505 (ADS entry)

Pour-Imani, H., Kennefick, D., Kennefick, J., Davis, B. L., Shields, D. W., & Shameer Abdeen, M. 2016, Astrophysical Journal Letter, 827, L2 (ADS entry)

Prantzos, N., & Boissier, S. 2000, Monthly Notice of the Royal Astronomical Society, 313, 338 (ADS entry)

Puerari, I., & Dottori, H. 1997, Astrophysical Journal Letter, 476, L73 (ADS entry)

Qu, Y., Di Matteo, P., Lehnert, M. D., van Driel, W., & Jog, C. J. 2011, Astronomy and Astrophysics, 535, A5 (ADS entry)

Querejeta, M., et al. 2021, Astronomy and Astrophysics, 656, A133 (ADS entry)

—. 2024, Astronomy and Astrophysics, 687, A293 (ADS entry)

Quinn, J. R., et al. 2025, arXiv e-prints, arXiv:2507.22793 (ADS entry)

Ramón-Fox, F. G., & Bonnell, I. A. 2022, Monthly Notice of the Royal Astronomical Society, 512, 1111 (ADS entry)

Reid, M. J., et al. 2014, Astrophysical Journal, 783, 130 (ADS entry)

Remus, R.-S., & Forbes, D. A. 2022, Astrophysical Journal, 935, 37 (ADS entry)

Ristea, A., et al. 2022, Monthly Notice of the Royal Astronomical Society, 517, 2677 (ADS entry)

Roberts, W. W., J. 1970, in The Spiral Structure of our Galaxy, Vol. 38, 415 (ADS entry)

Roberts, Jr., W. W., Roberts, M. S., & Shu, F. H. 1975, Astrophysical Journal, 196, 381 (ADS entry)

Robinson, H., Wadsley, J., Sellwood, J. A., & Pudritz, R. E. 2025, arXiv e-prints, arXiv:2506.16515 (ADS entry)

Robles, S., Gómez, J. S., Ramírez Rivera, A., Padilla, N. D., & Dujovne, D. 2022, Monthly Notice of the Royal Astronomical Society, 514, 3692 (ADS entry)

Robotham, A. S. G., Davies, L. J. M., Driver, S. P., Koushan, S., Taranu, D. S., Casura, S., & Liske, J. 2018, Monthly Notice of the Royal Astronomical Society, 476, 3137 (ADS entry)

Robotham, A. S. G., et al. 2011, Monthly Notice of the Royal Astronomical Society, 416, 2640 (ADS entry)

Rodríguez-Baras, M., Díaz, A. I., Rosales-Ortega, F. F., & Sánchez, S. F. 2018, Astronomy and Astrophysics, 609, A102 (ADS entry)

Rosario, D. J., Mendel, J. T., Ellison, S. L., Lutz, D., & Trump, J. R. 2016, Monthly Notice of the Royal Astronomical Society, 457, 2703 (ADS entry)

Rosse, T. E. O. 1850, Philosophical Transactions of the Royal Society of London Series I, 140, 499 (ADS entry)

Rots, A. H., & Shane, W. W. 1975, Astronomy and Astrophysics, 45, 25 (ADS entry)

Röttgers, B., Naab, T., & Oser, L. 2014, Monthly Notice of the Royal Astronomical Society, 445, 1065 (ADS entry)

Roškar, R., Debattista, V. P., Quinn, T. R., & Wadsley, J. 2012, Monthly Notice of the Royal Astronomical Society, 426, 2089 (ADS entry)

Rozas, M., Knapen, J. H., & Beckman, J. E. 1996, Astronomy and Astrophysics, 312, 275 (ADS entry)

Ruiz-Lara, T., et al. 2017, Astronomy and Astrophysics, 604, A4 (ADS entry)

Rupke, D. S. N., Kewley, L. J., & Barnes, J. E. 2010a, Astrophysical Journal Letter, 710, L156 (ADS entry)

Rupke, D. S. N., Kewley, L. J., & Chien, L. H. 2010b, Astrophysical Journal, 723, 1255 (ADS entry)

Ryder, S. D., Walsh, W., & Malin, D. 1999, Publications of the Astronomical Society of Australia, 16, 84 (ADS entry)

Sakhibov, F., Gusev, A. S., & Hemmerich, C. 2021, Monthly Notice of the Royal Astronomical Society, 508, 912 (ADS entry)

Salo, H., Laurikainen, E., Buta, R., & Knapen, J. H. 2010, Astrophysical Journal Letter, 715, L56 (ADS entry)

Salpeter, E. E. 1955, Astrophysical Journal, 121, 161 (ADS entry)

Sánchez, S. F., et al. 2015, Astronomy and Astrophysics, 573, A105 (ADS entry)

Sánchez-Gil, M. C., Jones, D. H., Pérez, E., Bland-Hawthorn, J., Alfaro, E. J., & O'Byrne, J. 2011, Monthly Notice of the Royal Astronomical Society, 415, 753 (ADS entry)

Sánchez-Menguiano, L., Sánchez Almeida, J., Muñoz-Tuñón, C., & Sánchez, S. F. 2020, Astrophysical Journal, 903, 52 (ADS entry)

Sánchez-Menguiano, L., et al. 2016, Astrophysical Journal Letter, 830, L40 (ADS entry)

—. 2018, Astronomy and Astrophysics, 609, A119 (ADS entry)

Santoro, F., et al. 2022, Astronomy and Astrophysics, 658, A188 (ADS entry)

Sarzi, M., et al. 2006, Monthly Notice of the Royal Astronomical Society, 366, 1151 (ADS entry)

Savchenko, S., Marchuk, A., Mosenkov, A., & Grishunin, K. 2020, Monthly Notice of the Royal Astronomical Society, 493, 390 (ADS entry)

Scarano, S., & Lépine, J. R. D. 2013, Monthly Notice of the Royal Astronomical Society, 428, 625 (ADS entry)

Schaye, J., et al. 2015, Monthly Notice of the Royal Astronomical Society, 446, 521 (ADS entry)

Scheepmaker, R. A., Lamers, H. J. G. L. M., Anders, P., & Larsen, S. S. 2009, Astronomy and Astrophysics, 494, 81 (ADS entry)

Schinnerer, E., et al. 2013, Astrophysical Journal, 779, 42 (ADS entry)

Sellwood, J. A. 2011, Monthly Notice of the Royal Astronomical Society, 410, 1637 (ADS entry)

Sellwood, J. A., & Binney, J. J. 2002, Monthly Notice of the Royal Astronomical Society, 336, 785 (ADS entry)

Sellwood, J. A., & Carlberg, R. G. 1984, Astrophysical Journal, 282, 61 (ADS entry)

—. 2014, Astrophysical Journal, 785, 137 (ADS entry)

Sellwood, J. A., & Carlberg, R. G. 2019, Monthly Notices of the Royal Astronomical Society, 489, 116 (Link)

Sellwood, J. A., & Masters, K. L. 2022, Annual Review of Astronomy and Astrophysics, 60 (ADS entry)

Semczuk, M., Lokas, E. L., & del Pino, A. 2017, Astrophysical Journal, 834, 7 (ADS entry)

Semczuk, M., Lokas, E. L., Salomon, J.-B., Athanassoula, E., & D'Onghia, E. 2018, Astrophysical Journal, 864, 34 (ADS entry)

Sempere, M. J., Garcia-Burillo, S., Combes, F., & Knapen, J. H. 1995, Astronomy and Astrophysics, 296, 45 (ADS entry)

Seo, W.-Y., & Kim, W.-T. 2014, Astrophysical Journal, 792, 47 (ADS entry)

Sextl, E., et al. 2024, Astrophysical Journal, 960, 83 (ADS entry)

—. 2025, Astrophysical Journal, 987, 138 (ADS entry)

Shabani, F., et al. 2018, Monthly Notice of the Royal Astronomical Society, 478, 3590 (ADS entry)

Shapley, A. E., et al. 2019, The Astrophysical Journal, 881, L35 (Link)

Sharda, P., Ginzburg, O., Krumholz, M. R., Forbes, J. C., Wisnioski, E., Mingozzi, M., Zovaro, H. R. M., & Dekel, A. 2023, arXiv e-prints, arXiv:2303.15853 (ADS entry)

Sharda, P., Krumholz, M. R., Wisnioski, E., Forbes, J. C., Federrath, C., & Acharyya, A. 2021, Monthly Notice of the Royal Astronomical Society, 502, 5935 (ADS entry)

Sharp, R., et al. 2016, in Society of Photo-Optical Instrumentation Engineers (SPIE) Conference Series, Vol. 9908, Ground-based and Airborne Instrumentation for Astronomy VI, ed. C. J. Evans, L. Simard, & H. Takami, 99081Y (ADS entry)

Shimizu, I., Todoroki, K., Yajima, H., & Nagamine, K. 2019, Monthly Notice of the Royal Astronomical Society, 484, 2632 (ADS entry)

Shu, F. H. 2016, Annual Review of Astronomy and Astrophysics, 54, 667 (ADS entry)

Silva-Villa, E., & Larsen, S. S. 2012, Astronomy and Astrophysics, 537, A145 (ADS entry)

Simpson, C., Wilson, A. S., Bower, G., Heckman, T. M., Krolik, J. H., & Miley, G. K. 1997, Astrophysical Journal, 474, 121 (ADS entry)

Slater, R., et al. 2019, Astronomy and Astrophysics, 621, A83 (ADS entry)

Smith, B., Sigurdsson, S., & Abel, T. 2008, Monthly Notice of the Royal Astronomical Society, 385, 1443 (ADS entry)

Soto, K. T., Lilly, S. J., Bacon, R., Richard, J., & Conseil, S. 2016, Monthly Notice of the Royal Astronomical Society, 458, 3210 (ADS entry)

Spitoni, E., Cescutti, G., Minchev, I., Matteucci, F., Silva Aguirre, V., Martig, M., Bono, G., & Chiappini, C. 2019, Astronomy and Astrophysics, 628, A38 (ADS entry)

Spitoni, E., et al. 2023, Astronomy and Astrophysics, 680, A85 (ADS entry)

Springel, V. 2005, Monthly Notice of the Royal Astronomical Society, 364, 1105 (ADS entry)

Springel, V., Di Matteo, T., & Hernquist, L. 2005, Monthly Notice of the Royal Astronomical Society, 361, 776 (ADS entry)

Springel, V., & Hernquist, L. 2003, Monthly Notice of the Royal Astronomical Society, 339, 289 (ADS entry)

Springel, V., White, M., & Hernquist, L. 2001, ApJ, 549, 681, _eprint: astro-ph/0008133

Springel, V., et al. 2008, Monthly Notice of the Royal Astronomical Society, 391, 1685 (ADS entry)

Stadel, J., Potter, D., Moore, B., Diemand, J., Madau, P., Zemp, M., Kuhlen, M., & Quilis, V. 2009, Monthly Notice of the Royal Astronomical Society, 398, L21 (ADS entry)

Steinicke, W. 2012, Journal of Astronomical History and Heritage, 15, 19 (ADS entry)

Struck, C., Dobbs, C. L., & Hwang, J.-S. 2011, Monthly Notice of the Royal Astronomical Society, 414, 2498 (ADS entry)

Sundelius, B., Thomasson, M., Valtonen, M. J., & Byrd, G. G. 1987, Astronomy and Astrophysics, 174, 67 (ADS entry)

Sutherland, R. S., & Dopita, M. A. 1993, Astrophysical Journal Supplement, 88, 253 (ADS entry)

Sánchez, S., et al. 2015, Galaxies, 3, 164–183 (Link)

Tagger, M., Sygnet, J. F., Athanassoula, E., & Pellat, R. 1987, Astrophysical Journal Letter, 318, L43 (ADS entry)

Tamburro, D., Rix, H. W., Walter, F., Brinks, E., de Blok, W. J. G., Kennicutt, R. C., & Mac Low, M. M. 2008, Astronomical Journal, 136, 2872 (ADS entry)

Taylor, E. N., et al. 2011, Monthly Notice of the Royal Astronomical Society, 418, 1587 (ADS entry)

Thatte, N., et al. 2021, The Messenger, 182, 7 (ADS entry)

Thielemann, F. K., et al. 2003, Nuclear Physics A, 718, 139 (ADS entry)

Thomasson, M., Elmegreen, B. G., Donner, K. J., & Sundelius, B. 1990, Astrophysical Journal Letter, 356, L9 (ADS entry)

Tinsley, B. M., & Larson, R. B. 1978, Astrophysical Journal, 221, 554 (ADS entry)

Toomre, A. 1964, Astrophysical Journal, 139, 1217 (ADS entry)

—. 1969, Astrophysical Journal, 158, 899 (ADS entry)

—. 1977, Annual Review of Astronomy and Astrophysics, 15, 437 (ADS entry)

Toomre, A. 1981, in Structure and Evolution of Normal Galaxies, ed. S. M. Fall & D. Lynden-Bell, 111–136 (ADS entry)

Toomre, A., & Toomre, J. 1972, Astrophysical Journal, 178, 623 (ADS entry)

Torrey, P., Vogelsberger, M., Genel, S., Sijacki, D., Springel, V., & Hernquist, L. 2014, Monthly Notice of the Royal Astronomical Society, 438, 1985 (ADS entry)

Tsukui, T., & Iguchi, S. 2021, Science, 372, 1201 (ADS entry)

Tutukov, A. V., & Fedorova, A. V. 2006, Astronomy Reports, 50, 785 (ADS entry)

Tweed, D., Devriendt, J., Blaizot, J., Colombi, S., & Slyz, A. 2009, Astronomy and Astrophysics, 506, 647 (ADS entry)

Vallée, J. P. 2022, Astrophysics and Space Science, 367, 26 (ADS entry)

van der Velden, E. 2020, Journal of Open Source Software, 5, 2004 (Link)

van Dokkum, P., et al. 2023, Astrophysical Journal Letter, 946, L50 (ADS entry)

Vazdekis, A., Ricciardelli, E., Cenarro, A. J., Rivero-González, J. G., Díaz-García, L. A., & Falcón-Barroso, J. 2012, Monthly Notices of the Royal Astronomical Society, 424, 157 (Link)

Vazdekis, A., et al. 2015, Monthly Notice of the Royal Astronomical Society, 449, 1177 (ADS entry)

Villalobos, Á., & Helmi, A. 2008, Monthly Notice of the Royal Astronomical Society, 391, 1806 (ADS entry)

Vogelsberger, M., Marinacci, F., Torrey, P., & Puchwein, E. 2020, Nature Reviews Physics, 2, 42 (ADS entry)

Vogelsberger, M., et al. 2014a, Monthly Notice of the Royal Astronomical Society, 444, 1518 (ADS entry)

—. 2014b, Nature, 509, 177 (ADS entry)

Vogt, F. P. A., Pérez, E., Dopita, M. A., Verdes-Montenegro, L., & Borthakur, S. 2017, Astronomy and Astrophysics, 601, A61 (ADS entry)

Vollmer, B., Wong, O. I., Braine, J., Chung, A., & Kenney, J. D. P. 2012, Astronomy and Astrophysics, 543, A33 (ADS entry)

von Hoerner, S. 1960, Zeitschrift für Astrophysik, 50, 184 (ADS entry)

Wada, K., Baba, J., & Saitoh, T. R. 2011, Astrophysical Journal, 735, 1 (ADS entry)

Wang, L., Dutton, A. A., Stinson, G. S., Macciò, A. V., Penzo, C., Kang, X., Keller, B. W., & Wadsley, J. 2015, Monthly Notice of the Royal Astronomical Society, 454, 83 (ADS entry)

Wei, P., Zou, H., Lin, L., Zhou, X., Liu, X., Kong, X., Ma, L., & Ma, S.-G. 2021, Research in Astronomy and Astrophysics, 21, 006 (ADS entry)

Weilbacher, P. M., et al. 2020, Astronomy and Astrophysics, 641, A28 (ADS entry)

Werk, J. K., Putman, M. E., Meurer, G. R., Thilker, D. A., Allen, R. J., Bland-Hawthorn, J., Kravtsov, A., & Freeman, K. 2010, Astrophysical Journal, 715, 656 (ADS entry)

Wetzel, A., et al. 2023, Astrophysical Journal Supplement, 265, 44 (ADS entry)

Wetzel, A. R., Hopkins, P. F., Kim, J.-h., Faucher-Giguère, C.-A., Kereš, D., & Quataert, E. 2016, Astrophysical Journal Letter, 827, L23 (ADS entry)

Weżgowiec, M., Beck, R., Hanasz, M., Soida, M., Ehle, M., Dettmar, R. J., & Urbanik, M. 2022, Astronomy and Astrophysics, 665, A64 (ADS entry)

Wild, V., Charlot, S., Brinchmann, J., Heckman, T., Vince, O., Pacifici, C., & Chevallard, J. 2011, Monthly Notice of the Royal Astronomical Society, 417, 1760 (ADS entry)

Willett, K. W., et al. 2013, Monthly Notice of the Royal Astronomical Society, 435, 2835 (ADS entry)

—. 2017, Monthly Notice of the Royal Astronomical Society, 464, 4176 (ADS entry)

Wisnioski, E., et al. 2015, Astrophysical Journal, 799, 209 (ADS entry)

Yin, S. Y., Liang, Y. C., Hammer, F., Brinchmann, J., Zhang, B., Deng, L. C., & Flores, H. 2007, Astronomy and Astrophysics, 462, 535 (ADS entry)

York, D. G., et al. 2000, Astronomical Journal, 120, 1579 (ADS entry)

Yu, S.-Y., & Ho, L. C. 2018, Astrophysical Journal, 869, 29 (ADS entry)

—. 2019, Astrophysical Journal, 871, 194 (ADS entry)

Zaritsky, D., et al. 2023, Monthly Notice of the Royal Astronomical Society, 524, 1431 (ADS entry)

Zhang, K., et al. 2017a, Monthly Notice of the Royal Astronomical Society, 466, 3217 (ADS entry)

—. 2017b, Monthly Notice of the Royal Astronomical Society, 466, 3217 (ADS entry)